COMPRESSIVE BEHAVIOR AND FAILURE OF COMPOSITE SANDWICH PANELS

by

Tracy J. Vogler

B. S. E. S. M., Virginia Polytechnic Institute and State University

(1992)

Submitted to the Department of Aeronautics and Astronautics

in partial fulfillment of

the requirements for the degree of

Master of Science

in Aeronautics and Astronautics

at the

Massachusetts Institute of Technology

September 1994

Signature of Author _____

Department of Aeronautics and Astronautics

June 27, 1994

Certified by _____

Professor Paul A. Lagace

Thesis Supervisor

Accepted by _____

Professor Harold Y. Wachman

Chairman, Departmental Graduate Committee

Compressive Behavior and Failure of Composite Sandwich Panels

by

Tracy J. Vogler

Submitted to the Department of Aeronautics and Astronautics on June 27, 1994 in partial fulfillment of the requirements for the degree of Master of Science.

Abstract

Work was conducted to examine the effect of damage on the behavior and failure of composite sandwich panels loaded in compression, including effects of finite specimen size. Sandwich panels of three in-plane sizes (153 by 51 mm, 331 by 203 mm, and 712 by 381 mm) with twelve-ply facesheets (2.4 mm thick) of two layups made of T300/F584 graphite/epoxy tape and a 19 mm thick HRP-3/16-8.0 reinforced phenolic honeycomb core were tested in the undamaged condition, with notches, and with impact damage. Notches used were narrow slits with rounded ends and had nominal lengths of 3.2, 6.4, 9.5, 12.7, 25.4, 50.8, and 76.2 mm. Strain gages and photoelastic coatings were used to examine the strain field in specimens. The observed patterns of the photoelastic coatings were compared to predictions made using Lekhnitskii's solution for an anisotropic plate with an elliptical hole. The observed patterns were similar to those predicted, and the similarity increased as the notch length increased. Based on examinations of the strain field, it was concluded that the effect of the size of the specimen on the strain field of the notch was minimal for the cases considered. Because some structural behavior of the specimen is inevitable, the property to be measured and the fidelity required in the measurements must be considered in designing a fixture and test specimens. Failure data of notched specimens was fit well by the Mar-Lin correlation. However, the value of the parameter H_c was found to decrease as notch size was increased. Thus, correlations such as the Mar-Lin correlation should not be used to predict the failure strengths of larger notch sizes by extrapolation on data obtained from specimens with smaller notch sizes. Impact damage was created at two levels based on the velocity of the impactor. Growth of the dimple created by impact was monitored using out-of-plane moiré interferometry, and predictions of the dimple growth were made using an existing model. Predicted growth was much less than that observed due primarily to the damage in the impacted facesheet. Thus, the damage state of the specimens must be known and the dimple growth model modified to include the effects of this damage. Failure of the impacted specimens is relatively well predicted using the Mar-Lin correlation with the damage in the specimens used as the notch size. However, the mechanism of damage propagation is different for impacted and notched specimens. Thus, great care should be exercised when using notched failure criteria to predict the failure of impacted specimens. Tools for assessing the effects of finite specimen size have been developed and their usefulness examined throughout the examination.

Advisor: Paul Lagace
Title: Professor, Department of Aeronautics and Astronautics, Massachusetts Institute of Technology

Acknowledgments

I would like to gratefully acknowledge the support of the Fannie and John Hertz Foundation during the past two years.

I would like to thank my advisor, Professor Paul Lagace, for the chance to work in TELAC and his time and energy in helping to complete this thesis. I also would like to thank the other faculty of TELAC, Professors John Dugundji and Hugh McManus, for their advice and encouragement. Thanks also to the people who really keep the laboratory running: Deborah Bowser, who always has something funny to say, and Al Supple, who knows the answer to everything or at least some of the right questions.

The other graduate students in the laboratory have shared their knowledge, insight, and gripes with me for two years. The "older generation" of Narendra Bhat, Wilson Tsang, and Hari Budiman (without them I never would have passed those two classes), Stacey Priest, and Steve Thomas was very important. For two years, the modus operandi was: when in doubt, ask one of these guys. "My generation" of graduate students, some of whom are gone already, suffered through classes, research, and thesis writing along with me. Thanks to Rich Kroes (how can a Dutch guy be a California surfer dude?), Cecilia Park, Brian Wardle, and Lauren Kucner. This thesis would not have been possible without the help of two UROPers, Randy Stevens and Nate Crosswhite.

Many people outside of MIT were very important in making it through the last two years. First, I would like to thank my fellow runners in CSU for helping me mature as a runner and providing a sanity

(insanity??) break once a week. I'd also like to thank my roommates this past year: Sharon, for all her witty exchanges (shut up!), Erin, who would have made a great sister, and Charity, who can have a hug any time she wants one (thanks for the bear when I needed it). Finally, thanks Gaggi for putting up with me these past months, for the late night snacks, and for just being there.

Foreword

This work was performed in the Technology Laboratory for Advanced Composites (TELAC) in the Department of Aeronautics and Astronautics at the Massachusetts Institute of Technology. This work was sponsored by the Boeing Commercial Aircraft Group, a division of The Boeing Company, under Boeing Purchase Order Number FZ-282568-0755N as part of the NASA Advanced Composite Technology program. Additional support was also provided through the Leaders for Manufacturing Program at M.I.T.

Table of Contents

List of Figures 9

List of Tables 20

Nomenclature 24

1. Introduction 27

2. Previous Work 31

   2.1 Compressive Failure of Notched Composites 31

      2.1.1 Damage Mechanisms 31

      2.1.2 Experimental Observations on Failure 33

      2.1.3 Notched Compressive Failure Strength 34

   2.2 Post-Impact Compressive Behavior of Composite Sandwich Panels 40

   2.3 Summary 43

3. Approach 45

   3.1 Description of Specimens 46

   3.2 Test Program 47

   3.3 Analyses 56

4. Analytical Methods 62

   4.1 Stresses in a Notched Laminate 62

   4.2 Mar-Lin Correlation 70

   4.3 Dimple Propagation Model 72

5. Experimental Procedure 83

   5.1 Manufacture of Specimens 83

   5.2 Preparation of Specimens 86

      5.2.1 Potting of Specimens 89

5.2.2 Milling of Specimens 93
5.2.3 Machining of Notches 97
5.2.4 Impact of Specimens 100
5.3 Instrumentation 104
5.3.1 Photoelasticity 104
5.3.2 Moiré Method 111
5.3.3 Strain Gages and Configuration 117
5.4 Test Fixture and Techniques 127
5.5 Data Reduction 141
6. Results 144
6.1 Undamaged Compressive Behavior 144
6.2 Notched Compressive Behavior 159
6.2.1 Deflection and Strain Gage Data 163
6.2.2 Photoelastic Images 182
6.2.3 Failure Stress and Failure Mode 233
6.3 Compression After Impact Behavior 243
7. Discussion 286
7.1 Test Methods 286
7.2 Effects of Specimen Size 295
7.3 Notched Compressive Behavior 301
7.3.1 Photoelastic Images 302
7.3.2 Failure and Strength Correlation 303
7.4 Compression After Impact Behavior 319
7.4.1 Dimple Growth 319
7.4.2 Failure Prediction 331
8. Conclusions and Recommendations 336

References 342

Appendix A: Specimen Designations 351

Appendix B: Program Listing 354

Appendix C: Specimen Data 359

Appendix D: Slopes of Stress-Strain Curves 364

List of Figures

Figure 3.1	Specimen configuration.	48
Figure 3.2	Scaled illustration of (left) small, (center) medium, and (right) large specimens.	49
Figure 4.1	Illustration of uniaxially loaded plate with elliptical notch.	63
Figure 4.2	Sample contour plot of differences in principal strains obtained by Lekhnitskii's solution. The solution is for a specimen of the A layup with an ellipse with a major axis of 50.8 mm and a minor axis of 5.0 mm at an applied stress of -112 MPa. The calculated far-field value of the difference of principal strains is 2940 microstrain.	71
Figure 4.3	Sketch of stress-strain curve of flatwise compression test of HRP-3/16-8.0 honeycomb core, after [45].	79
Figure 5.1	Illustration of cure assembly for panels.	85
Figure 5.2	Pressure and temperature history during cure cycle.	87
Figure 5.3	Photograph of typical waviness of the plies within the "rough" side facesheet of a B specimen.	88
Figure 5.4	Locations for measurements of specimen widths.	90
Figure 5.5	Schematic of mold used in potting of specimens.	92
Figure 5.6	Schematic of setup for milling small specimens.	94
Figure 5.7	Schematic of setup for milling medium and large specimens.	96
Figure 5.8	Photograph of typical notch for medium and large specimens.	99
Figure 5.9	Photograph of typical dimple created by a level 1 impact event (specimen A-M-IL1).	101
Figure 5.10	Photograph of typical dimple created by a level 2 impact event (specimen A-M-IL2).	102

Figure 5.11	Illustration of placement of photoelastic coating on half of one side of specimen.	110
Figure 5.12	Schematic of setup for photoelastic technique.	112
Figure 5.13	Photograph of moiré fringe pattern of machined dimple in an aluminum bar.	114
Figure 5.14	Schematic of moiré setup.	116
Figure 5.15	Comparison of measurements along the x-axis via dial gauge and moiré techniques of a machined dimple in an aluminum bar.	118
Figure 5.16	Comparison of measurements along the y-axis via dial gauge and moiré interferometry of machined dimple in aluminum bar.	119
Figure 5.17	Photograph of moiré fringe pattern for unloaded specimen damaged by a level 1 impact event (specimen A-M-IL1).	120
Figure 5.18	Comparison of measurements of the dimple along the x-axis via dial gauge and moiré techniques for an unloaded specimen damaged by a level 1 event (specimen A-M-IL1).	121
Figure 5.19	Comparison of measurements of the dimple along the y-axis via dial gauge and moiré techniques for an unloaded specimen damaged by a level 1 event (specimen A-M-IL1).	122
Figure 5.20	Illustration of "Notch 1" configuration of strain gages for notched specimens with photoelastic coating covering the entire notched side.	124
Figure 5.21	Illustration of "Notch 2" configurations of strain gages for notched specimens.	125
Figure 5.22	Illustration of "Notch 3" configuration of strain gages for notched specimens.	126
Figure 5.23	Illustration of "Impact" configuration of strain gages for impacted specimens.	128
Figure 5.24	Illustration of "Undamaged 1" configuration of strain gages used for undamaged specimens B-S-Ua and A-S-Ua.	129

Figure 5.25	Illustration of "Undamaged 2" configuration of strain gages used for undamaged specimen B-S-Ub.	130
Figure 5.26	Illustration of "Undamaged 3" configuration of strain gages used for undamaged specimen A-S-Ub.	131
Figure 5.27	Illustration of "Undamaged 4" configuration of strain gages used for undamaged specimen A-M-U.	132
Figure 5.28	Schematic of test fixture.	134
Figure 6.1	Representative plot of stroke versus far-field applied stress (specimen A-S-Ua).	146
Figure 6.2	Plot of out-of-plane deflection versus far-field applied stress in which the deflection increases monotonically (specimen A-S-Ua).	147
Figure 6.3	Plot of out-of-plane deflection versus far-field applied stress in which the deflection is nonmonotonic (specimen A-M-U).	148
Figure 6.4	Representative plot of strain versus far-field applied stress for undamaged specimens with gage configuration Undamaged 1 (specimen A-S-Ua).	151
Figure 6.5	Plot of strain versus far-field applied stress for the undamaged medium specimen with strain gage configuration Undamaged 4 (specimen A-M-U).	153
Figure 6.6	Plot of strain versus far-field applied stress for the undamaged specimen tested with configuration Undamaged 2 (specimen B-S-Ub).	154
Figure 6.7	Photograph of undamaged small specimen which failed at the potting line. The potting material is located directly above the upper part of the visible core and facesheets (specimen A-S-Ua).	157
Figure 6.8	Photograph of brooming failure in medium undamaged specimen (specimen A-M-U).	158
Figure 6.9	Plot of out-of-plane deflection versus far-field applied stress in which deflection grows increasingly rapidly (specimen A-L-SN25).	166

Figure 6.10	Plot of out-of-plane deflection versus far-field applied stress in which there is a perturbation in deflection at loads near failure (specimen A-L-DN76).	167
Figure 6.11	Representative plot of strain versus far-field applied stress for Notch 1 configuration (specimen B-S-SN13a).	172
Figure 6.12	Representative plot of strain versus far-field applied stress for Notch 2 strain gage configuration (specimen A-S-SN10a).	173
Figure 6.13	Plot of strain versus far-field applied stress for a specimen with Notch 2 strain gage configuration which exhibited highly nonlinear behavior at low stress levels (specimen B-S-DN6).	175
Figure 6.14	Representative plot of strain versus far-field applied stress for Notch 3 configuration (specimen B-M-DN51).	179
Figure 6.15	Sketch showing region in which principal strains are not aligned with the x and y axes in an A specimen with a 3.8 mm notch at an applied far-field stress of 162 MPa (specimen A-S-SN3a).	184
Figure 6.16	Sketch showing region in which principal strains are not aligned with the x and y axes in an A specimen with a 13.8 mm notch at an applied far-field stress of 162 MPa (specimen A-S-SN13a).	185
Figure 6.17	Experimental contour plot of the difference in principal strains which shows symmetry about the vertical axis of the specimen (specimen A-S-SN13a).	189
Figure 6.18	Experimental contour plot of the difference in principal strains which shows symmetry about the horizontal axis of the specimen (specimen A-S-SN9a).	191
Figure 6.19	Experimental contour plot of the difference in principal strains, determined via the photoelastic technique, for a medium A specimen with a 25.9 mm notch at a far-field stress level of -45 MPa (calculated far-field value of $\Delta\varepsilon$ is 980 $\mu\varepsilon$) (specimen A-M-DN25).	192

Figure 6.20	Experimental contour plot of the difference in principal strains, determined via the photoelastic technique, for a medium A specimen with a 25.9 mm notch at a far-field stress level of -90 MPa (calculated far-field value of $\Delta\varepsilon$ is 1950 $\mu\varepsilon$) (specimen A-M-DN25).	193
Figure 6.21	Experimental contour plot of the difference in principal strains, determined via the photoelastic technique, for a medium A specimen with a 25.9 mm notch at a far-field stress level of -135 MPa (calculated far-field value of $\Delta\varepsilon$ is 2930 $\mu\varepsilon$) (specimen A-M-DN25).	194
Figure 6.22	Predicted contour plot of the difference in principal strains for an A specimen with a 3.2 mm notch at a far-field stress level of -162 MPa (calculated far-field value of $\Delta\varepsilon$ is 4240 $\mu\varepsilon$).	196
Figure 6.23	Experimental contour plot of the difference in principal strains, determined via the photoelastic technique, for a small A specimen with a 3.8 mm notch at a far-field stress level of -162 MPa (specimen A-S-SN3a).	197
Figure 6.24	Predicted contour plot of the difference in principal strains for an A specimen with a 6.4 mm notch at a far-field stress level of -162 MPa (calculated far-field value of $\Delta\varepsilon$ is 4240 $\mu\varepsilon$).	199
Figure 6.25	Experimental contour plot of the difference in principal strains, determined via the photoelastic technique, for a small A specimen with a 6.5 mm notch at a far-field stress level of -162 MPa (specimen A-S-SN6a).	200
Figure 6.26	Predicted contour plot of the difference in principal strains for an A specimen with a 9.5 mm notch at a far-field stress level of -162 MPa (calculated far-field value of $\Delta\varepsilon$ is 4240 $\mu\varepsilon$).	201
Figure 6.27	Experimental contour plot of the difference in principal strains, determined via the photoelastic technique, for a small A specimen with a 9.6 mm notch at a far-field stress level of -162 MPa (specimen A-S-SN10a).	202

Figure 6.28	Predicted contour plot of the difference in principal strains for an A specimen with a 12.7 mm notch at a far-field stress level of -162 MPa (calculated far-field value of $\Delta\varepsilon$ is 4240 $\mu\varepsilon$).	204
Figure 6.29	Experimental contour plot of the difference in principal strains, determined via the photoelastic technique, for a small A specimen with a 12.8 mm notch at a far-field stress level of -162 MPa (specimen A-S-SN13a).	205
Figure 6.30	Predicted contour plot of the difference in principal strains for an A specimen with a 25.4 mm notch at a far-field stress level of -90 MPa (calculated far-field value of $\Delta\varepsilon$ is 2350 $\mu\varepsilon$).	206
Figure 6.31	Experimental contour plot of the difference in principal strains, determined via the photoelastic technique, for a medium A specimen with a 25.9 mm notch at a far-field stress level of -90 MPa (specimen A-M-DN25).	207
Figure 6.32	Predicted contour plot of the difference in principal strains for an A specimen with a 50.8 mm notch at a far-field stress level of -90 MPa (calculated far-field value of $\Delta\varepsilon$ is 2350 $\mu\varepsilon$).	209
Figure 6.33	Experimental contour plot of the difference in principal strains, determined via the photoelastic technique, for a medium A specimen with a 51.2 mm notch at a far-field stress level of -90 MPa (specimen A-M-DN51).	210
Figure 6.34	Predicted contour plot of the difference in principal strains for an A specimen with a 76.2 mm notch at a far-field stress level of -96 MPa (calculated far-field value of $\Delta\varepsilon$ is 2510 $\mu\varepsilon$).	211
Figure 6.35	Experimental contour plot of the difference in principal strains, determined with the photoelastic technique, for a large A specimen with a 76.6 mm notch at a far-field stress level of -96 MPa (specimen A-L-DN76).	21
Figure 6.36	Predicted contour plot of the difference in principal strains for a B specimen with a 3.2 mm notch at a far-field stress level of -162 MPa (calculated far-field value of $\Delta\varepsilon$ is 3507 $\mu\varepsilon$).	215

Figure 6.37	Experimental contour plot of the difference in principal strains, determined via the photoelastic technique, for a small B specimen with a 3.1 mm notch at a far-field stress level of -162 MPa (specimen B-S-SN3a).	216
Figure 6.38	Predicted contour plot of the difference in principal strains for a B specimen with a 6.4 mm notch at a far-field stress level of -162 MPa (calculated far-field value of $\Delta\varepsilon$ is 3507 $\mu\varepsilon$).	217
Figure 6.39	Experimental contour plot of the difference in principal strains, determined via the photoelastic technique, for a small B specimen with a 6.1 mm notch at a far-field stress level of -162 MPa (specimen B-S-SN6a).	218
Figure 6.40	Predicted contour plot of the difference in principal strains for a B specimen with a 9.5 mm notch at a far-field stress level of -162 MPa (calculated far-field value of $\Delta\varepsilon$ is 3507 $\mu\varepsilon$).	219
Figure 6.41	Experimental contour plot of the difference in principal strains, determined via the photoelastic technique, for a small B specimen with a 9.8 mm notch at a far-field stress level of -162 MPa (specimen B-S-SN10a).	220
Figure 6.42	Predicted contour plot of the difference in principal strains for a B specimen with a 12.7 mm notch at a far-field stress level of -162 MPa (calculated far-field value of $\Delta\varepsilon$ is 3507 $\mu\varepsilon$).	222
Figure 6.43	Experimental contour plot of the difference in principal strains, determined via the photoelastic technique, for a small B specimen with a 12.1 mm notch at a far-field stress level of -162 MPa (specimen B-S-SN13a).	223
Figure 6.44	Predicted contour plot of the difference in principal strains for a B specimen with a 25.4 mm notch at a far-field stress level of -90 MPa (calculated far-field value of $\Delta\varepsilon$ is 1950 $\mu\varepsilon$).	224

Figure 6.45	Experimental contour plot of the difference in principal strains, determined via the photoelastic technique, for a medium B specimen with a 25.6 mm notch at a far-field stress level of -90 MPa (specimen B-M-DN25).	225
Figure 6.46	Predicted contour plot of the difference in principal strains for a B specimen with a 50.8 mm notch at a far-field stress level of -90 MPa (calculated far-field value of $\Delta\varepsilon$ is 1950 $\mu\varepsilon$).	226
Figure 6.47	Experimental contour plot of the difference in principal strains, determined via the photoelastic technique, for a medium B specimen with a 51.0 mm notch at a far-field stress level of -90 MPa (specimen B-M-DN51).	227
Figure 6.48	Predicted contour plot of the difference in principal strains for a B specimen with a 76.2 mm notch at a far-field stress level of -96 MPa (calculated far-field value of $\Delta\varepsilon$ is 2080 $\mu\varepsilon$).	229
Figure 6.49	Experimental contour plot of the difference in principal strains, determined via the photoelastic technique, for a large B specimen with a 76.3 mm notch at a far-field stress level of -96 MPa (specimen B-L-DN76).	230
Figure 6.50	Side view photograph of a representative small notched specimen in which both facesheets failed (specimen A-S-SN3a)	235
Figure 6.51	Side view photograph of a representative specimen in which only the notched facesheet failed (specimen A-S-SN13b).	236
Figure 6.52	Photograph of typical failure across the width of a notched specimen (specimen A-M-DN25).	238
Figure 6.53	Photograph of specimen after failure in which damage has grown in a cone shape out from the notch along the y-axis (specimen B-M-DN51).	239
Figure 6.54	Side view photograph of a notched specimen which has a permanent out-of-plane deflection after failure (specimen B-M-SN25).	240

Figure 6.55	Stress-strain curves for a specimen which experienced visible cracking of the potting material during testing (specimen B-S-SN6b).	242
Figure 6.56	Plot of out-of-plane deflection versus far-field applied stress for a large A specimen damaged by a level 1 impact event (specimen A-L-IL1)	249
Figure 6.57	Plot of strain versus far-field applied stress for a medium B specimen damaged by a level 1 impact event (specimens B-M-IL1)	251
Figure 6.58	Plot of strain versus far-field applied stress for a medium B specimen damaged by a level 2 impact event (specimen B-M-IL2).	253
Figure 6.59	Plot of strain versus far-field applied stress for a medium A specimen damaged by a level 1 impact event (specimen A-M-IL1).	254
Figure 6.60	Plot of strain versus far-field applied stress for a medium A specimen damaged by a level 2 impact event (specimen A-M-IL2).	255
Figure 6.61	Plot of strain versus far-field applied stress for a large A specimen damaged by a level 1 impact event (specimen A-L-IL1).	257
Figure 6.62	Plot of strain versus far-field stress level for a large B specimen damaged by a level 1 impact event (specimen B-L-IL1)	258
Figure 6.63	Digitized moiré fringe patterns for a medium A specimen under compressive loading after damage by a level 1 impact (specimen A-M-IL1).	260
Figure 6.64	Digitized moiré fringe patterns for a medium B specimen under compressive loading after damage by a level 1 impact (specimen B-M-IL1).	262
Figure 6.65	Digitized moiré fringe patterns for a medium A specimen under compressive loading after damage by a level 2 impact (specimen A-M-IL2).	263
Figure 6.66	Digitized moiré fringe patterns for a medium B specimen under compressive loading after damage by a level 2 impact (specimen B-M-IL2).	264

Figure 6.67	Dimple profiles along the x-axis at various applied stress levels for a medium A specimen damaged by a level 1 impact (specimen A-M-IL1).	266
Figure 6.68	Dimple profiles along the y-axis at various applied stress levels for a medium A specimen damaged by a level 1 impact (specimen A-M-IL1).	267
Figure 6.69	Dimple profiles along the x-axis at various applied stress levels for a medium B specimen damaged by a level 1 impact (specimen B-M-IL1).	268
Figure 6.70	Dimple profiles along the y-axis at various applied stress levels for a medium B specimen damaged by a level 1 impact (specimen B-M-IL1).	269
Figure 6.71	Dimension of dimple parallel to the y-axis versus far-field applied stress level for A specimens damaged by level 1 and level 2 impacts (specimens A-M-IL1, A-L-IL1, and A-M-IL2).	270
Figure 6.72	Dimension of dimple parallel to the y-axis versus far-field applied stress level for B specimens damaged by level 1 and level 2 impacts (specimens B-M-IL1, B-L-IL1, and B-M-IL2).	272
Figure 6.73	Initial measured dimple profile and the assumed dimple profile along the y-axis for an A specimen damaged by a level 1 impact (specimen A-M-IL1).	275
Figure 6.74	Initial measured dimple profile and the assumed dimple profile along the y-axis for a B specimen damaged by a level 1 impact (specimen B-M-IL1).	276
Figure 6.75	Experimental and predicted dimple profiles along the y-axis at various applied stress levels for a medium A specimen damaged by a level 1 impact (specimen A-M-IL1).	277
Figure 6.76	Experimental and predicted dimple profiles along the y-axis at various applied stress levels for a medium B specimen damaged by a level 1 impact (specimen B-M-IL1).	278
Figure 6.77	Digitized moiré fringe patterns for the dimple before testing and after the shutdown of the testing machine in a large A specimen damaged by a level 1 impact event.	280

Figure 6.78	Dimple profile along the y-axis for a large A specimen damaged by a level 1 impact. Stress levels shown represent the beginning of the test, the point just prior to machine shutdown, and unloaded after hydraulic shutdown (specimen A-L-IL1).	281
Figure 6.79	Photograph of a typical failure of an impacted specimen of the A layup along the y-axis of the impacted facesheet (specimen A-M-IL1).	282
Figure 6.80	Photograph of a typical failure of an impacted specimen of the B layup along y-axis of impacted facesheet (specimen B-M-IL2).	283
Figure 7.1	General regions A, B, C, and D of strain gage locations.	288
Figure 7.2	Schematic of misalignment of loading plates with axis of load application.	289
Figure 7.3	Sketch of a metal cylinder tested in compression exhibiting "barreling" behavior.	297
Figure 7.4	Experimental failure stress and predicted failure stress by the Mar-Lin correlation versus notch length for the notched specimens of the A layup.	312
Figure 7.5	Experimental failure stress and predicted failure stress by the Mar-Lin correlation versus notch length for the notched specimens of the B layup.	315
Figure 7.6	Plot of the composite fracture parameter H_c versus notch length for specimens of the A layup.	316
Figure 7.7	Plot of the composite fracture parameter H_c versus notch length for specimens of the B layup.	317
Figure 7.8	Predicted, with reduced core stiffness, and observed dimple growth of an A specimen impacted at level 1.	321
Figure 7.9	Predicted, with a larger region of initial core crushing, and observed dimple growth of a medium A specimen impacted at level 1.	322
Figure 7.10	Predicted, with reduced bending stiffness of the facesheet, and observed dimple growth of a medium A specimen impacted at level 1.	325

List of Tables

Table 3.1	Test matrix for small specimens for each layup	51
Table 3.2	Test matrix for medium specimens of first round	54
Table 3.3	Test matrix for large specimens in first round	55
Table 3.4	Test matrix for the second round of tests	57
Table 3.5	Summary of specimens of the A layup and their test conditions	58
Table 3.6	Summary of specimens of the B layup and their test conditions	59
Table 4.1	T300/F584 ply properties	66
Table 4.2	Elastic constants for laminates	67
Table 4.3	HRP-3/16-8.0 honeycomb core properties used for program MODK1K2	75
Table 4.4	Graphite/epoxy facesheet properties used for program MODK1K2	76
Table 4.5	Input parameters for HRP-3/16-8.0 honeycomb core used for program GROWTH	80
Table 4.6	Input parameters for graphite/epoxy facesheets for program GROWTH	81
Table 5.1	Area of delamination created by impact events	103
Table 5.2	Colors of the photoelastic coating and their corresponding fringe orders [52]	107
Table 5.3	Alignment method used for A specimens	138
Table 5.4	Alignment method used for B specimens	139
Table 6.1	Maximum value and characterization of out-of-plane deflection of undamaged specimens	149
Table 6.2	Measured longitudinal moduli of undamaged specimens	156
Table 6.3	Failure stresses of undamaged specimens	160

Table 6.4	Measured lengths of machined notches in specimens of the A layup	161
Table 6.5	Measured lengths of machined notches in specimens of the B layup	162
Table 6.6	Instrumentation scheme used for notched specimens of the A layup	164
Table 6.7	Instrumentation scheme used for notched specimens of the B layup	165
Table 6.8	Maximum value and characterization of out-of-plane deflection of notched specimens of the A layup	169
Table 6.9	Maximum value and characterization of out-of-plane deflection of notched specimens of the B layup	170
Table 6.10	Average slopes and relative differences in slope for the far-field gages of specimens tested with Notch 2 strain gage configuration	177
Table 6.11	Average initial slopes of far-field gages and the relative difference between the slopes of each back-to-back pair for specimens tested with Notch 3 strain gage configuration	181
Table 6.12	Failure stresses for notched specimens of the A layup	244
Table 6.13	Failure stresses for notched specimens of the B layup	245
Table 6.14	Maximum value and characterization of out-of-plane deflection behavior of impacted specimens of layup A	247
Table 6.15	Maximum value and characterization of out-of-plane deflection behavior of impacted specimens of layup B	248
Table 6.16	Additional input parameters for program GROWTH for A specimen	273
Table 6.17	Failure stresses for impacted specimens	285

Table 7.1	Initial slopes of strain gages located in regions shown in Figure 7.1, for small specimens tested after alignment of test fixture by method 1	291
Table 7.2	Initial slopes of strain gages located in regions shown in Figure 7.1, for small specimens tested after alignment of test fixture by method 2	293
Table 7.3	Values of notch length, failure stress, and composite fracture parameter H_c for specimens of the A layup	309
Table 7.4	Values of notch length, failure stress, and composite fracture parameter H_c for specimens of the B layup	310
Table 7.5	Average values of H_c and associated coefficients of variation for various subsets of the notched A specimens	311
Table 7.6	Average values of H_c and associated coefficients of variation for various subsets of the notched B specimens	314
Table 7.7	Reduced values of the facesheet bending stiffness of the A layup used as input for the dimple growth model	324
Table 7.8	Measured damage sizes of impacted specimens	329
Table 7.9	Predicted strength of impacted specimens using Mar-Lin correlation	333
Table A.1	Designations for specimens of the A layup	352
Table A.2	Designations for specimens of the B layup	353
Table C.1	Measured widths of A specimens	360
Table C.2	Measured widths of B specimens	361
Table C.3	Summary of information for specimens of the A layup	362
Table C.4	Summary of information for specimens of the B layup	363

Table D.1	Initial slopes a for strain gages of undamaged specimens with strain gage configuration Undamaged 1	365
Table D.2	Initial slopes a for strain gages of the undamaged specimen with strain gage configuration Undamaged 2	366
Table D.3	Initial slopes a for strain gages of undamaged specimens with strain gage configuration Undamaged 3 and Undamaged 4	367
Table D.4	Initial slopes a for strain gages of undamaged specimens with strain gage configuration Notch 1	368
Table D.5	Initial slopes a for strain gages of notched specimens with strain gage configuration Notch 2	369
Table D.6	Initial slopes a for strain gages of notched specimens with strain gage configuration Notch 3	370
Table D.7	Initial slopes a for strain gages of impacted specimens with strain gage configuration Impact	371

Nomenclature

a	width of notch in loading direction
a_{ij}	elements of laminate in-plane compliance matrix
A_{ij}	elements of laminate in-plane stiffness matrix
b	length of notch transverse to loading direction
d_x	dimension of the dimple propagation model along the loading direction
d_y	dimension of the dimple propagation model perpendicular to the loading direction
D_{ij}	elements of laminate bending stiffness matrix
$E_{apparent}$	apparent modulus of facesheet in loading direction due to stiffening effect of a transverse constraint
E_{trans}	through-thickness modulus of facesheet
$E_{in\text{-}plane}$	in-plane modulus of facesheet
E_x	laminate modulus in loading direction
E_y	laminate modulus in direction perpendicular to loading
E_1	longitudinal modulus of ply
E_2	transverse modulus of ply
f	fringe value of photoelastic coating
G_{xy}	laminate in-plane shear modulus
G_{xz}	shear modulus of facesheet in through-thickness direction
G_{12}	in-plane shear modulus of ply
h	thickness of facesheet
H_c	composite fracture parameter in Mar-Lin correlation
k_1	parameter used to characterize the two-parameter foundation

k_2	parameter used to characterize the two-parameter foundation
L	specimen length
m	singularity of crack in Mar-Lin correlation
N	fringe order of photoelastic coating or moiré fringe pattern
p	pitch of moiré grating
R_o	initial radius of core crushing
R_p	size of model for determining foundation parameters
R_x	initial dimension of dimple in loading direction
R_y	initial dimension of dimple perpendicular to loading direction
t	nominal ply thickness
w	specimen width
x	axis along loading direction
y	axis perpendicular to loading direction
z	axis out of plane of specimen
z_j	complex coordinates in an anisotropic plate
α	angle of incidence of light for moiré method
α_1	loading parameter for an anisotropic plate with an elliptical hole
β_1	loading parameter for an anisotropic plate with an elliptical hole
γ_{xy}	shear strain in x-y coordinate system
$\Delta\varepsilon$	difference in principal strains
ε_x	x-component of strain
ε_y	y-component of strain
ε_l	larger principal strain

ε_{II}	smaller principal strain
μ_1, μ_2	roots of the characteristic equation for an anisotropic plate
ν_{xy}	laminate major Poisson's ratio
ν_{yx}	laminate minor Poisson's ratio
ν_{12}	Poisson's ratio of ply
ξ_o	initial dimple depth
σ_f	failure stress of laminate
$\sigma_{plateau}$	support reaction provided by the crushed core
σ_{ult}	flatwise compression strength of the honeycomb core
σ_x	x-component of stress
σ_x^*	far-field applied stress in analytical model of an anisotropic plate with an elliptical hole
σ_y	y-component of stress
σ_{zz}	reaction stress of two-parameter foundation
τ_{xy}	shear stress in x-y coordinate system
ϕ_1, ϕ_2	complex stress functions for an anisotropic plate

Chapter 1

Introduction

Advanced composite materials, especially those in which long fibers reinforce a comparatively less stiff and less strong material, have found increasing application in the aerospace industry. One such material which is commonly used is graphite/epoxy. This material can provide a higher stiffness to weight ratio, a higher strength-to-weight ratio, and a greater resistance to cyclic loading than aluminum.

Many of the early uses of composites in aircraft were in military aircraft. Current military aircraft, especially the B-2 stealth bomber and the F-117 stealth fighter make extensive use of the composites throughout their structures. For these planes, composites can also provide radar eluding abilities in addition to their advantages as structural materials.

Composites have also been used in commercial aircraft. For example, the Beechcraft Starship is constructed mainly of composites. In large transport aircraft, composites have generally been used to replace heavier metallic parts in secondary structures. However, composites are used in the Boeing 777 in a structural application in the empennage. This is a primary structure in the operation of the aircraft and has, in fact, a span as wide as the wings of some smaller commercial aircraft such as the Boeing 757.

NASA's Advanced Composite Technology (ACT) program is an effort to develop better techniques to design and build composite primary structures in large passenger aircraft. This program builds on earlier NASA programs such as the Aircraft Energy Efficiency (ACEE) program. One component of the ACT program is the Advanced Technology Composite

Aircraft Structures (ATCAS) program carried out by the Boeing Company. This program focuses on the design and construction of composite fuselages for large transport aircraft.

The goal of using composites in primary aircraft structures entails numerous challenges. Such an aircraft must be economically feasible , and the aircraft must be certified. In order to be certified, the safety and reliability of the design must be demonstrated.

A key philosophy in the design of such aircraft structures is one of damage tolerance. Damage tolerance is the ability of a structure to perform a specific task with a known damage present. Such damage can be intentional or the result of an accidental event. Refined analytical and numerical tools such as fracture mechanics exist to evaluate the damage tolerance of metallic structures. However, this is not yet the case with composite structures. The ability of composite structures to perform with damage can only be accurately determined by testing of the structure or its substructures.

Intentional damage is introduced as the inevitable holes for such purposes as fasteners, servicing needs, and cable routing. These holes act as stress raisers in the structure. Composites are generally unable to relieve these stress concentrations due to their brittle behavior. Thus, damage can occur at holes and propagate leading to failure of the structure.

Accidental damage can occur when an aircraft structure is impacted in the course of service. Examples of possible impact events are a dropped tool during maintenance, a bird-strike during flight, a rock kicked-up during takeoff or landing, or a broken blade impact as the result of an engine failure. Such impacts can break fibers, crack the matrix, and lead to delaminations that can seriously compromise the performance of the

structure.

For composite structures to be economically advantageous compared to traditional materials, it is probable that new construction techniques and configurations will have to be used. For example, the side and bottom regions of an aircraft fuselage are loaded largely in compression along with some bending. In these regions of the fuselage, a high bending stiffness is required in order to avoid buckling under the compressive loading. The most efficient configuration for bending stiffness is often a sandwich construction. Furthermore, sandwich construction can potentially save manufacturing costs for composites applications as compared to a traditional skin and stringer construction. In a composite sandwich panel, two laminates, called facesheets, are separated by a layer called the core which has comparatively low density and stiffness. Examples of core materials are aluminum and Nomex honeycomb and lightweight foam. Such a structure provides high bending stiffness while remaining very light.

Sandwich construction presents its own challenges. The facesheets must be bonded to the core, and this can prove to be a weak point. Also, if the facesheets are cured separately, they must then be bonded to the core as a separate step in the manufacturing process. To avoid this step and perhaps reduce costs, there is interest in curing the laminates at the same time that they are bonded to the core. However, in such a cocure process, the pressure often must be reduced below that of a normal laminate cure cycle in order to avoid crushing the core. This low pressure can result in voids in the laminates. The pressure can also create waviness of the plies if the core is of a honeycomb type.

In the present work, the failure of sandwich panels subjected to compressive loading is investigated via an experimental program. A variety

of conditions are examined with notched, impacted, and undamaged panels. Analytical methods are used to correlate or predict the behavior observed experimentally. The primary objective of this research is to examine the effect of damage on the behavior of composite sandwich panels loaded in compression. This includes the damage modes which develop as well as the final failure load. Furthermore, the effects of the specimen size relative to the damage size is examined to better understand their influence on the introduction of load in such panels. These results are compared to results of previous tests conducted within the ATCAS program. This research thus adds to the existing database for the ATCAS program and will help lead to a greater understanding of composite sandwich panels under compressive loading.

A review of the work that has been done on the key issues of concern is presented in Chapter 2. The problem definition and the approach taken to address it are given in Chapter 3. The analytical methods used are discussed in Chapter 4. Details of the experimental procedure followed are described in Chapter 5. In Chapter 6, results of the tests and analyses are presented. These results and their implications are discussed in Chapter 7. Finally, in Chapter 8, conclusions are drawn from this study and recommendations are made for future research.

Chapter 2

Previous Work

The performance of composite structures can be reduced significantly by damage such as notches and that due to impact events. These phenomena create a region where the stress state is markedly different from that of the laminate without such a discontinuity. Previous work on the effects of notches and impact events on the behavior and failure of composite panels loaded in compression is reviewed in this chapter. In the case of notched behavior, the work done by other researchers has focused on monolithic laminates with little work done on sandwich panels. In the examination of the effects of impact damage, the discussion is focused on that work done concerning sandwich panels.

2.1 Compressive Failure of Notched Composites

Notches have long been recognized as detrimental to the performance of composite laminates. They cause stress concentrations which lead to local damage in the vicinity of the notch. This local damage can propagate and lead to the catastrophic failure of the laminate. For the purposes of this work, notches is a generic term applied to both holes and slits.

2.1.1 Damage Mechanisms

Several researchers have examined the damage that occurs in notched composites loaded in compression [1-9]. Such failure is, of course, a complex process, and determining an exact sequence of events is quite

difficult as several damage types may be present at once.

The first type of damage detected seems to depend upon the experimental techniques used to monitor the specimen. Shear failure of the matrix has been identified as the first damage type by some researchers [3], while other researchers [4] have detected shear crippling, in which a local kink region forms in the fibers, first. In both of these investigations, the damage state was determined by stopping the test and sectioning the specimen. Others [5, 9] have identified surface protrusion of 0° fibers at the hole surface as the first manifestation of damage. The first of these investigations used the deply technique to detect damage, while the second used an optical microscope. These differences may be due to the effectiveness of a specific monitoring technique to detect a certain type of damage, or due to the existence of other forms of damage beyond the initial one before the test is stopped. It is also possible that the physical behavior observed was the same in the different tests, but different terms were used to describe the behavior.

Regardless of which is the first damage mode, shear crippling is generally recognized as a critical form of damage. Shear crippling, also called shear banding, is characterized by the formation of a kink in the fibers across the region of damage. Some researchers [2, 3, 10] have successfully related the size of the shear crippling zone to the characteristic distance for the Whitney-Nuismer [11, 12] point stress criterion (which is discussed later). The development of shear crippling has been found to lead to delamination [3-5, 9]. Such delamination can lead directly to sublaminate buckling, and delamination buckling can be a key mechanism in the spreading of the damage to the undamaged area of the plate [9]. Such propagation of damage eventually results in final failure.

2.1.2 Experimental Observations on Failure

The failure of compressively loaded monolithic composite laminates has been examined by a number of researchers [1-10, 13-21]. One key parameter measured is failure stress. Increased notch size generally results in lower failure stress. In addition to the notch size, certain other parameters affect the notched strength. These include the shape of the notch and the size of the notch relative to the specimen.

All of the investigations cited included testing of specimens with circular holes, so this can be regarded as the reference configuration. A few other notch shapes have been tested: square holes with the diagonal oriented with the loading [15], machined slits [3], and razor-sharpened slits [5-7]. The failure load for specimens with square holes oriented diagonally to the loading was found to be nearly the same as that for specimens with circular holes the same diameter as the diagonal of the square hole [15]. Quasi-isotropic specimens with machined cracks were found to fail at a stress level 10 to 20% lower than that of a circular hole [3]. This was especially noticeable as the notch length became much larger than the characteristic distance d_0 from the Whitney-Nuismer [11, 12] point stress criterion. The authors attribute this behavior to the different stress distributions around cracks and circular holes. At a distance d_0, the stresses are about the same for both types for small notch lengths. However, when the notch length is two orders of magnitude greater than d_0, the stress at the distance d_0 is more than twice as large in the cracked specimens as in those with holes. Experimental evidence from an investigation in which both razor-sharpened slits and circular holes were considered [5-7] showed that the failure strengths of laminates with

sharpened slits were approximately equal to those with circular holes of the same diameter as the slit length in the cases considered.

Actual test specimens have a finite width and gauge length, the size of which can influence the behavior in the vicinity of the notch. The effect of the finite specimen width on the stress state has been investigated using a finite element model for a quasi-isotropic laminate and an orthotropic laminate [3]. For the case of circular holes, it was recommended that the ratio of hole diameter to specimen width be kept under 0.33 to avoid increasing the stress concentration in the vicinity of the notch. Little difference was found between the quasi-isotropic laminate and the orthotropic laminate in this regard. An alternative approach is to use a finite-width correction factor, which can be obtained by analytical or numerical means. It has been indicated [6] that the isotropic correction gives only small errors when applied to orthotropic laminates. The effect of length to width ratio on the failure stress of notched laminated loaded in compression has not been investigated as such in the literature. This is probably because the length of most types of test specimens is constrained in order to avoid Euler column buckling.

2.1.3 Notched Compressive Failure Strength

A number of researchers have developed models and empirical relationships to predict the failure of notched composites. A comprehensive review of the work on tensile loading of notched composites was conducted by Awerbach and Madhukar [22]. Several of the models for notched composites were developed for tensile loading [11, 23] but have been applied successfully to compressive loading as well. Others [14, 19] were developed for general loading. One model [5-7] has been developed specifically for

compressively loaded notched composites. These models are generally better suited to laminates whose behavior is fiber-dominated.

Early researchers attempted to apply linear elastic fracture mechanics (LEFM) to composite laminates, but these efforts were largely unsuccessful. The Mar-Lin [23] correlation is a more successful model which is similar in form to traditional LEFM, though it is not based on energy considerations. As the Mar-Lin correlation is used in this investigation, it is discussed further in Chapter 4.

The two Whitney-Nuismer criteria [11, 12] are based on an attempt to use the statistical behavior of composites to explain the failure of notched composites. The argument is based on the fact that as the hole size is increased, the amount of material influenced by its stress concentration increases. As more material is loaded at a high stress level, it becomes more likely that a flawed or weak part of the composite will be subjected to a stress which causes failure. Using the elastic stress distribution in the vicinity of the notch, the point stress model indicates that laminate failure will occur when the stress at a point on the notch line and a distance d_0 from the edge of the notch reaches the unnotched strength of the laminate. The average stress criterion calls for failure when the stress averaged on the notch line from the edge of the notch to a distance a_0 reaches the unnotched strength of the laminate. These parameters, d_0 and a_0, have been found to be functions of material, stacking sequence, and type of loading [17, 24]. Other parameters such as hole surface finish may also affect the failure strength.

The two Whitney-Nuismer criteria have been successfully applied to compression loading situations. Nuismer and Labor [17] observed that a_0 should be larger for a laminate loaded in compression than for one loaded in

tension. They reasoned this since the material near the notch which failed due to compressive stresses would continue to carry load, while material which failed in tension probably would not. Others [2-4] have used the point stress criteria successfully for laminates with circular holes loaded in compression. Rhodes *et al.* [3] also point out one shortcoming of the Whitney-Nuismer criteria for application to compression in that the theory requires the unnotched compression strength of the laminate and "it is difficult to obtain an accurate value of the ultimate compression strain of a filament-controlled composite laminate because test results are influenced significantly by the test techniques and specimen supports." This increases the uncertainty of the model and makes comparisons of work by different researchers more difficult.

A similar model to the Whitney-Nuismer criteria is the first ply failure (FPF) criterion of Tan [18-21]. For a laminate with an elliptical notch, this model postulates that the following ratio holds:

$$\frac{\textit{FPF of unnotched laminate}}{\textit{max stress of unnotched laminate}} = \frac{\textit{FPF of notched laminate at a point}}{\textit{max stress of notched laminate}} \tag{2.1}$$

The stresses in the notched laminate are determined by an elasticity solution, making this criterion valid for arbitrary loading. First ply failure can be predicted by any failure model; Tan used the Tsai-Wu [25] criteria. In the case of notches perpendicular to the loading, the point considered is some distance b_1 away from the notch on the notch line. For arbitrary loading, the point considered is at some distance b_0 on a curve that satisfies the equation:

$$\frac{x^2}{(a+b_0)^2} + \frac{y^2}{(b+b_0)^2} = 1 \tag{2.2}$$

where a and b are the major and minor axes of the ellipse respectively. The

parameter b_1 or b_0 is thus a characteristic distance similar to those of the Whitney-Nuismer criteria. As with the other semi-empirical models, agreement with experiments is generally good because of the curve-fit nature of the model.

Certain researchers [1, 5-7, 10] have attempted to apply the Dugdale / Barenblatt [26, 27] model for holes to a compressively loaded notched laminate. This model was originally formulated for a hole in a steel plate loaded in tension. When the steel behaves in an elastic/perfectly plastic manner, the elastic solution is modified in the region of the hole where yielding occurs. In this region, the stress in the steel remains constant at the yield stress. Researchers applying the principles of this model have suggested that the region around a crack behaves in a manner similar to the elastic/plastic steel. They assume that after damage occurs near the edge of the hole, the damaged area continues to carry load, though at a level below what it would carry if it continued to behave elastically. They define a region along the notch line in which damage occurs. The stress carried by this region is assumed as zero [5], as constant [1, 6, 10], or as linearly increasing away from the hole [1, 6, 7, 10].

The work by Soutis *et al.* [6, 7] is more successful in this approach. The region in question is termed the microbuckling length, which was observed as a region of fiber kinking. Thus, it is assumed that local fiber buckling is the damage mechanism which leads to failure. The size of this region is determined as the region where the calculated elastic stresses exceed the unnotched strength of the laminate. This region is viewed as an imaginary crack growing off the original hole which has a surface traction applied in the form of a crack-closing stress. This stress is distributed over this region as a constant or linearly increasing from zero such that the

stress intensity factor at the edge of the imaginary crack is zero. For a given length of imaginary crack, the stress carried by the laminate can be calculated. By incrementing the length of the crack until the load carried decreases, the critical crack length and the corresponding critical load can be determined.

The assumption that the traction force varies linearly was found to provide better predictions. The model proved accurate for predicting the size of the microbuckle zone, measured by deplying specimens prior to failure, as a function of the load applied. For a wide range of lay-ups, the model proved capable of predicting the failure load. The model proved less accurate with certain types of laminates, however. For example, the failure stresses of a layups dominated by ±45° plies were underestimated, perhaps due to the greater amount of damage and nonlinearity which occurs in such laminates. Failure stresses for a laminate with external 0° plies were overestimated. The authors attribute this to the premature buckling of these external plies.

The model requires the unnotched strength of the laminate and the "fracture toughness" of the laminate in compression as parameters. The fracture toughness is measured for each lay-up by testing a specimen with a knife-sharpened notch. Using a J-integral formulation, the critical strain energy release rate is found from the failure load. The fracture toughness is then found using the relationship between fracture toughness and critical strain energy release rate for an orthotropic plate. It should be noted that the existence of a laminate fracture toughness, particularly in compression, is not generally accepted within the composites community. The authors justify its use by pointing out that the damage zone is much smaller than the other specimen dimensions.

One other notable approach has been taken in the modeling of notches: that of a progressive failure numerical simulation. Originally developed for tensile loading [28], it has also been applied to compressive loading [14]. In such a model, the laminate is numerically discretized using finite elements. Stresses and strains are calculated within the laminate as loading is increased incrementally. At each load level, the stresses within each element are checked for failure by applying a chosen failure criterion. If failure is indicated within an element, the stiffness properties of the element are reduced according to the type of failure indicated. The size and shape of the elements chosen may thus influence the results of the simulation, though this is true of any finite element model. After the stiffness properties are degraded, stresses are recalculated and checked to see if they cause failure in any elements. When this process has converged for a load level, the load is increased by another increment. When the model no longer converges, the laminate is assumed to have failed.

The progressive failure approach to the problem of notches shows potential, though much remains to be done. It promises to determine the notched laminate behavior based only on the properties of the unnotched, unidirectional material. As computing power increases, this approach will probably become more popular. However, at the present time, several problems exist. The approach requires an accurate failure model, but this still does not seem to exist. Also, the manner in which stiffness should be reduced after failure is indicated is not well understood. Finally, the model does not include all the possible modes of damage in the laminate, namely delamination. Without including all modes of damage, it is impossible to fully model the failure of the laminate.

In summary, several models have been developed to predict or

correlate the strength of notched composites loaded in compression. The various models incorporate some insight into the nature of the problem and, in some cases, the modes of failure. However, all are semi-empirical models that require testing of the laminate in question in the notched condition to achieve good results.

All of the work discussed thus far has dealt with monolithic laminates. Limited work has been carried out on notched sandwich panels in tension [29] and in compression [30]. The use of sandwich panels complicates the problem by introducing additional structural effects. However, the specimens generally behave as two independent laminates tested together. If fact, for the compressive tests [30], the sandwich configuration was regarded as merely a fixture which allowed thin laminates to be tested [31]. Thus, it appears that the work on monolithic laminates is directly applicable to composite sandwich panels, provided the structural effects of the sandwich panel are taken into account.

2.2 Post-Impact Compressive Behavior of Composite Sandwich Panels

Impact damage has been identified as leading to significant reductions in the strength of composites. Numerous types of damage are possible: delamination, fiber breakage, matrix splitting, etc. A large body of work has been accumulated on the subject of impact events in monolithic composites. Good references on this can be found in the review papers by Abrate [32] and by Cantwell and Morton [33].

Less work has been done on impact of sandwich panels. However,

such structures can also be quite sensitive to impact events and to the damage due to such events. Furthermore, the sandwich structure introduces the possibility of additional modes of damage. For example, the bond between the facesheet and the core can be damaged [34]. The core can also be crushed, by cell collapse in the case of foam core [35] or by cell wall buckling in the case of honeycomb [36]. However, the nature of a sandwich structure normally results in the back (undamaged facesheet) remaining as an alternate load path even if one facesheet is severely limited in its load-carrying ability [34, 37].

The problem of impact has been divided into two parts: damage resistance and damage tolerance [38]. Damage resistance is a measure of the extent of damage which occurs in the laminate or structure for a specific event, in this case an impact event. Damage tolerance is defined as the ability of a structure to perform given that damage is present. It should be noted that this distinction is not universally recognized and that several works on impact of sandwich panels merely examine the residual strength as a function of the impact energy. This approach, therefore, involves both damage resistance and damage tolerance without separating the effects of either on the final result, residual strength.

Several different test methods have been used to evaluate residual strength of composite sandwich panels. These include fatigue [39], three or four point bending [40-42], uniaxial compression [35, 37, 42-44], and in-plane shear [34, 43]. However, it has been noted that the initial failure mode in shear loading is, in fact, compressive failure [37]. This failure mode will be discussed further.

Some researchers have attempted to correlate the residual strength of an impacted sandwich panel with the residual strength of a sandwich

panel with a drilled hole. Both Adsit and Waszczak [40] and Rhodes [36] used the area of visible damage in this comparison. However, comparison of visible inspection with C-scan inspection shows that the C-scan always revealed a substantially larger damage area than that detected visually [40]. The approach of correlating notched and impacted residual strengths raises two issues. The first is that an impact event which does not create visible damage can still result in a reduction of strength [40]. This, along with the earlier comparison of damage sizes, brings into question the suitability of visible damage area as a valid damage parameter. The second is that the failure modes can differ for the cases of panels with impact damage and panels with notches.

The failure mechanisms of notched composites have been well documented, as discussed earlier in this chapter. However, the literature contains only one identified failure mode for impacted sandwich panels, and that only for limited cases. For the case of sandwich panels with thin (two-ply) fabric facesheets tested in uniaxial compression, the initial dent from impact damage has been observed to grow stably in a direction perpendicular to the loading. This growth is followed by catastrophic failure [37]. As mentioned previously, failure mode due to in-plane shear loading has been found to be the same [34]. Recently, Tsang [45, 46] has found the same mode of failure to occur when static indentation is used to create simulated impact damage. Using out-of-plane moiré interferometry, he was able to measure the initial profile of the dimple and to observe and measure its stable growth. In addition, when a composite sandwich panel was manufactured with the shape of a dimple caused by impact but without the facesheet damage normally found, the same failure mode was found to result. It should be noted that this mode has only been observed in

sandwich panels with very thin facesheets.

An analytical model developed by Minguet [47] and later modified by Tsang [45] has proven capable of capturing this failure mode. In this model, the facesheet is modeled as an initially deformed plate and the core as an orthotropic continuum. The model does not account for initial damage in the facesheet. Because this model is used in this investigation, it will be discussed in more detail in Chapter 4.

In summary, although numerous residual strength tests have been conducted, only one failure mode has been identified for the failure of impacted composite sandwich panels. There exists a model which incorporates this type of damage growth and has proven capable of predicting it for the case of thin-faced composite sandwich panels.

2.3 Summary

The review of the literature reveals several needs which are addressed in the current investigation. For panels with notches, several models have been developed to predict the failure stress. However, except for the progressive failure numerical simulation which has not yet reached the point where it can be used with confidence, these models are all semi-empirical. Thus, tests on notched laminates are required to predict the behavior of laminates with notches as part of the damage tolerance approach to design.

Other factors should be addressed regarding the compressive strength of notched laminates. Among these are the effects of the ratio of the notch length to specimen width and also the ratio of notch length to specimen length. The effects of the sandwich structure on the notched behavior are also not fully understood.

The effects of impact damage on the compressive behavior of composite sandwich panels is also not well understood. Attempts have been made to relate the strength of impacted sandwich panels to the strength of a notched laminate. In this approach, the actual failure mechanisms of the impacted panel are ignored. Currently, only one failure mode for impacted sandwich panels loaded in compression has been identified, and that only for limited cases. The existence of this failure mode for other configurations should be investigated. Also, the usefulness of methods developed to model this failure mode should be examined for other cases.

Chapter 3

Approach

As mentioned in Chapter 1, the principal objective of this investigation is to examine the effect of damage on the behavior of composite sandwich panels loaded in compression. This objective is motivated by the need for an aircraft with a composite fuselage to operate with damage present, whether that damage is deliberate or accidental. In addition to the final failure load, the stress field is examined, as are the mechanisms involved in the propagation of damage. Finally, the effects of scaling the specimen and damage are examined by testing specimens of different sizes and with different damage sizes. An experimental program and existing analytical models were used to meet the stated goals. The overall approach of this investigation is presented in this chapter. Details of the analytical and experimental methods are presented in Chapters 4 and 5, respectively.

The experimental component of the test includes testing of undamaged, notched, and impacted specimens in compression. In addition to strain gages which were used in all tests, photoelastic coatings were used to examine the strain field of the notched specimens. The strain fields thus recorded are compared to predictions from an analytical solution. The final failure stress is correlated using the Mar-Lin criterion. For the impacted specimens, out-of-plane moiré interferometry was used to monitor the growth of damage during loading. These measurements are compared to predictions of the damage growth from an existing model.

Testing was conducted in two rounds. The first round contained the

majority of the specimens. The configurations of these specimens were determined before testing began. The second round was planned to allow issues raised in the first round of testing to be addressed. The second round included those specimens held in reserve as well as specimens moved from the first round as discussed in the following sections.

3.1 Description of Specimens

Because of the use of sandwich construction within the ATCAS program, sandwich specimens were tested in this investigation. The graphite/epoxy tape, T300/F584, and the glass-reinforced phenolic honeycomb core, HRP-3/16-8.0, were chosen for this investigation by the sponsor. Specimens from two panels were tested. The first, A, has a layup of $[+45/0/-45/90/0/-45/+45/0/90/-45/0/+45/\text{core}]_S$, while the layup of the B panel is $[+30/-30/0/90/0/-45/+45/0/90/0/-30/+30/\text{core}]_S$. In both cases, the core thickness was 19.1 mm.

Specimens for this investigation were prepared from these panels. Fourteen small specimens with nominal in-plane dimensions of 203 mm by 50.8 mm (8 in by 2 in), five medium specimens of 381 mm by 203 mm (15 in by 8 in), and four large specimens of 762 mm by 381 mm (30 in by 15 in) were prepared and tested for each layup. The medium and large specimens are of the same size as specimens tested previously within the ATCAS program. The size of the small specimens was chosen to reduce the amount of material required for each specimen. Prior to testing, the ends of each specimen were mounted in a 25 mm thick block of epoxy in order to stabilize the ends and prevent brooming failure. This resulted in a total gage length of 153 mm, 331 mm, and 712 mm for the small, medium, and large

specimens, respectively. The general specimen configuration with such epoxy added is shown in Figure 3.1. All three specimen sizes are shown together in Figure 3.2 for comparative purposes.

Specimen designations are in the following form: A-M-DN25. The initial letter, "A" or "B," designates the layup of the specimen. The second letter, "S," "M," or "L," designates the specimen size as small, medium or large. The third group can be of three forms, depending on the testing conditions for the specimen. A "U" indicates that the specimen was tested in an undamaged state. An "I" indicates that the specimen was impacted prior to testing. Following the "I" in this case is "L1" or "L2," denoting the impact level. The energy levels are discussed more fully in Section 3.2. The letters "SN" indicate that the specimen was tested with a notch in one facesheet, while the letters "DN" indicate that the specimen had a notch in both facesheets. For the notched specimens, the final number indicates the nominal notch length in millimeters. Finally, if two specimens were tested in identical configurations, the letter "a" or "b" was appended to the specimen designation to distinguish between the two. For example, B-L-SN76 is a large B specimen with a single, 76 mm notch, while A-M-IL2 is a medium A specimen impacted with a level 2 impact event. Each specimen tested within this investigation also has a specimen number which was assigned by the sponsor. The designations given by the sponsor, along with the designations used in this investigation, are given in Appendix A.

3.2 Test Program

The test program was determined in consultation with the program sponsor in order to satisfy their needs and to meet the objectives of the

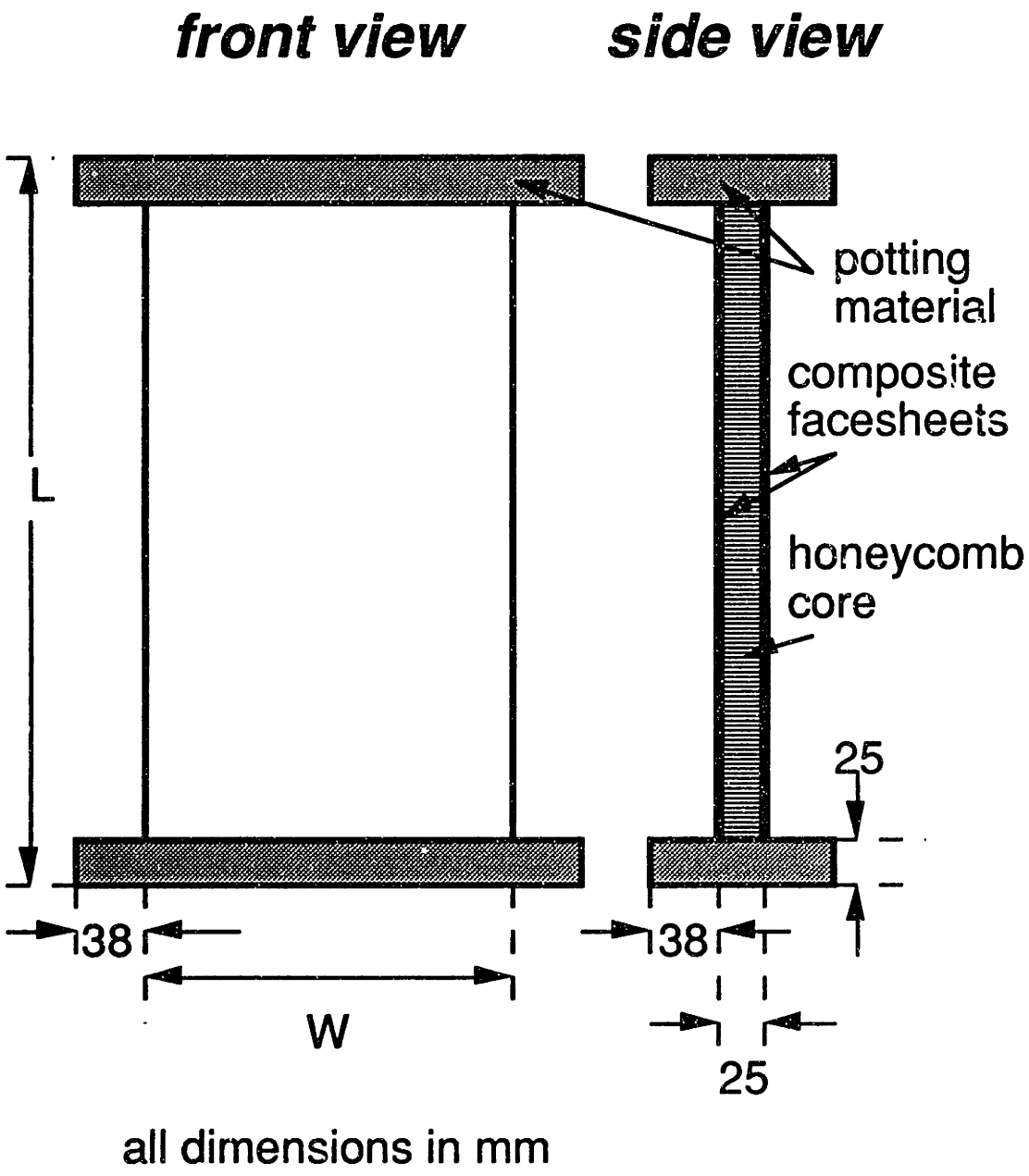

Figure 3.1 Specimen configuration.

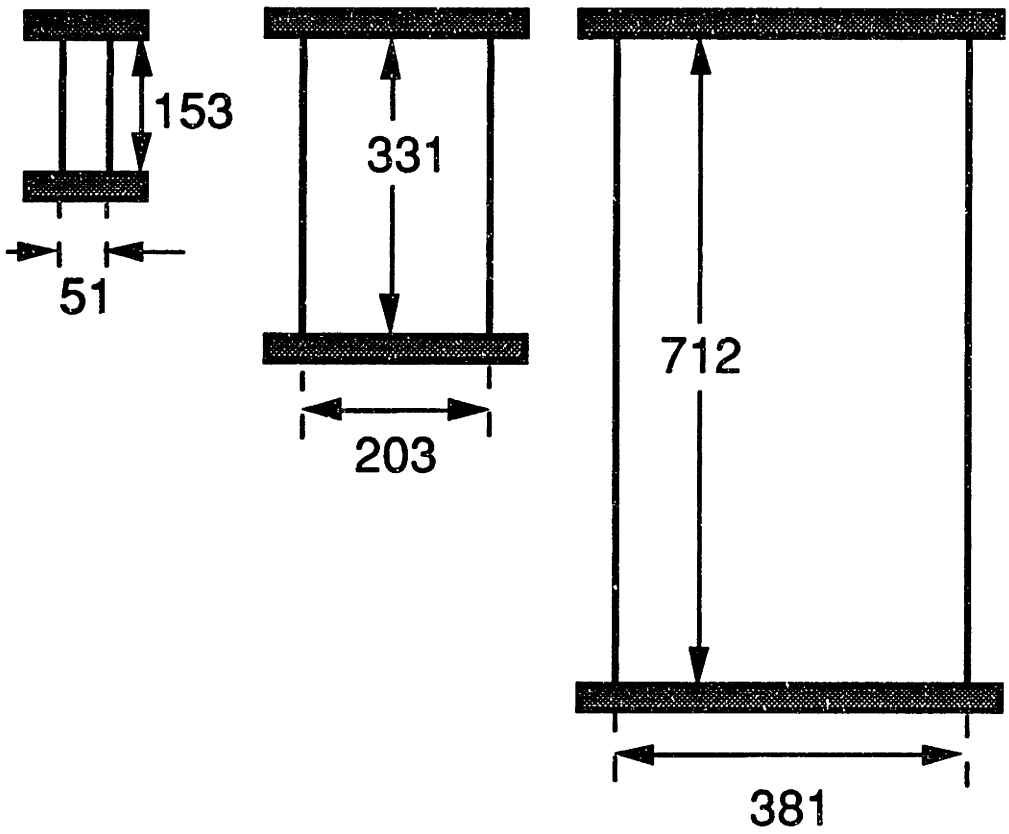

Figure 3.2 Scaled illustration of *(left)* small, *(center)* medium, and *(right)* large specimens.

program as previously stated. An initial plan was determined which reserved one medium and one large specimen of each layup for a second round of testing. After the other specimens had been completed, the testing configuration of these specimens would be determined.

The small specimens were to be used to investigate the notched compressive strain distribution and failure of the sandwich panels as well as the unnotched strength. From these tests, the undamaged strength was to be determined as well as the reduction in strength due notches of various sizes. Thus, for each layup, two specimens were tested in the unnotched condition. Three specimens from each layup were tested with each of the following notch lengths: 3.2, 6.4, 9.5, and 12.7 mm (0.125, 0.25, 0.375, and 0.5 in). These notch sizes were chosen to represent a wide range of damage but still keep the ratio of the specimen width to the notch length greater than four. It has been shown for circular holes [24] that if this ratio is kept over four, the effects of finite width will be small. Other researchers [3] have recommended the ratio be kept over three. The shape of the notch was chosen by the sponsor to be a narrow slit with rounded ends. These notches were to be placed only in one facesheet of the specimen. The notching process is discussed further in Chapter 5. After the initial tests, it was decided that one specimen from each layup at each notch size should be tested with both facesheets notched. This was done to examine the effect of notching one side versus two and also to match the previous tests conducted by the sponsor in which both sides were notched. A summary of the tests conducted on the small specimens is given in Table 3.1.

Both strain gages and photoelastic coatings were used to examine the behavior of the small notched specimens during testing. Strain gages provide an accurate reading of the average strain over a small region. A

Table 3.1 Test matrix for small specimens for each layup

Notch Length	Number of Sides Notched		
	0	1	2
unnotched	1[a]	-	-
3.2 mm	-	2[b]	1
6.4 mm	-	2[b]	1
9.5 mm	-	2[b]	1
12.7 mm	-	2[b]	1

a Indicates the number of specimens tested.

b One of each of these was tested with a photoelastic coating on notched side.

photoelastic coating, on the other hand, provides a general picture of the strain across a wide area of the specimen but with less accuracy. The first notched specimens tested, which had 12.7 mm notches, were tested with a piece of photoelastic coating placed over the entire notched face. After these tests, it was determined that using the coating on only half of the notched facesheet would be sufficient because of the symmetry of the specimen about the vertical centerline. One specimen of each layup was tested at the remaining notch lengths with a coating placed in this manner. Also, the first specimen tested with notches in both facesheets had a photoelastic coating applied to half of one facesheet. The remainder of the specimens were tested with strain gages only.

After the testing of the small specimens was completed, the testing of the medium and large specimens was begun. Test conditions for these specimens included unnotched, notched, and impacted. The impacted specimens were damaged before testing by an impact event with a 25.4 mm diameter hemispherical steel impact device. The mass of the impactor was 6.16 kg and the nominal impactor velocities were 2.7 m/s and 4.3 m/s. An impact at a velocity of 2.7 m/s is referred to as a level 1 impact, while an impact at a velocity of 4.3 m/s is referred to as a level 2 impact. Level 1 and 2 impacts result in nominal impact energies of 22.6 J and 56.5 J, respectively. The parameters of the impact events were chosen by the sponsor to simulate an actual impact event which might damage a composite aircraft fuselage during service. For these specimens, the damage growth was monitored during testing using the out-of-plane moiré method, details of which are given in Chapter 5.

Included in the first round were one medium and one large specimen of each layup tested with 51 mm (2 in) and 76.2 mm (3 in) long notches in

both sides, respectively. These notch sizes were chosen by the sponsor to provide data on the strength reduction due to a wide range of notch sizes. The use of these sizes of specimens was necessary in order to keep the ratio of specimen width to notch length above four as with the small specimens. The specimens were notched on both sides to match previous testing within the ATCAS program. Instrumentation for these notched specimens included strain gages and a photoelastic coating on half of one facesheet.

The final specimens of the first round were one medium and one large specimen of each layup which were planned to be tested in the unnotched condition. However, capacity of the testing machine was determined to be insufficient to test the large specimens to failure. Therefore, the large specimens were not tested unnotched and were added to the second round. The medium specimen from the A layup was tested unnotched, but it was decided not to test the one from the B layup in this manner. It too was added to the second round. The resulting test matrix for the first round is shown for the medium specimens in Table 3.2, and for the large specimens in Table 3.3.

The testing configuration of the second round specimens was determined based upon the results of the previous tests. A large gap in the notched strength test data would be filled by tests with notches in the range of 25 mm (1 in). Also, there was interest in examining the effect of notching only one facesheet instead of both for these larger specimens. Finally, there was a desire to examine the effects of specimen size on the strength of specimens with the same size notch. Therefore, it was decided to test the remaining seven specimens with notches of 25.4 mm (1 in) length. These specimens included medium and large specimens and specimens notched on one facesheet or both. The manner of testing of these specimens is detailed

Table 3.2 Test matrix for medium specimens of first round

Configuration	Layup	
	A	B
Impacted, level 1	1[a]	1
Impacted, level 2	1	1
51 mm notch	1	1
undamaged	1	-

[a] Indicates the number of specimens tested.

Table 3.3 Test matrix for large specimens in first round

Configuration	Layup	
	A	B
Impacted, level 1	1[a]	1
51 mm notch	1	1

[a] Indicates the number of specimens tested

in Table 3.4. All of these specimens were tested with a photoelastic coating on half of the smooth face.

A summary of the specimens from the A layup and their testing configurations are given in Table 3.5, and a summary of the specimens with the B layup is given in Table 3.6. The only difference between the two tables concerns the medium specimen which was tested in the undamaged condition in the case of the A layup, while its counterpart from the B layup was tested with a single 25.4 mm notch.

3.3 Analyses

Various existing analytical techniques are used to correlate or predict the compressive behavior of the specimens tested. The stress distribution around a through-thickness elliptical hole in an anisotropic plate has been solved by Lekhnitskii [48]. The results of this analysis are used to predict the strain distribution observed during testing with the photoelastic coating on the notched specimens. The predicted and experimental strain distributions are then compared, and these results are used to examine the effects of the finite specimen length and width on the strain distribution and the final failure load.

As discussed in Chapter 2, several models exist for correlating the notched strength of monolithic composites loaded in compression. Since the in-plane behavior of the sandwich panel is dominated by the composite facesheets, these models should be applicable to the sandwich panel as well. Most of these models require one or more unnotched strength parameters, with the compression strength especially difficult to measure accurately. The Mar-Lin correlation, however, uses an extremely simple form to

Table 3.4 Test matrix for the second round of tests [a]

	Layup A		Layup B	
	1 Side Notched	2 Sides Notched	1 Side Notched	2 Sides Notched
Small	-	-	-	-
Medium	-	1[b]	1	1
Large	1	1	1	1

[a] All specimens of the second round tested with 25.4 mm long notches.

[b] Indicates the number of specimens tested.

Table 3.5 Summary of specimens of the A layup and their test conditions

Damage	Specimen Size		
	Small	Medium	Large
undamaged	2[a]	1	-
3.2 mm notch (one side)	2	-	-
3.2 mm notch (two sides)	1	-	-
6.4 mm notch (one side)	2	-	-
6.4 mm notch (two sides)	1	-	-
9.5 mm notch (one side)	2	-	-
9.5 mm notch (two sides)	1	-	-
12.7 mm notch (one side)	2	-	-
12.7 mm notch (two sides)	1	-	-
25.4 mm notch (one side)	-	-	1
25.4 mm notch (two sides)	-	1	1
50.8 mm notch (two sides)	-	1	-
76.2 mm notch (two sides)	-	-	1
level 1 impact	-	1	1
level 2 impact	-	1	-

[a] Indicates the number of specimens tested.

Table 3.6 Summary of specimens of the B layup and their test conditions

Damage	Specimen Size		
	Small	Medium	Large
undamaged	2[a]	-	-
3.2 mm notch (one side)	2	-	-
3.2 mm notch (two sides)	1	-	-
6.4 mm notch (one side)	2	-	-
6.4 mm notch (two sides)	1	-	-
9.5 mm notch (one side)	2	-	-
9.5 mm notch (two sides)	1	-	-
12.7 mm notch (one side)	2	-	-
12.7 mm notch (two sides)	1	-	-
25.4 mm notch (one side)	-	1	1
25.4 mm notch (two sides)	-	1	1
50.8 mm notch (two sides)	-	1	-
76.2 mm notch (two sides)	-	-	1
level 1 impact	-	1	1
level 2 impact	-	1	-

a Indicates the number of specimens tested.

correlate/predict the notched strength. For a given material system, only one notched strength measurement is required. However, the accuracy of this criterion when the range of notch sizes is large is not well established.

Notched strength has also been used to predict the residual strength of an impacted composite laminate [36, 40]. Therefore, the Mar-Lin criterion will also be applied to the impacted specimens in an attempt to predict their residual strength based on the size of the visible damage. However, sandwich panels which are impacted and then loaded in compression have been observed to have a unique failure mode which can limit the applicability of models for monolithic laminates. Sandwich panels experience a growth of the dimple caused by impact. Such growth occurs via out-of-plane deflection of the facesheet. This deflection is strongly influenced by the core. Thus, while compressive failure of impacted monolithic laminates is largely an in-plane process, sandwich panels impacted and then loaded in compression experience out-of-plane damage growth and failure.

A model has been developed by Minguet [47] which predicts the growth of the impact dimple in this manner. Tsang [45] has modified this model and correlated it with the growth of the dimple and final failure of the sandwich panels. This model only accounts for the core damage and may be inaccurate for an impact event which results in damage to the facesheets. Also, this mode of failure and the work of Minguet and Tsang were all based on sandwich panels with thin facesheets. The facesheets of the sandwich panels used in this investigation are substantially thicker, 2.4 mm versus 0.7 mm in the previous work. This fact may make predictions with the existing model inaccurate. The accuracy of the Minguet/Tsang model for the impacted sandwich panels of this investigation will be

examined by comparing the predictions of this model with the dimple growth as monitored by moiré interferometry. Also, failure of the specimens will be predicted using the model, and these predictions compared to experimental failure loads.

Chapter 4

Analytical Methods

Three analytical techniques were used to correlate or predict the compressive behavior of the composite sandwich panels. The first is the elasticity solution for the stresses in an orthotropic plate with a hole. This is compared with the results obtained using the photoelasticity technique discussed in the following chapter. The second is the Mar-Lin correlation [23] which is a semi-empirical model used to predict the strength of composite laminates with discontinuities. The third is the Minguet/Tsang [45, 47] model for the propagation of a dimple in a sandwich panel. These models explore different aspects of the behavior: the elastic stress distribution and the final failure load for notched panels, and the mechanism of failure for impact damaged panels.

4.1 Stresses in a Notched Laminate

The stress distribution of an infinite anisotropic plate with a through-thickness elliptical opening has been solved using complex potentials by Lekhnitskii [48]. A very straightforward treatment of Lekhnitskii's solution is given by Tan [20]. In order to examine the effects of the notch on the stress distribution and whether these effects would be influenced by the proximity of the edge of the specimen, this analysis was performed for the notched sandwich specimens. The problem considered is shown in Figure 4.1. The variables used are σ_x^*, the applied far-field stress, and b and a, the lengths of the major and minor axes of the ellipse, respectively. The values

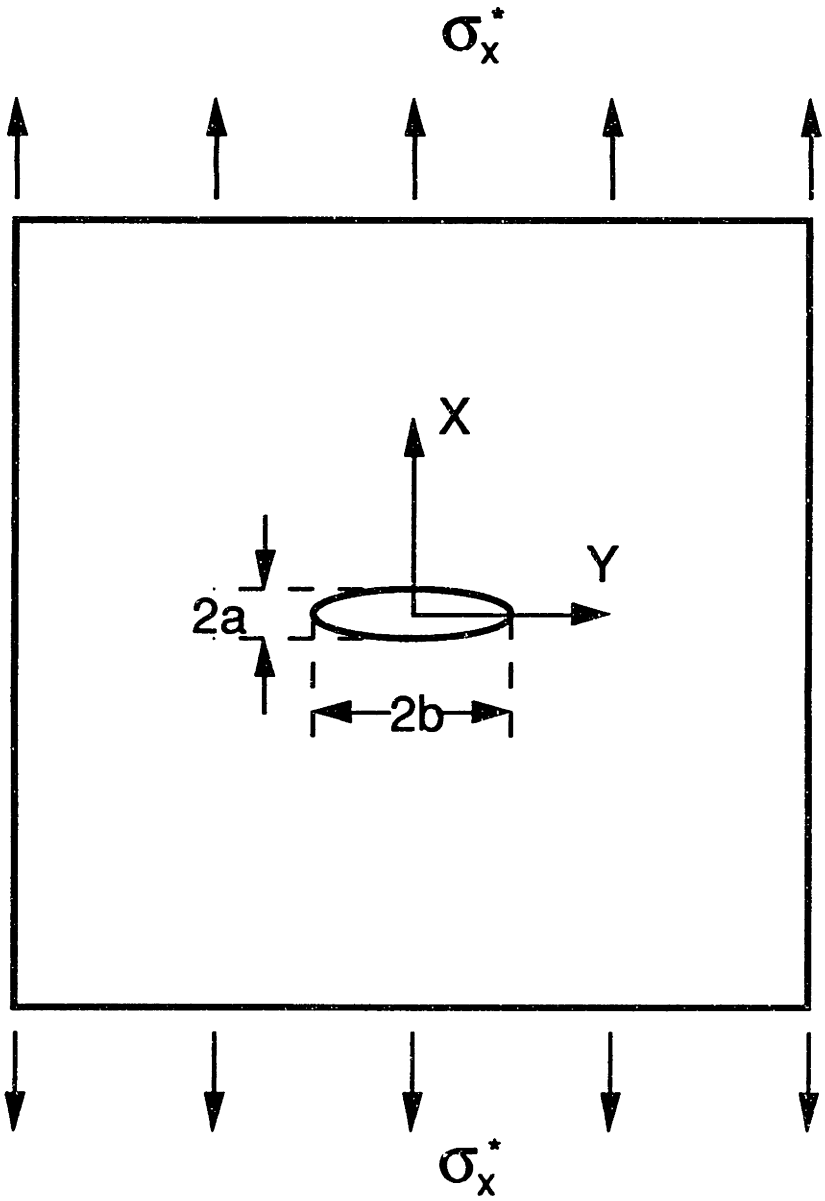

Figure 4.1 Illustration of uniaxially loaded plate with elliptical notch.

of a and b were chosen so that 2a and 2b would equal the nominal experimental notch width and length, respectively. Although the ellipse differs in shape from the notches used experimentally, it was felt that the comparison would be useful.

The assumptions made in the derivation of the solution are:

i) the plate is in plane stress

ii) the plate is homogeneous and anisotropic

iii) the plate is infinite, such that the plate is large compared to the size of the hole and the hole is located far from the edges of the plate

iv) the deformation is small so that linear strain-displacement relations can be used

v) the material is linearly elastic

Furthermore, for this investigation, the plate is assumed to be orthotropic because the sandwich panel as a whole is balanced and symmetric. The degree to which the experimental case approaches these ideals is examined and discussed in Chapter 7.

The solution given by Lekhnitskii [48] is outlined here. The first step is to determine the complex parameters of the plate. These parameters characterize, in part, the anisotropy of the plate. They are found by solving the characteristic equation which arises from the differential equation which must be satisfied by a stress function in an anisotropic plate:

$$a_{11}\mu^4 - 2a_{16}\mu^3 + (2a_{12} + a_{66})\mu^2 - 2a_{26}\mu + a_{22} = 0 \qquad (4.1)$$

where a_{ij} are the elements of the in-plane compliance matrix for the laminate. For the case of an orthotropic plate, Equation 4.1 reduces to:

$$\mu^4 + (\frac{E_x}{G_{xy}} + 2\upsilon_{xy})\mu^2 + \frac{E_x}{E_y} = 0 \tag{4.2}$$

where E_x, E_y, G_{xy}, and υ_{xy} are the elastic constants for the orthotropic plate calculated using classic laminated plate theory with the axes defined in Figure 4.1. Material parameters for the system used in this investigation are shown in Table 4.1. These parameters are utilized to calculate the laminate-level elastic constants (E_x, E_y, G_{xy}, υ_{yx}, and υ_{xy}) used in this analysis. Disregarding certain degenerate cases, the roots of Equation 4.2 can be of three classes:

$$\mu_1 = \beta\, i,\ \mu_2 = \delta\, i \tag{4.3 a}$$

$$\mu_1 = \mu_2 = \beta\, i \tag{4.3 b}$$

$$\mu_1 = \alpha + \beta\, i,\ \mu_2 = -\alpha + \beta\, i \tag{4.3 c}$$

where α, β, and δ take on values greater than 0 and where i is the imaginary number. Equation 4.2 was solved iteratively using the program Mathematica. The constants used to evaluate Equation 4.2 are given in Table 4.2. For the A laminate, the result is:

$$\mu_1 = 0.135 + 1.09\, i \tag{4.4 a}$$

$$\mu_2 = -0.135 + 1.09\, i \tag{4.4 b}$$

For the B laminate, the result is:

$$\mu_1 = 0.862\, i \tag{4.5 a}$$

$$\mu_2 = 1.66\, i \tag{4.5 b}$$

Two complex potential functions are needed to determine the stress state. They are given by:

Table 4.1 T300/F584 ply properties

Ply Property	Value
t	0.20 mm (0.008 in)
E_1	114 GPa (16.6 Msi)
E_2	8.96 GPa (1.30 Msi)
G_{12}	4.59 GPa (666 ksi)
υ_{12}	0.324

Table 4.2 Elastic constants for laminates

Elastic Constant	Laminate	
	A	B
E_x	52.7 GPa (7.64 Msi)	64.3 GPa (9.32 Msi)
E_y	36.7 GPa (5.33 Msi)	31.7 GPa (4.56 Msi)
G_{xy}	17.1 GPa (2.48 Msi)	15.0 GPa (2.18 Msi)
υ_{xy}	0.378	0.392
υ_{yx}	0.264	0.192

$$\phi_1 = \frac{\beta_1 - \mu_2\alpha_1}{\mu_1 - \mu_2}\frac{1}{\zeta_1} \tag{4.6}$$

$$\phi_2 = \frac{\beta_1 - \mu_1\alpha_1}{\mu_1 - \mu_2}\frac{1}{\zeta_2} \tag{4.7}$$

where α_1 and β_1 are the loading parameters. For the case considered, these are given by:

$$\alpha_1 = 0 \tag{4.8}$$

and

$$\beta_1 = -\frac{\sigma_x^* bi}{2} \tag{4.9}$$

The variables ζ_1 and ζ_2 represent the mapping function and are given by:

$$\zeta_j = \frac{z_j + \sqrt{z_j^2 - a^2 - \mu_j^2}}{a - \mu_j bi}, \quad j = 1, 2 \tag{4.10}$$

where the complex variables z_j are given by:

$$z_j = x + \mu_j y, \quad j = 1, 2 \tag{4.11}$$

The stresses in the plate are thereby determined from:

$$\sigma_x = \sigma_x^* + 2Re[\mu_1^2\phi_1' + \mu_2^2\phi_2'] \tag{4.12}$$

$$\sigma_y = 2Re[\phi_1' + \phi_2'] \tag{4.13}$$

$$\tau_{xy} = -2Re[\mu_1\phi_1' + \mu_2\phi_2'] \tag{4.14}$$

where the derivatives of the stress functions after substitution of Equations 4.8 through 4.10 into Equations 4.6 and 4.7 are given by:

$$\phi_1' = \frac{\partial\phi_1}{\partial z_1} = -\frac{\beta(a - \mu_1 bi)}{(\mu_1 - \mu_2)\left(z_1 + \sqrt{z_1 - a^2 - \mu_1^2 b^2}\right)^2}\left(1 + \frac{z_1}{\sqrt{z_1 - a^2 - \mu_1^2 b^2}}\right) \tag{4.15}$$

and

$$\phi_2' = \frac{\partial \phi_2}{\partial z_2} = \frac{\beta(a - \mu_2 bi)}{(\mu_1 - \mu_2)\left(z_1 + \sqrt{z_2 - a^2 - \mu_2^2 b^2}\right)^2}\left(1 + \frac{z_2}{\sqrt{z_2 - a^2 - \mu_2^2 b^2}}\right) \tag{4.16}$$

For a given point (x, y), the values of z_j are determined from Equation 4.11. The values of the derivatives of the stress functions are then calculated from Equations 4.15 and 4.16. Finally, stresses are calculated from Equations 4.12, 4.13, and 4.14.

Strains in the plate are calculated from the equations of an orthotropic plate, namely:

$$\varepsilon_x = \frac{\sigma_x}{E_x} - \frac{\nu_{yx}\sigma_y}{E_y} \tag{4.17}$$

$$\varepsilon_y = -\frac{\nu_{xy}\sigma_x}{E_x} + \frac{\sigma_y}{E_y} \tag{4.18}$$

and

$$\gamma_{xy} = \frac{\tau_{yx}}{G_{xy}} \tag{4.19}$$

In order to allow comparison with the results of tests with the photoelastic coating results as later described, the difference in principal strains must be calculated at each point:

$$\Delta\varepsilon = \varepsilon_I - \varepsilon_{II} = \sqrt{\gamma_{xy}^2 + \left(\varepsilon_x - \varepsilon_y\right)^2} \tag{4.20}$$

This parameter is considered as the end result of the calculation.

A FORTRAN77 program named ELLIPSE was written to implement the calculations described. The program takes as input the coordinates x and y, the notch dimensions a and b, and the orthotropic elastic constants E_x, E_y, G_{xy}, υ_{yx}, and υ_{xy} determined for the particular laminate in question. The stresses, strains, and $\Delta\varepsilon$ are then calculated for that point. The listing of this program is contained in Appendix B. The output file of ELLIPSE

containing the coordinates and the values of $\Delta\varepsilon$ is used to create a contour plot of $\Delta\varepsilon$. The program SYSTAT is used to produce contour plots of the values of $\Delta\varepsilon$. These plots are exported to the program MacDraw Pro for final modifications. A sample of such a plot for an A specimen with an ellipse with a major axis of 50.8 mm and a minor axis of 5.0 mm at an applied far-field stress of -112 MPa is shown in Figure 4.2.

4.2 Mar-Lin Correlation

The Mar-Lin correlation [23] is a semi-empirical model developed to correlate/predict the strength of a notched composite laminate. It was originally developed for notched laminates loaded in tension. It has been used with reasonable success to correlate the strength of laminates with both circular holes and slits. It has also been used to correlate the strength of notched composites loaded in compression [30]. It has further been applied to a sandwich panel with simulated impact damage loaded in compression [45]. However, it was less satisfactory for this purpose.

The Mar-Lin correlation is used to predict the far-field stress at which failure will occur based on the notch length. The form of the correlation is:

$$\sigma_f = H_C(2b)^{-m} \tag{4.21}$$

where σ_f is the failure strength, H_C is the composite fracture parameter, 2b is the length of the discontinuity (hole, slit, etc.), and m is related to the singularity of the crack tip at the micromechanical level [23]. This formulation implies that there is no dependence of the failure strength on the shape of the notch. The parameters H_C and m must be determined by tests or some other method, making this a semi-empirical method. Because small variations in the experimental data can result in large swings in m if

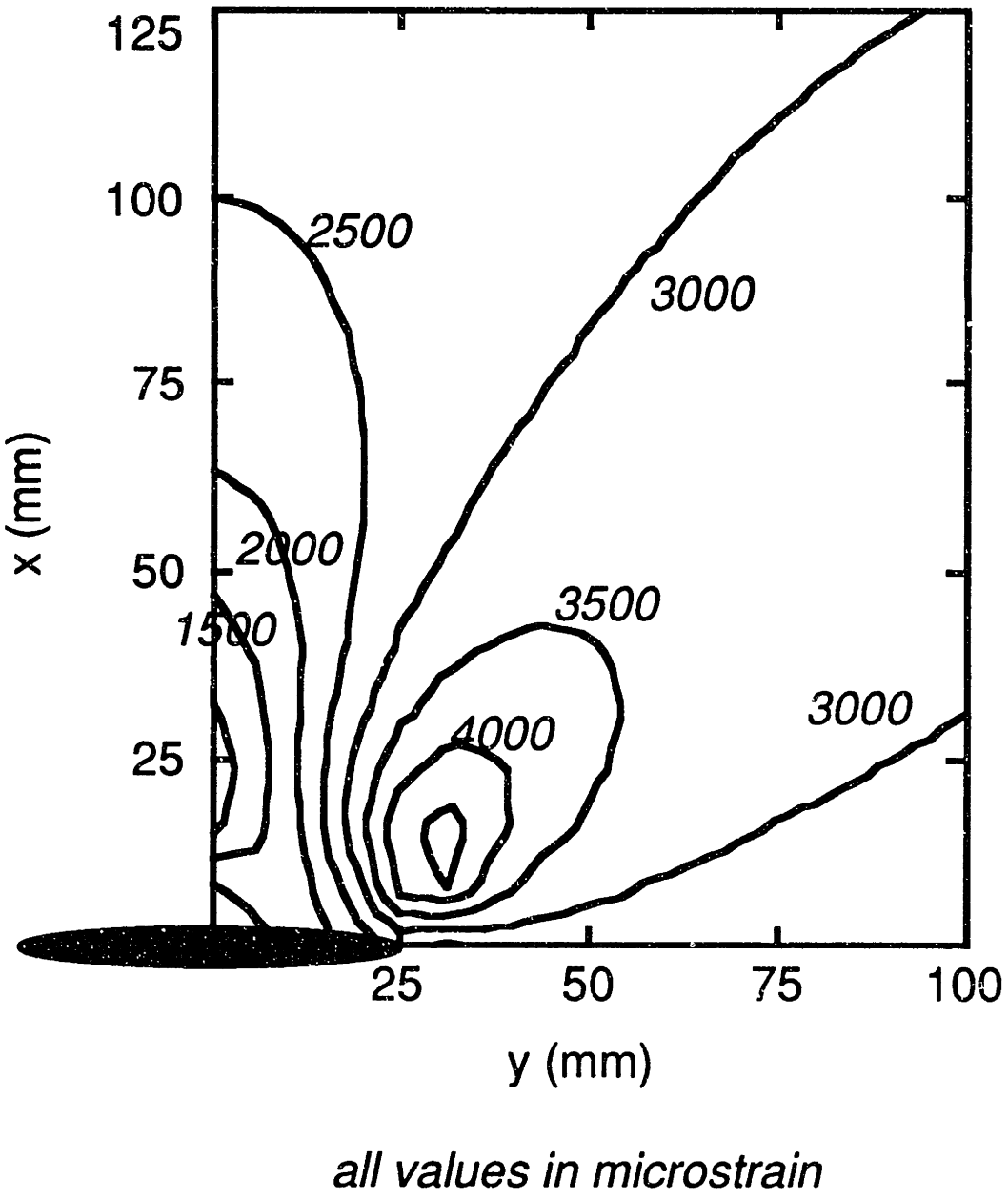

Figure 4.2 Sample contour plot of differences in principal strains obtained by Lekhnitskii's solution. The solution is for a specimen of the A layup with an ellipse with a major axis of 50.8 mm and a minor axis of 5.0 mm at an applied stress of -112 MPa. The calculated far-field value of the difference of principal strains is 2940 microstrain.

both parameters are determined by a logarithmic least-squares best fit, Lagace [24] fixed m based on the theoretical value of the singularity of a crack at a bimaterial interface [49]. For typical graphite/epoxy material systems, the value of m is 0.28.

The relationship between a macroscopic crack in a composite laminate and a microcrack at the fiber/matrix interface is somewhat tenuous. There is at least a plausible relationship in the case of tensile loading. When loading is compressive, however, there appears to be less of a relation between the two. The utility of the model for application to compressive loading is more an indication of the general form of the equation rather than any physics of the problem contained in the formulation. For this case, m must be regarded as a parameter arbitrarily fixed.

For the current investigation, the method of Lagace is followed for applying the Mar-Lin criterion. The parameter m is fixed at 0.28 in all cases. In order to determine the value of H_C, its value is calculated from Equation 4.21 for each specimen tested. The value of H_C for a group of specimens is then calculated as the average of H_C for all the members of the group in question. The coefficient of variation for that set of data is a measure of the "goodness of fit" of the correlation.

4.3 Dimple Propagation Model

As discussed in Chapter 2, a model has been developed to predict the growth of a dimple caused by an impact event [47] or by static indentation [45, 46] in a sandwich panel under compressive loading. The model was developed by Minguet [47] and modified by Tsang [45, 46]. This model will

be referred to as the dimple propagation model. For this investigation, the model as implemented by Tsang is used without modification in order to gain some insight into the applicability of the model to the cases considered herein. Complete details of this model and its implementation can be found in [45].

The essence of the model is the consideration of an orthotropic plate with existing local curvature in the form of a dimple resting on a foundation which provides supporting reactions. For the case considered, the orthotropic plate represents the facesheet, the existing curvature represents the dimple, and the foundation represents the sandwich core. Furthermore, the core damage due to the impact or indentation and core damage due to subsequent crushing during dimple propagation is modeled. The method by which this is done is later described It should be noted that the back, undamaged facesheet is assumed to be unaffected by the dimple growth on the impacted facesheet.

While Minguet modeled the honeycomb as an orthotropic continuum, Tsang modeled the honeycomb as a two-parameter foundation model. The two-parameter foundation model considers the reaction forces of the foundation to be caused by both the displacements and the curvature of the plate, as given by:

$$\sigma_{zz}(x,y) = k_1 w(x,y) + k_2 \nabla^2 w(x,y) \tag{4.22}$$

A previous elasticity model by Tsang [50] was used to calculate the parameters k_1 and k_2. Using this model, the stresses and displacements at the facesheet/core interface are determined for a Hertzian contact loading of the facesheet. The parameters are then calculated from a least-squares fit of these results to the form of Equation 4.22.

An existing computer code is used to evaluate the foundation parameters. A FORTRAN77 computer code called MODK1K2 [50] is used to calculate the parameters k_1 and k_2 of the foundation. The size of the region modeled, R_p, is chosen to be 63.5 mm or five times the indentor radius. Additional input parameters for MODK1K2 are the thickness and elastic constants of the core and facesheets. Values for the core (as obtained from the manufacturer) and facesheets used in this work are shown in Tables 4.3 and 4.4, respectively. The parameter $E_{in\text{-}plane}$ of the facesheet is chosen as the average of E_x and E_y for the laminate. The parameter ν_{xz} of the facesheet is set equal to ν_{12} for a ply, while the parameter G_{xz} is set equal to G_{12} for a ply. In previous investigations, the in-plane stiffness of the core has been set to the same value as the through-thickness stiffness [50] or half of the through-thickness stiffness [45]. In this investigation, the in-plane stiffness of the core, $E_{in\text{-}plane}$, is assumed to be half of the value of the transverse stiffness, E_{trans}. The values obtained for the foundation parameters are the same, to two significant digits, for the two panels:

$$k_1 = 93 \text{ MN/m}^3 \tag{4.23 a}$$

$$k_2 = -350 \text{ kN/m} \tag{4.23 b}$$

It has furthermore been shown [45] that the results of the dimple propagation model are relatively insensitive to the choice of the foundation parameters, k_1 and k_2.

The facesheet, modeled as an orthotropic plate, is assumed to rest on the two-parameter foundation characterized by k_1 and k_2. The out-of-plane displacements of the facesheet are assumed to be an infinite double sine series in terms of the coordinates x and y. The series is truncated according

Table 4.3 HRP-3/16-8.0 honeycomb core properties used for program MODK1K2

Parameter	Value
t	19.1 mm
$E_{in\text{-}plane}$	0.11 GPa
E_{trans}	1.13 GPa
υ_{xy}	0.5
υ_{xz}	0.1
G_{xz}	179 MPa

Table 4.4 Graphite/epoxy facesheet properties used for program MODK1K2

Parameter	Laminate	
	A	B
h	2.44 mm	2.44 mm
$E_{in\text{-}plane}$	44.7 GPa	48.0 GPa
E_{trans}	8.96 GPa	8.96 GPa
υ_{xy}	0.326	0.292
υ_{xz}	0.324	0.324
G_{xz}	4.56 GPa	4.56 GPa

to the degree of accuracy desired. Similarly, the stresses in the plate are represented by an Airy stress function in the form of a double cosine series. The displacements and stresses are related using the large deformation formulation for anisotropic plates. The resulting nonlinear equations are solved iteratively. Applied axial stresses cause further deflections of the dimple region due to the curvature. The foundation (honeycomb core) resists the deflection as a two-parameter foundation.

However, the core does not behave strictly in an elastic manner. During the impact event, the core is damaged. Additionally, the core can be further damaged by the growth of the dimple. It has been shown [45], that the damage takes the form of cell wall buckling when the core is a honeycomb material. All such damage reduces the ability of the core to support the facesheet.

In order to model this damage, the core is discretized into a uniform grid which can be thought of as individual springs. In order to reduce computational difficulties, the grid is chosen in this investigation as a 102 mm square. This size is over four times the size of the dimple, so the choice of grid size should not affect the results. The initial region of core crushing is chosen to be the region within the zeroeth order fringe from the moiré interferometry measurements discussed in Chapter 5. Because this region of the core is crushed far down during the impact event, this region is assumed to be incapable of supporting the facesheet at any time in the loading, that is, the reaction force of the foundation is set to zero. Loading to the facesheet resting on the foundation is subsequently applied in discrete increments. For each load level, the stresses and displacements of the facesheet and core are calculated. The stresses in the core at the discrete points are then examined. If these stresses exceed σ_{ult}, the critical

stress at which crushing occurs, the point of the core is "relaxed" to simulate core crushing at that point. After relaxation, the load carried by that point is assumed to be constant regardless of the further deformation of the facesheet. This constant is related to the "plateau stress" of the core, $\sigma_{plateau}$. The behavior of the core which yields the values σ_{ult} and $\sigma_{plateau}$ is illustrated in Figure 4.3 [45]. If relaxation occurs at any point in the core during the loading increment, the stresses and strains must be recalculated taking into account the new core crushing. Convergence is reached when no further points are relaxed.

A second FORTRAN77 program, called GROWTH [45], is used to calculate the growth of the dimple. Parameters for the two panels analyzed with GROWTH are shown in Tables 4.5 and 4.6. The parameters d_x and d_y are the dimensions of the grid, while the parameters R_x and R_y are the initial dimple radii in the x and y directions, respectively. The parameter ξ_0 represents the initial depth of the center of the dimple. Furthermore, R_0 is the initial radius of core crushing, and h is the thickness of the facesheet. The parameters A_{ij} and D_{ij} are the elements of the laminate stiffness matrix calculated from classical laminated plate theory. It should be noted that each facesheet is slightly nonsymmetric in that the center two plies are at -45° and +45° angles. This results in nonzero elements of the laminate B matrix. However, the values of the elements of the B matrix are small and will have little, if any, consequence and are thus ignored in the analysis. The program was run to provide predictions of dimple growth by incrementing the loading. As output, the program provides displacements, stresses, and strains of the facesheet at the discretized points. The results of the analyses are given in Chapter 6 and the results compared to those obtained using out-of-plane moiré interferometry as described in Chapter 5.

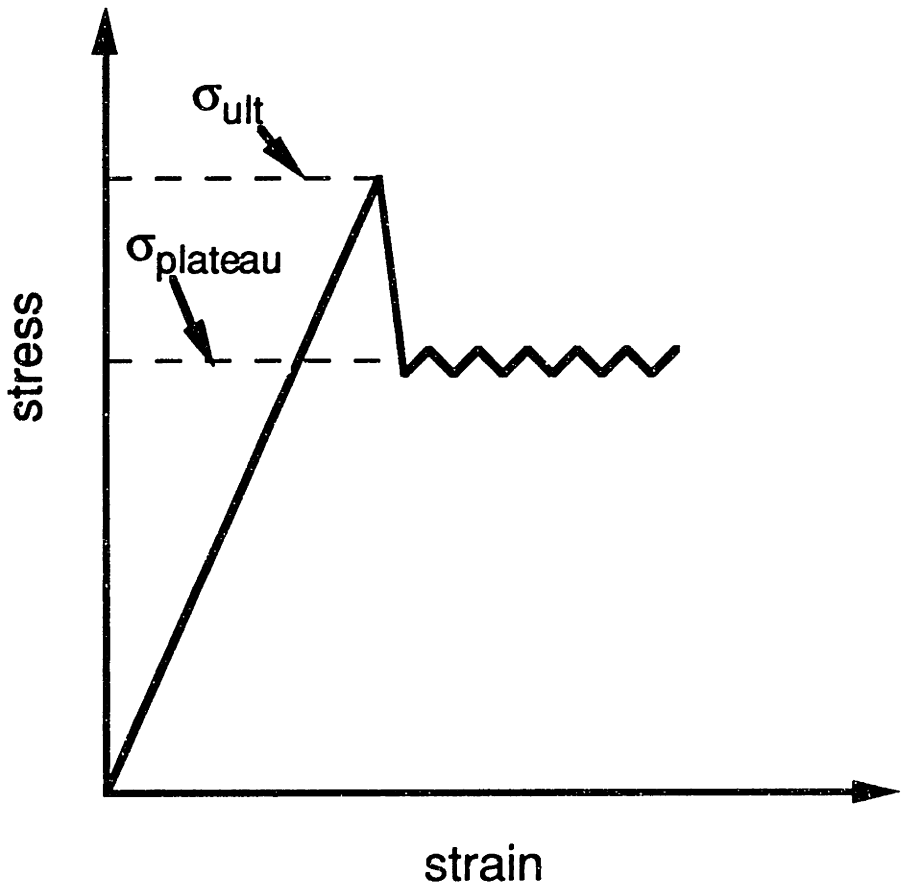

Figure 4.3 Sketch of stress-strain curve of flatwise compression test of HRP-3/16-8.0 honeycomb core, after [45].

Table 4.5 Input parameters for HRP-3/16-8.0 honeycomb core used for program GROWTH

Parameter	Value
d_x	203 mm
d_y	203 mm
R_x	determined for each specimen
R_y	determined for each specimen
R_o	determined for each specimen
ξ_o	determined for each specimen
σ_{ult}	10.5 MPa
$\sigma_{plateau}$	7.77 MPa
k_1	93 GN/m^3
k_2	-350 kN/m

Table 4.6 Input parameters for graphite/epoxy facesheets for program GROWTH

Parameter	Laminate	
	A	B
A_{11}	142 MN/m	169 N/m
A_{12}	37.7 MN/m	32.6 N/m
A_{16}	0	0
A_{22}	99.6 MN/m	83.0 N/m
A_{26}	0	0
A_{66}	41.7 MN/m	36.7 N/m
D_{11}	71.7 Nm	89.1 Nm
D_{12}	21.6 Nm	19.6 Nm
D_{16}	8.03 Nm	5.68 Nm
D_{22}	42.5 Nm	29.0 Nm
D_{26}	8.03 Nm	2.04 Nm
D_{66}	23.6 Nm	21.7 Nm
h	2.44 mm	2.44 mm

One significant limitation of this model is that, although the damage to the core is modeled, damage in the facesheets is not taken into account. Such damage could occur during the impact event and also during the subsequent compressive loading. Damage would affect the bending behavior of the facesheet in the dimple area.

Failure of the impacted sandwich panels is defined as fracture of the impacted facesheet. As reported by Tsang [45], Minguet [47] used the unstable growth of the dimple as the criterion for failure of the panel. Tsang, however, used the longitudinal membrane stress along the centerline as the parameter to determine failure. In this investigation, it was intended to follow the method of Tsang to predict failure. However, it is first necessary to examine the applicability of the model to the growth of the cases considered in this investigation.

Chapter 5

Experimental Procedure

The techniques used in preparing and testing the specimens are presented in this chapter. The contents of this chapter include descriptions of the materials used, the manufacturing procedures, the steps taken to prepare the specimens for testing, the instrumentation used, the experimental setup, the methods used in testing, and the data reduction techniques.

5.1 Manufacture of Specimens

Specimens were made by the Boeing Aircraft Company in their composite manufacturing facility. The specimens were part of two large panels. The A specimens came from a panel designated AK-9A, while the B specimens came from panel AK-9B. These panels had a nominal size of 2.44 m by 1.22 m (96 in by 48 in). The difference between the two panels is the layup of the twelve-ply facesheets as discussed previously. The layup for the facesheets of panel AK-9A is $[+45/0/-45/90/0/-45/+45/0/90/-45/0/+45]_T$. The layup for the facesheets of panel AK-9b is $[+30/-30/0/90/0/-45/+45/0/90/0/-30/+30]_T$. It should be noted that the individual facesheets are not exactly symmetric, but the sandwich panel as a whole is symmetric about its centerline.

The facesheets were made from prepreg tape T300/F584 laid up by hand. This prepreg is made by Hexcel Corporation and has a nominal ply thickness of 0.20 mm (0.008 in). A honeycomb core of 19 mm (0.75 in)

thickness with the ribbon direction aligned with the 0° fibers was placed in the center between the facesheets. The core was type HRP-3/16-8.0 manufactured by the Hexcel Corporation. This is a glass-reinforced phenolic honeycomb with a cell size of 4.76 mm (3/16 in) and a density of 128 kg/m^3 (8 pcf). In order to achieve a good bond between the facesheets and the core, a 0.2 mm (0.008 in) thick layer of film adhesive of type 1515-3M grade 05, made by Narmco Metalbond, was placed between the facesheets and the core. This entire assembly was cocured.

During the curing process, layers of various materials were placed around the panel to allow easy release, to maintain the required pressure, and to remove volatile gases. The entire assembly was placed on a flat aluminum plate called the tool. A layer of "non-perforated parting film," which is similar to teflon, was placed on the plate followed by the assembled layup. Another layer of parting film was added, then a pressure pad, and then a breather. Aluminum fairing bars were placed at the edge of the panels to prevent crushing of the core at the edges. Finally, a vacuum bag was placed around the entire assembly and sealed at the edges to the aluminum plate using vacuum sealer tape. This assembly is illustrated in Figure 5.1.

The bag was checked for leaks by applying a vacuum of 560 mm Hg (22 in Hg). The vacuum was then reduced to 102 mm Hg (4 in Hg), and the cure assembly was placed in an autoclave oven. This low pressure was necessary in order to avoid crushing the honeycomb core. The pressure inside the autoclave was raised to 310 kPa (45 psi). When the pressure in the autoclave reached 138 kPa (20 psi), the vacuum bag was vented to atmospheric pressure. When the pressure in the autoclave reached 310 kPa, the autoclave temperature was raised. Once the temperature reached

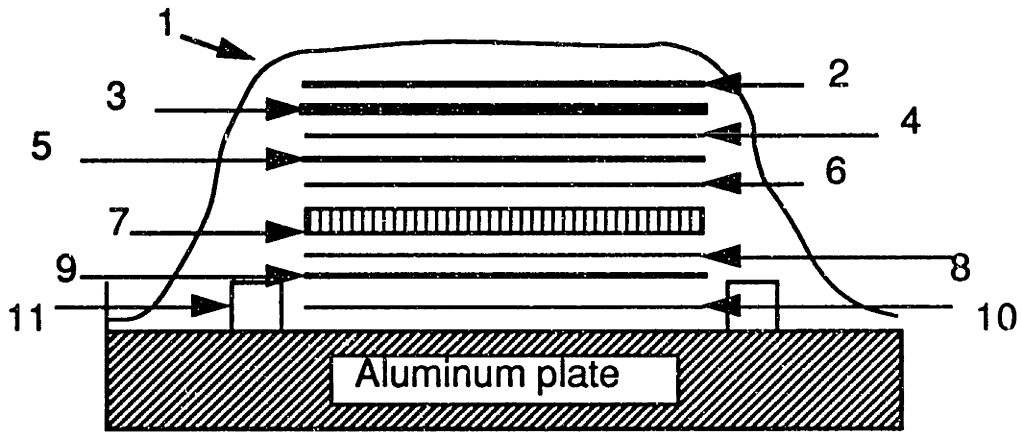

1 = vacuum bag

2 = breather

3 = pressure pad

4 = release film

5 = graphite/epoxy facesheet, uncured

6 = film adhesive

7 = honeycomb core

8 = film adhesive

9 = graphite/epoxy facesheet, uncured

10 = release film

11 = fairing bars

Figure 5.1 Illustration of cure assembly for panels.

54°C (130°F), the heating rate was specified at 0.6 to 2.8°C (1 to 5°F) per minute, as measured by a thermocouple placed on the panel, until the temperature reached 166°C. The heat-up rate was then changed to 0.2 to 2.8°C (0.3 to 5°F) per minute until the temperature reached 179°C (355°F). This temperature was maintained for 120 to 180 minutes. The temperature was then reduced at a maximum rate of 2.8°C (5°F) per minute. When the temperature reached 60°C (140°F), the pressure was released and the assembly removed from the autoclave. A diagram of the pressure and temperature history during the cure cycle is shown in Figure 5.2.

The curing process resulted in two distinct sides to the composite panels. The facesheet which was on the bottom of the assembly developed a relatively smooth outer surface. This facesheet is referred to as the "smooth" side facesheet. The other facesheet developed an uneven surface. This side is referred to as the "rough" side. The curing process also resulted in waviness of the plies in the facesheet. This waviness was created by external pressure forcing the facesheets onto the honeycomb core. The waviness was visible to the naked eye when the facesheet was cut. In fact, it was visible on the outer surface of the rough facesheet in some cases. A cross section of a specimen in which the ply waviness can be seen is shown in Figure 5.3.

5.2 Preparation of Specimens

Specimens were received from the Boeing Company in a pre-cut state. The sizes of these specimens are discussed in Chapter 3. Four of the pieces received from Boeing, which were cut such that the 0° fibers were aligned with the shorter side, were cut into the 28 small specimens. This cutting

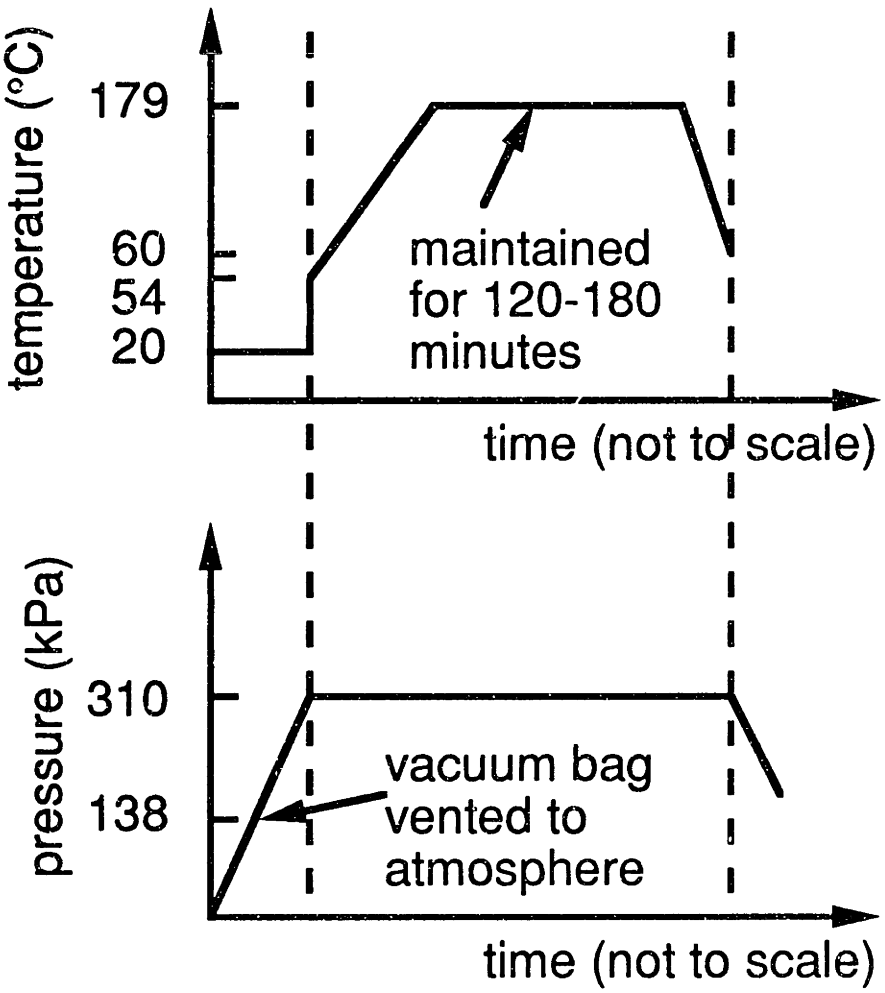

Figure 5.2 Pressure and temperature history during cure cycle.

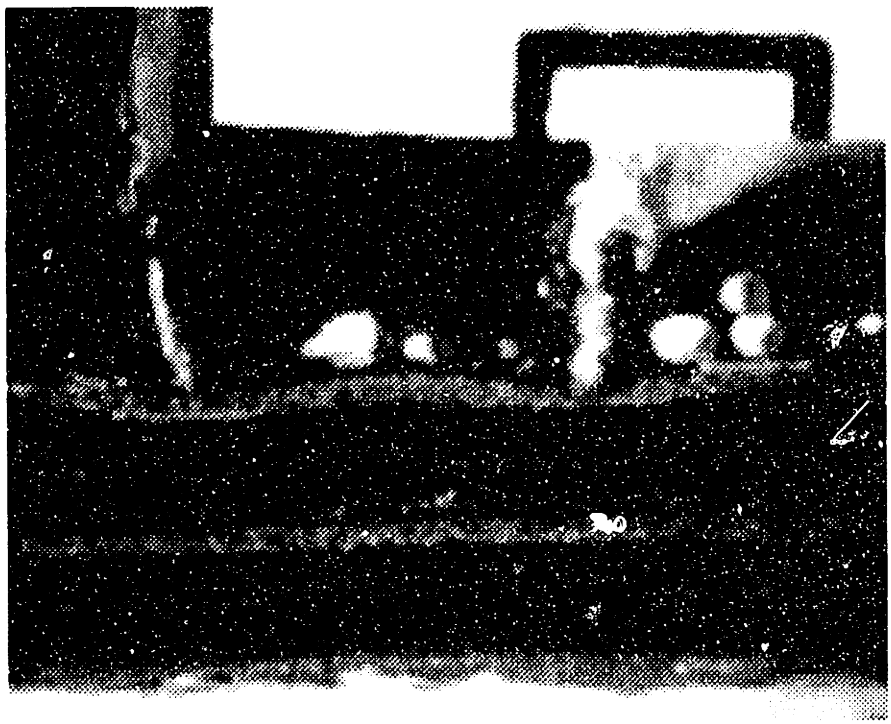

Figure 5.3 Photograph of typical waviness of the plies within the "rough" side facesheet of a B specimen.

was done on a milling machine equipped with a diamond-grit cutting wheel and water cooling. The cutting was done at a table feed rate of 58 mm/min (2.3 in/min).

The widths of the specimens were measured at three locations as shown in Figure 5.4. For the small and medium specimens, calipers were used in this measurement. For the large specimens, a ruler was used. These measurements can be found in Appendix C. No thickness measurements were taken because it was impossible to determine the individual contributions of the facesheets and the core. Similarly, no measurements of the specimen lengths were made because of the additional preparation steps which could change the specimen lengths. In all calculations, nominal specimen thicknesses and widths are used.

Several further steps were taken to prepare the specimens for testing. Specimens were mounted in epoxy and the ends were then machined flat. Instrumentation in the form of strain gages and photoelastic coatings were placed on the specimens. Notches were machined in some specimens, while others had previously been impacted. Details of these preparation steps are given in the following sections.

5.2.1 Potting of Specimens

In order to prevent brooming of the ends of the facesheets when loaded, the ends of the specimens were mounted in an epoxy block. This process is referred to as potting. The potting material used was a two-part epoxy obtained from Ciba-Geigy's Furane division and designated 1636AB. This epoxy was chosen to match that used in the previous tests as part of the ATCAS program.

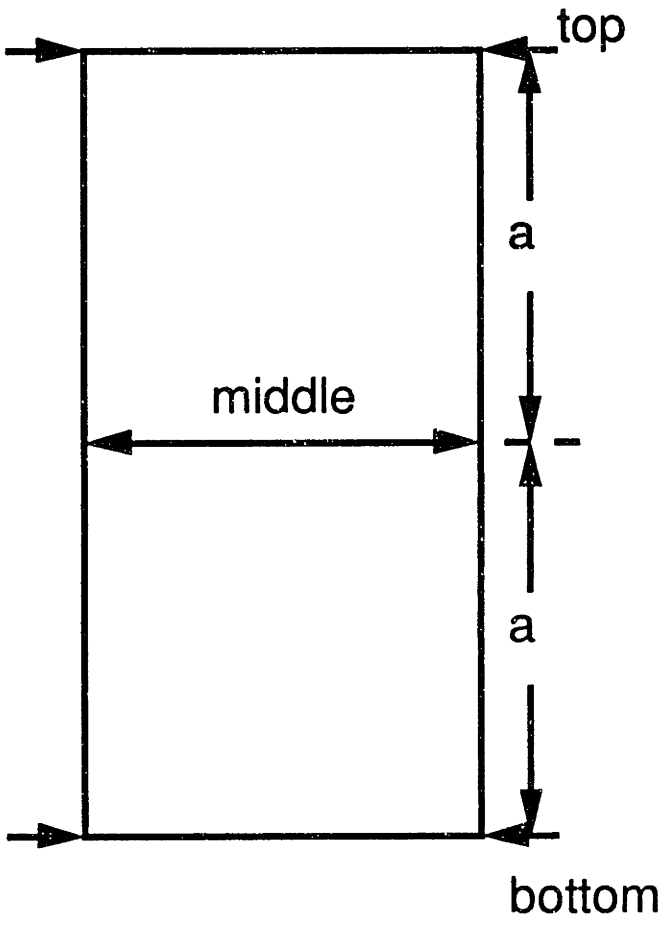

specimen size	a (mm)
small	102
medium	191
large	381

Figure 5.4 Locations for measurements of specimen widths.

The epoxy was mixed in proportions by weight of 100 parts resin to 8 parts hardener. The epoxy was then stirred with a metal paint stirrer mounted in a hand drill. The epoxy was stirred for 2 to 3 minutes to assure good mixing.

A mold was constructed in which to pour the potting material. This is illustrated in Figure 5.5. On an aluminum or steel plate, square 25.4 mm (1 in) aluminum bar stock was used to form a rectangle whose inner dimensions were approximately 76 mm (3 in) larger in each direction than the dimensions of the specimen in question. The specific inner dimensions of the rectangle formed were 127 mm by 102 mm (5 in by 4 in) for the small specimens, 279 mm by 102 mm (11 in by 4 in) for the medium specimens, and 457 mm by 102 mm (18 in by 4 in) for the large specimens. Two teflon sheets were used to prevent adhesion of the potting material to the plate and aluminum bars. The epoxy was poured into this mold, and the specimens were then placed end-first into it. A structure was used to hold the specimens while the epoxy hardened. Since further finishing would be done on the specimens, it was not necessary to assure exact alignment of the specimens relative to the epoxy mold. A ruler was used to center the specimen within the mold, and a hand level was used to check that the specimen was roughly vertical.

The epoxy was allowed to harden for a minimum of six hours. The potted specimen was then removed from the mold. Normally, a small amount of potting material came in contact with the bars and adhered despite the teflon sheets. In this case, the bars were either pried off by hand or separated from the potting material with a hand chisel. Care was taken to do this without causing damage to the specimen or potting material. The teflon sheets themselves were easily peeled off.

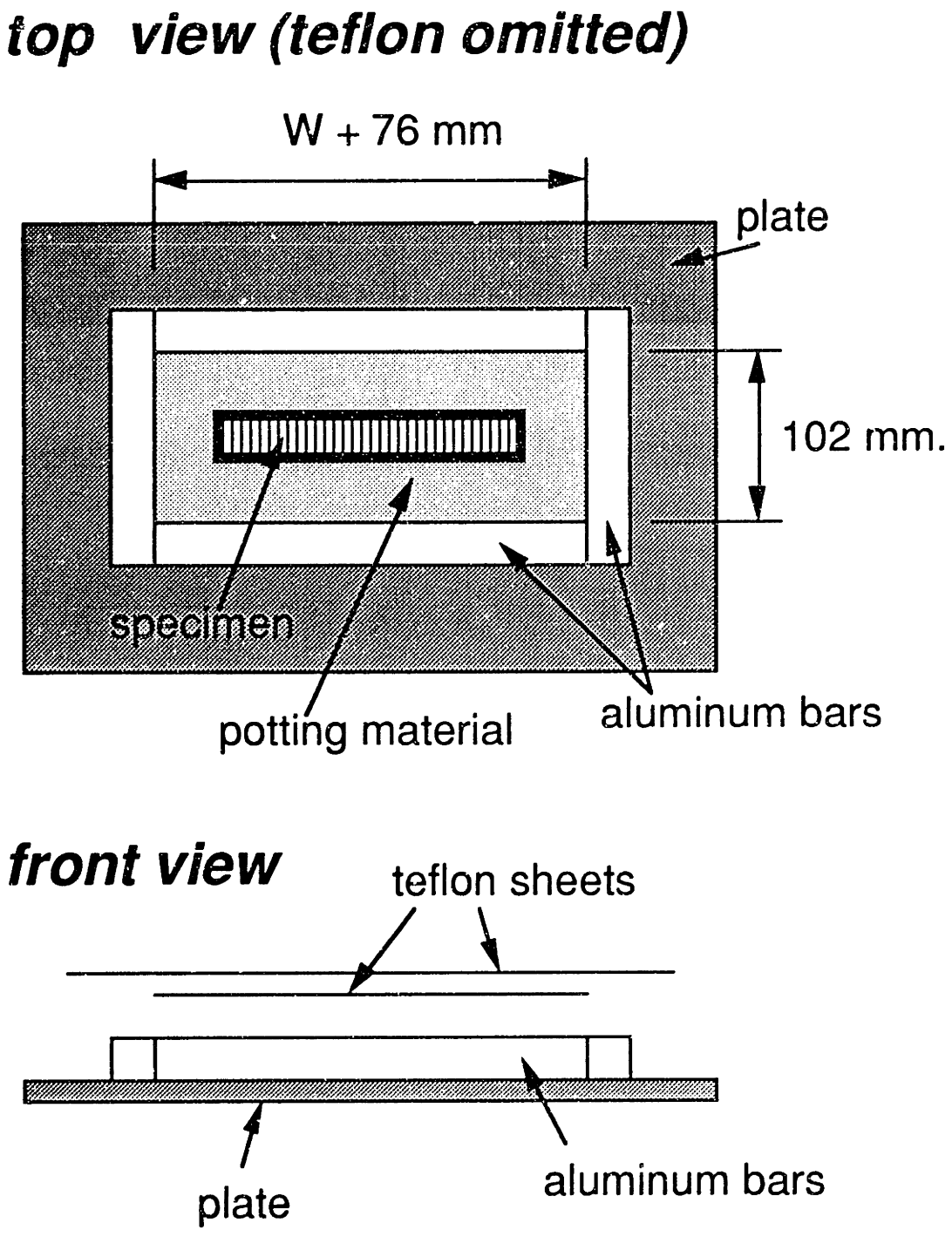

Figure 5.5 Schematic of mold used in potting of specimens.

5.2.2 Milling of Specimens

In order to assure that the ends of the specimen were flat and parallel to each other, the ends which had been potted were machined. The procedure differed slightly for the different sizes of specimens. The basic setup was to hold the specimen horizontally on a horizontal milling machine. A rotating, bladed cutter was then passed over the ends of the specimen, cutting away the high points. The specimen was then moved closer to the blade, and the process repeated. Milling continued until the composite itself was exposed fully along its entire length and all the potting material had been milled flat. In some cases, areas of the epoxy were substantially lower than the rest of the epoxy or the end of the composite panel. These areas were left unmilled provided they were small compared to the size of the epoxy.

Small specimens were held with the smooth side up in a vise mounted on the table of the milling machine. The edge of the vise against which the specimen rested was aligned to be perpendicular to the direction of table travel within ±0.03 mm (0.001 in) over a length of approximately 125 mm. Also, the top surface of the specimen was aligned to within ±0.05 mm (±0.002 in) over the 150 mm (6 in) length between the potting material. A single high speed steel flycutter was used to mill the specimen. The circle made by the end of the cutting tool was greater in diameter than the total depth of the specimen and the potting, which was approximately 100 mm (4 in) for all size specimens. A schematic of the setup for milling the small specimens is shown in Figure 5.6. A rotational rate of 225 revolutions per minute was used for the cutter. Initial cuts were made at a horizontal table feed of 24 to 38 mm per minute (0.94 to 1.5 in/min). However, final cuts were always done at 24 mm/min.

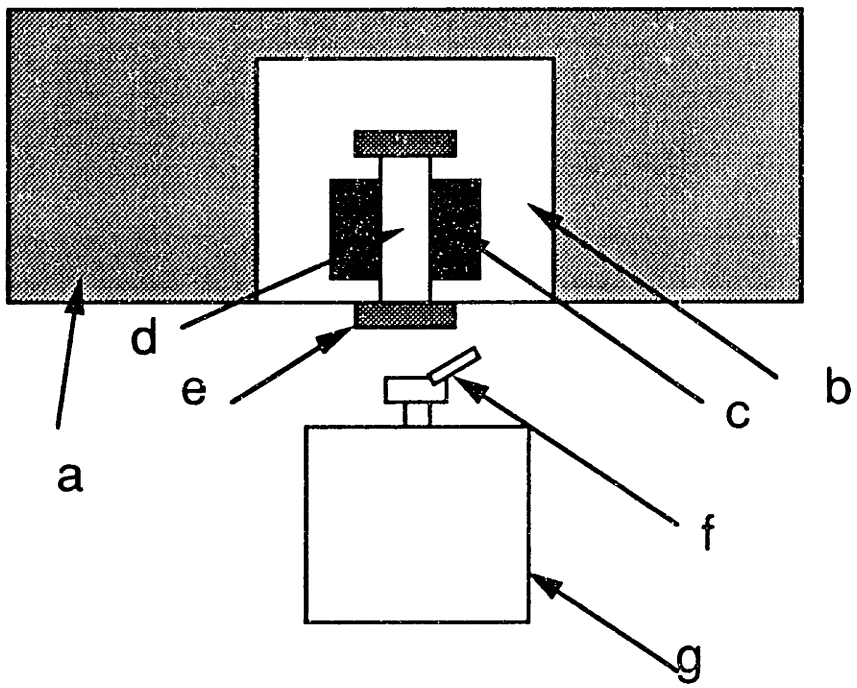

a = milling machine table

b = vise

c = vise grips

d = specimen

e = potting material

f = flycutter

g = milling machine

Figure 5.6 Schematic of setup for milling small specimens.

The medium specimens were placed on a piece of plywood and then clamped directly to the table of the milling machine, smooth side up. One edge of the specimen was arbitrarily chosen as the reference edge. This edge was placed against a steel bar which had been aligned to be perpendicular to the direction of the motion of the table within 0.025 mm over a length of approximately 250 mm. After one end had been milled, the specimen was rotated about the vertical axis so that the reference side of the specimen was placed against a second aligned steel bar. Rotational rate and table speeds were the same as with the small specimens. A schematic of the setup for milling the medium specimens is shown in Figure 5.7. After milling was completed, the specimens were checked to see if they met the required tolerances regarding the milled ends being parallel. The specimen was clamped to the table of a milling machine with one of the milled ends down. The table of the machine was moved, and a dial gage mounted vertically in the milling machine was used to measure the height of the ends of the facesheets. Both ends were done in this way. If these measurements indicated a deviation from parallel over 0.18 mm (0.007 in), the specimen was remilled and rechecked. This tolerance was chosen to be slightly better than the 0.25 mm specified by the sponsor.

The large specimens were milled using the same process as that for the medium specimens except with regard to the cutting tool used and the way in which the alignment was checked. The setup for the milling of the large specimens is also shown in Figure 5.7. Instead of a single flycutter, a multi-blade tool steel cutter was used. This allowed higher table speeds: 60 to 89 mm per minute (2.4 to 3.5 in/min) for rough cuts and 60 mm/min for the final cut. However, when the tool reached the graphite/epoxy, considerable heat could build up. This was noted after the potting of one

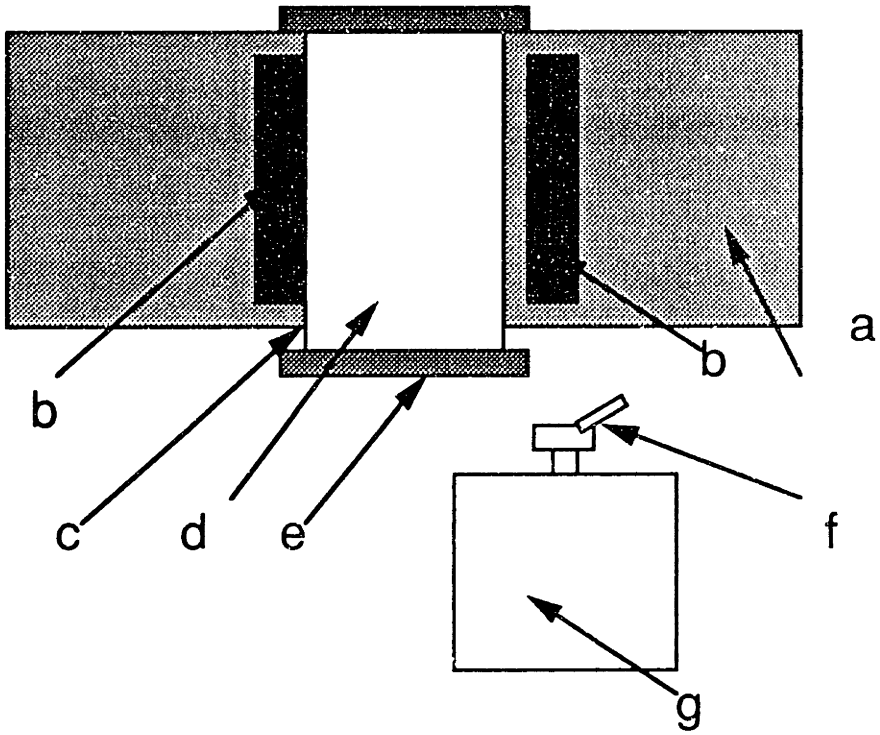

a = milling machine table

b = steel blocks aligned with milling machine table

c = reference edge of specimen

d = specimen

e = potting material

f = cutting tool

g = milling machine

Figure 5.7 Schematic of setup for milling medium and large specimens.

specimen, A-L-DN25, cracked during or after milling. The cause of the cracking was not determined, but it was decided to take the precaution of reducing the temperature of the cutting tool and the specimen being machined. For the remaining specimens, namely B-L-DN25, A-L-SN25, B-L-SN25, and the repotted A-L-DN25, the temperature of the cutter was checked between passes. If the cutter became hot to the touch, it was allowed to cool before another pass. To check the parallelness of the ends of a large specimen, the specimen was held horizontally on the table of a vertical milling machine with the axial direction of the specimen aligned with the direction of maximum travel of the milling machine table. By moving the machine table with a dial gage placed against the end of the specimen, the parallelness of the specimen ends was checked. Those specimens not meeting the tolerances given for the medium specimens were remilled.

For the specimen on which the potting material cracked, A-1, the remaining potting material was sawed off using a circular table saw, leaving approximately a 5 mm thick layer of potting material on the smooth side of the specimen. The potting process was then repeated, and the specimen was remilled.

5.2.3 Machining of Notches

Several specimens were notched before testing. If the specimen was to have a photoelastic coating (discussed in section 5.3.1), that was bonded to the specimen first. The specimen was held on the movable table of a milling machine. A Dremel Moto-Tool held in a special attachment to the milling machine and equipped with a diamond coated bit was used to cut the slit. The length of the slit was then measured with calipers. No effort

was made to sharpen the ends of the notch. The length of the notches are given in Chapter 6.

For the small specimens, the nominal diameter of the bit was 0.74 mm (0.029 in). First, the ends of the notch were determined by putting the bit through the facesheet like a drill. This gave the ends of the notch a smooth surface and defined the extent of the travel. Several passes were made with the bit between these two holes to cut the notch. The depth of each cut was approximately 0.25 mm (0.010 in). Cutting was done past the nominal thickness of the facesheet to a depth of approximately 3.05 mm (0.12 in) to insure that all of the facesheet and film adhesive was removed. However, little of the honeycomb was removed. The resulting notch had a width of approximately 1.0 mm (0.04 in) due to eccentricities in the rotating bit.

When notching the medium and large specimens, a 3.2 mm (0.125 in) diameter bit was used. The extreme ends of the notch were again first determined by placing the bit directly through the facesheet. This resulted in a hole at each end of the line where the notch was to be placed. The table was then moved so that the bit cut a strip between these two holes in two or more passes. Deeper cuts, approximately 1.3 mm (0.05 in), could be made with this bit. Also, the minimum width of the notch as required by the sponsor was 4.83 mm (0.190 in) necessitating that the slit be widened from that created by a single cut of the bit. The notch was widened by making another pass with the bit on each side of the strip already cut. These two cuts were slightly shorter, resulting in the end of the notch having a round, semi-circular shape. A typical resulting notch is shown in Figure 5.8.

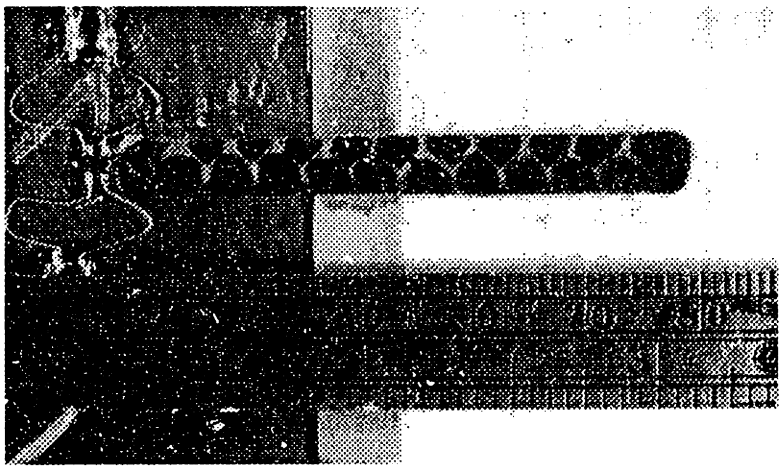

Figure 5.8 Photograph of typical notch for medium and large specimens.

5.2.4 Impact of Specimens

Impacting of certain panels was conducted by Integrated Technologies, Inc. A Dynatup 8250 instrumented drop-weight tower was used, and the velocity of the impactor was measured just prior to impact. The impactor had a mass of 6.15 kg, and the point of impact was a 25.4 mm hemispherical tup. This tup was made of hardened A2 steel. Impacts were done with an impactor velocity of 2.7 m/s for level 1 events and 4.3 m/s for level 2 events. The specimens were simply-supported in the z-direction in a 102 mm square window centered on the point of impact.

Impacts at both levels created easily visible damage in the specimens. The visible damage consisted of a depression (termed the dimple), matrix cracking, and fiber breakage. For level 1 impacts, little matrix cracking and no fiber breakage were detected by a visual inspection, as can be seen in Figure 5.9. Specimens damaged by a level 2 event developed a deeper dent, a large area of matrix cracking, and significant fiber breakage. A typical dimple from such an impact is shown in Figure 5.10.

In addition to visual inspection of the impacted panels, through-transmission ultrasonic C-scans were conducted in Boeing facilities. These scans revealed an approximately circular region of delamination, centered at the point of impact. The area of the delamination region was determined, and these areas are presented for the various specimens in Table 5.1. It should be noted that the ultrasonic scan provides only a measure of damage integrated through the thickness of the laminate. It provides no information about which ply interfaces develop delaminations. In general, the delamination area is higher in specimens damaged by a level 2 impact event. However, specimen A-M-IL1 displayed the second largest delamination area despite being damaged by only a level 1 impact. The

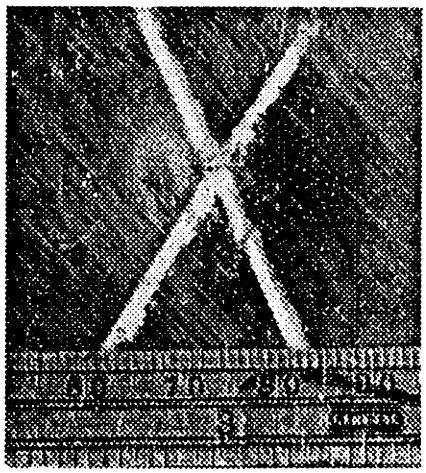

Figure 5.9 Photograph of typical dimple created by a level 1 impact event (specimen A-M-IL1).

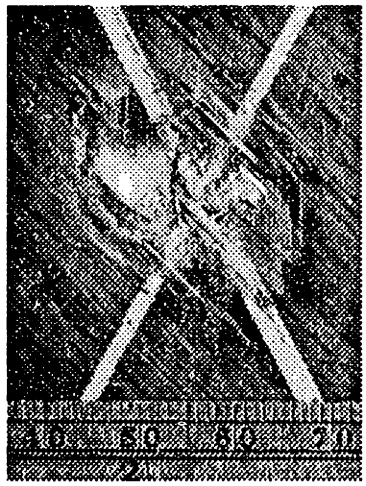

Figure 5.10 Photograph of typical dimple created by a level 2 impact event (specimen A-M-IL2).

Table 5.1 Area of delamination created by impact events

Specimen	Impact Level	Delamination Area (mm^2)
A-M-IL1	1	1295
A-M-IL2	2	1285
A-L-IL1	1	1017
B-M-IL1	1	1010
B-M-IL2	2	1374
B-L-IL1	1	1046

reason for this is not known. The delamination region is substantially larger than the impactor cross-section of 507 mm^2.

5.3 Instrumentation

Several instrumentation schemes were used in the tests. A linear variable displacement transducer (LVDT) placed at the horizontal centerline of the back (rough) side was used in all tests to measure out-of-plane deflection of the specimen. For small specimens notched on one side or unnotched, it was placed at the vertical centerline. For all other specimens, it was placed near the edge of the specimen. The LVDT was mounted on an aluminum beam attached to the testing machine so that the LVDT was perpendicular to the surface of the facesheet. Data provided by this instrument were used to assess the bending or buckling of specimens during testing. Strain gages were used to measure the strain at various locations of the specimens. These locations were away from the notch to measure the far-field strain, or very close to the notch to monitor the strain behavior in that region. Also, for some notched specimens, a photoelastic coating was placed on part of the specimen. The patterns from the photoelastic coating provided information about the strain field in the specimen over a large area. Finally, for impacted specimens, out-of-plane ("shadow") moiré interferometry was used to monitor out-of-plane displacements which indicated the growth of the dimple as discussed in Chapter 2. Details of the use of these techniques are subsequently given.

5.3.1 Photoelasticity

A photoelastic coating was used on some small and all medium and

large notched specimens to examine the strain field of the specimen and how it was affected by the presence of the notch. An excellent reference on photoelasticity is found in Zandman et al. [51]. The photoelastic technique uses the fact that certain transparent materials are optically anisotropic. As they are deformed, the index of refraction changes within the material. By passing a polarized light through such a material when deformed and viewing that light through another polarizer rotated 90°, a color pattern can be seen. This setup is termed a plane polariscope [52]. Black areas indicate regions of the specimen where the directions of the principal strains correspond to the axes of the polarizers. These are termed isoclinics.

In order to eliminate the black regions so that only the colors remain, a polarizer is inserted on each side of the material and the other polarizers. This polarizer is rotated at a 45° angle from the first. This setup is termed a circular polariscope.

The colors seen with either form of polariscope are related to the difference between the principal strains. The colors correspond to a certain fringe order for the material which is then related to the difference of the principal strains by the following equation:

$$\varepsilon_I - \varepsilon_{II} = Nf \tag{5.1}$$

Where ε_I and ε_{II} are the larger and smaller principal strains respectively, N is the fringe order, and f is the fringe value of the coating which is a function of its thickness, a material property that characterizes its optical anisotropy, and the wavelength of light used. Note that this does not provide the magnitude of either of the principal strains. This must be obtained by other techniques or by physical insight into the problem.

Two methods were used to evaluate the fringe order of the coating.

First, the approximate fringe order can be determined by looking up the color of the coating in the information provided by the manufacturer of the coating [52]. Photoelastic colors and their corresponding fringe orders are given in Table 5.2. However, these colors can be difficult to distinguish from one another. Therefore, a device known as a null-compensator [52] is used to measure the fringe order more precisely at points on the specimen. Null compensation measurements were used to more accurately determine the extent of the various colors.

The photoelastic technique can be used in two ways. A model of the part in question can be constructed of the photoelastic material. The light then passes from one side and out the other to be viewed. The other manner in which the technique can be used is to bond a thin sheet of the photoelastic material to the part in question, as is done in this investigation. A reflective coating is added to one side of the coating, and the coating is then bonded to a specimen with the reflective coating between the specimen and the photoelastic coating. If the coating deforms in the same manner as the specimen, the strains of the coating correspond to the strains of the specimen.

Coatings of type PS-1, manufactured by the Photoelastic Division of the Measurements Group, Inc, were used in this investigation. The first small specimen tested, A-S-SN13a, was tested with a PS-1E coating with a nominal thickness of 0.25 mm (0.010 in). However, this coating proved to be not sufficiently sensitive, so all other small specimens and the first round of medium and large specimens were tested with a PS-1D coating of 0.5 mm (0.020 in) nominal thickness. This thickness was chosen to keep the reinforcing effect of the coating small while still providing adequate resolution at the expected strain levels. The reinforcing effect of the coating

Table 5.2 Colors of the photoelastic coating and their corresponding fringe orders [52]

Color	Fringe Order
gray	0.28
white	0.45
pale yellow	0.60
orange	0.80
dull red	0.90
purple	1.00
deep blue	1.08
blue-green	1.22
green-yellow	1.39
orange	1.63
rose red	1.82
purple	2.00
green	2.35
green-yellow	2.50
red	2.65
red / green transition	3.00
green	3.10
pink	3.65
pink / green transition	4.00
green	4.15

is discussed later in this section. The coating was cut to the correct size with scissors. In order to obtain better resolution at the lower strain levels found in the medium and large specimens with larger notches, it was decided to use a thicker coating, PS-1C, with a 1.0 mm (0.040 in) nominal thickness. This was, in fact, used for the medium specimens tested in the second round. However, due to difficulty obtaining further coating material, the large specimens of the second round were tested with PS-1B coating which has a nominal thickness of 2.0 mm (0.080 in). It should be noted that the thickness of each individual sheet of photoelastic coating has a tolerance of ±10% from the specified thickness of the sheet.

Before bonding, the surface of the specimen was roughened slightly using a Scotch Brite cleanser. The surface of the specimen and the reflective surface of the coating were then cleaned using isopropyl alcohol and cheesecloth, and the region around the area to be coated was covered with masking tape. The coating was then bonded to the specimen using liquid plastic type PL-1 from the same supplier. This two-part adhesive was mixed according to the manufacturer's specifications of 1 part by weight hardener to 10 parts resin. The resin was preheated for approximately one minute using a hot air blower. The hardener was added and the mixture stirred by hand for two to three minutes. Following the manufacturer's recommendations, 1 gram of adhesive was used per 960 mm^2 (1.5 in^2) of photoelastic coating to be bonded. The adhesive was then poured on the specimen and spread evenly to cover the surface. The coating was placed on top and air and excess bonding material squeezed out. The manufacturer states that this results in an adhesive thickness of 0.1 to 0.25 mm (0.003 to 0.010 in), but no effort was made to measure this. The bonding material was allowed to cure at room temperature for a minimum of 24 hours.

Further explanation of the bonding procedure can be found in [53]. For the first two specimens tested, A-S-SN13a and B-S-SN13a, the coating was bonded to the entire smooth side. For the remainder of the specimens tested, the coating covered only one side of the vertical centerline. The placement of the photoelastic coating for these specimens is shown in Figure 5.11. Normally, a gap existed between the upper and lower edges of the coating and the potting material. The gap was approximately 6 or 13 mm for the small specimens, approximately 40 mm for the medium specimens of the first round, and approximately 100 mm for the large specimens of the first round. For specimens of the second round, the gap was reduced to approximately 13 mm for the medium specimens and 50 mm for the large specimens.

The photoelastic coating also has the effect of reinforcing the specimen in the area it covers. A measure of the longitudinal reinforcing effect of the coating is:

$$\frac{(E\,t)_{coating}}{(E_x t)_{facesheet}} \tag{5.2}$$

where E is the modulus and t is the thickness. For the A specimens, the less stiff of the two specimen types, the calculated longitudinal modulus, E_X, is 53 GPa (7.6 Msi). The nominal thickness of the facesheet is 2.4 mm (0.096 in). The modulus of the coating is 2.5 GPa (360 ksi). The value of this ratio for the PS-1D, PS-1C, and PS-1B coatings are 0.98%, 2.0%, and 3.9%. The ratio would be less for the B specimens due to their higher modulus. These values were judged to be acceptable.

In the present investigation, a polariscope manufactured by the Photoelastic Division of the Measurements Group, Inc., 030 Series Modular Reflection Polariscope was used. This device has the capability to perform

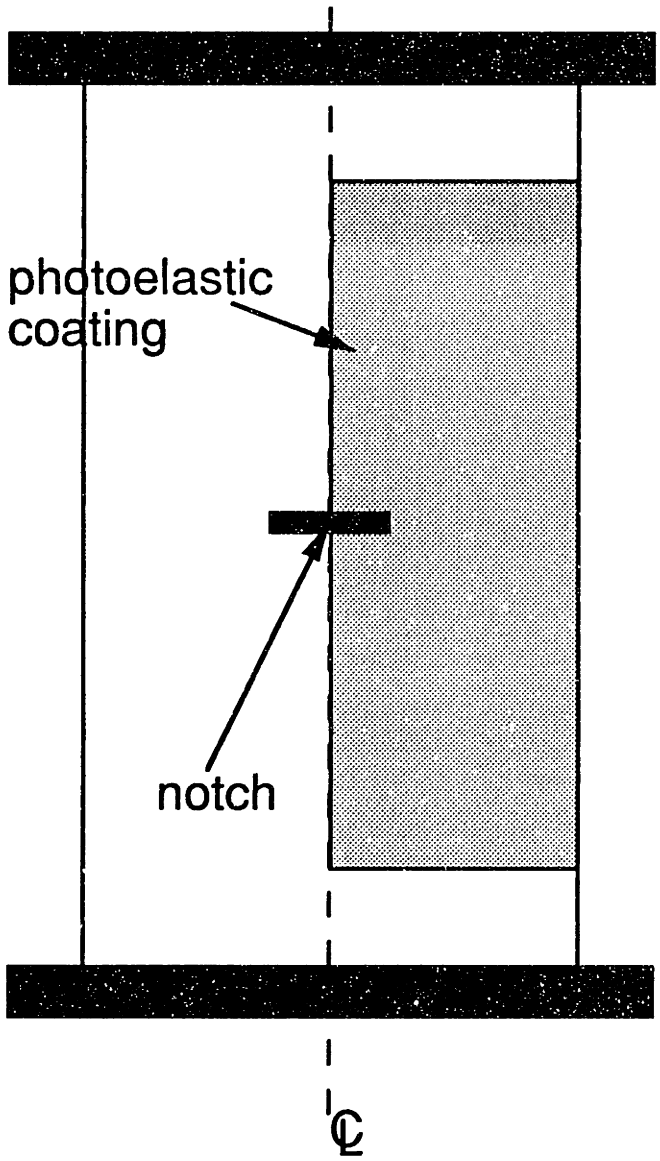

Figure 5.11 Illustration of placement of photoelastic coating on half of one side of specimen.

as both a plane and a circular polariscope and includes a high intensity light source. A Model 232 Manual Null-Balance Compensator was used for compensation measurements. The pattern of fringes was recorded with a 35 mm SLR camera with a zoom lens using Kodak tungsten compensated slide film. A schematic of the setup used for this technique is shown in Figure 5.12.

During tests in which a photoelastic coating was used, the testing machine would be temporarily held at a constant load while pictures were taken. For those specimens in the first round, measurements using null-compensation were also taken at locations previously marked on the specimen. Approximately fifteen points were marked on the specimen. Several of the points were along the notch line, and the remainder were placed in a regular spacing on the rest of the coating. However, the exact pattern varied slightly for the different specimens tested. Load levels for these pictures and measurements were 13.3, 26.7, 40.0, and 53.4 kN for the small specimens, though the first of these was not always done. For the medium specimens, the load levels were 44.5, 89.0, and 111.2 kN. For the large specimens, the load levels were 89.0 and 177.9 kN. At load levels higher than these, it was deemed undesirable to interrupt the test because the specimen was approaching failure. Therefore, pictures taken near failure were taken as loading of the specimen proceeded.

5.3.2 Moiré Method

In out-of-plane moiré interferometry, also known as shadow moiré, the optical interference created by shining a light through a grating of closely spaced lines is used to measure out-of-plane displacement. In this investigation, the shadow moiré method was used to measure the profile of

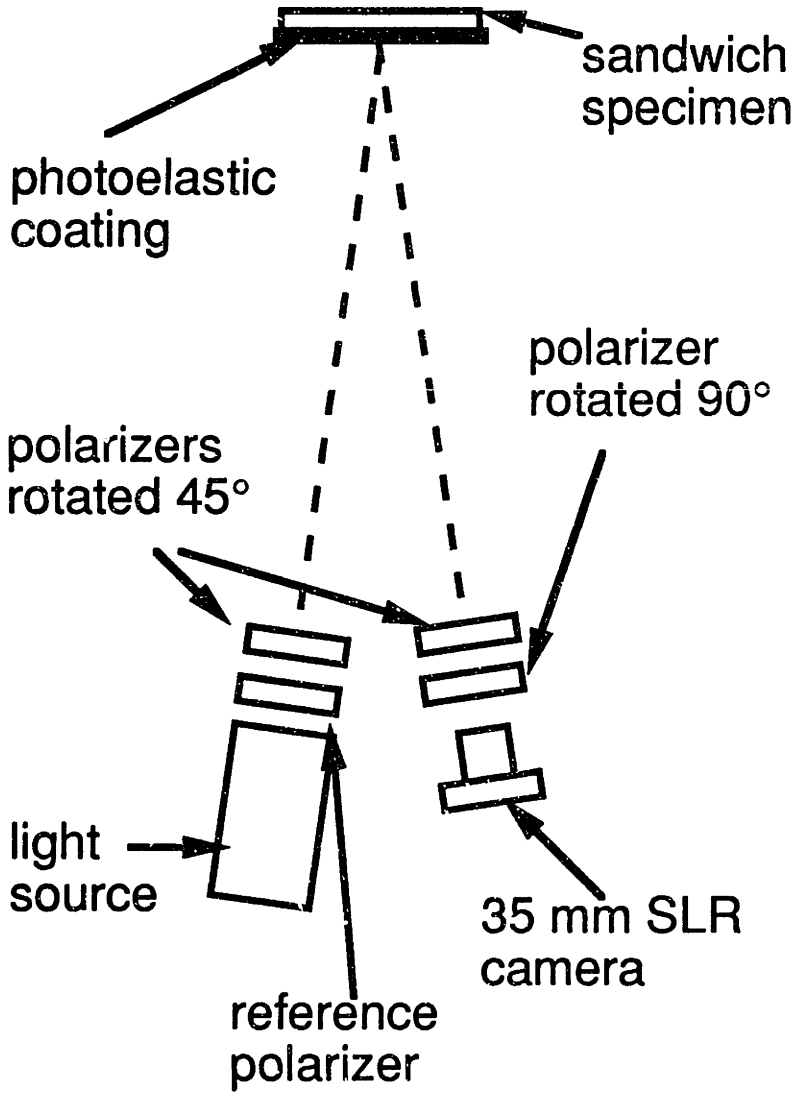

Figure 5.12 Schematic of setup for photoelastic technique.

a dimple, originally created by impact, as it grows during testing. A complete review of the technique of shadow moiré is provided in [54]. A summary of the experimental setup is given here. For further details, refer to [45].

Shadow moiré on a surface which is not flat results in fringes which indicate the relative displacement in the z-direction, i.e. out of the plane. An example of these fringes is shown in Figure 5.13. The quality of this fringe pattern is low; better quality was achieved during actual testing. However, it does serve to illustrate the principles of the technique. The observed fringes correspond to the surface contours of constant values of z. With the surface of the specimen taken as the given flat surface after alignment of the system, the first fringe is assigned the zeroth-order, thereby assigning it the value of 0 for z. The next fringe moving toward the center of the circles is termed the first-order, and the following fringe second-order, and so on. In this case, these fringes indicate an inward dimple, giving a positive value of z. The z-value along a fringe can be determined by the following equation:

$$z = \frac{Np}{\tan\alpha} \tag{5.3}$$

where z is the value of the out-of-plane coordinate along the fringe, N is the order of the fringe, p is the pitch of the grating, and α is the angle of incidence. The pitch is the inverse of the number of lines on the grating per unit length in the horizontal direction. For this investigation, p is equal to 0.127 mm^{-1} (0.005 in^{-1}) while α is approximately 35^{o}. This gives a displacement per fringe of approximately 0.181 mm (0.007 in).

A grating was held close to the region of the specimen to be measured. A light was shown on the grating at a measured angle. This

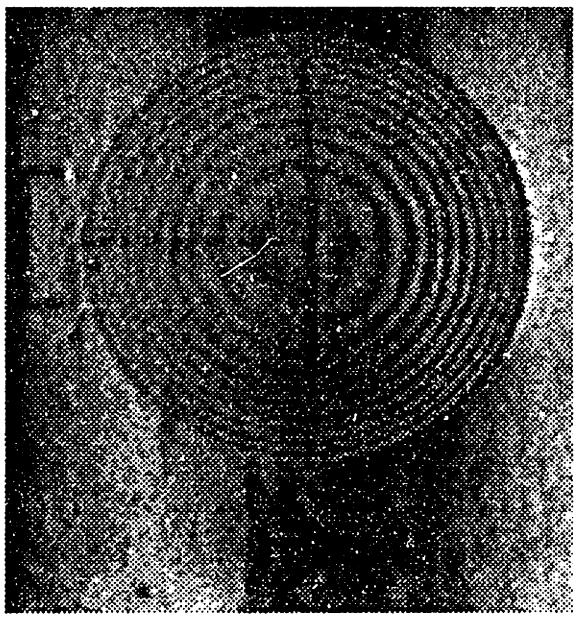

Figure 5.13 Photograph of moiré fringe pattern of machined dimple in an aluminum bar.

resulted in interference patterns on the specimen which were due to both the shape of the specimen in the dimple area and fact that the grating was not parallel to the surrounding flat surface of the specimen. The position of the grating was adjusted using a fixture developed by Tsang [45] until all of the fringes outside of the dimple region disappear. This means that the interference pattern remaining is due only to the shape of the dimple area and that the surface of the panel and the grating are parallel. The grating was placed as close as possible to the specimen (within 1 to 2 millimeters) without touching it to give the sharpest images possible. The image was recorded using a Cannon A1 MarkII 8 mm camcorder which recorded the image at 30 frames per second. The camcorder was connected to a television so that the image being recorded could be seen while the test was conducted. A schematic of the moiré setup is given in Figure 5.14.

As the test was conducted, one experimenter called out the load measured by the load cell of the test machine in 1000 pound (4500 N) increments. These readings were recorded by the camcorder on the audio channel and were used to determine the load at which a given image was taken. Selected fringe patterns were subsequently chosen and digitized using ComputerEyes hardware and software by Digital Vision. These images were printed and the x and y axes marked so that the origin was at the deepest point of the dimple. The distance of fringes from the origin were then measured to determine a z-profile along the axes.

It is necessary to examine the accuracy of this technique. The dimple in the aluminum bar shown in Figure 5.13 was measured with a dial gage which is accurate to 0.025 mm (0.001 in). The bar was placed on the table of a vertical milling machine equipped with a digital readout for the horizontal directions. The table was moved so that the dial gage passed over the x and

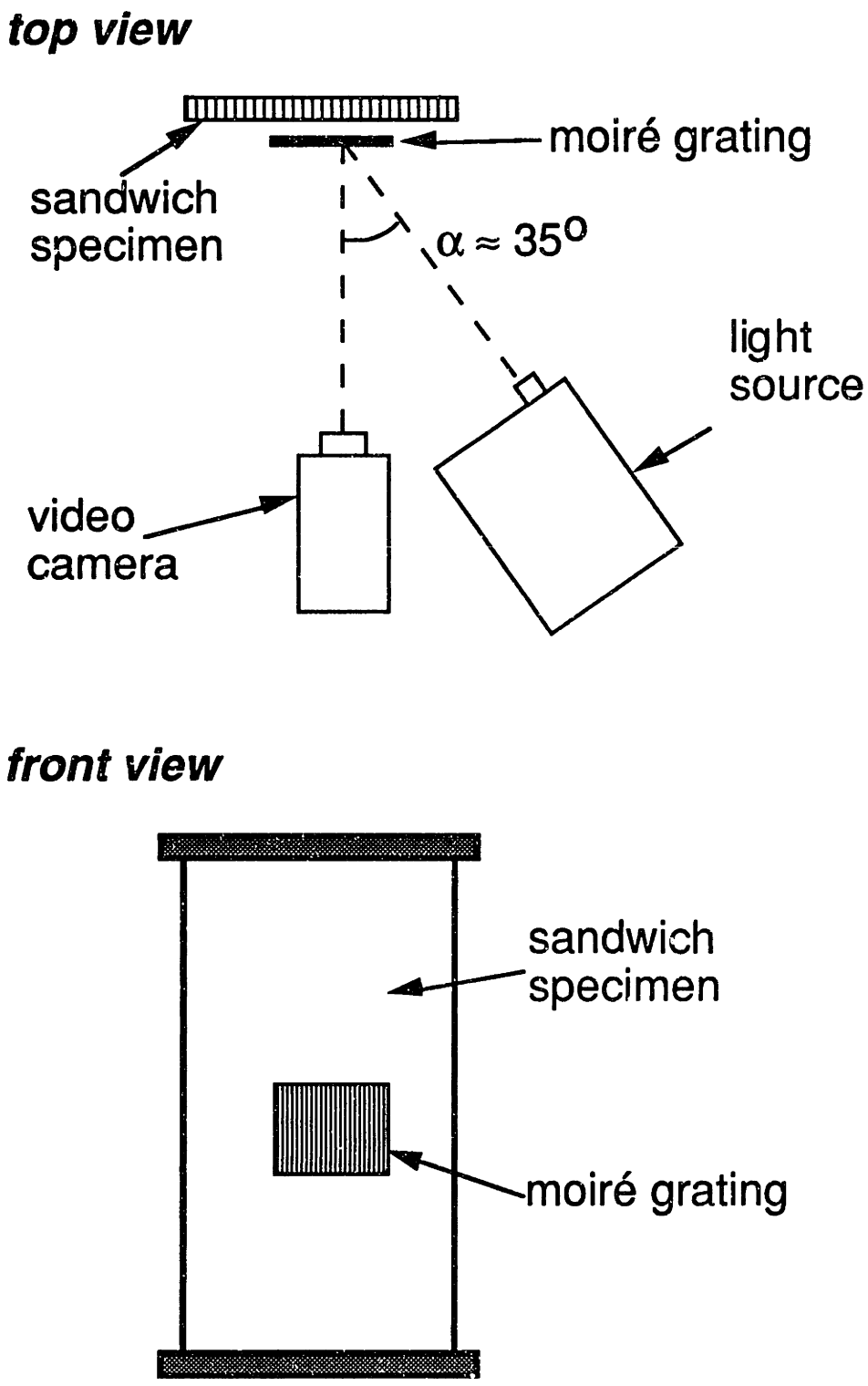

Figure 5.14 Schematic of moiré setup.

y axes of the dimple and the depth recorded at intervals of approximately 2 mm. The measurements by shadow moiré are compared to those taken by dial gage in Figures 5.15 and 5.16. The agreement is quite good. The fringe pattern of an unloaded impacted specimen, specimen A-M-IL1, is shown in Figure 5.17. The moiré measurements are compared with the dial gage measurements in Figures 5.18 and 5.19. Again, agreement between the two measurement techniques is quite good, although the moiré does not provide measurements in the very center of the dimple. This is due to the difficulty of distinguishing fringes in this region, in part because of surface damage to the specimens.

5.3.3 Strain Gages and Configuration

Strain gages were used to monitor the far-field strain, to check for bending of the specimens, and to monitor the strain at the tip of the notches. For different tests, different types of gages were used, and their placement on the specimens differed. All gages were manufactured by Micro-Measurements Division of Measurements Group, Inc. Those referred to as "normal" gages were of type EA-06-125AD-120, while those referred to as "small" gages were of type EA-06-031DE-120. The gage element of the normal gages is a 3.18 mm (0.125 in) square, while the element of the small gages is 0.79 mm (0.031 in) long and 0.81 mm (0.032 in) wide. Details of the procedure for attaching strain gages can be found in Reference [55].

For the notched specimens, three configurations of gages were used. For the first two small specimens tested, a photoelastic coating was used on the entire front (notched) facesheet. These specimens were gaged only on the back, unnotched, rough side facesheet in order to measure possible variations in strain in the back facesheet. This configuration, termed

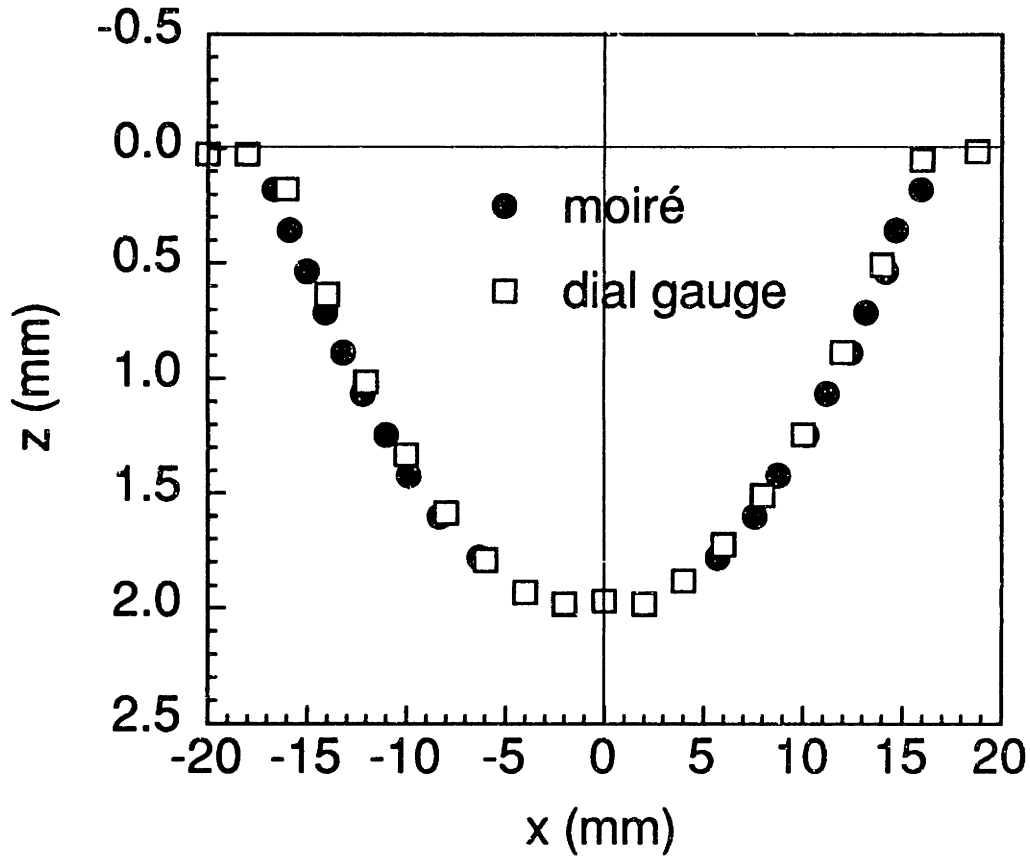

Figure 5.15 Comparison of measurements along the x-axis via dial gauge and moiré techniques of a machined dimple in an aluminum bar.

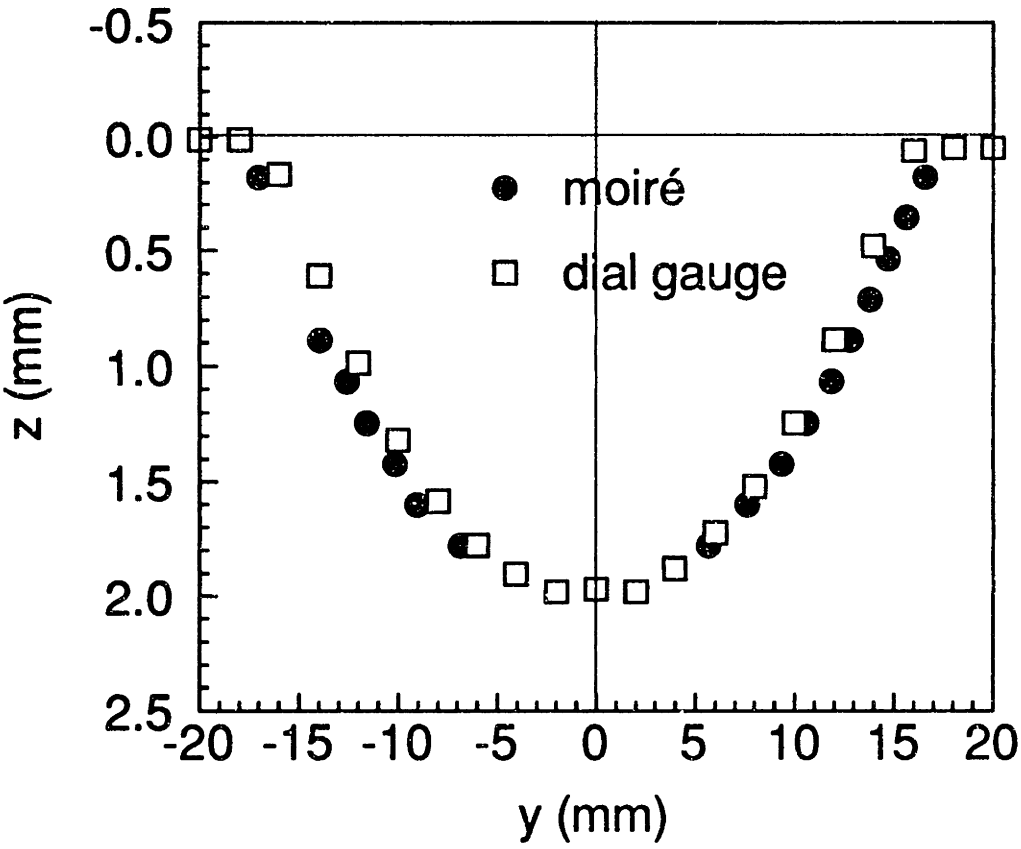

Figure 5.16 Comparison of measurements along the y-axis via dial gauge and moiré interferometry of machined dimple in aluminum bar.

Figure 5.17 Photograph of moiré fringe pattern for unloaded specimen damaged by a level 1 impact event (specimen A-M-IL1).

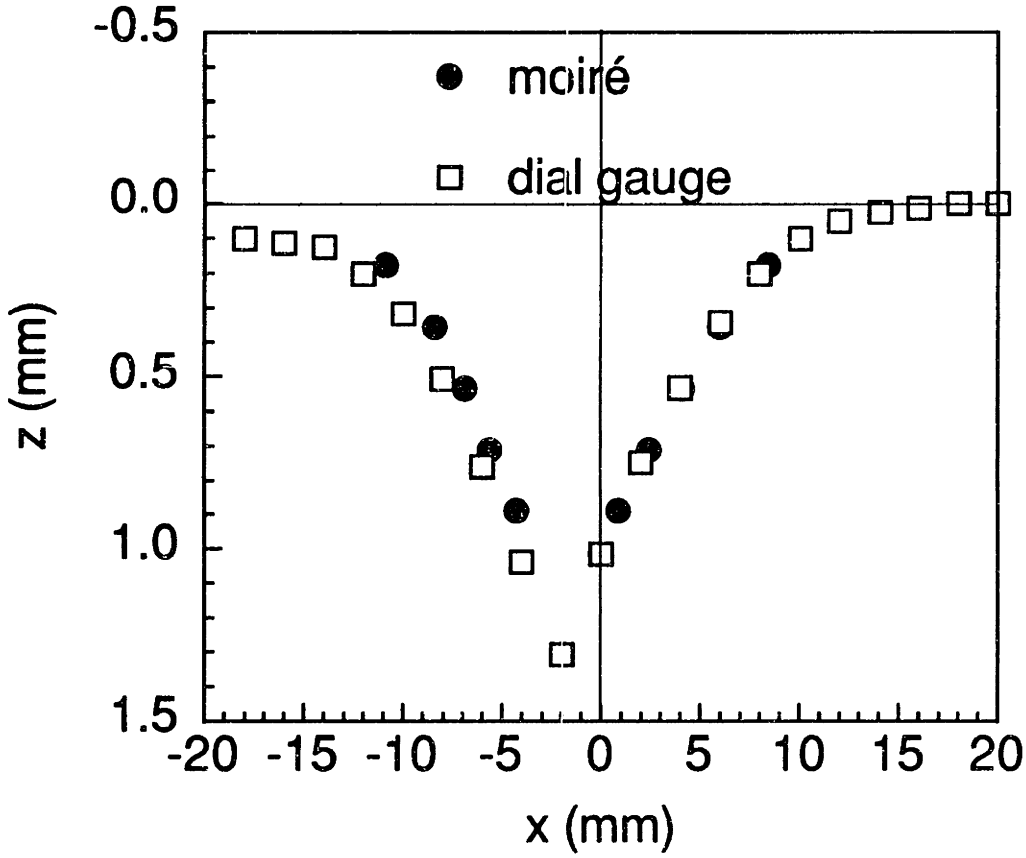

Figure 5.18 Comparison of measurements of the dimple along the x-axis via dial gauge and moiré techniques for an unloaded specimen damaged by a level 1 event (specimen A-M-IL1).

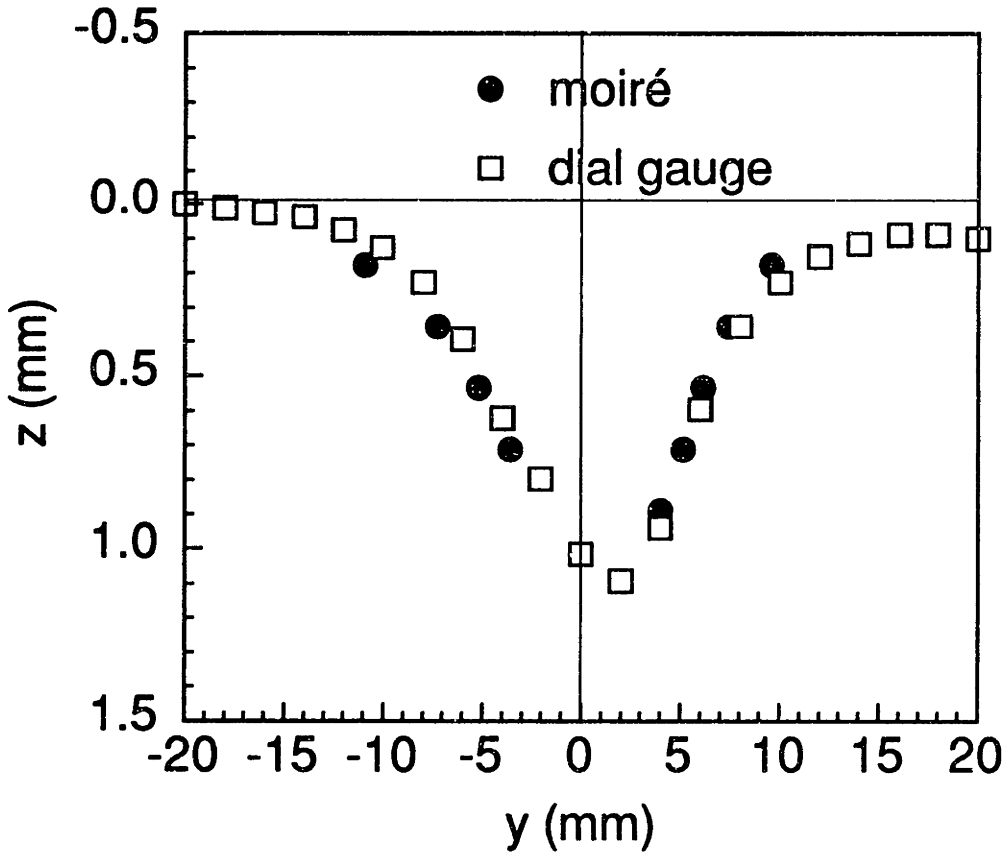

Figure 5.19 Comparison of measurements of the dimple along the y-axis via dial gauge and moiré techniques for an unloaded specimen damaged by a level 1 event (specimen A-M-IL1).

"Notch 1", is shown in Figure 5.20. Note that a third gage was placed on specimen B-S-SN13a which was not present in specimen A-S-SN13a.

The remainder of the notched specimens were gaged in two ways. In order to monitor the strain state near the notch tip, two small gages were placed next to each other at the tip of the notch along the notch line on the smooth side. The inner gage was trimmed of excess backing material on both sides with a razor blade. The second gage was trimmed only on the side closest to the notch. The inner gage was placed as close as possible to the edge of the notch. The gage element of the second notch was measured to be 0.4 mm to 0.8 mm from the element of the first. To measure far-field strain and to detect any bending present, a pair of front-and-back gages was placed halfway between the notch and the loaded end of the specimen and halfway between the notch tip and the edge of the specimen. For the majority of the small specimens, a fifth gage was placed on the notch line, halfway between the edge of the specimen and the notch tip. This configuration is termed "Notch 2" and is shown in Figure 5.21. For the remainder of the small specimens, the medium specimens, and the large specimens, another pair of far-field gages was used instead of the third gage on the notch tip. This configuration, referred to as "Notch 3", is shown in Figure 5.22.

For the impacted specimens, three pairs of back-to-back gages were used. The first pair was placed halfway between the centerline and the edge in the y-direction and halfway between the horizontal centerline and the loaded end of the specimen. These gages were intended to be used to monitor bending of the specimen at a "far-field" location. The other two pairs were placed along the vertical centerline, halfway between the horizontal centerline and the loaded ends. These pairs were intended to

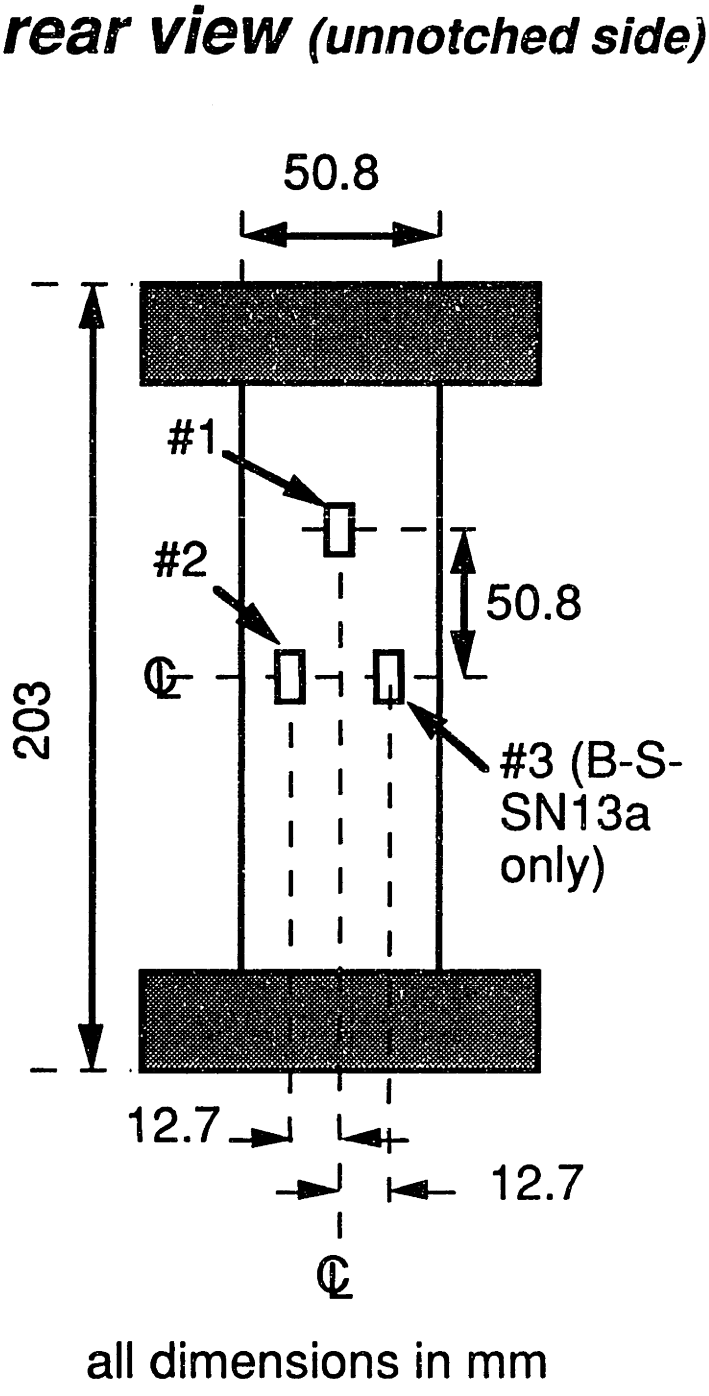

Figure 5.20 Illustration of "Notch 1" configuration of strain gages for notched specimens with photoelastic coating covering the entire notched side.

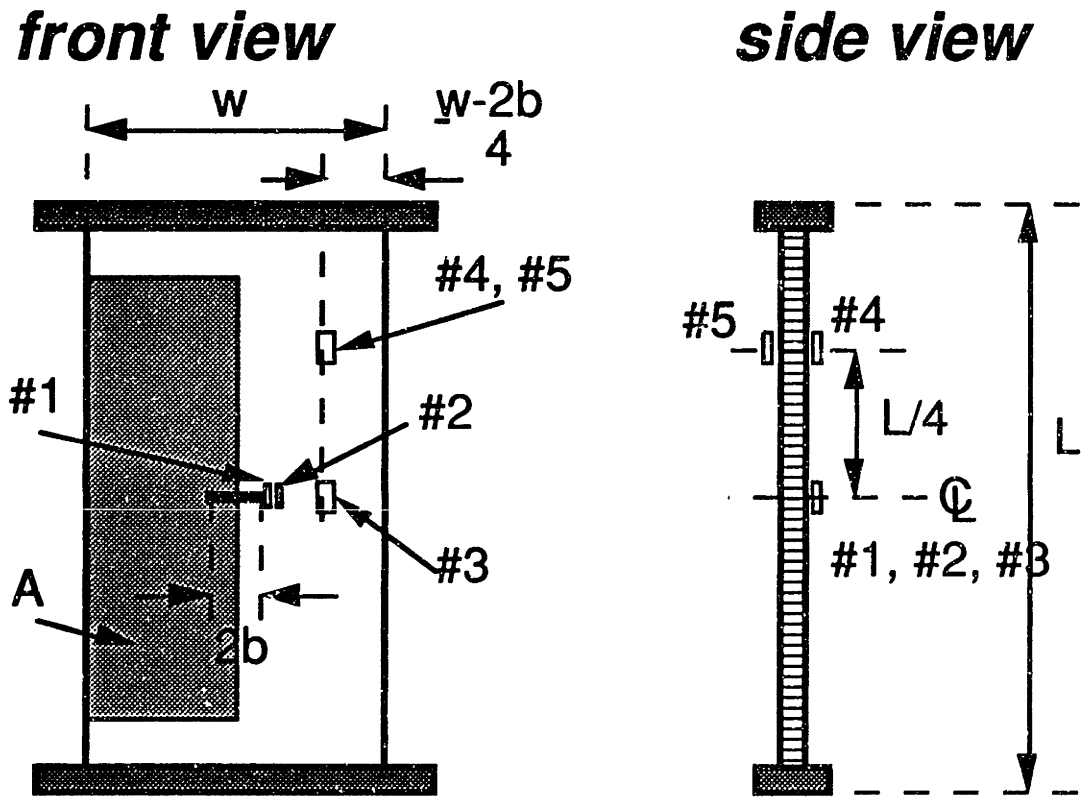

A = photoelastic coating (may not be present)

#1, #2 = trimmed small gages at notch tip (#1 at notch tip, #2 adjacent)

#3 = normal gage between notch tip and edge

#4, #5 = back-to-back normal gages (#4 on front, #5 on back)

Figure 5.21 Illustration of "Notch 2" configurations of strain gages for notched specimens.

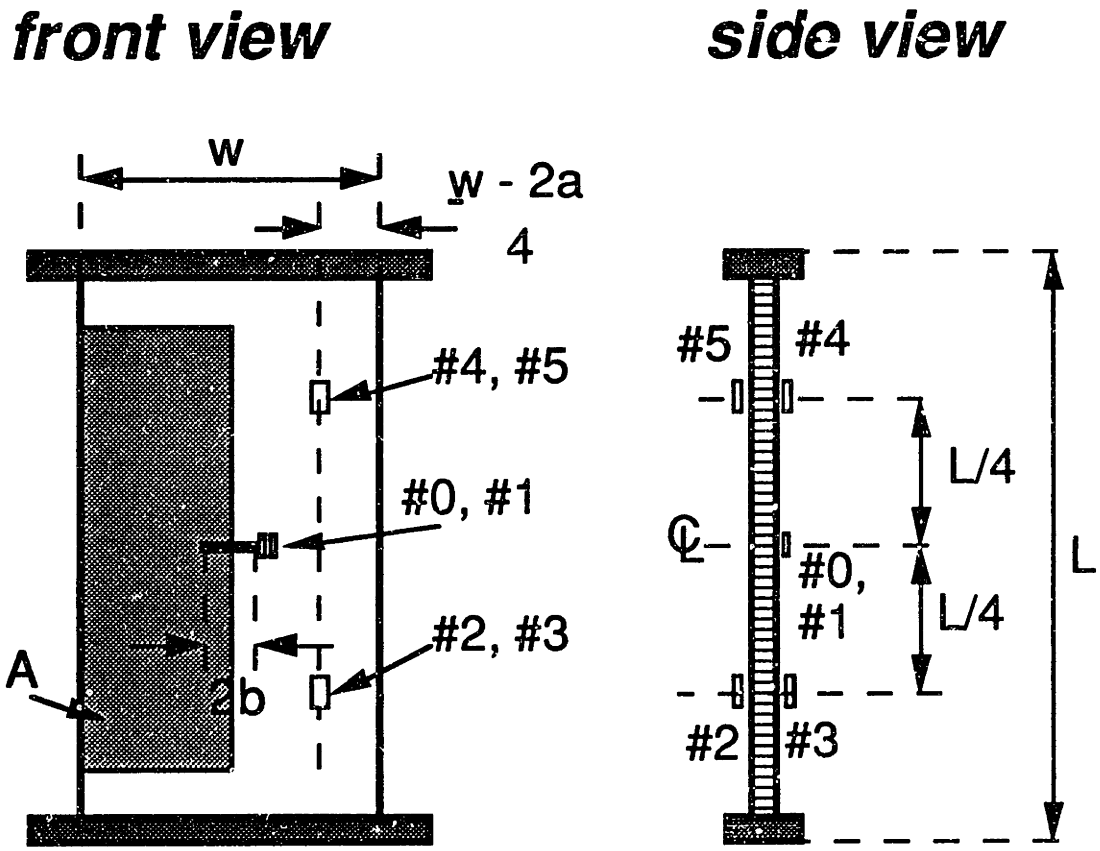

A = photoelastic coating (may not be present)

#0, #1 = trimmed small gages at notch tip (#0 at notch tip, #1 adjacent)

#2, #3 = back-to-back normal gages (#2 on front, #3 on back)

#4, #5 = back-to-back normal gages (#4 on front, #5 on back)

Figure 5.22 Illustration of "Notch 3" configuration of strain gages for notched specimens.

determine the effect of the dimple on the strain distribution along the vertical line by comparison between the front and the back face. This configuration, referred to as "Impact", is shown in Figure 5.23.

Four strain gage configurations were used with the five undamaged specimens. The placement of gages in configuration "Undamaged 1" was chosen to examine the variation of strain in the x and y directions within one facesheet. This configuration was used with specimens B-S-Ua and A-S-Ua and is shown in Figure 5.24. The "Undamaged 2" configuration was chosen to examine the variation of strain along the vertical centerline of the specimen, and also to examine whether strains were the same in the smooth side and rough side facesheets. This configuration, used with specimen B-S-Ub, is shown in Figure 5.25. The "Undamaged 3" configuration was chosen to measure the strain distribution along the horizontal centerline in the smooth side and rough side facesheets. This configuration was used with specimen A-S-Ub and is shown in Figure 5.26. A slight variation of this configuration was used with specimen A-M-U. This configuration is shown in Figure 5.27. For the undamaged specimens, normal gages were always used. The numbering schemes for the gages are shown in the figures.

5.4 Test Fixture and Techniques

All tests were performed using an MTS 810 uniaxial testing machine. The load cell (Model 661-23A-02) of this machine has been calibrated to a maximum capacity of 444.8 kN (100,000 lbs). A special fixture, which will be described in detail, was placed in the machine to provide a flat area for compression loading. For the small specimens and six of the medium specimens, the hydraulic grips remained on the machine. During testing,

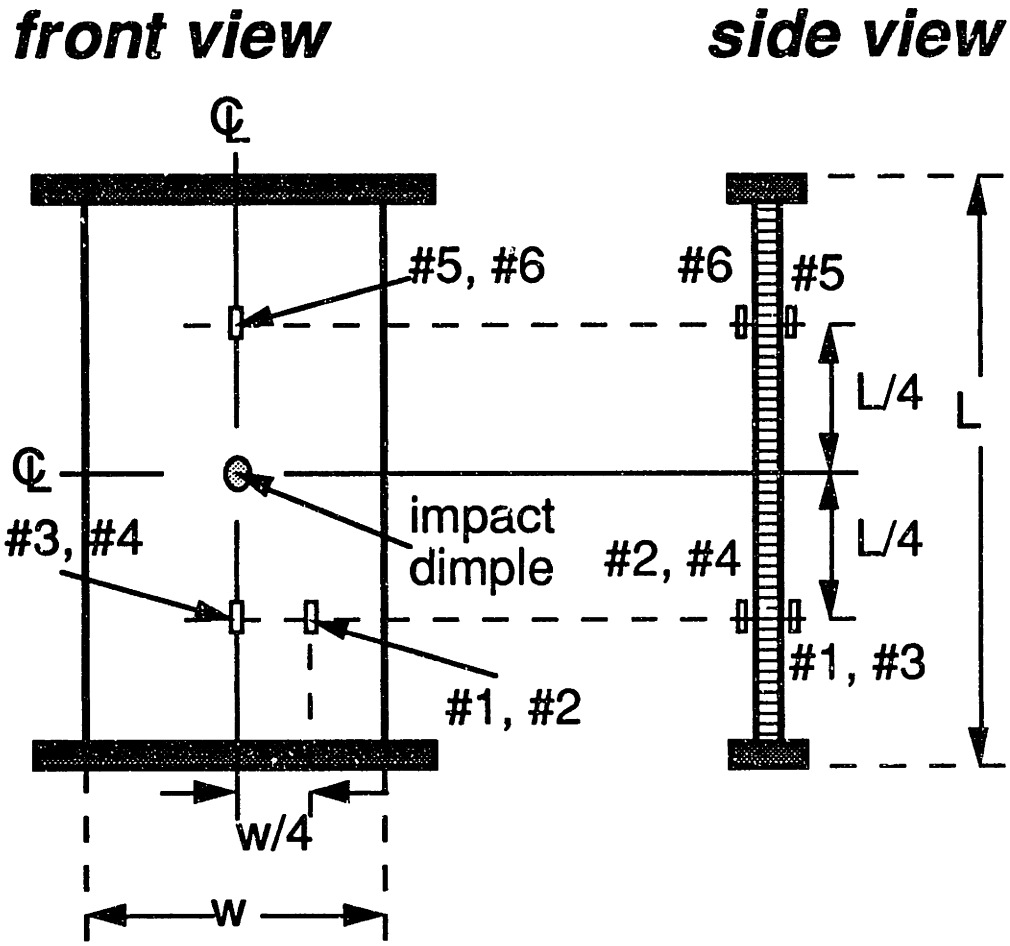

#1, #2 = back-to-back strain gages (#1 on front, #2 on back)

#3, #4 = back-to-back strain gages (#3 on front, #4 on back)

#5, #6 = back-to-back strain gages (#5 on front, #6 on back)

Figure 5.23 Illustration of "Impact" configuration of strain gages for impacted specimens.

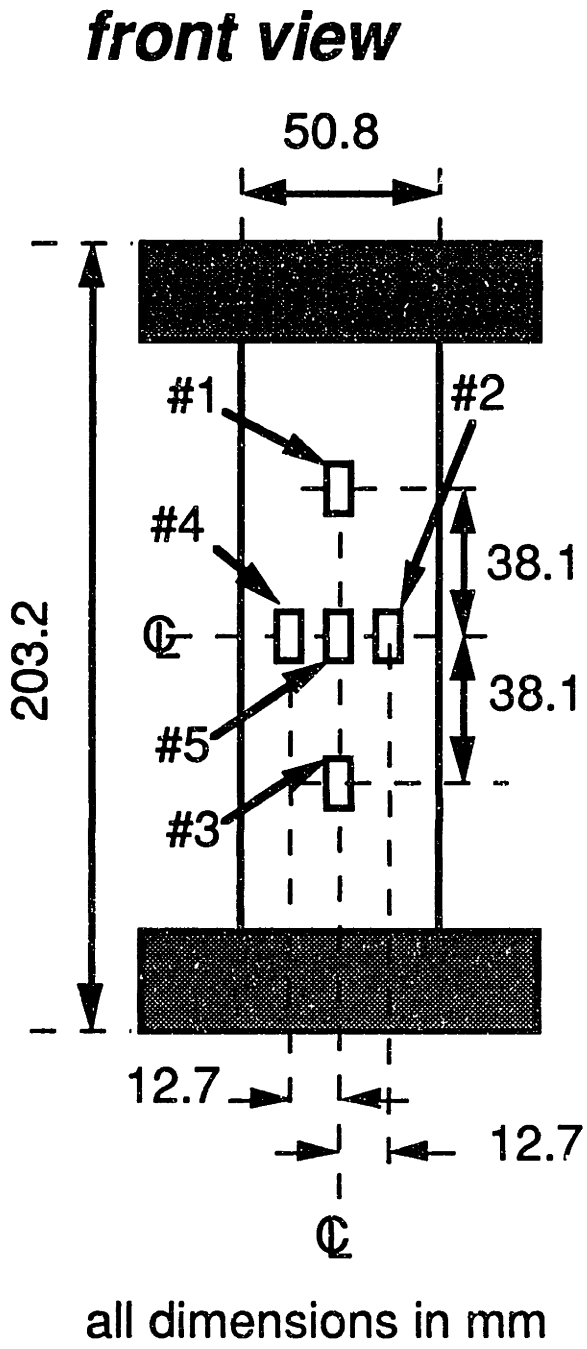

Figure 5.24 Illustration of "Undamaged 1" configuration of strain gages used for undamaged specimens B-S-Ua and A-S-Ua.

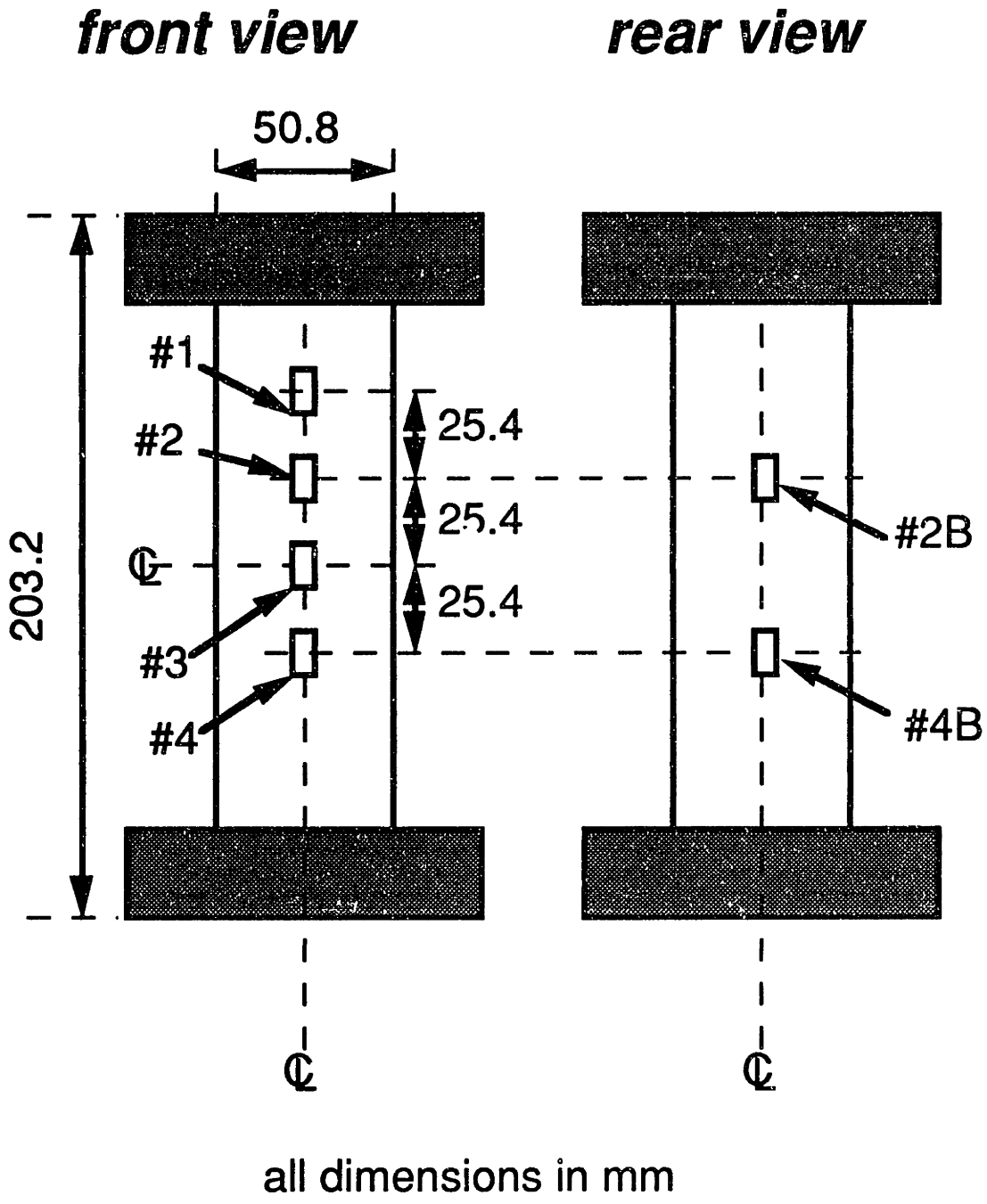

Figure 5.25 Illustration of "Undamaged 2" configuration of strain gages used for undamaged specimen B-S-Ub.

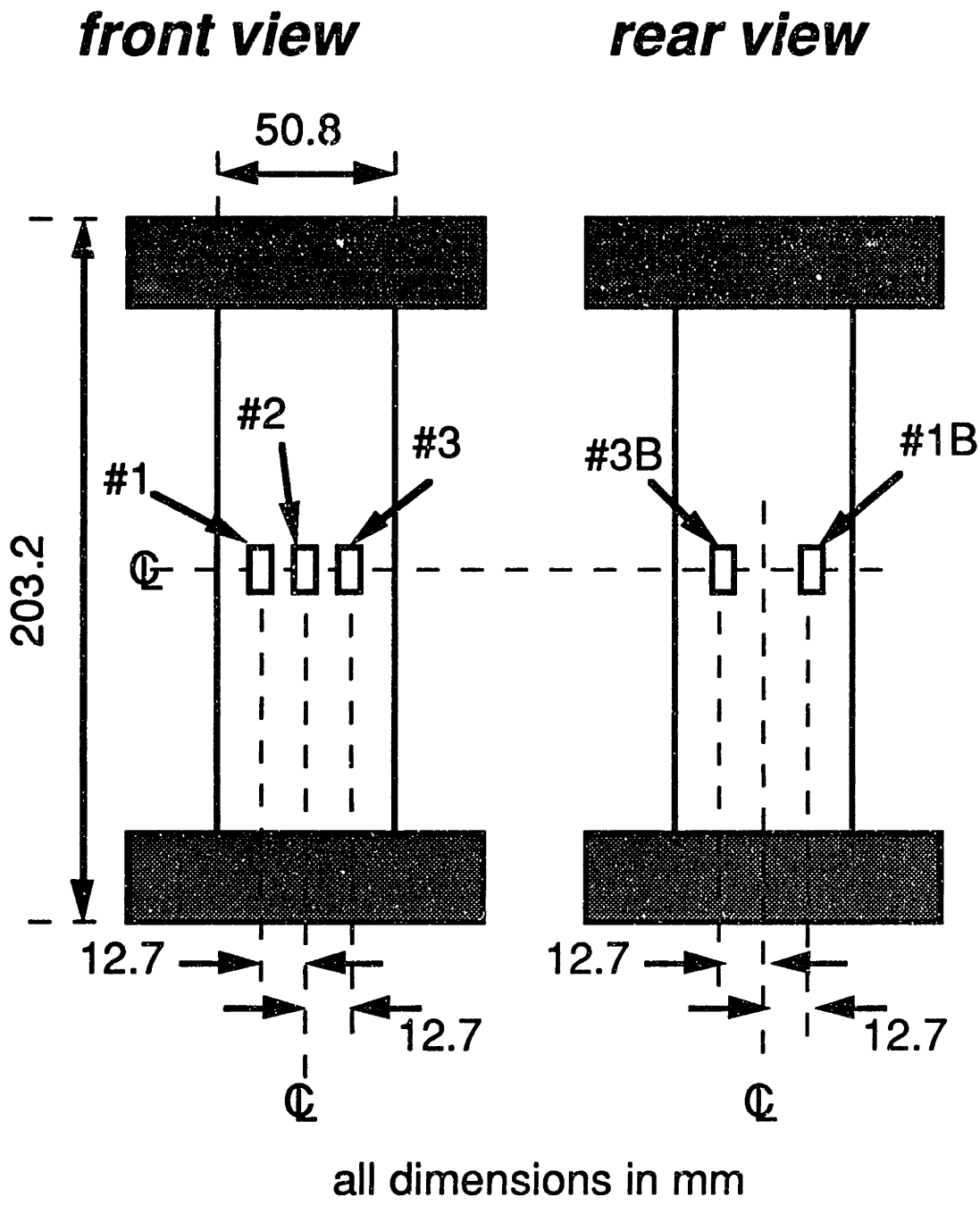

Figure 5.26 Illustration of "Undamaged 3" configuration of strain gages used for undamaged specimen A-S-Ub.

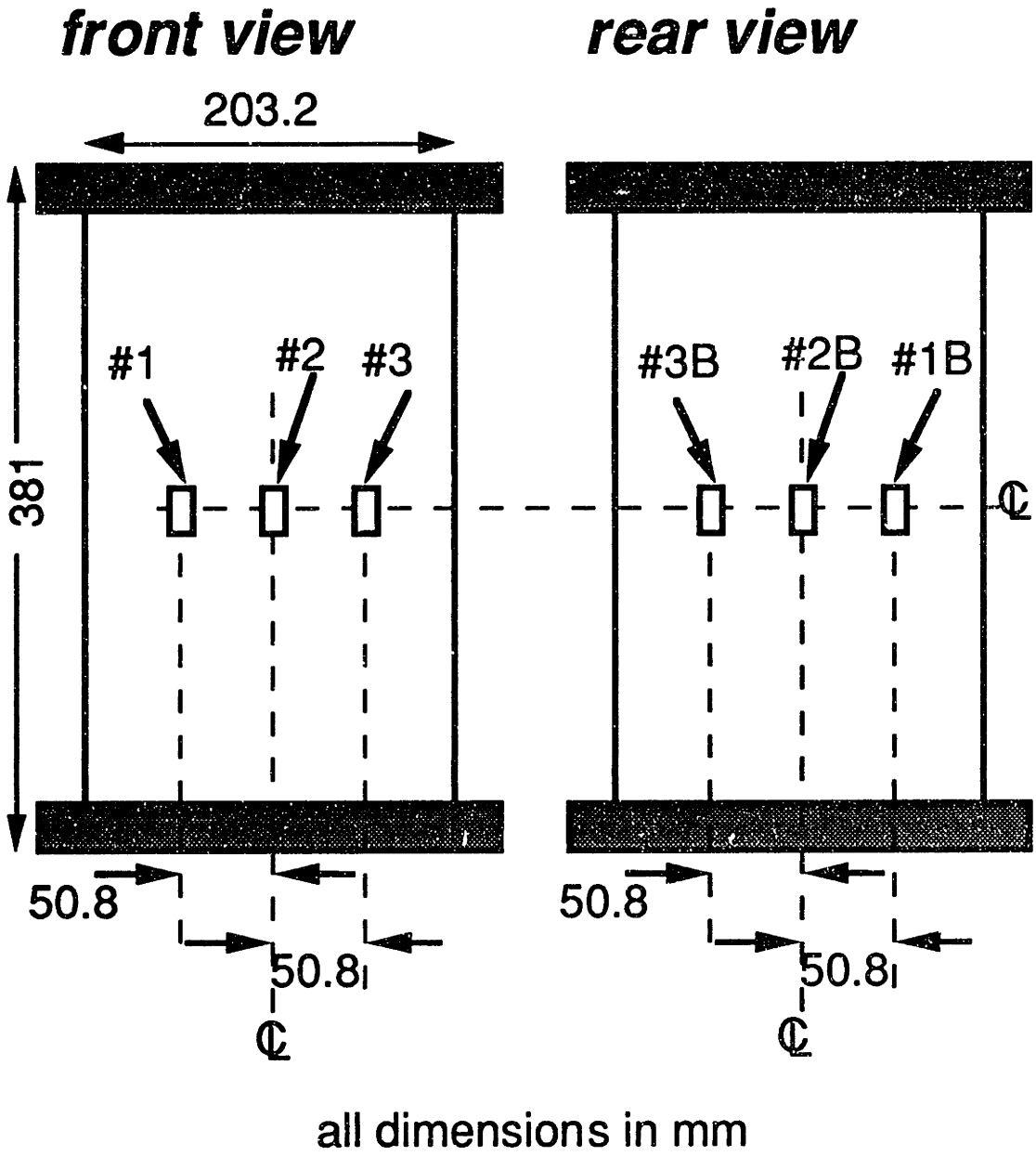

Figure 5.27 Illustration of "Undamaged 4" configuration of strain gages used for undamaged specimen A-M-U.

the grips were tightened on a steel block to prevent damage to the grips by the loading. For the remainder of the tests, due to spacing and load capacity constraints, the grips were removed and the fixture was placed directly on the load cell and the bottom hydraulic piston.

In order to have a wide, flat surface with which to load the specimens, a special fixture was constructed based on the fixture used in previous ATCAS tests. It was designed to be stiff in bending so that displacement imposed on the end of the specimen would be nearly constant along its width. The fixture is shown schematically in Figure 5.28. The steel plates provide a flat surface for loading the end of the specimen. The I-beams provide a stiff base for the plate and transfer the load to the testing machine. The steel loading plates provide flat surfaces to rest on the testing machine. They are also bolted to the beams to help the threaded rod hold the beams together.

All plates and beams used in the fixture are made of A36 structural steel. Part d, the steel plates with in-plane dimensions of 229 mm by 610 mm (9.0 in by 24.0 in), were specified as 38 mm thick and finished to a thickness of approximately 35 mm. The top and bottom surfaces of these plates were finished to a flatness tolerance of ±0.06 mm (±0.0025 in), while these surfaces were parallel to each other by the same tolerance. Parts c are steel I-beams of standard configuration with nominally 63.5 mm (2.5 in) wide flanges and a web thickness of 8.4 mm (0.33 in). The nominal total height of the I-beams was 76 mm (3.0 in). These beams were unfinished and are attached to each other with threaded rod, parts e. Parts b are 6.4 mm (0.25 in) thick steel plates placed between the I-beams and the flat surface of the grips or load cell as appropriate. This plate was bolted to the I-beams to hold them together and reduce any shifting of the beams.

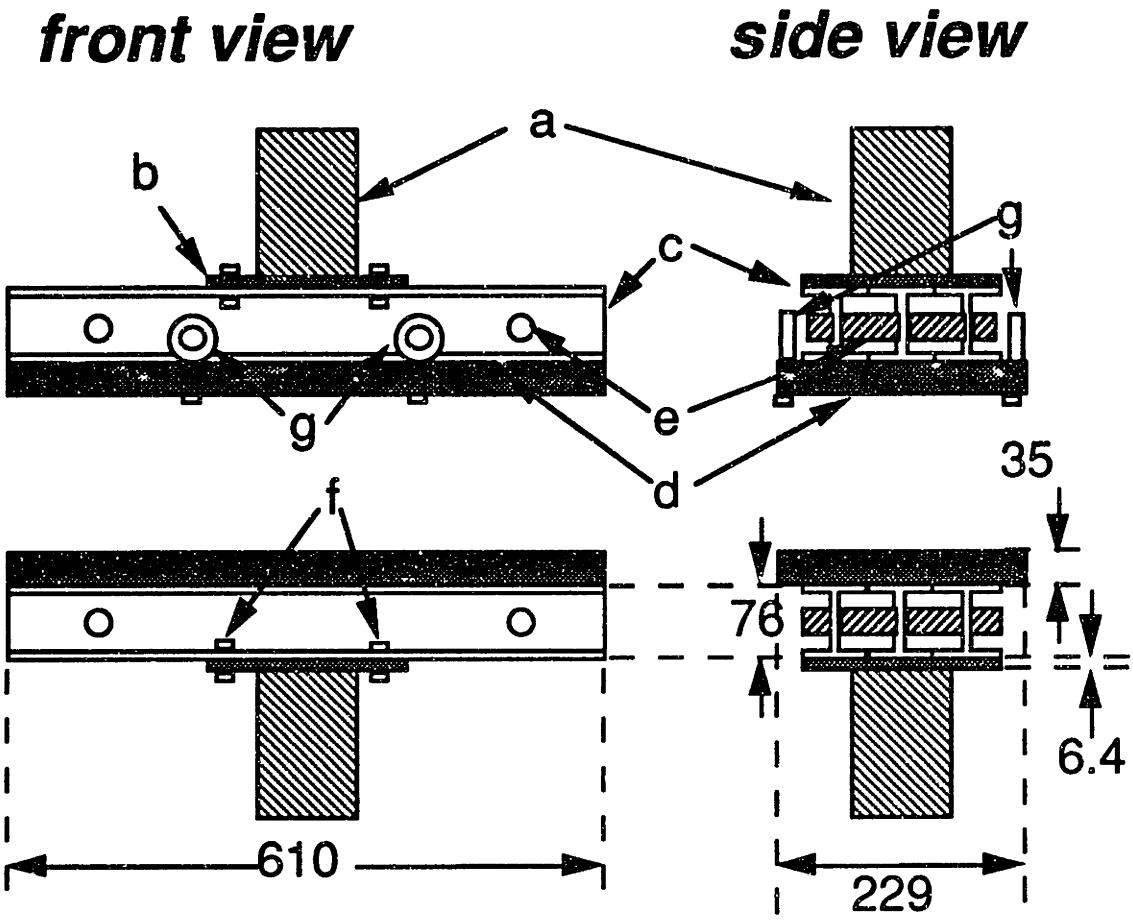

All dimensions in mm

a = hydraulic grips or load cell/piston

b = steel plate

c = steel I-beams

d = steel loading plate

e = threaded rod

f = bolts attaching loading plate to I-beams

g = eye-hooks for suspending upper half of fixture

Figure 5.28 Schematic of test fixture.

The bottom half of the fixture rested directly on the lower grip/hydraulic piston. No attachment was made between the grip and the fixture or between the I-beams and the loading plate. The top half of the fixture was suspended from the crosshead of the testing machine by four turnbuckles. These turnbuckles were attached to eyehooks through the loading plate and eyehooks in the crosshead of the machine. Chains were used to provide extra length if the turnbuckles were too short. The turnbuckles were then tightened by hand to preload the fixture to the upper grip/load cell.

An attempt was made to align the surfaces of the top and bottom half of the fixture so that they were parallel. Also, it was realized that the surfaces should be perpendicular to the loading axis of the test machine. No completely satisfactory solution to this alignment issue was found. Initially, one technique was used, but this was replaced by another two-part procedure because the first proved inadequate.

The first aligning technique involved bringing the plates nearly together, leaving an opening of slightly greater than 25 mm (1.0 in). The separation of the plates was then measured by inserting a square aluminum bar, and measuring the gap left with feeler gages. The aluminum bar itself was not measured, but all measurements were taken from the same location on the bar. These measurements were taken near the four corners of the plates. A tolerance for these measurements was chosen based on the tolerances required for the milled specimens. If the measurements differed by more than 0.25 mm (0.010 in), brass or steel shim was placed between the fixture and the hydraulic grips. The measurements were taken again, and the process repeated if necessary.

Unfortunately, this process did not account for the deformations the

fixture might undergo when loaded, nor did it check that the plates were perpendicular to the loading axis of the machine. Therefore, a new procedure was developed. An aluminum bar was placed between the plates, and a load of approximately 44 kN (10,000 lbs) was applied. The alignment was then checked as previously described. The machine was subsequently unloaded and shimmed if necessary. Then, two bars on top of each other were similarly loaded. A small hand level was used to check that the plates were parallel to the flat surface of the testing machine around the loading piston. If a misalignment of the order of a quarter of the bubble in the level (approximately 0.5°) was noted, shimming was again done, and the first part of the procedure repeated. The entire process could be quite lengthy. This alignment procedure was used for the remaining small specimens and the medium specimens.

Even this process was not completely satisfactory as it did not evaluate the alignment of the plates in the actual position used during testing. For example, before the testing of the first large specimen, A-L-DN76, and just after the grips had been removed, the plates were aligned as described in the second procedure. The crosshead was raised to the height necessary to bring the plates far enough apart for the large specimens to be tested, approximately 790 mm (31 in). When the specimen was placed on the lower plate, it was noted that the top of the specimen was not parallel with the upper plate. When the specimen touched the plate on the left side, a large gap was remained on the right side. Although this gap was not measured, it was estimated to be of the order of 1 to 2 mm. Recall that the specimen had been measured and found to be parallel to within 0.18 mm. Apparently, the alignment at a separation of 25 mm is substantially different from the alignment at a separation of 760 mm In this case, a piece

of brass shim was place between the loading piston and the lower part of the fixture and the unloaded alignment checked visually. Visual alignment was used for all large specimens. The alignment method used for the A specimens is given in Table 5.3, while the method used for the B specimens is given in Table 5.4.

Tests were conducted under stroke control with the stroke rate set to achieve a nominal strain rate of 2500 μstrain/min. Thus, the stroke rates for the small, medium, and large specimens were 0.508, 0.953, and 1.91 mm/min, respectively. In most tests, eight channels of data were recorded: load and deflection, measured by the LVDT, were recorded for all cases. If five strain gages or less were used, the stroke was recorded. Otherwise, a sixth strain gage was recorded. The analog-digital board used for data acquisition was MacADIOS II/16 manufactured by GW instruments. The software was LabVIEW made by National Instruments which was run on a Macintosh IIx computer. The sampling rate was increased for the medium and large specimens because these specimens normally failed at lower strains than the small specimens. The rate was set at 0.5 Hz for the tests of small specimens, 1.0 Hz for tests of the medium specimens, and 2.0 Hz for tests of the large specimens. The resolution of load was 109 N (24.4 lbs) for the small specimens with the load cell set at 50% of full scale, while the resolution for the medium and large specimens was 217 N (48.9 lbs) at 100% of full scale. Resolution of the strain gages was 10 μstrain, while that of the stroke was 0.0124 mm (0.000489 in). The resolution of the LVDT was approximately 0.008 mm (0.0003 in).

For the medium and large specimens and those small specimens aligned under method 2, preliminary tests were conducted to determine if the specimen was properly aligned to give even loading. In these cases, the

Table 5.3 Alignment method used for A specimens

Specimen	Alignment Method Used
A-S-Ua	1
A-S-Ub	1
A-S-SN3a	1
A-S-SN3b	2
A-S-DN3	2
A-S-SN6a	1
A-S-SN6b	1
A-S-DN6	2
A-S-SN10a	1
A-S-SN10b	1
A-S-DN10	2
A-S-SN13a	1
A-S-SN13b	1
A-S-DN13	2
A-M-U	2
A-M-DN25	2
A-M-DN51	2
A-M-IL1	2
A-M-IL2	2
A-L-SN25	visual
A-L-DN25	visual
A-L-DN76	visual
A-L-IL1	visual

Table 5.4 Alignment method used for B specimens

Specimen	Alignment Method Used
B-S-Ua	1
B-S-Ub	2
B-S-SN3a	1
B-S-SN3b	2
B-S-DN3	2
B-S-SN6a	1
B-S-SN6b	2
B-S-DN6	2
B-S-SN10a	1
B-S-SN10b	2
B-S-DN10	2
B-S-SN13a	1
B-S-SN13b	1
B-S-DN13	2
B-M-SN25	2
B-M-DN25	2
B-M-DN51	2
B-M-IL1	2
B-M-IL2	2
B-L-SN25	visual
B-L-DN25	visual
B-L-DN76	visual
B-L-IL1	visual

specimen was loaded to one or more low load levels and the values of the far-field gages recorded. The load levels were never more than 20% of the expected failure load of the specimen. If it was determined that one facesheet of the specimen was loaded substantially more than the other as shown by a consistent difference of greater than 10% between the front and back gages, shim in the form of one or more thicknesses of aluminum foil was placed under the facesheet which was loaded less. The process was then repeated. This process was largely a judgment call. On certain occasions, one facesheet was found to be loaded less initially. That side was shimmed so that it was loaded equally at the low load levels checked. As the actual test proceeded, however, the strain reading on this side could become substantially higher or lower than that of the other side. In other words, the behavior in the initial stages was not always a good indication of the behavior of the specimen in later stages of loading.

The actual test was begun by activating the testing machine and data acquisition simultaneously by the two researchers. For medium and large specimens, the specimen was loaded to approximately 9000 N (2000 lbs) and the test paused at this load level. The second researcher placed one mark on the computer record to indicate the test had been stopped and another to indicate that it had been restarted. While the test was paused, the LVDT was placed against the specimen. The LVDT was calibrated if it had not been calibrated in the same session. This was done by first recording by hand the computer reading obtained with the LVDT against the specimen. Two precision spacers of 3.175 mm (0.125 in) and 6.350 mm (0.250 in) were placed between the specimen and the LVDT. The computer readings were noted for each of these spacers. The known distances were divided by the difference in computer readings to determine a calibration factor for the

LVDT. If the specimen had been impacted, the moiré grating was adjusted as described previously and the video camera started recording. When these tasks were completed, the loading process was restarted. If a photoelastic coating was used, the test was paused at predetermined loads and pictures of the photoelastic patterns taken. Compensation measurements, if taken, were also done at this time. The pausing and restarting of the records were marked by the second researcher as before. During loading on most tests, audible popping or cracking heard by the experimenter at the computer was also marked on the computer record. These marks did not conflict with the marks for pausing and restarting because the noises occurred at higher loads than the pausing. Loading was continued to failure. The specimen failure in all cases was obvious and was characterized by damage propagation across the width of at least one facesheet. After failure, the machine was paused and then loading was removed.

5.5 Data Reduction

Several steps were taken in order to bring the data in the computer record to a useful form. The computer record was saved as a text file on the hard drive of the Macintosh computer. This file was opened using the KaleidaGraph program. Data between marks for the pausing and restarting of the test was deleted. Readings taken by the LVDT before calibration was complete were removed from consideration by masking. Masking preserves the data in the file, but it does not appear in any plots of this data. For medium and large specimens, the initial reading of the LVDT after calibration was taken as the zero, and all readings were adjusted

accordingly. For the small specimens, the reading at a load level 4.5 kN was taken as the zero. This load level was chosen based on observations of the recorded data. The load level was chosen to be small so that little bending would occur, but the specimen would have a sufficient load applied to be well seated on the plates. Then, the calibration factor was multiplied by the computer reading in order to obtain the displacement measurement. Stress was calculated as applied load divided by the nominal cross-sectional area of the facesheets. No reduction was performed on the other recorded data. Plots of the data were produced using the KaleidaGraph program.

The slope of the stress-strain curves produced from the strain gage readings were determined using the program LIN6 [56]. This program identifies linear regions in experimental data. Because several slopes can be identified, the initial slope of a stress-strain curve was chosen as the first linear region identified for which the bulk of the data points were recorded above a given stress level. This stress level was chosen for the small, medium, and large specimens to be 72 MPa, 36 MPa, and 38 MPa, respectively. These stress levels were chosen after examination of the experimental stress-strain data to allow for seating of the specimen and settling of the test fixture while remaining low enough that the material behavior would be linear. The stress level for the small specimens was higher because there seemed to be more settling involved with this size.

Fringe patterns recorded using shadow moiré were digitized, printed and measured as discussed previously. The data points thus obtained were plotted using the KaleidaGraph program.

The images of the photoelastic patterns were recorded on slide film. These slides were projected onto a sheet of paper. The boundaries of the different colors represented were sketched onto the paper by hand. These

sketches were digitized with the Ofoto program. Plots were produced from the digitized sketches using the MacDraw Pro program. Scale was determined in these sketches using the known width of the coating. By using the values in Table 5.2, the fringe order N for the different color regions can be determined. The null compensation measurements were used to verify the validity of the sketches and better define the boundaries of the different colors. Equation 5.1 was then used to calculate the approximate difference of principal strains for each region.

Chapter 6

Results

All experimental results and selected analytical results are presented in this chapter. The results are divided into three categories: undamaged compressive behavior, notched compressive behavior, and compression after impact behavior. The undamaged compressive behavior results consist of strain and out-of-plane deflection measurements recorded during tests, failure strengths, and characterization of the failure mode. Results for notched compressive behavior include deflection and strain gage data, photoelastic images recorded, failure strengths, and characterization of the failure mode. In addition, the analytical predictions of the photoelastic patterns are given. Correlation of the failure strengths is discussed in Chapter 7. Results for compression after impact behavior include deflection and strain gage data, moiré images of dimple growth, failure strengths, and characterization of the failure mode. The moiré images are used to measure the growth of the dimple, while the dimple growth model detailed in Chapter 4 is used to predict the growth. Both the experimental measurements and the prediction of growth are presented in this chapter. Prediction of failure with the dimple growth model is discussed in Chapter 7.

6.1 Undamaged Compressive Behavior

As discussed in Chapter 3, a total of five specimens were tested in the undamaged configuration. Three additional undamaged specimens were

included in the original plan, but these specimens were moved to the second round of tests and tested in the notched configuration. The five undamaged specimens included two small specimens from each panel and one medium specimen from the A panel.

As detailed in Chapter 5, strain, out-of-plane deflection, and, in some cases, stroke of the testing machine were recorded for each of the undamaged specimens. A representative plot of the stroke versus applied far-field stress is shown in Figure 6.1. Little information is provided by these data because the compliances of the specimen, the testing machine and the test fixture cannot be distinguished.

The out-of-plane displacement was recorded for all of these specimens using an LVDT placed perpendicular to the rough side facesheet at the center of the specimen. Two types of behavior were observed. The first, for which a representative plot is shown in Figure 6.2, involves a monotonic and steady increase in the deflection. The deflection can be either positive (toward the rough side facesheet) or negative (in the direction of the smooth side facesheet). The second type of behavior, of which a representative plot is shown in Figure 6.3, is a nonmonotonic deflection pattern. It increases and then decreases in magnitude. A key parameter for these measurements is the maximum out-of-plane deflections. These are given for the undamaged specimens in Table 6.1. In addition, the type of out-of-plane deflection behavior, monotonic or nonmonotonic, is given for each specimen. The deflection for all cases except one is positive, i.e. toward the rough side facesheet. The maximum deflection recorded, 1.02 mm, is less than half of the thickness of a facesheet.

The stress-strain results for these specimens should be the same, provided the loading is even, no bending is present, and the local modulus of

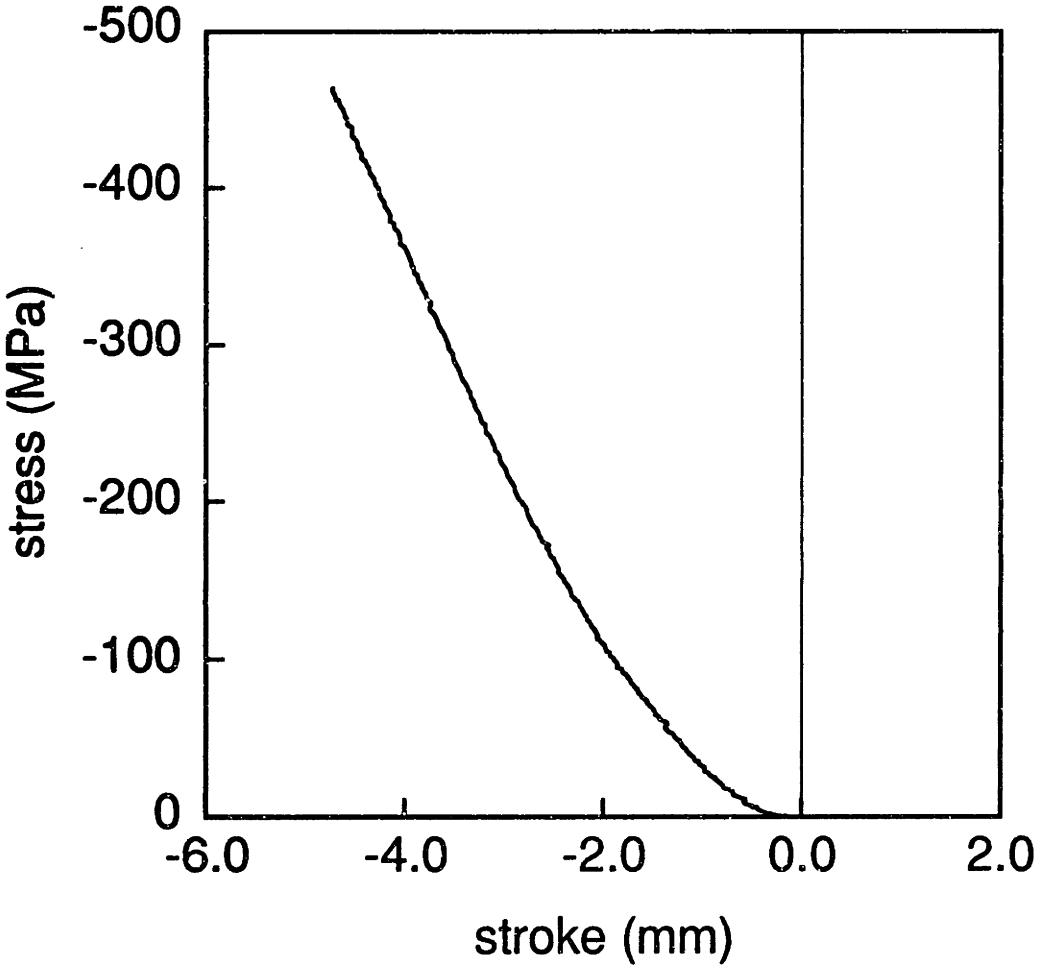

Figure 6.1 Representative plot of stroke versus far-field applied stress (specimen A-S-Ua).

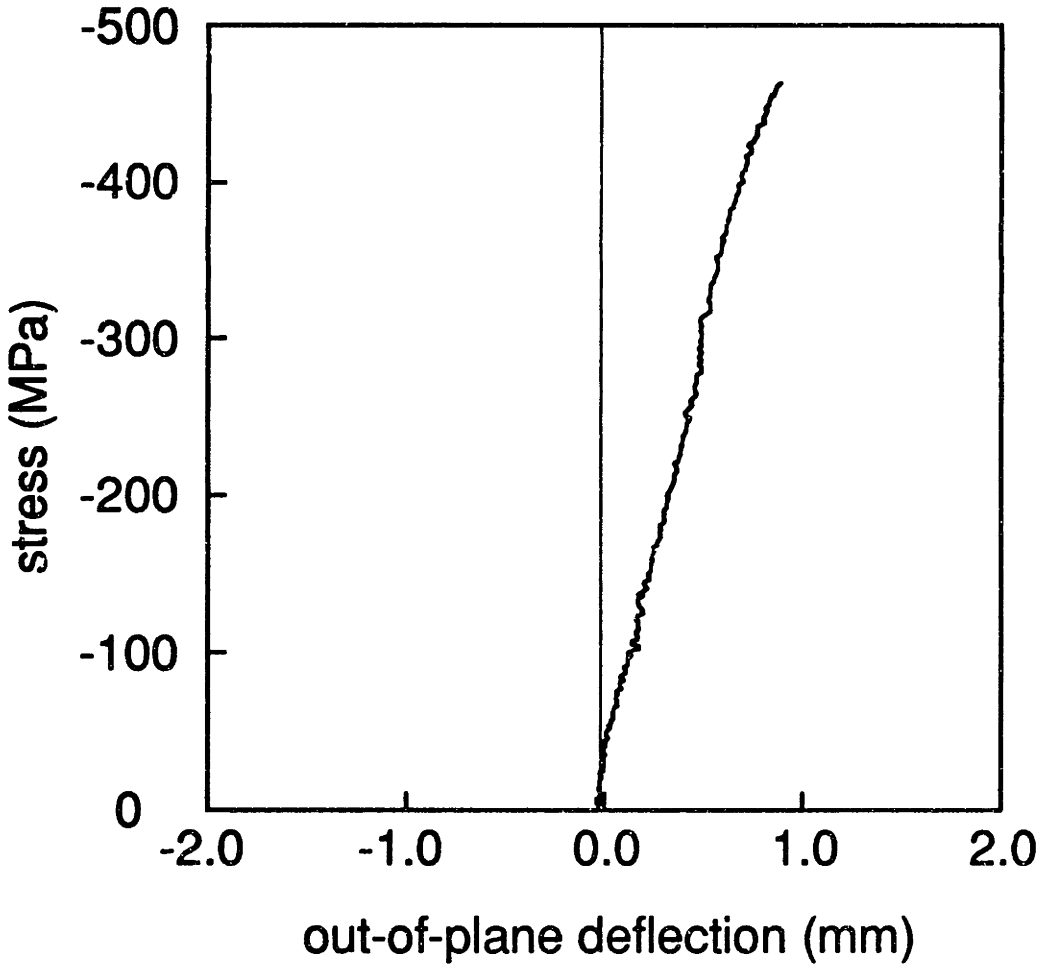

Figure 6.2 Plot of out-of-plane deflection versus far-field applied stress in which the deflection increases monotonically (specimen A-S-Ua).

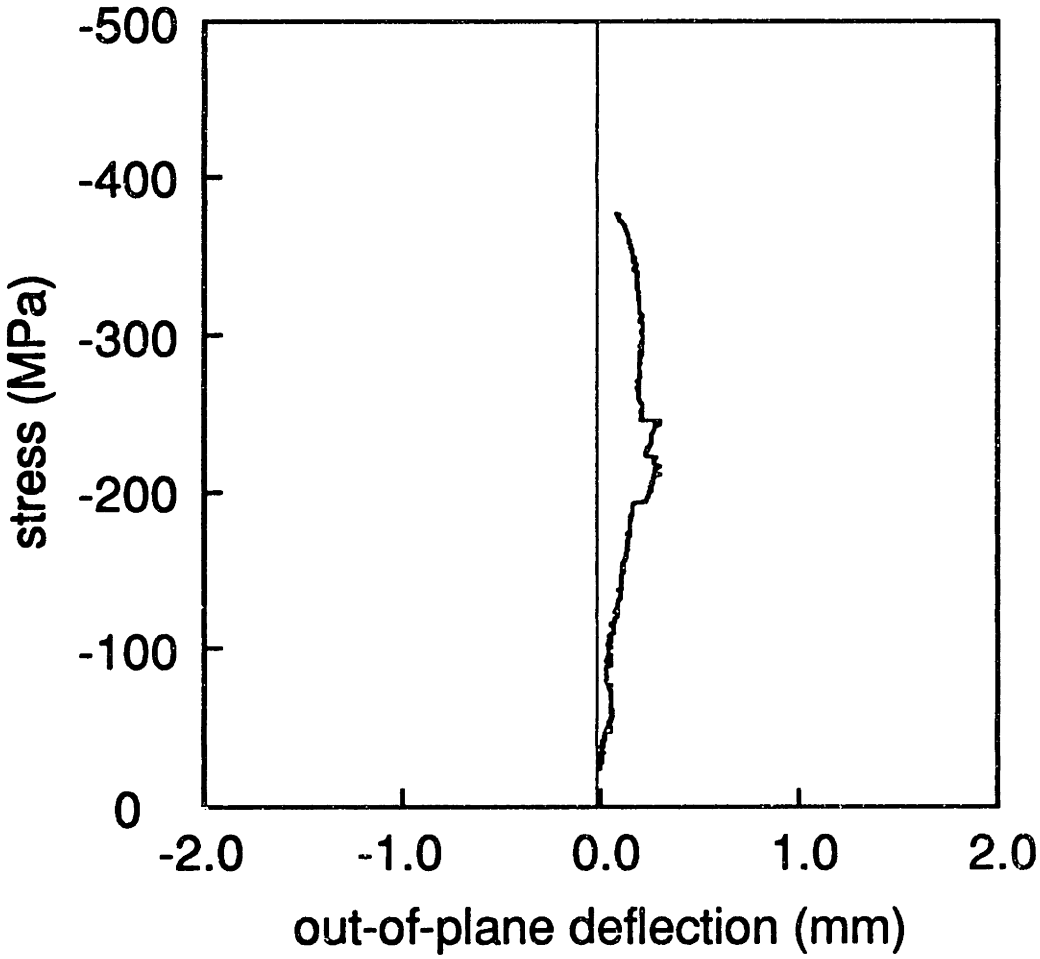

Figure 6.3 Plot of out-of-plane deflection versus far-field applied stress in which the deflection is nonmonotonic (specimen A-M-U).

Table 6.1 Maximum value and characterization of out-of-plane deflection of undamaged specimens

Specimen	Type of Behavior	Maximum Deflection
A-S-Ua	monotonic	0.89 mm
A-S-Ub	non-monotonic	0.35 mm
A-M-U	non-monotonic	0.30 mm
B-S-Ua	monotonic	1.02 mm
B-S-Ub	monotonic	-0.22 mm

the material is constant. The calculated modulus of the specimens from the A layup is 52.7 GPa, while that of the specimens of the B layup is 64.3 GPa. Initial slopes for all strain gages of all specimens tested can be found in Appendix D. A representative plot of the strain gages for the strain gage configuration Undamaged 1 (as detailed in Figure 5.24) is given in Figure 6.4. This specimen is from the A layup. It is evident that the readings are not all the same for the gages. The curves appear to be linear initially, but they show a reduction in slope at stress levels above approximately 250 MPa. Readings from gages 2, 4, and 5, which are located along the horizontal centerline, are all closely grouped throughout the test. The initial slope of these three curves is 47.4 GPa, somewhat lower than the calculated modulus. Gage 1, which is located above the centerline, exhibits a lower strain throughout the test than the grouped gages. The initial slope of this curve is 53.1 GPa, very close to the calculated modulus. On the other hand, gage 3, which is located below the centerline, shows a higher strain than the grouped gages. This difference is initially small but grows as the stress level increases. The initial slope of this gage is 42.7 GPa. A similar behavior is exhibited by the specimen of the B layup tested in this configuration: the three central gages are closely grouped, while gage 1 shows lower strain and gage 3 shows higher strain. The slope of the grouped gages is 54.7 GPa, while gages 1 and 3 have initial slopes of 65.7 GPa and 49.3 GPa, respectively. Again, the slope of the grouped gages is somewhat lower than the calculated modulus, while the slope of gage 1 is much closer.

The A specimen tested with configuration Undamaged 3, which is shown in Figure 5.26, also exhibited close grouping of the gages as with the grouped gages of the Undamaged 1 configuration. All five of these gages

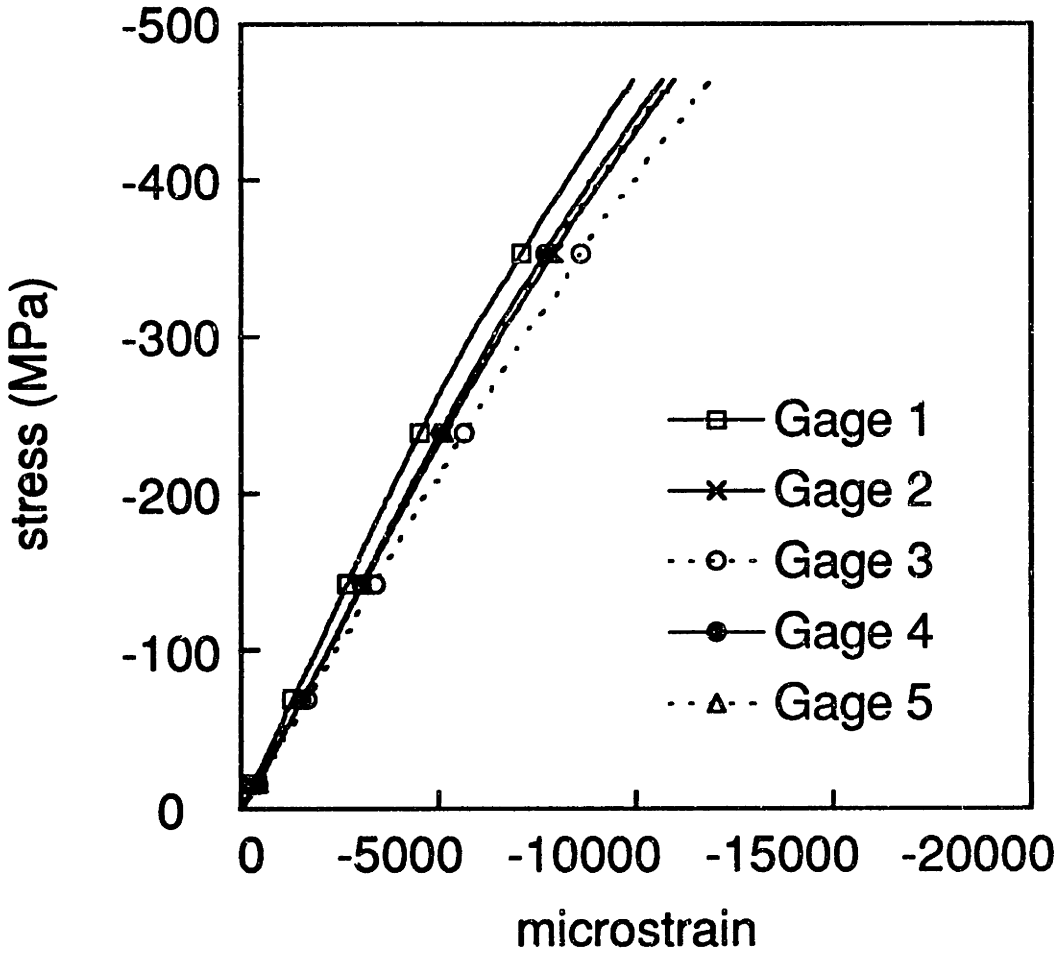

Figure 6.4 Representative plot of strain versus far-field applied stress for undamaged specimens with gage configuration Undamaged 1 (specimen A-S-Ua).

were placed on the horizontal centerline of the smooth and rough side facesheets. Their average initial slope is 52.0 GPa with values ranging from 54.3 to 47.6 GPa. There was no consistent difference observed between gages located on the smooth side and their counterparts on the rough facesheets.

The medium unnotched specimen was tested with the Undamaged 4 configuration as shown in Figure 5.27. This specimen exhibited a different behavior from the small specimen tested with a similar configuration, Undamaged 3. Strain gage readings for this specimen are shown in Figure 6.5. For this specimen, each gage on the smooth side facesheet and its counterpart on the rough side facesheet give very similar readings. However, the gages on the right (gages 3 and 3B) have higher readings than the gages on the vertical centerline (gages 2 and 2B), while the gages on the left (gage 1 and 1B) have slightly lower readings. The initial slopes up to a stress level of approximately 80 to 100 MPa of the gages on the right, center, and left are 45.2, 51.3, and 56.9 GPa, respectively. However, the slopes of the gages decrease by different amounts as the stress increases so that their slopes are closer to each other. It should be noted that in configuration Undamaged 4, gages 1 and 3 are over 100 mm apart, but are only 25 mm apart in the Undamaged 3 configuration.

A small specimen from the B layup tested with the Undamaged 2 strain gage configuration, shown in Figure 5.25, exhibited somewhat different stress-strain behavior than the other undamaged specimens. The strain gage readings from this specimen are shown in Figure 6.6. Readings from gages 2, 3, and 4, which are the central gages along the vertical centerline of the smooth side facesheet, are grouped closely together. The initial slope of these curves is 62.7 GPa. Gage 1, located above these three,

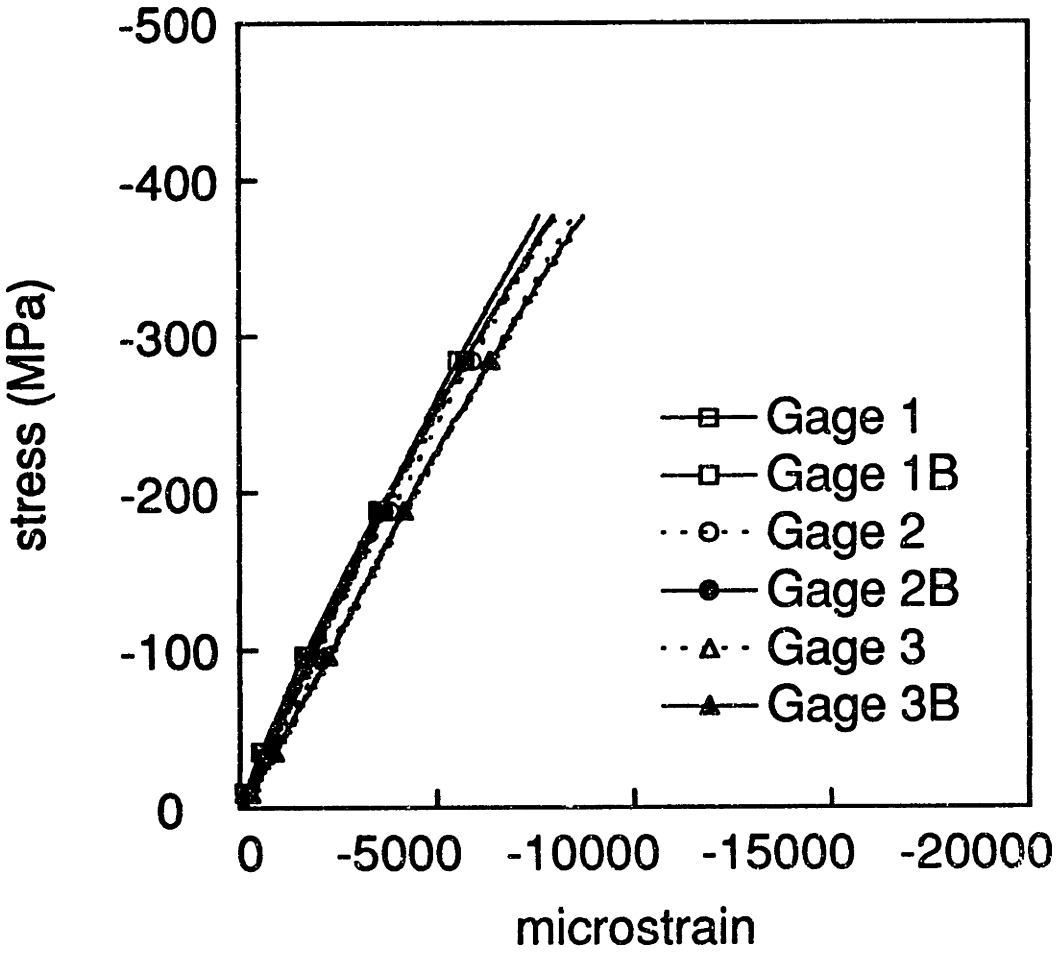

Figure 6.5 Plot of strain versus far-field applied stress for the undamaged medium specimen with strain gage configuration Undamaged 4 (specimen A-M-U).

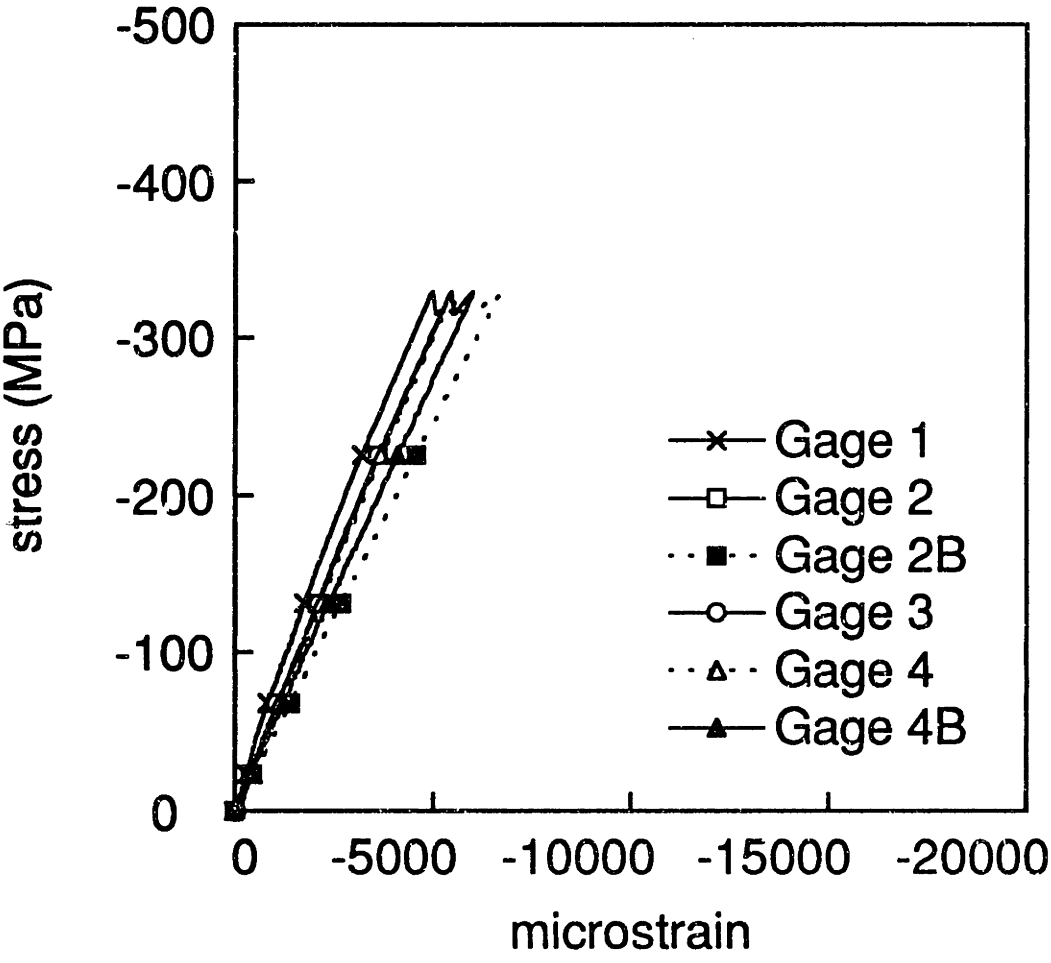

Figure 6.6 Plot of strain versus far-field applied stress for the undamaged specimen tested with configuration Undamaged 2 (specimen B-S-Ub).

exhibits a lower strain and an initial slope of 69.4 GPa. Gages 2B and 4B, located opposite gages 2 and 4 on the rough side facesheet, exhibit higher strains than their counterparts on the smooth side facesheet with an initial slope for gage 2B of 49.5 GPa and that for gage 4B of 54.4 GPa.

The average of the initial slopes of the strain gage is chosen as a measurement of the longitudinal modulus of the specimen. The moduli determined in this way are shown in Table 6.2. The coefficient of variation, calculated as one standard deviation divided by the average of the slopes is used as a measure of the scatter among the gages on a specimen. The slopes are most close on specimen A-S-Ub which had all gages on the horizontal centerline. The average measured modulus for the undamaged specimens is 50.2 GPa with a coefficient of variation of 8.4% for the A specimens and 58.1 GPa with a coefficient of variation of 11.5% for the B specimens. Thus, the measured modulus is approximately 5% lower than the calculated modulus of 52.7 GPa for the A laminates, but is nearly 10% lower than the calculated modulus of 64.3 GPa for the B layup.

For all undamaged specimens, failure occurred at or near the potting material on the ends of the specimens. The small undamaged specimens exhibited what will be termed a "potting-line failure." This involves fracture of the facesheets adjacent to the boundary of the potting material. This fracture was accompanied by a substantial amount of splitting of the plies of the facesheets. An example of this failure mode is shown in Figure 6.7. The medium undamaged specimen exhibited a different failure mode, namely a brooming failure at the end. This mode of failure is characterized by a crushing and splitting outward of the facesheets on the end which failed within the potting material. This specimen is shown after failure in Figure 6.8. It should be noted that the potting material has broken away

Table 6.2 Measured longitudinal moduli of undamaged specimens

Specimen	Modulus (GPa)	Coefficient of Variation
A-S-Ua	47.9	6.9%
A-S-Ub	52.0	4.4%
A-M-U	50.7	9.5%
B-S-Ua	55.9	9.8%
B-S-Ub	60.3	10.8%

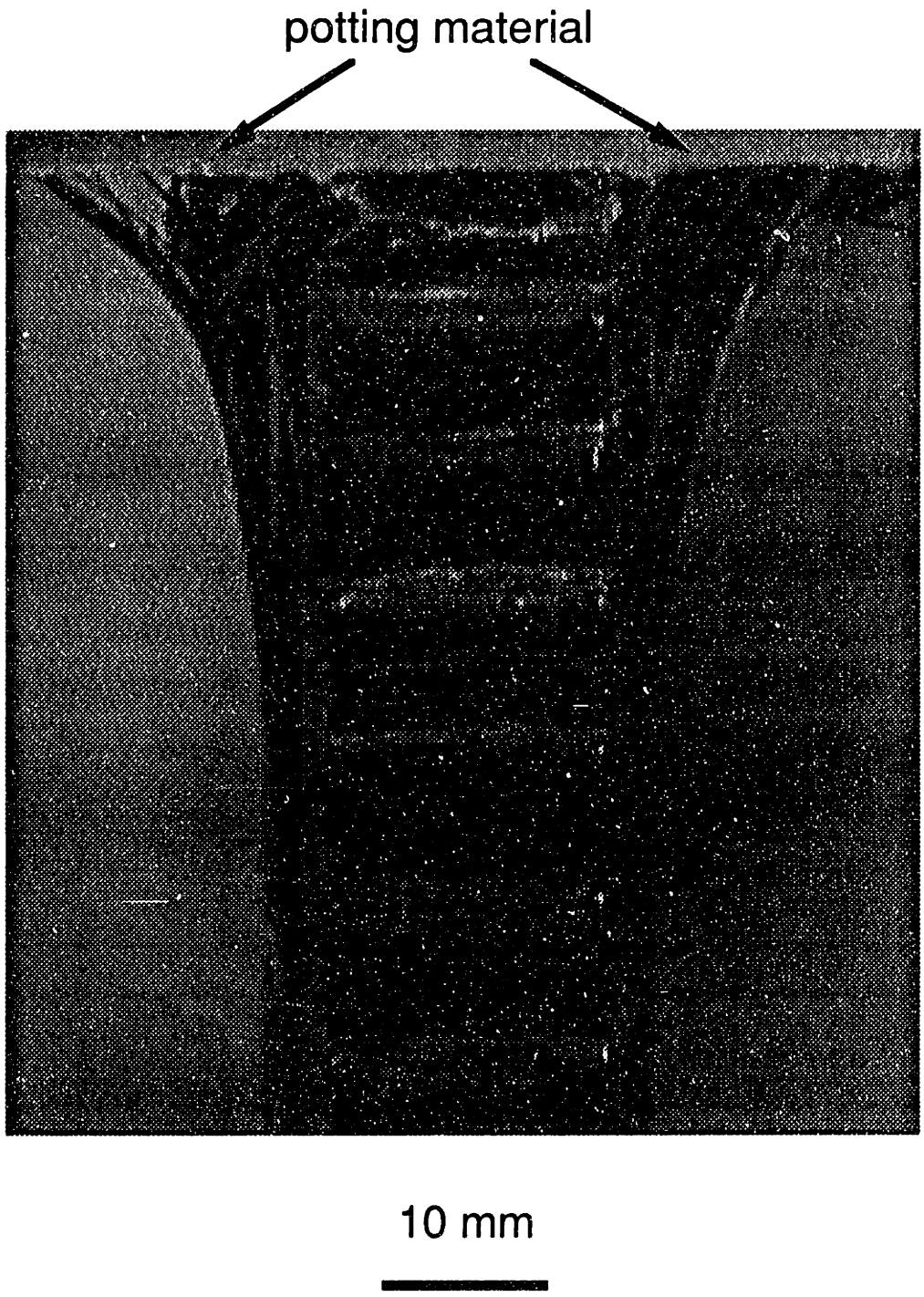

Figure 6.7 Photograph of undamaged small specimen which failed at the potting line. The potting material is located directly above the upper part of the visible core and facesheets (specimen A-S-Ua).

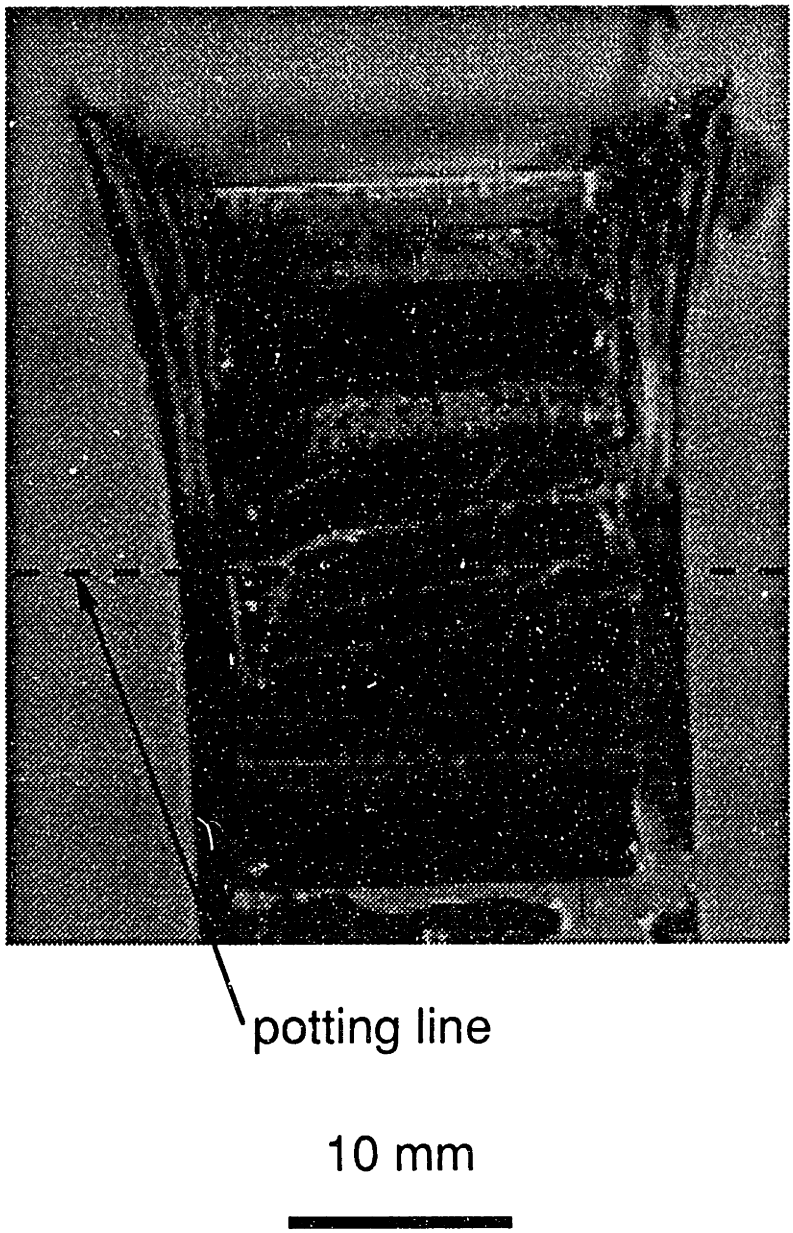

Figure 6.8 Photograph of brooming failure in medium undamaged specimen (specimen A-M-U).

from the specimen. It is not known whether this caused the brooming failure or was the result of specimen failure.

The failure stresses of the undamaged specimens are given in Table 6.3. Although specimen B-S-Ub failed in the same manner as the other undamaged specimens, its failure stress was significantly lower than the other B specimen tested in an undamaged state. This may be due to the repeated loadings of the specimen in the process of perfecting the testing techniques. Although none of these repeated loads was more than a third of the failure load of the other undamaged specimen of the B layup, the cumulative effect of the loading may have been able to damage the specimen in some non-visible manner. For this reason, this specimen is removed from any further consideration of undamaged compressive strength. Similarly, the medium undamaged specimen is not considered as its failure was in a different mode, namely a brooming failure at the end of the specimen, and at a substantially lower stress than the small specimens. For the remaining specimens, the average undamaged compressive strength of the A specimens is 492 MPa, while the strength of the B specimen was 451 MPa.

6.2 Notched Compressive Behavior

A total of thirty-five specimens were tested in the notched condition. As described in Chapter 5, a narrow slit was machined in one or both facesheets of the specimens. The width of the slits was approximately 1.0 mm for the small specimens and approximately 5.0 mm for the medium and large specimens. The measured lengths of the notches are given in Table 6.4 for the A specimens and Table 6.5 for the B specimens. It should be noted that some specimens have notches in only the smooth side facesheet

Table 6.3 Failure stresses of undamaged specimens

Specimen	Failure Stress (MPa)
A-S-Ua	465
A-S-Ub	518
A-M-U	377
B-S-Ua	451
B-S-Ub	329

Table 6.4 Measured lengths of machined notches in specimens of the A layup.

Specimen	Smooth Side (mm)	Rough Side (mm)
A-S-SN3a	3.8	-[a]
A-S-SN3b	3.1	-
A-S-DN3	3.4	3.4
A-S-SN6a	6.5	-
A-S-SN6b	6.3	-
A-S-DN6	6.6	6.7
A-S-SN10a	9.6	-
A-S-SN10b	9.4	-
A-S-DN10	9.6	9.5
A-S-SN13a	13.8	-
A-S-SN13b	12.2	-
A-S-DN13	12.8	13.1
A-M-DN25	25.8	25.9
A-L-SN25	25.4	-
A-L-DN25	25.4	25.4
A-M-DN51	51.5	50.9
A-L-DN76	76.5	76.6

[a] Indicates that only the smooth side facesheet was notched.

Table 6.5 Measured lengths of machined notches in specimens of the B layup

Specimen	Smooth Side (mm)	Rough Side (mm)
B-S-SN3a	3.1	-[a]
B-S-SN3b	3.3	-
B-S-DN3	3.3	3.4
B-S-SN6a	6.1	-
B-S-SN6b	6.7	-
B-S-DN6	6.5	6.4
B-S-SN10a	9.8	-
B-S-SN10b	9.8	-
B-S-DN10	9.7	9.8
B-S-SN13a	12.1	-
B-S-SN13b	13.1	-
B-S-DN13	12.8	12.8
B-M-SN25	25.9	-
B-M-DN25	25.6	25.6
B-L-SN25	25.4	-
B-L-DN25	25.3	25.7
B-M-DN51	50.7	51.3
B-L-DN76	76.3	76.4

[a] Indicates that only the smooth side facesheet was notched.

while others have notches in both facesheets.

Instrumentation schemes for the notched specimens are detailed in Chapter 5. Three different strain gage configurations were used. Eighteen specimens had a photoelastic coating on half of the smooth side facesheet, while two had the coating covering the entire smooth side facesheet. In Table 6.6, the instrumentation schemes used for the A specimens are given, while those used for the B specimens are given in Table 6.7.

6.2.1 Deflection and Strain Gage Data

Data recorded electronically during testing included load, strain, out-of-plane deflection, and, for specimens with gage scheme 1 or 2, the stroke of the testing machine. These files were stored and manipulated on a Macintosh computer with the Kaleidograph program.

As discussed previously, the recorded data of the stroke of the testing machine provides no useful information and is therefore not presented.

The out-of-plane deflection of the specimens generally behaved as described for the undamaged specimens: it increased monotonically and steadily until failure occurred, or it was non-monotonic and relatively small. However, two different deflection behaviors were also observed. The first was an increasing rate of deflection as shown in Figure 6.9. Deflection is small for the region of initial loading before increasing slightly at a stress of about 100 MPa. Rather than steadily increasing deflection, the rate of increase of deflection grows. This type of behavior was only observed in two specimens. Both of these were large specimens of the A layup with 25.4 mm notches in one or both facesheets. The second type of different deflection behavior is an increase or jump in deflection as the failure stress is neared. A good example of this behavior is given in Figure 6.10. This behavior could

Table 6.6 Instrumentation scheme used for notched specimens of the A layup

Specimen	Strain Gage Scheme [a]	Photoelastic Coating [b]
A-S-SN3a	2	half
A-S-SN3b	2	-
A-S-DN3	3	-
A-S-SN6a	2	half
A-S-SN6b	2	-
A-S-DN6	3	-
A-S-SN10a	2	half
A-S-SN10b	2	-
A-S-DN10	3	half
A-S-SN13a	1	full
A-S-SN13b	2	-
A-S-DN13	3	-
A-M-DN25	3	half
A-L-SN25	3	half
A-L-DN25	3	half
A-M-DN51	3	half
A-L-DN76	3	half

a Notch 1, Notch 2, or Notch 3 as discussed in Chapter 5.

b Photoelastic coating on half of smooth side facesheet or covering the full facesheet.

Table 6.7 Instrumentation scheme used for notched specimens of the B layup

Specimen	Strain Gage Scheme [a]	Photoelastic Coating [b]
B-S-SN3a	2	half
B-S-SN3b	3	-
B-S-DN3	3	-
B-S-SN6a	2	half
B-S-SN6b	2	-
B-S-DN6	2	-
B-S-SN10a	2	half
B-S-SN10b	2	-
B-S-DN10	3	-
B-S-SN13a	1	full
B-S-SN13b	2	-
B-S-DN13	2	-
B-M-SN25	3	half
B-M-DN25	3	half
B-L-SN25	3	half
B-L-DN25	3	half
B-M-DN51	3	half
B-L-DN76	3	half

[a] Notch 1, Notch 2, or Notch 3 as discussed in Chapter 5.
[b] Photoelastic coating on half of smooth side facesheet or covering the full facesheet.

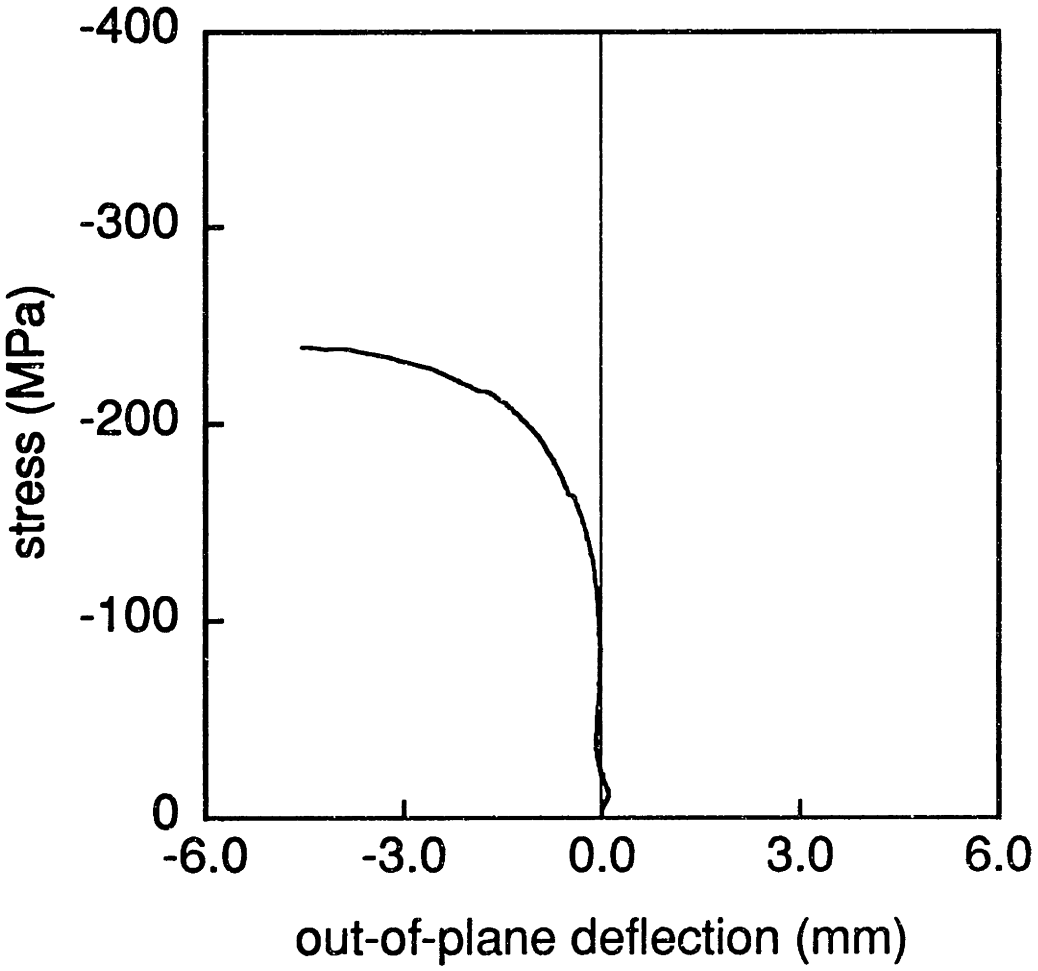

Figure 6.9 Plot of out-of-plane deflection versus far-field applied stress in which deflection grows increasingly rapidly (specimen A-L-SN25).

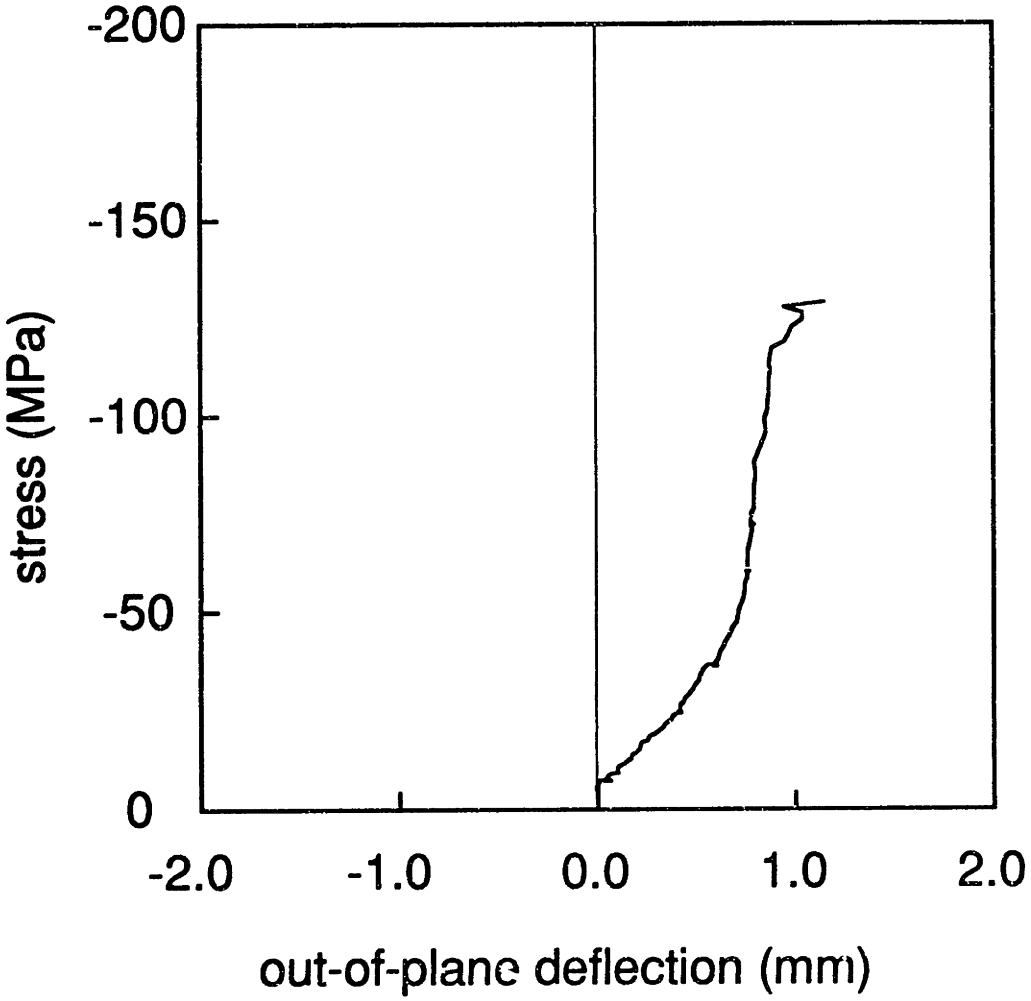

Figure 6.10 Plot of out-of-plane deflection versus far-field applied stress in which there is a perturbation in deflection at loads near failure (specimen A-L-DN76).

exist as an irregular deflection curve as shown or a small region in which the slope rapidly increases. This behavior was only observed in the medium and large specimens. The maximum out-of-plane deflections recorded for the notched A specimens, along with the type of behavior exhibited, are given in Table 6.8, while those of the B specimens are given in Table 6.9.

Among the small specimens of the A layup, deflection is generally in the positive direction. In all cases except one, the deflection is less than 1 mm. There is no definite effect of the notch length on the deflection behavior. Two of the four specimens with both sides notched deflect in the negative direction. The remaining two deflect in the positive direction with relatively small magnitudes of 0.42 and 0.26 mm. For specimens with 6.4 and 12.7 mm notches, the specimens with both facesheets notched deflect the least. Among specimens with 9.8 mm notches, the specimen with both facesheets notched falls in the middle regarding the magnitude of the maximum deflection. However, the deflection of this specimen is in the negative direction, while the deflection of the two is in the positive direction.

In contrast to the small specimens of the A layup, deflection is generally in the negative direction among the small specimens of the B layup. Only four specimens deflect in the positive direction, and the magnitude of three of these is quite small. No trend is discernible with regard to notch length, nor is there any discernible effect of notching one facesheet or both.

The only general trend observed with regard to deflection behavior of the medium and large specimens is that the large specimens generally have a larger magnitude of deflection than the medium specimens. The deflection of the medium specimens is of about the same magnitude as that of the small specimens. No differences in deflection behavior are observed

Table 6.8 Maximum value and characterization of out-of-plane deflection of notched specimens of the A layup

Specimen	Type of Behavior [a]	Maximum Deflection
A-S-SN3a	non-monotonic	0.61 mm
A-S-SN3b	monotonic	-0.31 mm
A-S-DN3	non-monotonic	0.42 mm
A-S-SN6a	monotonic	1.43 mm
A-S-SN6b	monotonic	0.51 mm
A-S-DN6	non-monotonic	-0.22 mm
A-S-SN10a	non-monotonic	0.20 mm
A-S-SN10b	monotonic	0.65 mm
A-S-DN10	monotonic	-0.50 mm
A-S-SN13a	monotonic	0.78 mm
A-S-SN13b	monotonic	0.67 mm
A-S-DN13	non-monotonic	0.26 mm
A-M-DN25	monotonic	0.47 mm
A-L-SN25	increasing rate	-4.54 mm
A-L-DN25	increasing rate	-1.56 mm
A-M-DN51	monotonic / end	-0.61 mm
A-L-DN76	monotonic / end	1.15 mm

[a] "non-monotonic" indicates deflection behavior is non-monotonic;
"monotonic" indicates deflection behavior is monotonic and steady;
"increasing rate" indicates increasing rate of deflection;
"end" indicates irregular behavior near end of test.

Table 6.9 Maximum value and characterization of out-of-plane deflection of notched specimens of the B layup

Specimen	Type of Behavior [a]	Maximum Deflection
B-S-SN3a	non-monotonic	-0.17 mm
B-S-SN3b	non-monotonic	-0.19 mm
B-S-DN3	non-monotonic	-0.20 mm
B-S-SN6a	monotonic	1.27 mm
B-S-SN6b	monotonic	-0.99 mm
B-S-DN6	monotonic	-0.38 mm
B-S-SN10a	non-monotonic	-0.15 mm
B-S-SN10b	non-monotonic	-0.20 mm
B-S-DN10	non-monotonic	0.14 mm
B-S-SN13a	monotonic	0.33 mm
B-S-SN13b	non-monotonic	0.09 mm
B-S-DN13	monotonic	-0.40 mm
B-M-SN25	non-monotonic	0.046 mm
B-M-DN25	monotonic	0.65 mm
B-L-SN25	monotonic	1.22 mm
B-L-DN25	monotonic	1.54 mm
B-M-DN51	monotonic	-1.18 mm
B-L-DN76	monotonic / end	0.50 mm

[a] "non-monotonic" indicates deflection behavior is non-monotonic; "monotonic" indicates deflection behavior is monotonic and steady; "end" indicates irregular behavior near end of test.

between medium and large specimens of the two layups.

Strain was recorded using strain gages as described in Chapter 5. Initial slopes for stress-strain curves of all the strain gages of the notched specimens are given in Appendix D. The two specimens tested with Notch 1 configuration, shown in Figure 5.20, show behavior similar to that for the unnotched specimens in that the strain gage readings are approximately linear to failure. The stress-strain curves for a small specimen of the B layup tested in configuration Notch 1 are given in Figure 6.11. Gage 1, which is located on the vertical centerline of the rough side (unnotched) facesheet at a distance of 50.8 mm from the horizontal centerline, produces a higher reading than gages 2 and 3. Gage 2 is located on the horizontal centerline to the left of the vertical centerline, while gage 3 is located to the right. Gage 3 gives slightly higher readings than gage 2 throughout the loading. The initial slopes of the stress-strain curves for gages 1, 2, and 3 are 51.1, 66.1, and 61.1 GPa, respectively. The slope of gages 2 and 3 is similar to the calculated modulus of 64.3 GPa. The behavior of the A specimen tested with this configuration is quite similar in that gage 1 consistently gives higher readings than gage 2 for the same stress level. A third strain gage was not used with this specimen. The initial slope of gage 1 for this specimen is 46.3 GPa, while that of gage 2 is 56.3 GPa. The slopes of both of these gages deviate from the calculated modulus of 52.7 GPa.

For specimens with strain gage configuration Notch 2, which is described in Chapter 5 and shown in Figure 5.21, the strain in the vicinity of the notch was measured as well as the far-field strain. All specimens testing with this configuration were small specimens. An example stress-strain plot for a specimen tested in this configuration is shown in Figure 6.12. Gages 1 and 2 measure the strain near the notch tip and therefore

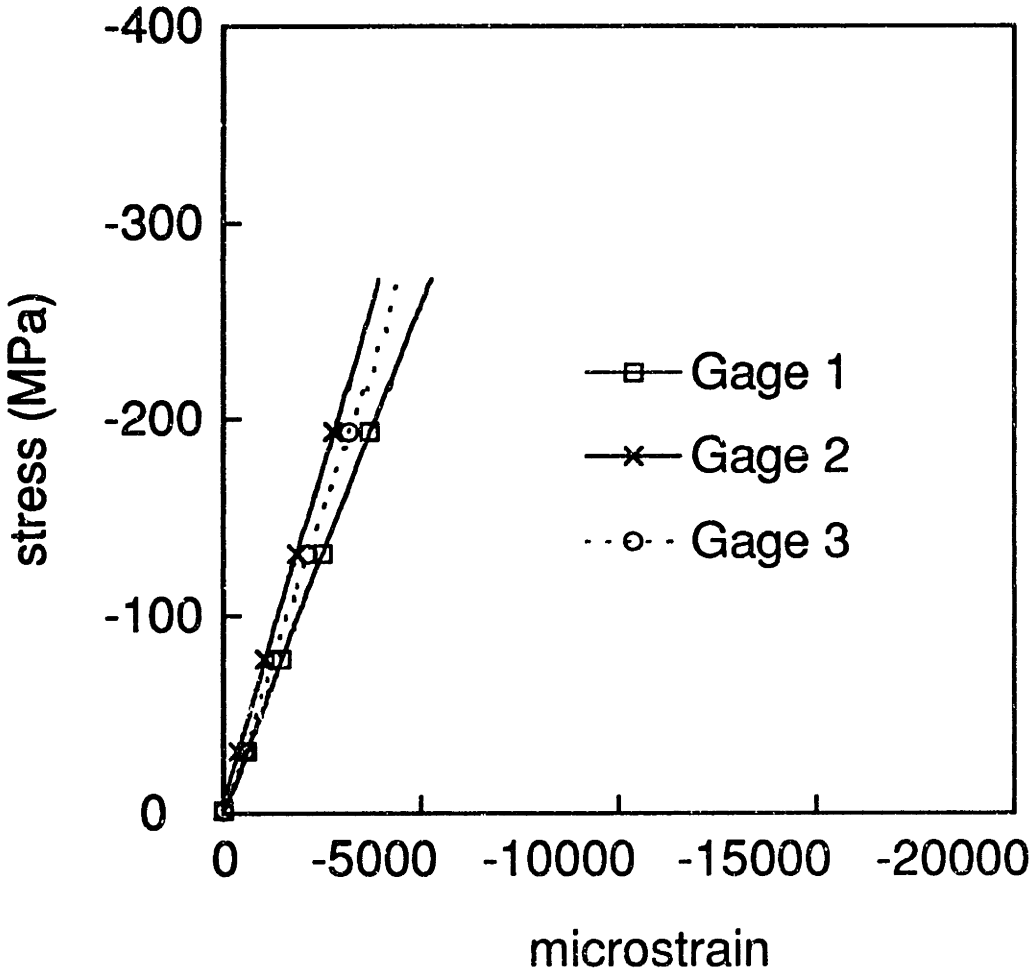

Figure 6.11 Representative plot of strain versus far-field applied stress for Notch 1 configuration (specimen B-S-SN13a).

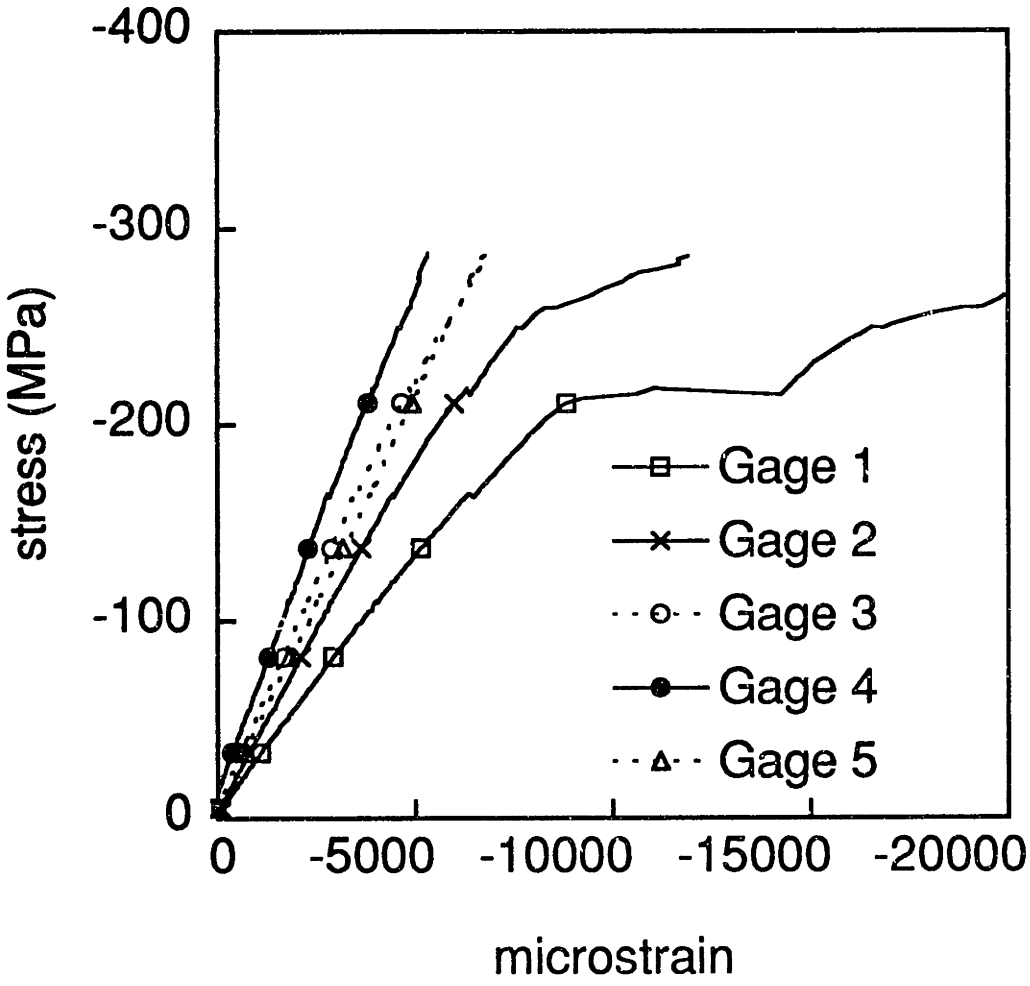

Figure 6.12 Representative plot of strain versus far-field applied stress for Notch 2 strain gage configuration (specimen A-S-SN10a).

record a higher level of strain than the other gages. At an applied stress lower than -200 MPa, the behavior of these gages is already nonlinear as they begin to behave erratically and the reading increases rapidly. This may be associated with damage in the notch region, or it may be due to damage to the gage. For the specimen shown, the reading for gage 1 goes above the scale of the recording device. The far-field gages, gages 4 and 5, behave in a more predictable manner, with strain increasing approximately linearly until failure. The reading for gage 5, located on the rough side facesheet, is generally higher than its counterpart on the smooth side facesheet, gage 4. The slope of gage 4 is 54.3 GPa and that of gage 5 is 42.3 GPa. This behavior is present in varying degrees in all of the specimens tested in the Notch 2 configuration. Finally, gage 3, which is located on the notch line halfway between the notch tip and the edge of the specimens gives readings similar to gage 5. In nearly all of the specimens tested with this configuration, the initial slope of this gage falls between the slopes of gages 4 and 5.

One specimen of the B layup tested with this gage configuration exhibited a highly nonlinear and unusual stress-strain behavior at a low stress level. A plot of the stress-strain readings for this specimen is shown in Figure 6.13. At an applied stress of about -50 MPa, the readings of the gages seem to branch into two paths. For the first branch, which includes gages 1 to 4, the gages indicate apparent stiffening of the specimen. Gages located adjacent to the notch tip (gages 1 and 2) give strain readings of the same level or lower than those of the far-field gages (gages 4 and 5). The cause of this behavior is unknown. The stress-strain behavior of this specimen is very different than the behavior of all other notched specimens and indicates that something unusual and unexplained occurred during

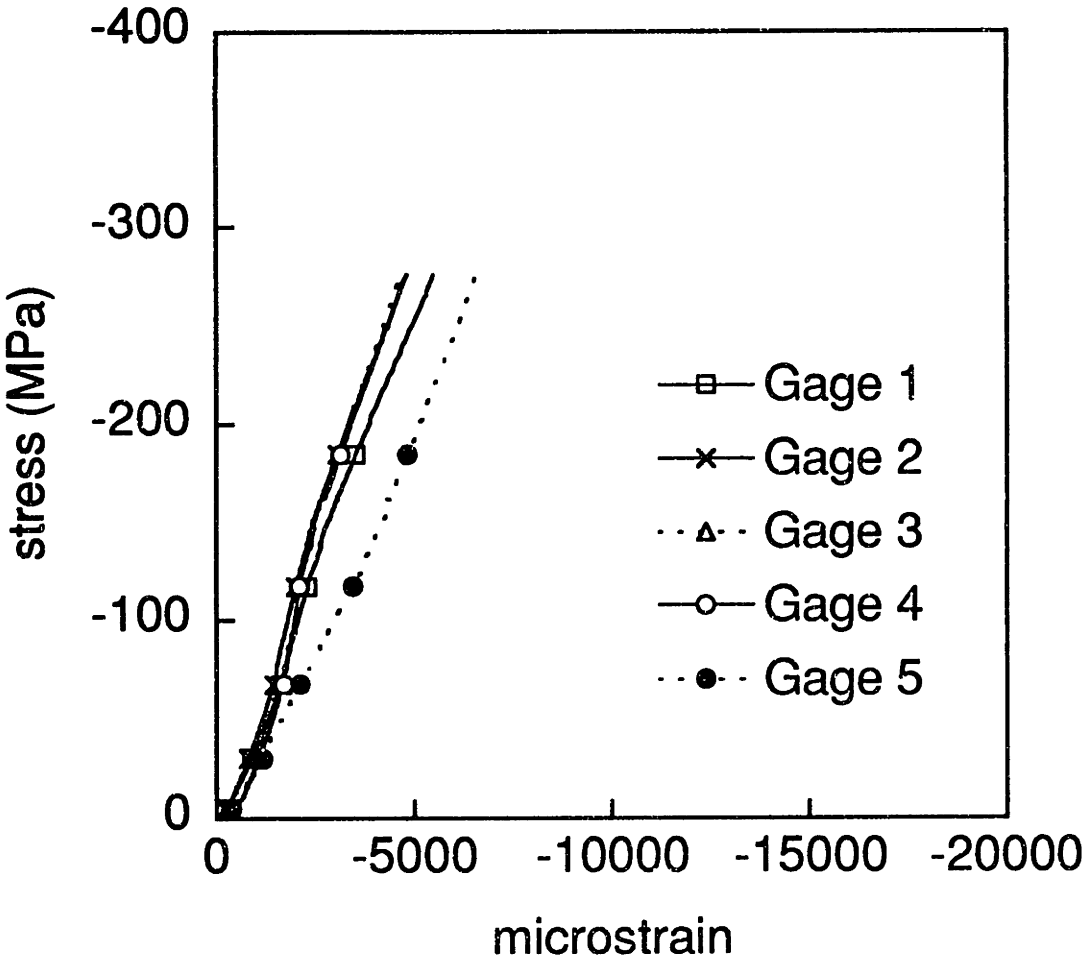

Figure 6.13 Plot of strain versus far-field applied stress for a specimen with Notch 2 strain gage configuration which exhibited highly nonlinear behavior at low stress levels (specimen B-S-DN6).

testing of this specimen. Therefore, the failure strength of this specimen is excluded from further failure analyses.

The far-field strain gages were intended to determine the modulus of the specimen and also to monitor any bending of the specimen. The average of the initial slopes of the stress-strain curves for the far-field gages 4 and 5, as well as the relative magnitude of their difference, is given in Table 6.10 for specimens tested in the Notch 2 strain gage configuration. In addition, the method used to align the fixture is given in Table 6.10. The majority of these specimens were tested after alignment with method 1. Two specimens did not have well-defined linear regions in their stress-strain curves, specimens B-S-SN6b and B-S-DN6. The first of these displayed nonlinear behavior different from all other specimens tested, as discussed previously in this section. During testing of the second of these, the potting material was observed to crack prior to specimen failure.

For all cases except one, which will be discussed in the following paragraph, the slope of the gage on the smooth side facesheet was higher than that of the gage on the rough side facesheet. The magnitude of this difference is not dependent upon the notch size, but this difference is less for specimens tested after alignment by method 2 than for method 1. The difference for method 1 specimens is 25 to 30%, while the difference for method 2 specimens is 10 to 18%. In general, the difference within the gage pair was less for the B specimens, but this may be due to the fact that more B specimens were tested after alignment method 2 was used.

In order to check whether the difference in readings of the far-field gages was always positive, specimen A-S-SN-10b was positioned differently in the test fixture. This specimen, although tested with the Notch 2 configuration of strain gages, was rotated 180° about the z-axis so that

Table 6.10 Average slopes and relative differences in slope for the far-field gages of specimens tested with Notch 2 strain gage configuration

Specimen	Alignment Method Used	Average Slope of Far-field Gages (GPa)	Percent Difference Between Gages
A-S-SN3a	1	49.7	+23.0[a]
A-S-SN3b	2	47.9	+9.6
A-S-SN6a	1	49.4	+23.7
A-S-SN6b	1	48.0	+29.4
A-S-SN10a	1	48.3	+24.8
A-S-SN10b	1	50.8	-31.5
A-S-SN13b	1	51.5	+34.8
B-S-SN3a	1	55.0	+24.5
B-S-SN6a	2	61.3	+10.4
B-S-SN6b	1	-[b]	-
B-S-DN6	2	-	-
B-S-SN10a	1	59.8	+24.1
B-S-SN10b	2	59.0	+16.8
B-S-SN13b	1	64.0	+16.9
B-S-DN13	2	54.7	+17.9

a Positive value indicates gage on smooth side facesheet has a greater slope than the gage on the rough side facesheet.
b Indicates no well-defined linear region of stress-strain curve existed.

gages 4 and 5 were located below the notch. Unlike all other specimens of the notch 2 configuration, this specimen displayed a higher slope for the gage on the rough side facesheet than for the gage on the smooth side facesheet.

The average slope of the far-field gages is 49.4 GPa for the A specimens, which compares quite well with the longitudinal modulus measured in the undamaged specimens of 50.2 GPa and is fairly close to the calculated modulus of 52.7 GPa. This suggests that the far-field behavior of the notched specimens is, in fact, the same as that of the unnotched specimens. The average slope of the far-field gages for the B specimens is 59.0 GPa for the B specimens, very close to the measured modulus of 58.1 GPa of the undamaged specimens. It should be noted that the calculated modulus for these specimens was 64.3 GPa, so the measured slopes for the notched B specimens fall between the measured and calculated moduli.

Because gage 1 is located next to the notch tip, it can serve as an indicator of the strain concentration of the notch. The strain concentration is the ratio of the slope of the far-field strain reading to the initial slope of gage 1. However, the measured strain at the notch tip is very sensitive to the exact placement of the gage, and thus the strain concentration cannot be accurately measured. Refer to Appendix D for the slopes of the stress-strain curves for gage 1.

The Notch 3 configuration is similar to Notch 2. The stress-strain plot for a representative specimen tested in this configuration is shown in Figure 6.14. Gage 0, located at the notch tip, experiences a much higher strain. The slight jaggedness is due to pauses in the test to allow photographs of the photoelastic coating to be taken. Gage 1, located adjacent to gage 0, also experiences a higher strain than the far-field gages.

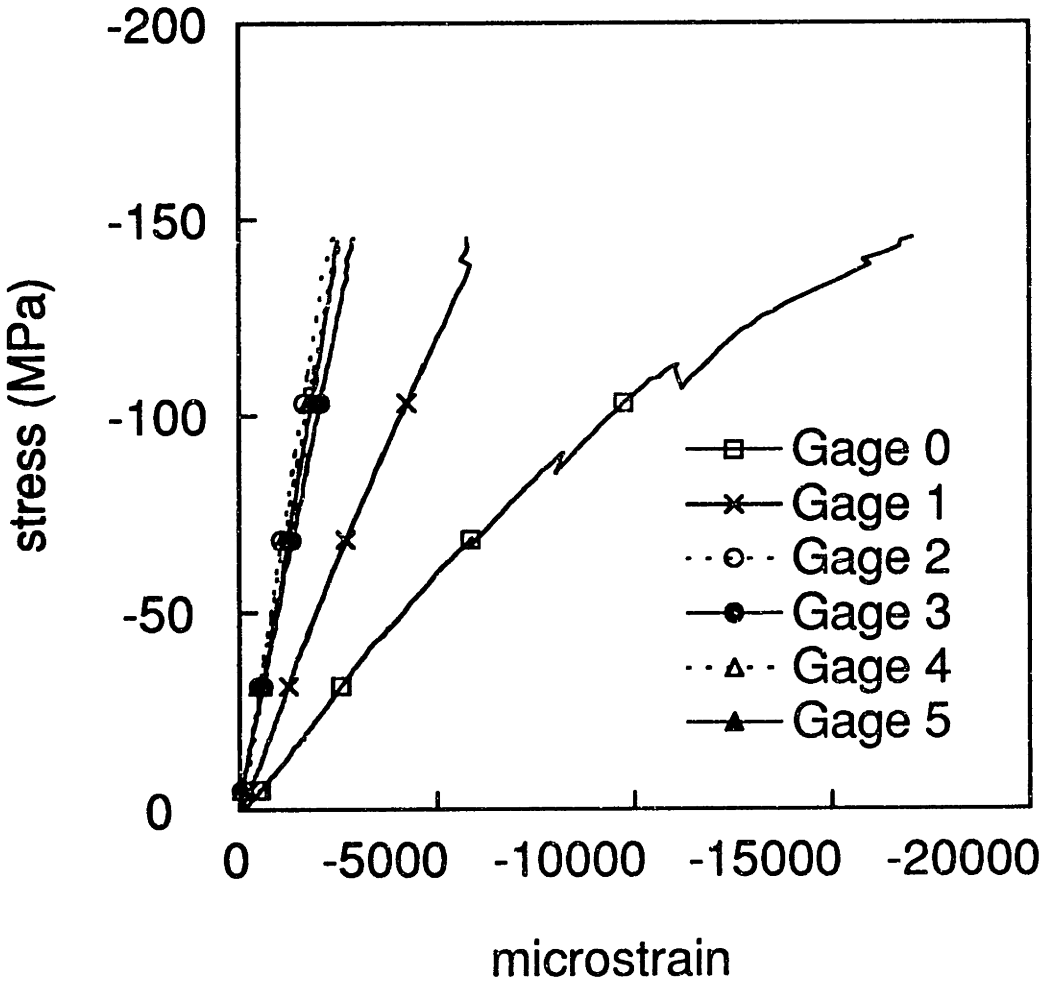

Figure 6.14 Representative plot of strain versus far-field applied stress for Notch 3 configuration (specimen B-M-DN51).

In this configuration, the far-field gages 2, 3, 4, and 5, are grouped together fairly well. The grouping of the far-field gages is generally better for the specimens tested in Notch 3 than in Notch 2. The average slopes of the two back-to-back pairs of far-field gages, as well as the relative differences of these slopes for specimens tested with this gage configuration, are shown in Table 6.11.

For specimens of the A layup, the average slope of gages 2 and 3 is 48.9 GPa, while the average for gages 4 and 5 is 48.2 GPa. These values are slightly lower than the measured modulus of 50.2 GPa for undamaged specimens and the average slope of 49.6 GPa for the far-field gages of notched specimens of strain gage configuration Notch 2. Nevertheless, the measured slopes agree well with each other. The only trend noted in slope is that the two large specimens with 25.4 mm notches display the highest slopes of all specimens. In general, the variation within the back-to-back pairs are smaller for specimens tested in this configuration than for those tested with Notch 2 gage configuration. Eight of nine specimens have a variation between the front and back of less than 10% for at least one back-to-back pair. Several specimens have a positive variation for one pair, and a negative variation for the other pair. There is a trend toward higher variation between gages as the notch length increases. However, given the small number of specimens, this observed trend is not a strong one. There is no detectable effect of specimen size as low and high variations are exhibited by all size specimens. It should be noted that all small and medium specimens with this configuration of gages were tested after the fixture had been aligned with method 2, while a visual alignment was used for all large specimens. The use of method 2 alignment seems to result in readings more closely matched in the back-to-back pairs.

Table 6.11 Average initial slopes of far-field gages and the relative difference between the slopes of each back-to-back pair for specimens tested with Notch 3 strain gage configuration

Specimen	Average Slope of Gages 2 & 3 (GPa)	Percentage Difference Between Gages 2 & 3	Average Slope of Gages 4 & 5 (GPa)	Percentage Difference Between Gages 4 & 5
A-S-DN3	47.5	+0.6[a]	42.2	+2.8
A-S-DN6	49.7	-1.6	47.1	+9.3
A-S-DN10	45.6	+11.6	44.1	-5.4
A-S-DN13	49.7	+9.5	45.8	+25.3
A-M-DN25	48.2	-3.3	46.1	0.0
A-L-SN25	51.6	+1.9	54.6	+5.3
A-L-DN25	51.9	+1.7	57.8	+6.2
A-M-DN51	48.8	+22.8	48.4	+20.5
A-M-DN76	47.0	-21.3	47.7	+4.6
B-S-SN3b	61.1	+8.8	62.4	+9.5
B-S-DN3	56.4	+12.8	60.3	+21.7
B-S-DN10	59.5	+6.7	54.4	+16.9
B-M-SN25	66.3	+6.0	57.1	+5.1
B-M-DN25	59.6	-9.2	55.0	+4.2
B-L-SN25	56.7	-2.3	72.9	+24.3
B-L-DN25	59.4	+12.1	62.5	-13.0
B-M-DN51	56.8	+25.7	57.9	-2.2
B-L-DN76	55.9	+16.3	54.2	-12.5

[a] Positive value indicates gage on smooth side facesheet has a greater slope than the gage on the rough side facesheet.

The specimens from the B layup had an average slope of 59.1 GPa for gage pair 2 and 3 and a slope of 60.6 for gage pair 4 and 5. These values are very similar to the average slope of 59.0 GPa for the specimens with Notch 2 gage configuration and the measured modulus of 58.1 GPa from the undamaged specimens. No dependence of slope on specimen or notch size is observed. Variation within the back-to-back pairs are greater for these specimens than for those of the A layup. Only six specimens have a pair with a variation of less than 10%. However, six of the nine specimens have a positive variation for one pair of gages and a negative variation for the other.

The strain concentration at the notch tip is inconsistently measured, as was the case with the specimens with notch 2 strain gage configuration. The strain measured by gage 0 is again quite sensitive to the exact placement of the gage relative to the notch tip. Strain at the notch tip is higher for specimens with notches of 25.4 mm and longer. The strain concentration of the notch is scaled according to the notch length. Because the size of the strain gage is constant, as the notch length is increased, the gage is effectively closer to the notch tip relative to the notch size and thus reads a higher strain. Refer to Appendix D for the slopes of the stress-strain curves for gage 0.

6.2.2 Photoelastic Images

Data recorded from the strain gages provided accurate readings of the strain over a small area. The photoelastic coatings provide a more qualitative view of the strain conditions in the specimens over a larger area, in most cases approximately half of one facesheet. As shown in Tables 6.6 and 6.7, twenty specimens were tested with a photoelastic coating.

Numerous pictures were taken of the patterns formed in the coatings during testing. Also, analytical calculations for the stress distribution around an elliptical hole are used to predict the type of strain patterns observed with the photoelastic coatings. Predictions and experimental results for the strain patterns are given in this section.

As discussed in Chapter 5, two pieces of information can be easily determined from the photoelastic technique. The first is the direction of the principal strains, which is determined using a plane polariscope as discussed in Chapter 5. In a specimen without a notch, the directions of principal strains should be aligned with the x and y directions in parts of the specimen away from boundaries. In the region of a notch, however, the uniform stress state is disrupted, and the directions of principal strains may not line up with the x and y directions. Due to the limitations of the photoelastic technique, only the region in which the principal strains were not aligned axially were determined. When the photoelastic coating is used for this purpose, the region in which the principal strains are not aligned with the axes has various colors, while the region where the strains are aligned is black.

The region in which the direction of principal strains differs from the x and y axes depends primarily on the size of the notch. It is not significantly affected by the load level, specimen size, or layup of the specimen. As the notch size is increased, the region grows. For example, when the notch size is increased from 3.81 mm, as shown in Figure 6.15, to 13.75 mm, as shown in Figure 6.16, the size of the region increases significantly. Despite this increased size, the region of non-aligned principal strains is still small compared to the size of the specimen.

The second piece of information which can be determined relatively

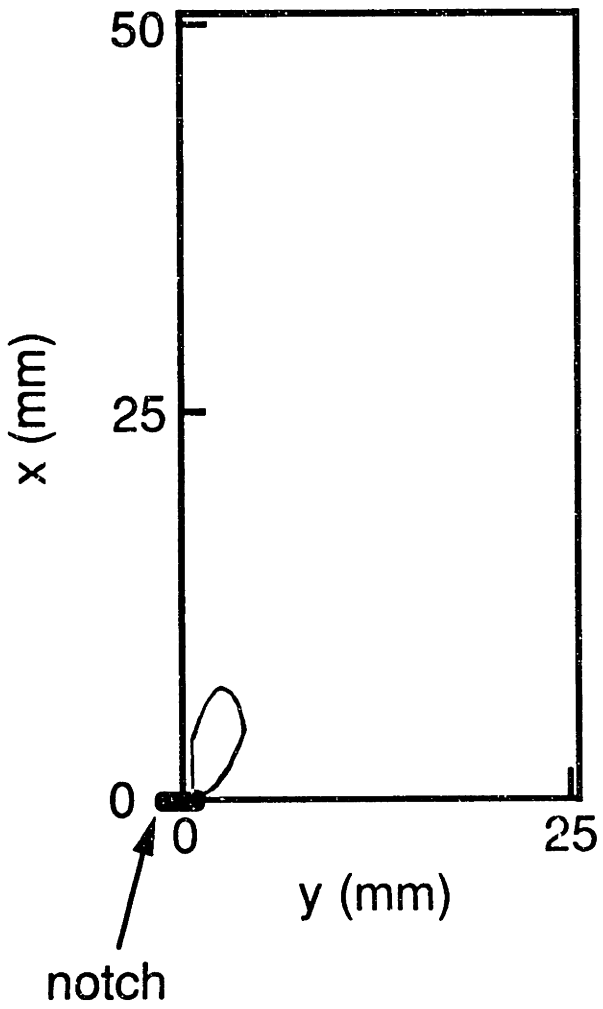

Figure 6.15 Sketch showing region in which principal strains are not aligned with the x and y axes in an A specimen with a 3.8 mm notch at an applied far-field stress of 162 MPa (specimen A-S-SN3a).

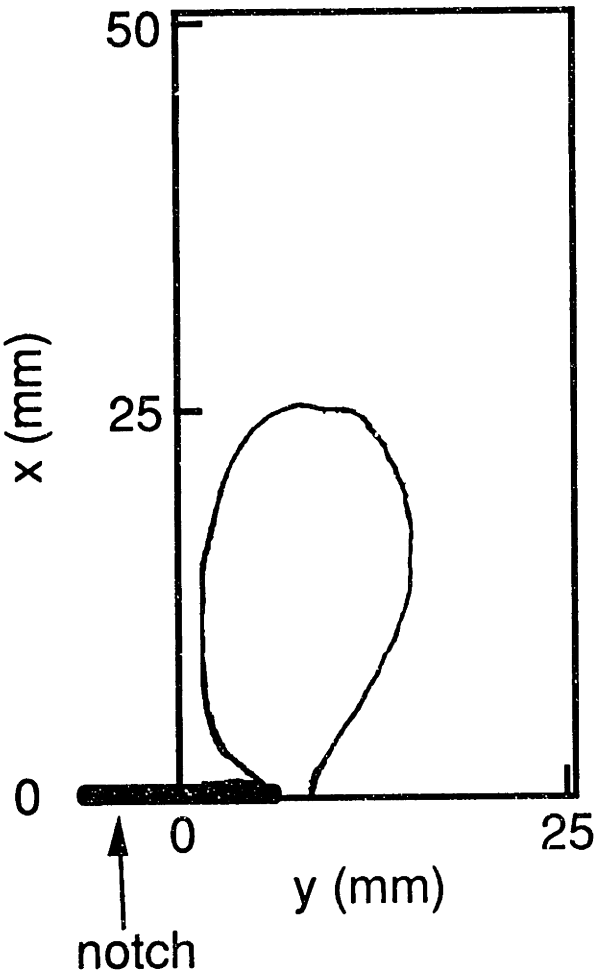

Figure 6.16 Sketch showing region in which principal strains are not aligned with the x and y axes in an A specimen with a 13.8 mm notch at an applied far-field stress of 162 MPa (specimen A-S-SN13a).

simply is the difference in principal strains, $\Delta\varepsilon$, in the region of the coating. This is accomplished using a different experimental setup called a circular polariscope. As detailed in section 5.3.1, the difference of the principal strains is proportional to the fringe order. The fringe order is related to the color of the coating. As described in Chapter 5, sketches of the colors of the coating were made. The regions of the different colors correspond to regions in which $\Delta\varepsilon$ is approximately constant. The differences in principal strain were also predicted using Lekhnitskii's solution for the stresses in a plate with an elliptical notch as described in Chapter 4. Contour plots of $\Delta\varepsilon$ were produced using the results of these calculations. In this case, the contour lines correspond to the points where $\Delta\varepsilon$ is equal to the value shown. The difference between the results of these two methods should be noted: the photoelastic technique provides regions in which the approximate value of $\Delta\varepsilon$ is known, while the prediction method yields regions in which the exact values of $\Delta\varepsilon$ are known at the boundaries. The numerical values and difference of $\Delta\varepsilon$ between each contour may not be the same for the predicted and observed contour plots. Contours for the predicted plots have a constant difference of strain value between them, but the observed contours depend upon the colors of the photoelastic coating, which are not evenly spaced as indicated in Table 5.2.

An important difference between the predicted and the observed strain patterns should be noted. An ellipse is used in the prediction of the pattern, but the specimens tested have slits with parallel sides and rounded corners. While the lengths and widths of the ellipse and the slit are the same, the shape of the end of the notch is different for the two. Thus, predicted and experimental patterns cannot be expected to match exactly.

During testing, an unusual feature was noted using the photoelastic

technique: the strain in the specimen varies in a pattern which corresponds to the shape of the honeycomb core. This was observed as a color pattern in the coating which resembled the honeycomb. The difference of principal strains, $\Delta\varepsilon$, was observed to be greater in the region of the facesheet adjacent to the center of the honeycomb than in the region adjacent to the honeycomb walls. The variation is more pronounce in the vertical direction than in the horizontal direction. It is difficult to measure the variation, but null compensation measurements of an A specimen were used to estimate it as 15% at a far-field stress level of 162 MPa, to 25% at a far-field stress level of 215 MPa. This variation is always present, though it is more visible at higher strain levels. Thus, it is observed to be stronger in the small specimens because they generally sustained a higher stress level than the medium and large specimens. In addition to the possibility that this variation increases as the stress level increases, the variation of $\Delta\varepsilon$ is more likely to create a difference in colors in the coating at high stress levels. This pattern can be seen in some sketches of photoelastic patterns from small specimens as an irregular boundary to the regions. In these sketches, the cell wall pattern could be captured without losing the nature of the plot. In others, the pattern was smoothed during the sketching process to simplify the plots.

The patterns of $\Delta\varepsilon$ for small specimens from experiment and analysis are given for a far-field stress level of -162 MPa (23.4 ksi). This stress level was chosen so that good quality images of the patterns existed along with compensation measurements for all specimens of interest. Patterns for the four notch sizes, 3.2 mm, 6.4 mm, 9.5 mm, and 12.7 mm are given for each of the layups, A and B. In predictions for the small specimens, [illegible] of the length of the major axis of the ellipse) is set to correspond to half of the

nominal notch length, while a (half of the length of the minor axis of the ellipse) is set to be 0.5 mm to correspond to half the notch width for these tests.

The characteristic pattern observed from the analytical and experimental results is a region of low strain above the notch, and a "lobe" of high strain which comes off of the notch tip at an angle of about 45°. In specimens for which the coating goes close to the potting line, a region of high strain differential is noted where the edge of the specimen meets the potting line. Also, a region of low strain differential is noted in the center of the specimen along the potting line. When examining the predicted and observed strain fields, one must also keep in mind that the values of strain given for the region very close to the notch may be inaccurate. For the analytical patterns, this is because the data points are too coarse in the notch tip region to produce accurate contours. Coarseness or jaggedness of the predicted contours is also the result of this coarse grid of data points. The data points used are exact, but the interpolation cannot be done accurately without sufficient points. For the experimental patterns, the difficulty is in tracing the boundaries of very small regions. Rather than attempt this, the region around the notch is left less detailed.

Symmetry about the vertical (loading) axis was observed in the tests of specimens with 12.7 mm notches. An example of the pattern from such a specimen is shown in Figure 6.17. Small differences exist between the patterns to the right and left of the x-axis, but, considering that there are sometimes no distinct boundaries between colors, they are very similar. Thus, remaining specimens were tested with the coating on only one side of the vertical centerline.

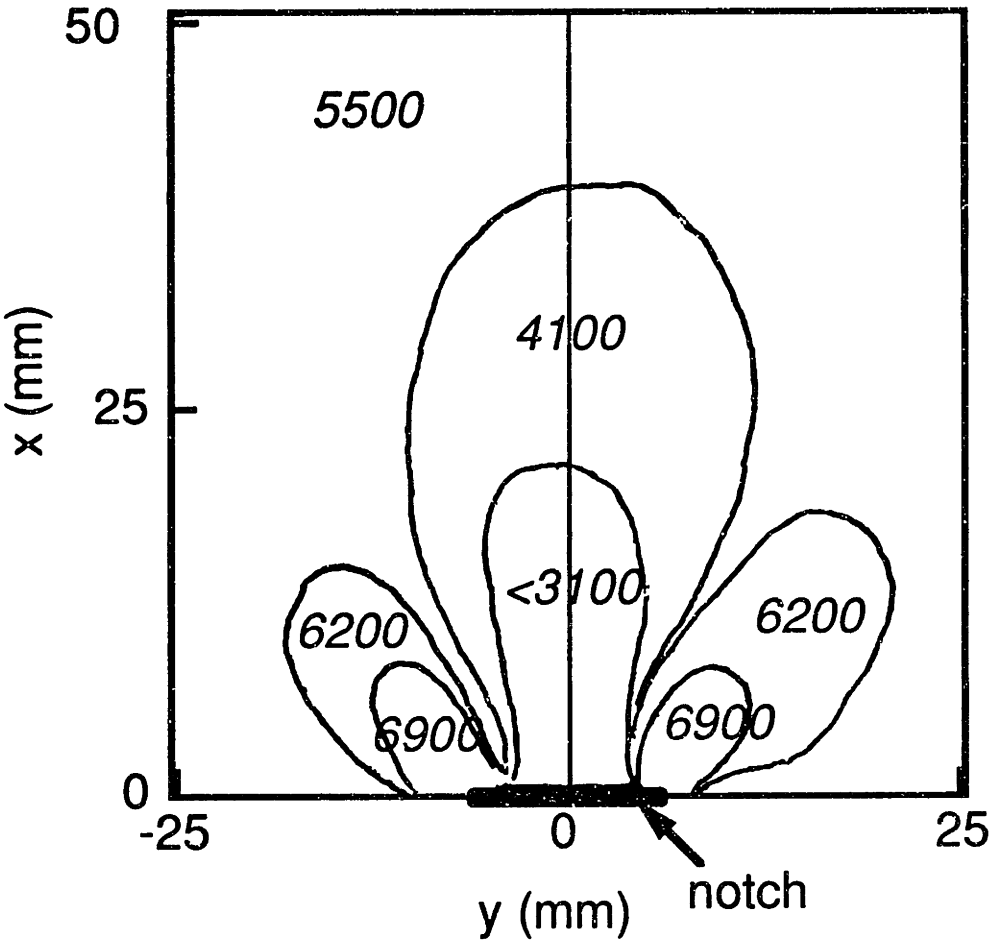

Figure 6.17 Experimental contour plot of the difference in principal strains which shows symmetry about the vertical axis of the specimen (specimen A-S-SN13a).

Symmetry was also observed about the horizontal axis of all specimens. An example of this symmetry is shown in Figure 6.18. For this specimen, the regions above and below the notch are very similar to each other. Likewise, the region of high strain differential to the right is nearly the same on both sides of the y-axis. The irregular boundaries of these regions are caused by the cell wall pattern. Away from the notch, a far-field area develops. However, within this area, several colors (which correspond with different levels of $\Delta\varepsilon$) exist as a result of the cell wall pattern. Thus, it is difficult to say what the strain differential level for this region is. In addition, a subtle gradient can be detected as the strain differential level increases as the value of x decreases. At about the centerline, a transition region exists as the coating color changes from blue-green and green-yellow above the notch line to blue-green, green-yellow, and orange below the notch line. Such a gradient is present in varying degrees in all specimens. For the small specimens, the gradient is always negative, i.e. strain levels increase as x decreases. For the medium and large specimens, the gradient is less noticeable and is generally positive, i.e. strain levels increase as x increases. The gradient is not due to the notch, but rather to some structural response of the specimen. However, the gradient can affect the strain patterns observed, and this should be kept in mind when examining the experimental patterns. Bearing in mind the existence of the gradient and its effects on the photoelastic patterns, the observed patterns are symmetric about the horizontal centerline. Thus, the pattern is given for only quadrant of each specimen's smooth side facesheet.

The patterns shown in this section are representative of the patterns present at other loads. To illustrate this point, the strain pattern in a medium specimen of the A layup is shown in Figures 6.19, 6.20, and 6.21 at

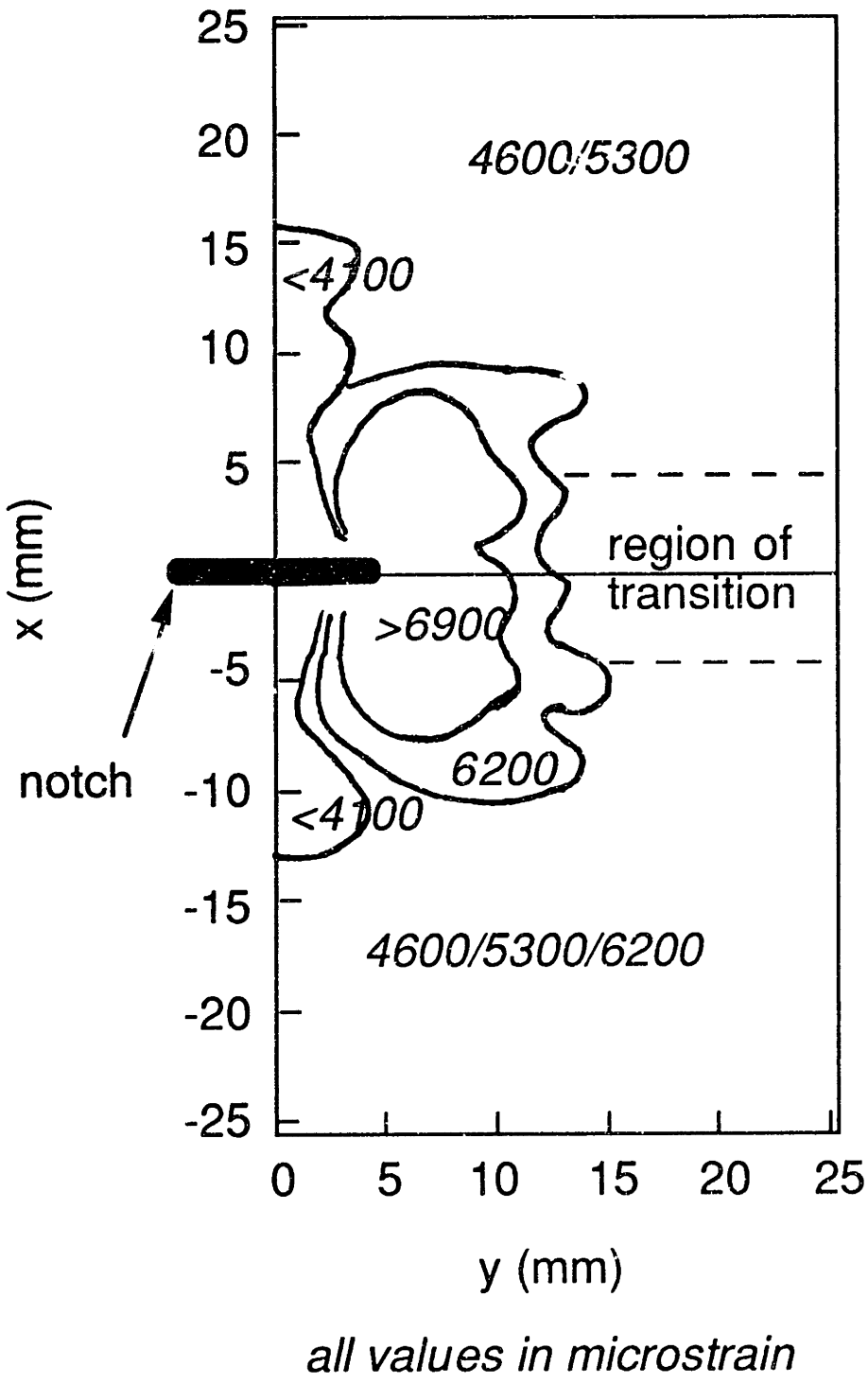

Figure 6.18 Experimental contour plot of the difference in principal strains which shows symmetry about the horizontal axis of the specimen (specimen A-S-SN9a).

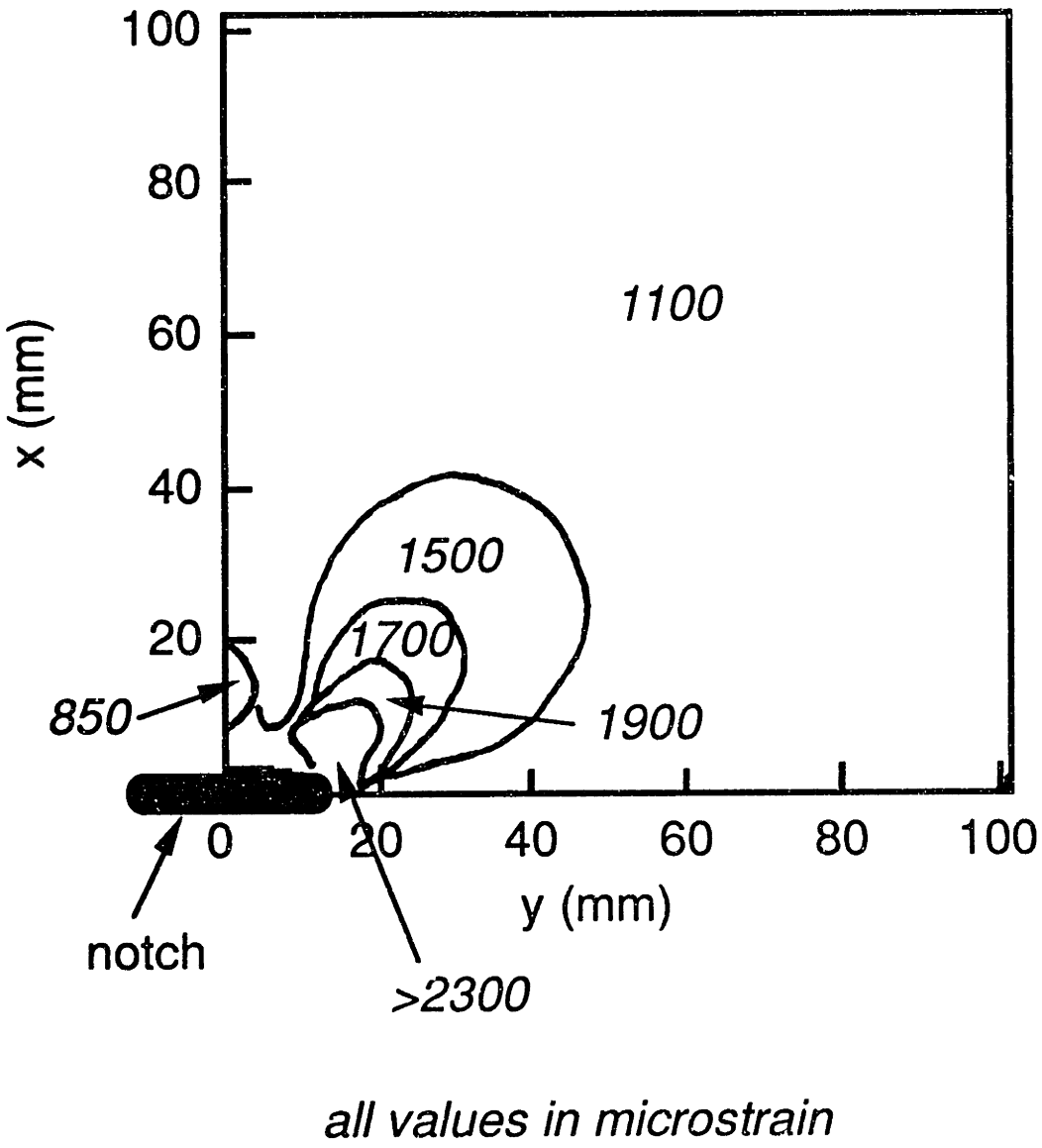

Figure 6.19 Experimental contour plot of the difference in principal strains, determined via the photoelastic technique, for a medium A specimen with a 25.9 mm notch at a far-field stress level of -45 MPa (calculated far-field value of $\Delta\varepsilon$ is 980 $\mu\varepsilon$) (specimen A-M-DN25).

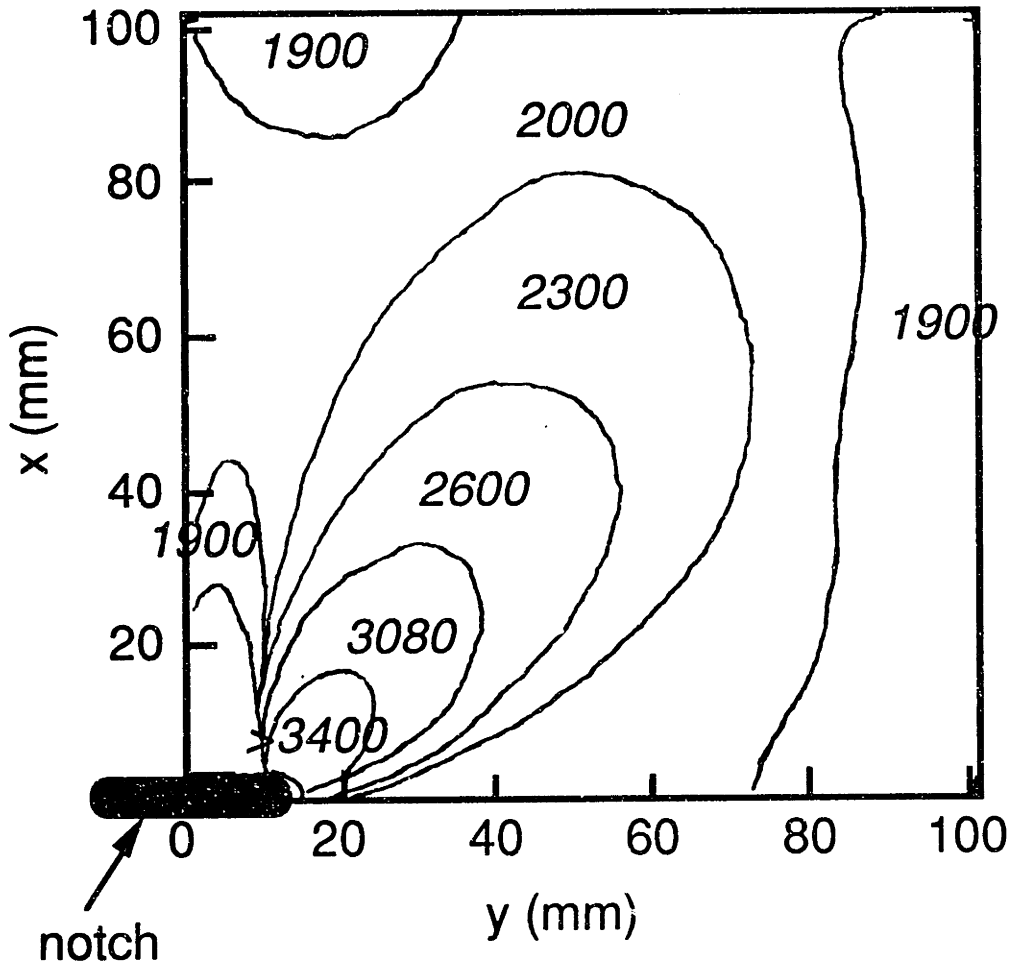

Figure 6.20 Experimental contour plot of the difference in principal strains, determined via the photoelastic technique, for a medium A specimen with a 25.9 mm notch at a far-field stress level of -90 MPa (calculated far-field value of $\Delta\varepsilon$ is 1950 $\mu\varepsilon$) (specimen A-M-DN25).

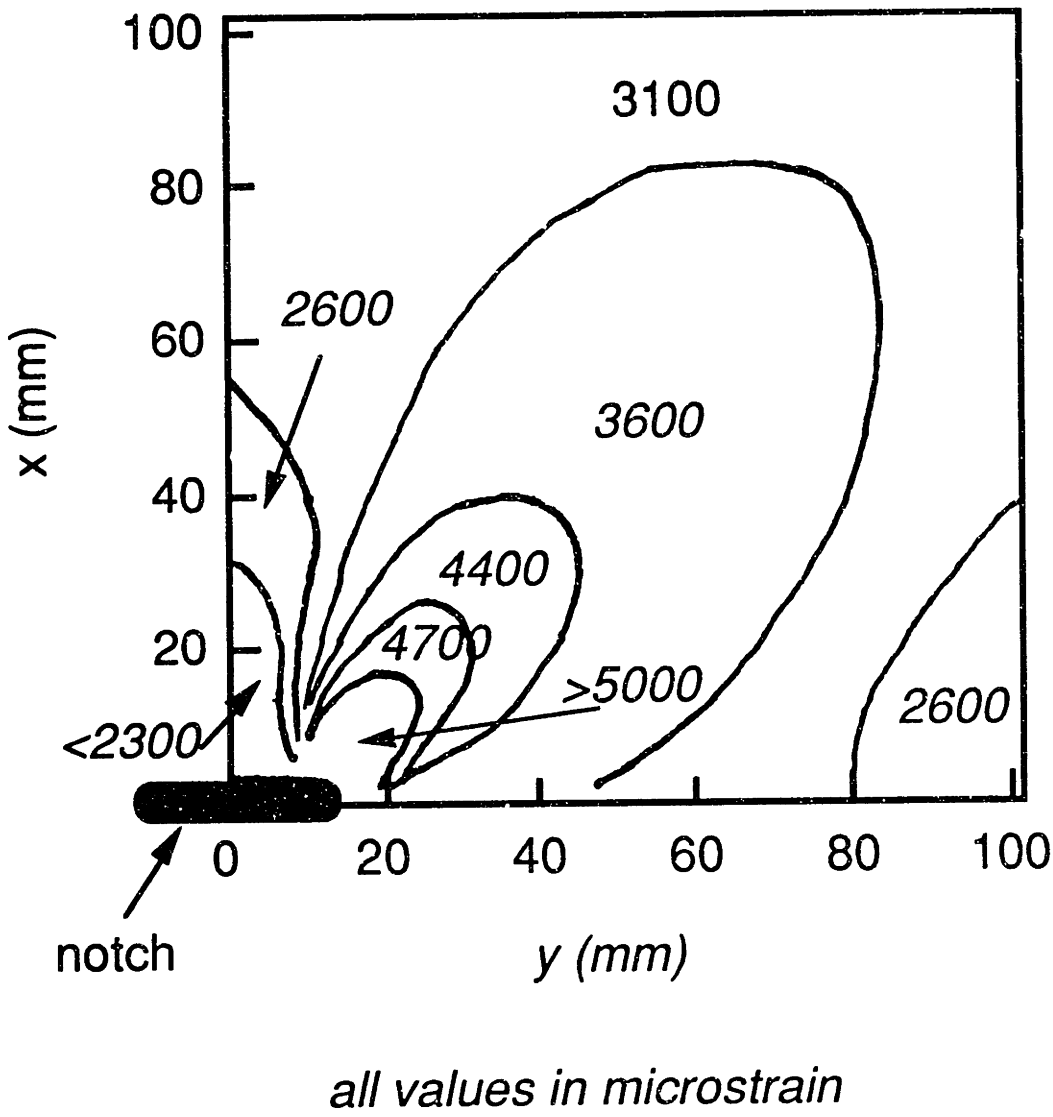

Figure 6.21 Experimental contour plot of the difference in principal strains, determined via the photoelastic technique, for a medium A specimen with a 25.9 mm notch at a far-field stress level of -135 MPa (calculated far-field value of $\Delta\varepsilon$ is 2930 $\mu\varepsilon$) (specimen A-M-DN25).

progressively increasing stress levels of -45, -90, and -135 MPa, respectively. Typical strain differential levels away from the notch are 1100, 2000, and 3100 μstrain for the three stress levels. Thus, strain differential away from the notch increases linearly with the applied far-field stress. The strain differential levels within the lobes also increases approximately linearly with the far-field stress. For example, consider the point 30 mm in the x and y directions. This point lies well within the lobes in all three sketches. It lies in the region where the typical strain level is 1500, 3080, and 4400 μstrain for the three stress levels, respectively. It appears that the strain increases linearly with stress in the lobe region as well for the case considered. As the overall strain differential level increases, more contours will come into existence. This can be seen by comparing the lobe size between Figures 6.19 and 6.20. The size of the outer contour of the lobe increases substantially because the overall strain differential has increased, resulting in more contours being represented. However, in Figures 6.20 and 6.21 the outer contours of the lobe regions are about the same size. The colors which are seen change, but the regions and their magnitudes relative to each other remain about the same. The patterns may be less linear for stresses higher than these examined, as would be the case with the small specimens. The predicted patterns, of course, are elastic. Thus, the predicted plots differ only by a constant from any other stress level.

The predicted and experimental patterns for an A specimen with a 3.2 mm notch are given in Figures 6.22 and 6.23. In the experimental pattern, a gradual change occurs at about 10 mm above the notch line. The change seems to be influenced by the in-plane gradient of the strain differential level. However, due to the cell wall pattern, it is impossible to determine exactly where the transition occurs. Thus, a dashed boundary is

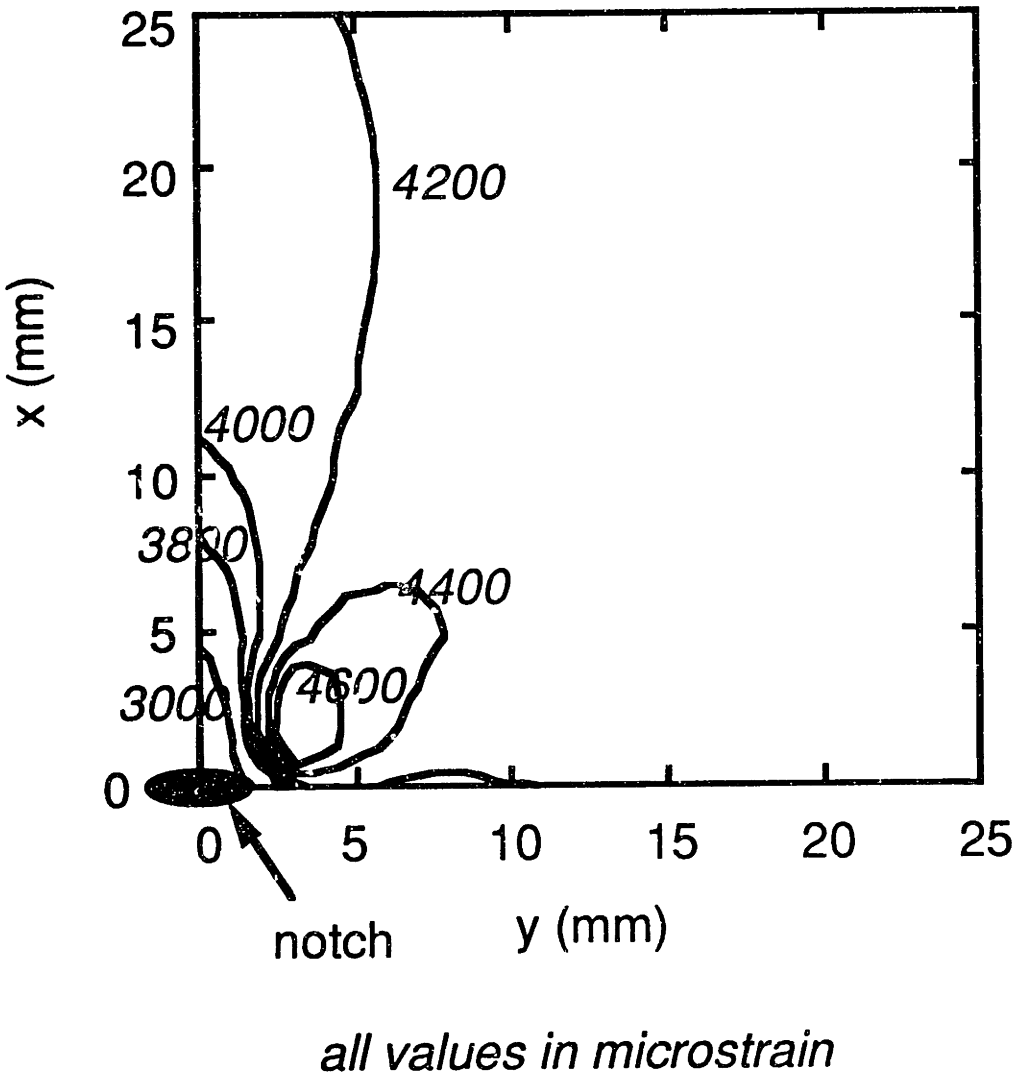

Figure 6.22 Predicted contour plot of the difference in principal strains for an A specimen with a 3.2 mm notch at a far-field stress level of -162 MPa (calculated far-field value of $\Delta\varepsilon$ is 4240 $\mu\varepsilon$).

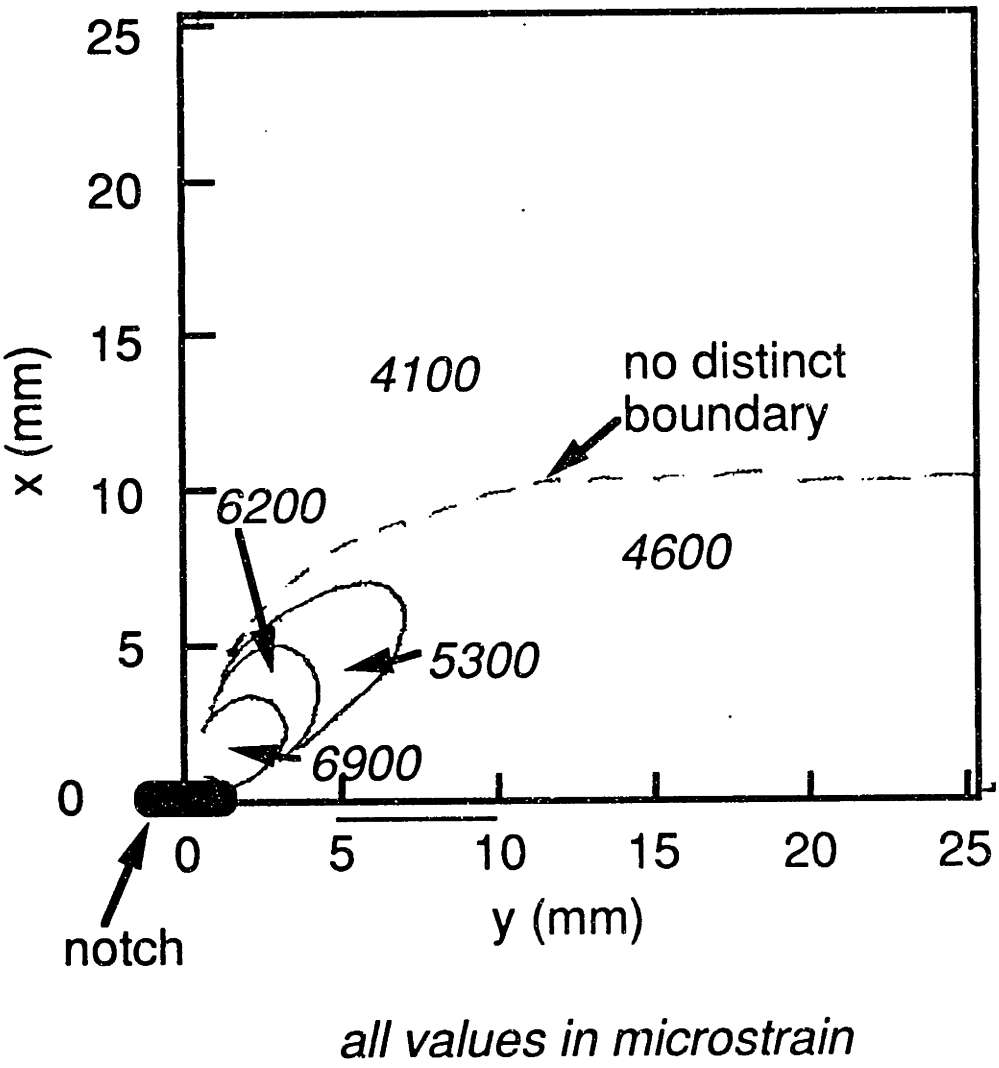

Figure 6.23 Experimental contour plot of the difference in principal strains, determined via the photoelastic technique, for a small A specimen with a 3.8 mm notch at a far-field stress level of -162 MPa (specimen A-S-SN3a).

shown between the two regions. The strain differential values away from the notch from experiment and analysis agree well. Also, the size and shape of the lobes from the notch tip is about the same. However, the measured strain differentials in the lobes are substantially higher than predicted. In addition, no region of lower strain above the notch was detected experimentally.

The predicted and experimental patterns for an A specimen with a 6.4 mm notch are given in Figures 6.24 and 6.25. Again, a gradual change obscured by the cell wall pattern is observed and shown as a dashed boundary. This gradual change is due primarily to the gradient discussed previously. The observed and predicted strain differentials away from the notch agree relatively well and are within approximately 10% of each other. For this case, a region of low strain differential is observed above the notch which is similar in size and strain magnitude to that predicted. The observed and predicted lobes from the notch tip are also of similar size. However, the observed pattern is more rounded and does not come back toward the notch on the bottom. Also, the observed strain differentials are again substantially higher than predicted.

The predicted and experimental patterns for an A specimen with a 9.5 mm notch are given in Figures 6.26 and 6.27. In this case, the observed cell wall pattern is especially pronounced with regard to the three outer region boundaries, resulting in wavy, irregular boundaries. The strain differentials away from the notch agree well with predictions. Also, the region of low strain differential above the notch agrees well with prediction. However, the lobes from the notch tip are again more rounded and are larger than predicted. They also have substantially higher values of strain differential. In fact, one could potentially interpret the region of strain

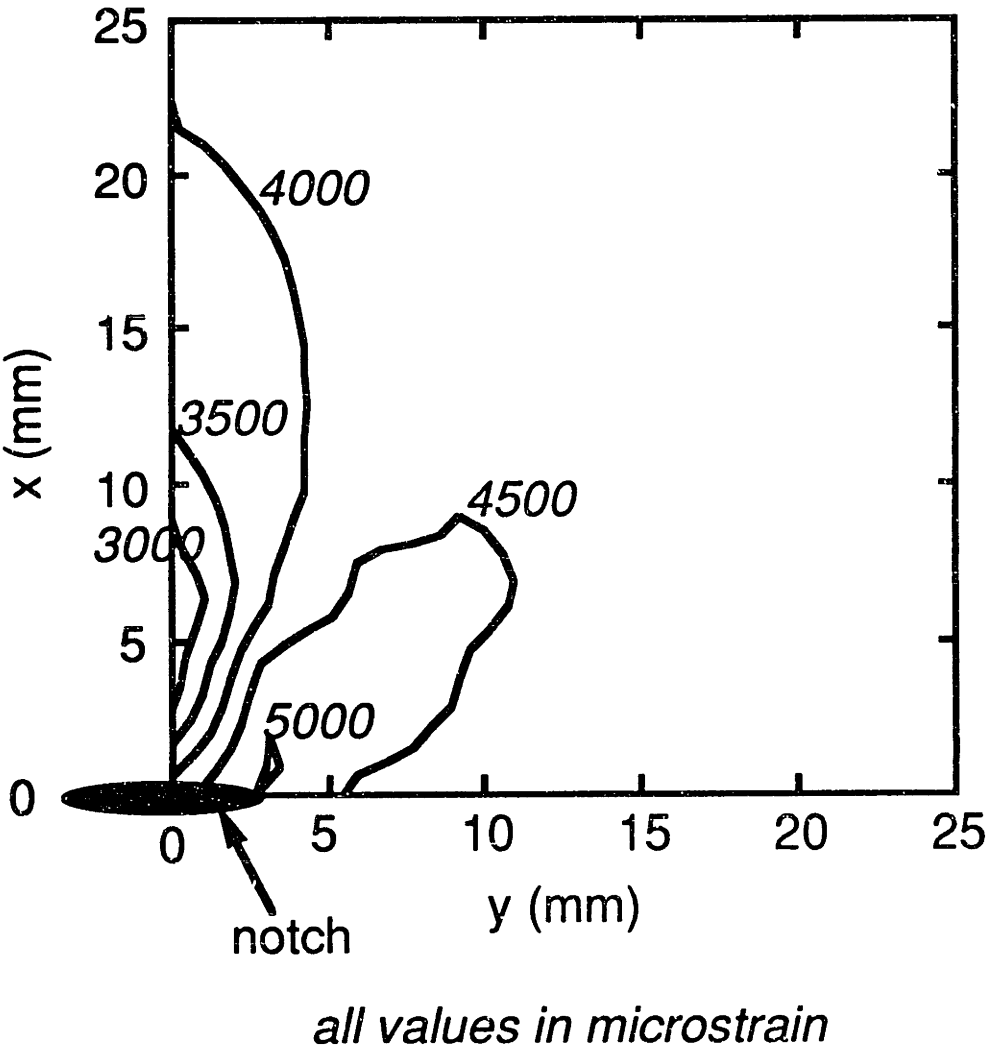

Figure 6.24 Predicted contour plot of the difference in principal strains for an A specimen with a 6.4 mm notch at a far-field stress level of -162 MPa (calculated far-field value of $\Delta\varepsilon$ is 4240 $\mu\varepsilon$).

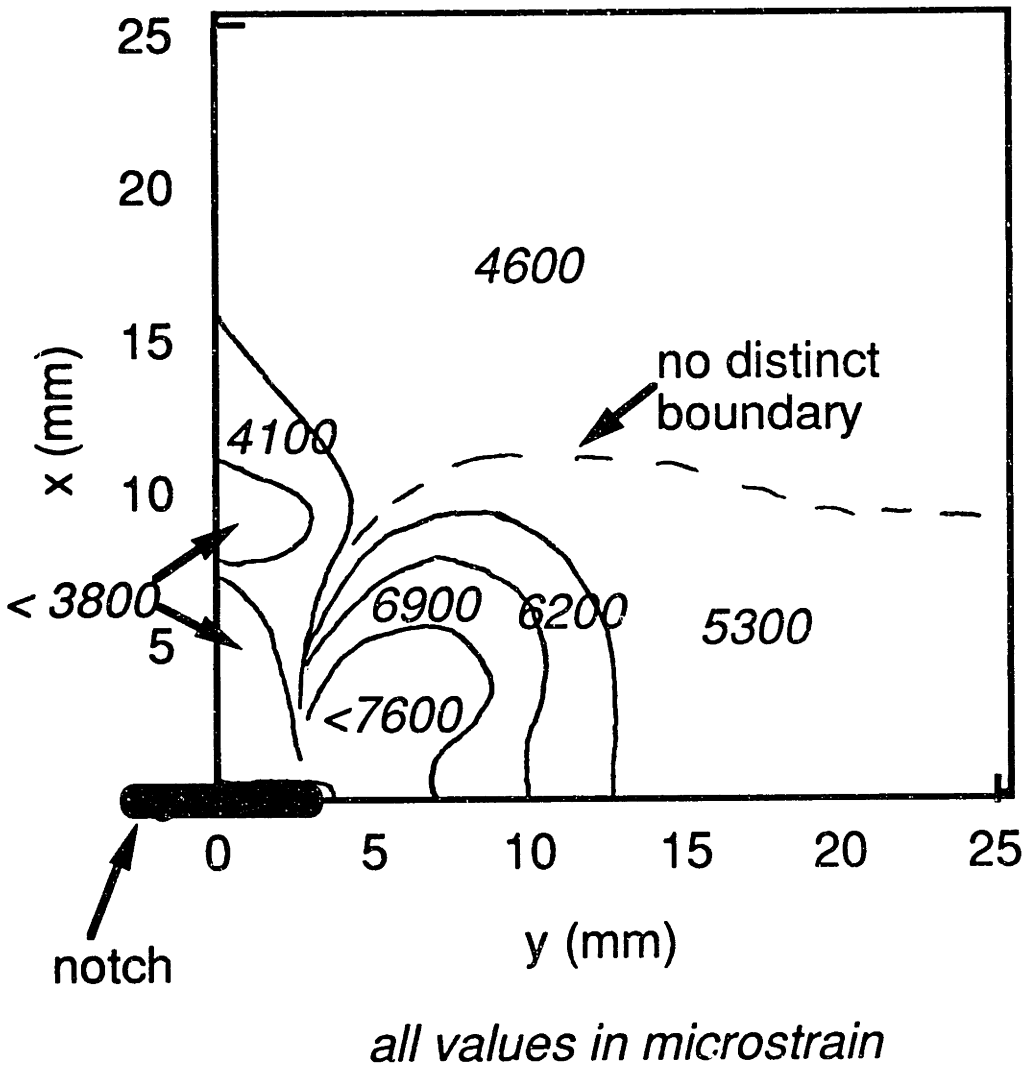

Figure 6.25 Experimental contour plot of the difference in principal strains, determined via the photoelastic technique, for a small A specimen with a 6.5 mm notch at a far-field stress level of -162 MPa (specimen A-S-SN6a).

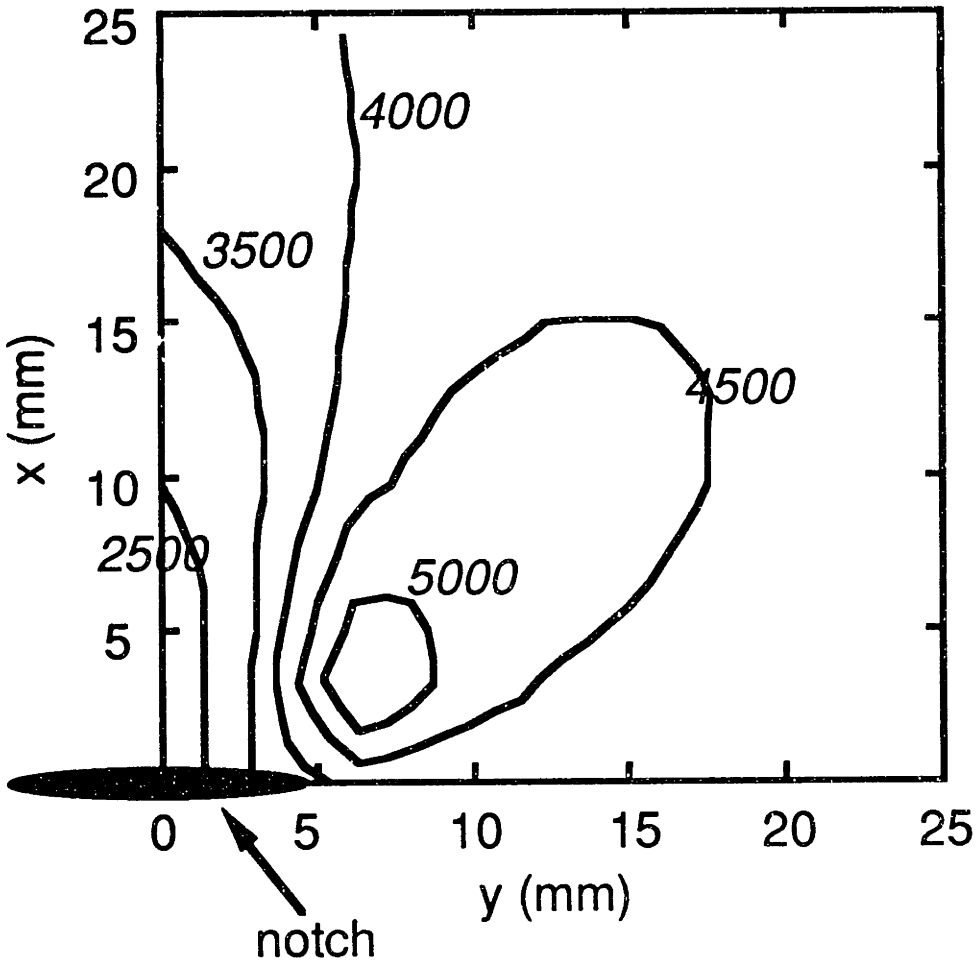

Figure 6.26 Predicted contour plot of the difference in principal strains for an A specimen with a 9.5 mm notch at a far-field stress level of -162 MPa (calculated far-field value of $\Delta\varepsilon$ is 4240 $\mu\varepsilon$).

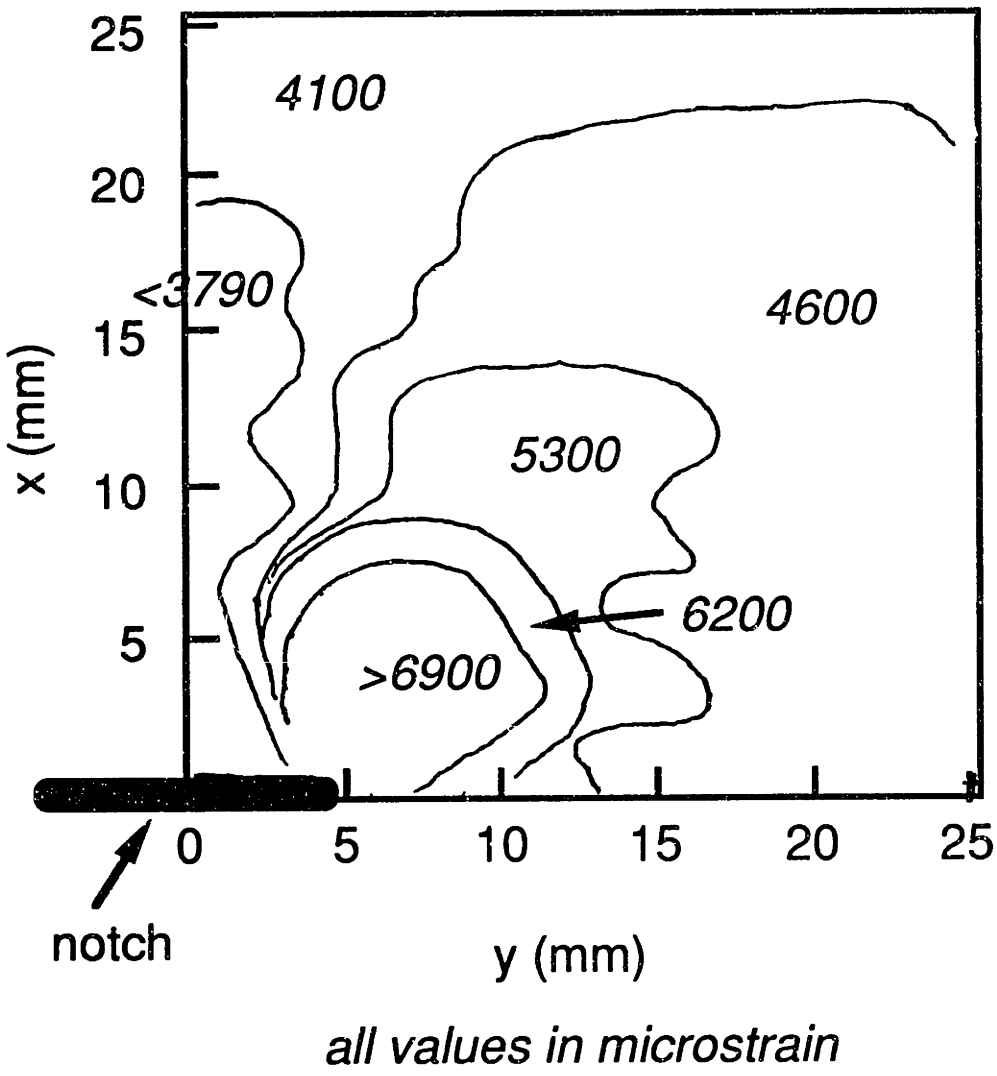

Figure 6.27 Experimental contour plot of the difference in principal strains, determined via the photoelastic technique, for a small A specimen with a 9.6 mm notch at a far-field stress level of -162 MPa (specimen A-S-SN10a).

differential designated by the value 4600 μstrain to be a lobe which has grown to meet the edge of the specimen. More likely, it is the far-field region as was the case for the specimen with the 6.4 mm notch.

The predicted and experimental patterns for an A specimen with a 12.7 mm notch are given in Figures 6.28 and 6.29. The strain differential away from the notch is higher for this specimen than for the other small notched A specimens, which may be a result of the lower resolution coating used with this specimen. The observed pattern agrees quite well with the prediction for the size of the lobes and the region above the notch. Agreement is also good concerning the magnitude of strain differential above the notch. However, the observed strain differential around the notch is again substantially higher than predicted.

Strain field predictions and measurements were also made for the medium and large notched specimens. For these specimens, the variable b is again set to half of the nominal notch length, while a is set to 2.5 mm to correspond to half of the nominal notch width. Stress levels for the strain fields shown for these specimens are substantially lower than the stress level in the small specimens. This is because of the lower strength of the specimens as the notch length increases. Strain differential fields for medium specimens with 25.4 mm and 50.8 mm notches are shown for a far-field stress level of -90 MPa, while large specimens with 76.2 mm notches are shown for a far-field stress level of -96 MPa.

The predicted and experimental patterns for a medium A specimen with a 25.4 mm notch are shown in Figures 6.30 and 6.31. For the specimen with a the 25.4 mm notch, a region of slightly lower $\Delta\varepsilon$ exists along the right side of the specimen. This region probably exists because the coating used on this specimen was more sensitive than that used on other specimens, and

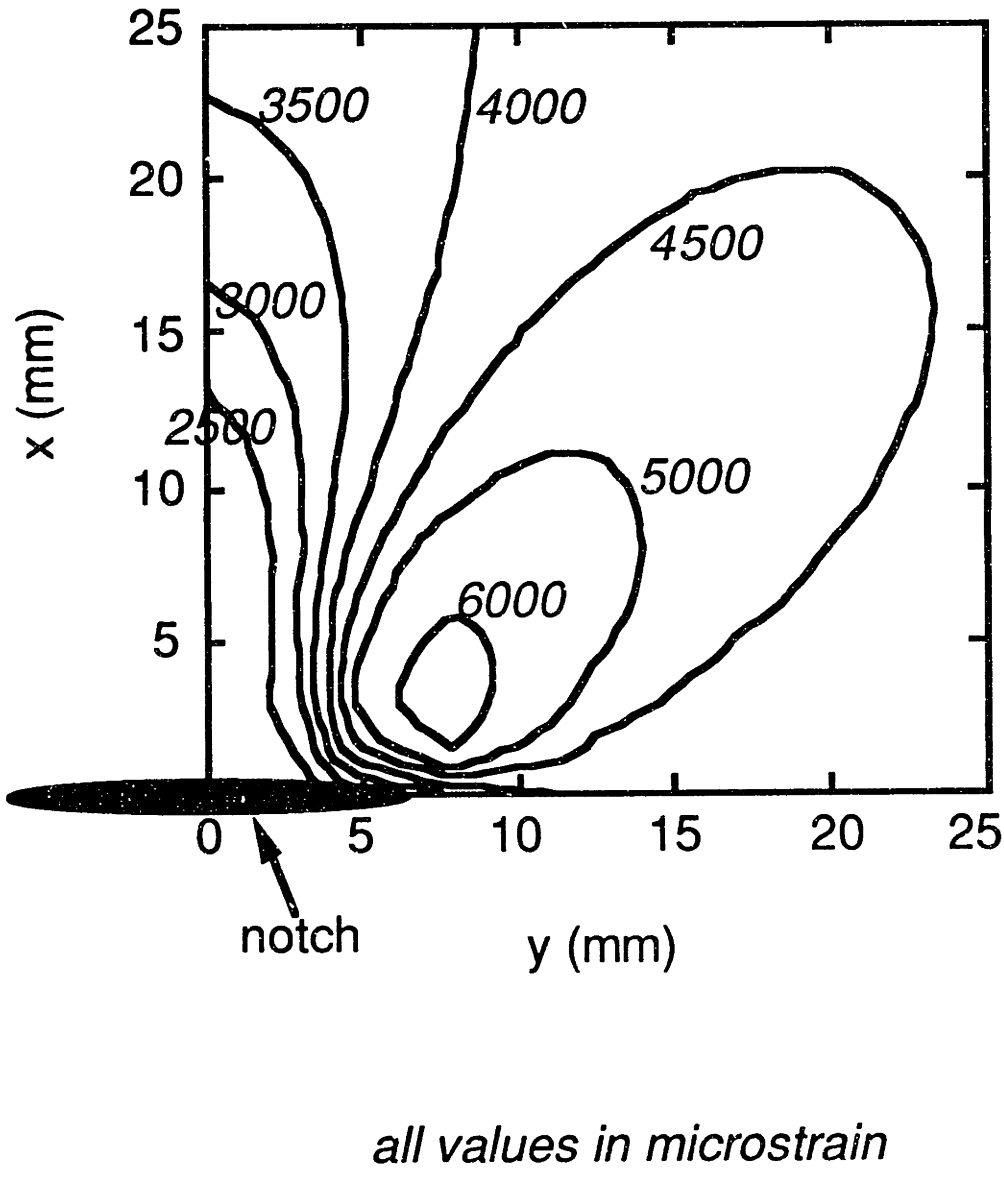

Figure 6.28 Predicted contour plot of the difference in principal strains for an A specimen with a 12.7 mm notch at a far-field stress level of -162 MPa (calculated far-field value of $\Delta\varepsilon$ is 4240 $\mu\varepsilon$).

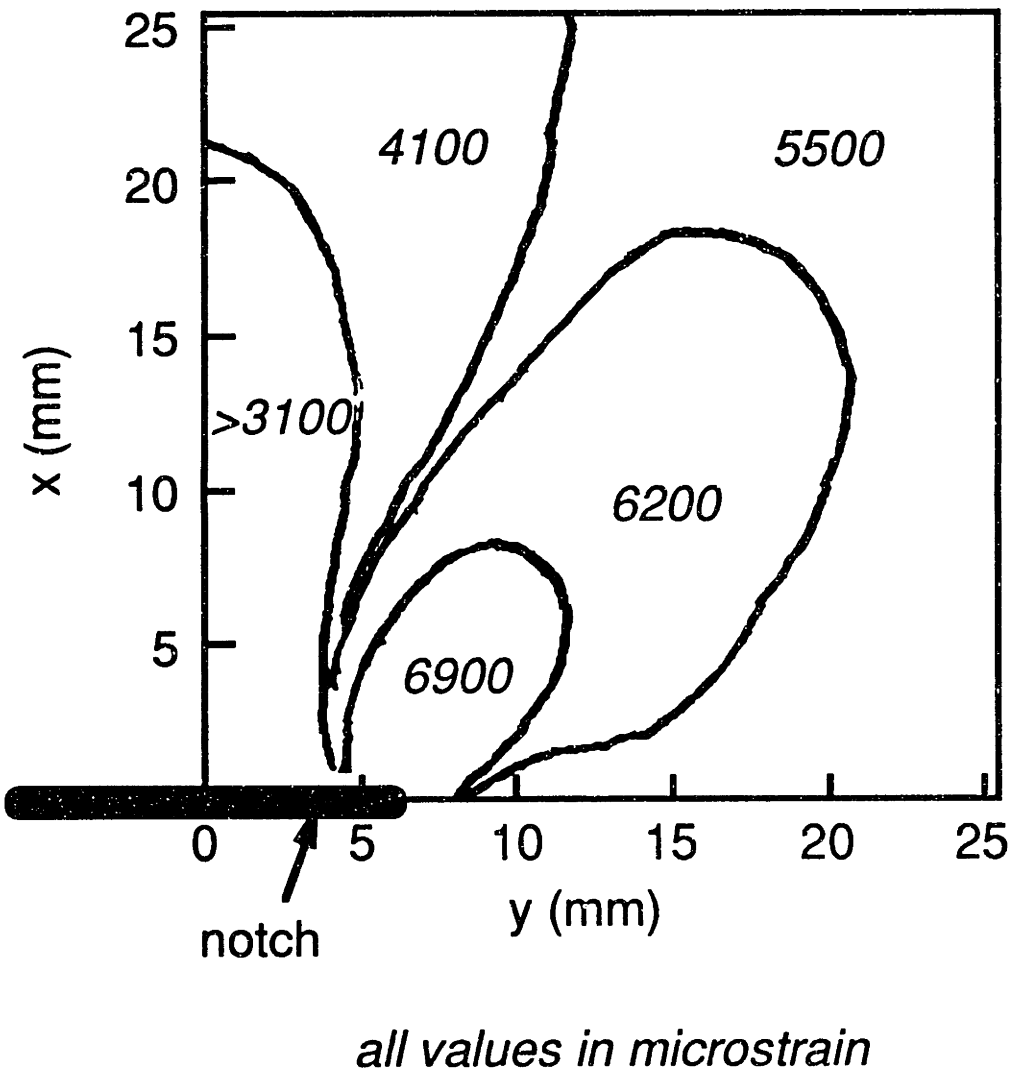

Figure 6.29 Experimental contour plot of the difference in principal strains, determined via the photoelastic technique, for a small A specimen with a 12.8 mm notch at a far-field stress level of -162 MPa (specimen A-S-SN13a).

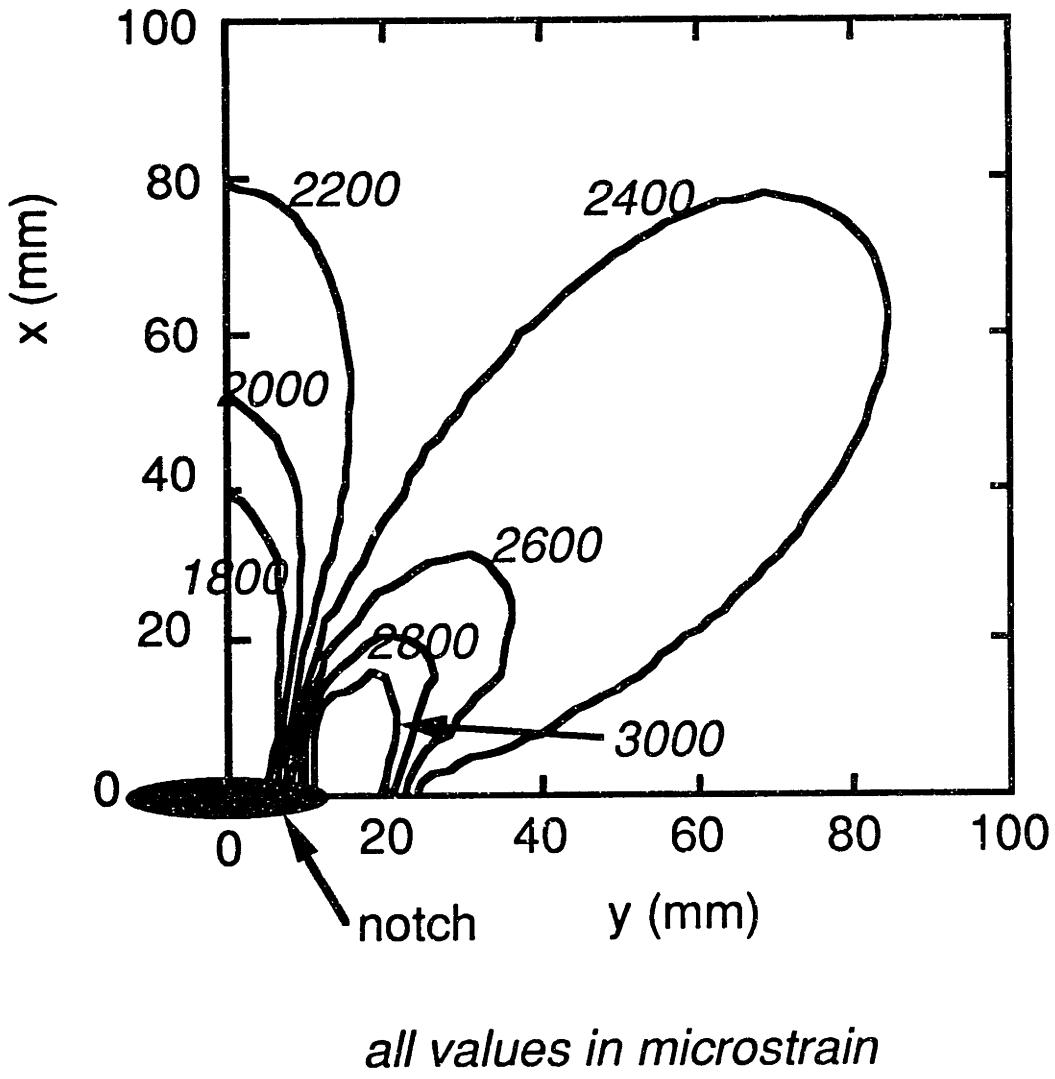

Figure 6.30 Predicted contour plot of the difference in principal strains for an A specimen with a 25.4 mm notch at a far-field stress level of -90 MPa (calculated far-field value of $\Delta\varepsilon$ is 2350 $\mu\varepsilon$).

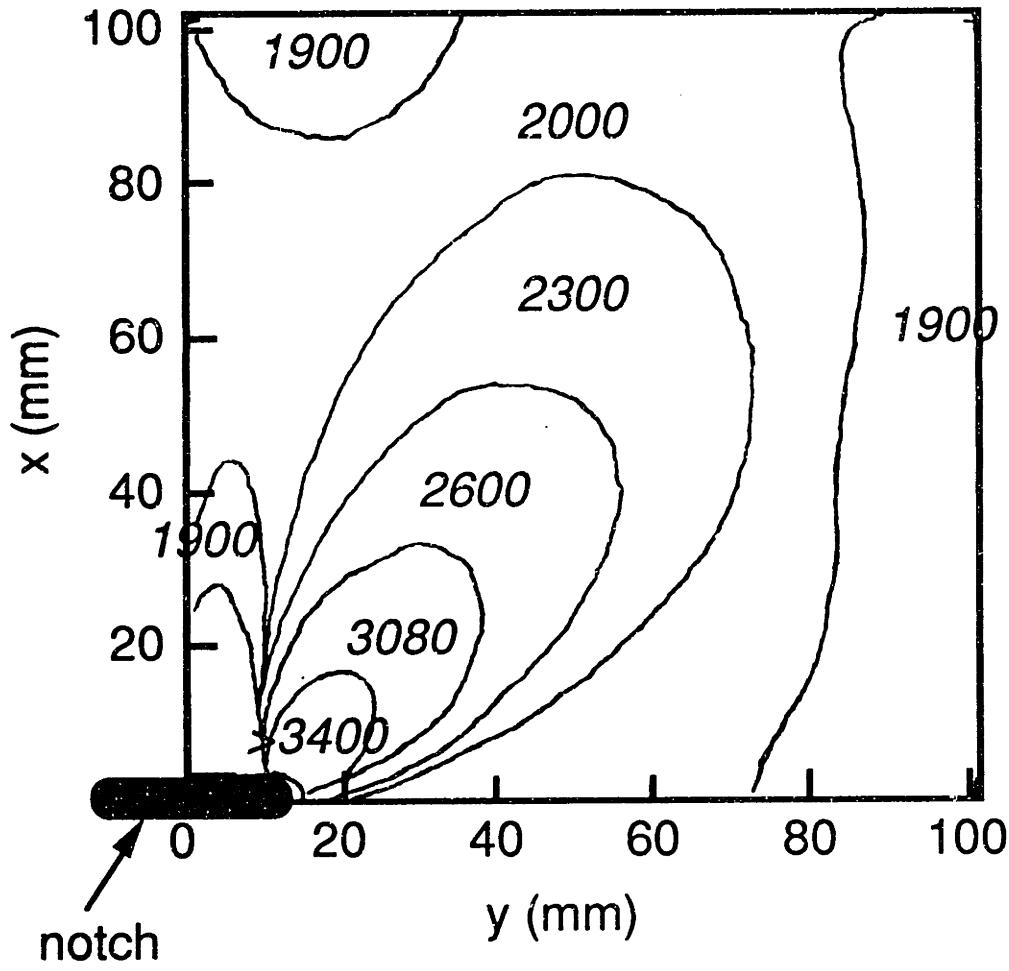

Figure 6.31 Experimental contour plot of the difference in principal strains, determined via the photoelastic technique, for a medium A specimen with a 25.9 mm notch at a far-field stress level of -90 MPa (specimen A-M-DN25).

the region is probably not significant. The strain differential level away from the notch is slightly lower than predicted, but only by about 10%. Well-defined regions of high and low $\Delta\varepsilon$ exist around the notch. The region of low strain is smaller than predicted, but the numerical values of strain for this region are similar to those predicted. The outer edge of the lobes from the notch tip are about the same size as predicted. However, the difference between strain differential levels is two or three times smaller for the predicted pattern than for the experimental pattern and the strain levels near the notch are higher than predicted. Thus, one must pay attention to the strain values as well as the contour boundaries when interpreting these plots.

The predicted and experimental patterns for a medium A specimen with a 50.8 mm notch are shown in Figures 6.32 and 6.33. The observed strain differential away from the notch, approximately 2200 μstrain, agrees well with the predicted level of 2350 μstrain. The region of low strain differential is similar to that predicted, and the strain levels agree well with predictions. The lobes from the notch are very similar in size to those predicted. Observed strain levels in the outer parts of the lobe agree well with predictions. However, the strain differential levels in the center of the lobes are again higher than predicted.

The predicted and experimental patterns for a large A specimen with a 76.2 mm notch are shown in Figures 6.34 and 6.35. Observed differential levels away from the notch agree with predictions. The observed region of low strain differential agrees quite well in shape and values with that predicted. The observed strain differential levels at the center of the lobe from the notch are again higher than predicted. The boundary between the 2200 μstrain and 2900 μstrain regions is very

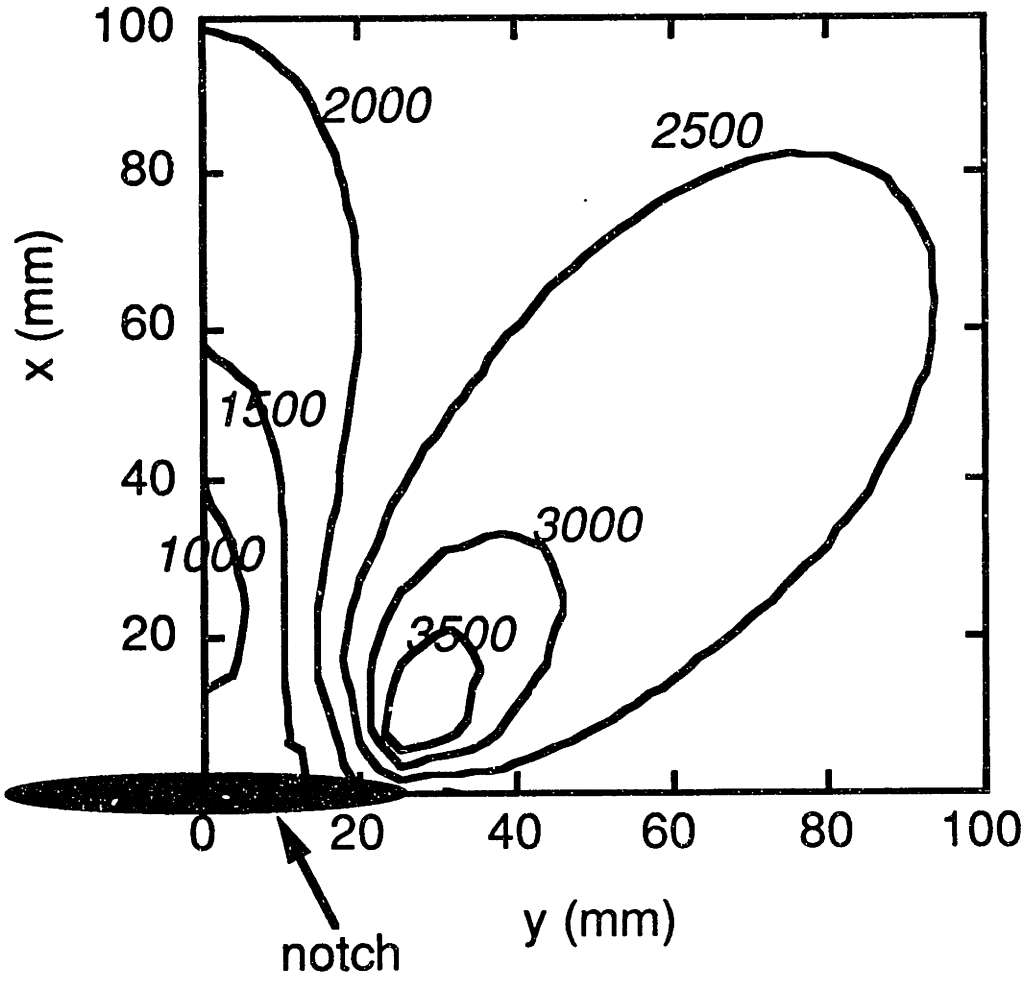

Figure 6.32 Predicted contour plot of the difference in principal strains for an A specimen with a 50.8 mm notch at a far-field stress level of -90 MPa (calculated far-field value of $\Delta\varepsilon$ is 2350 $\mu\varepsilon$).

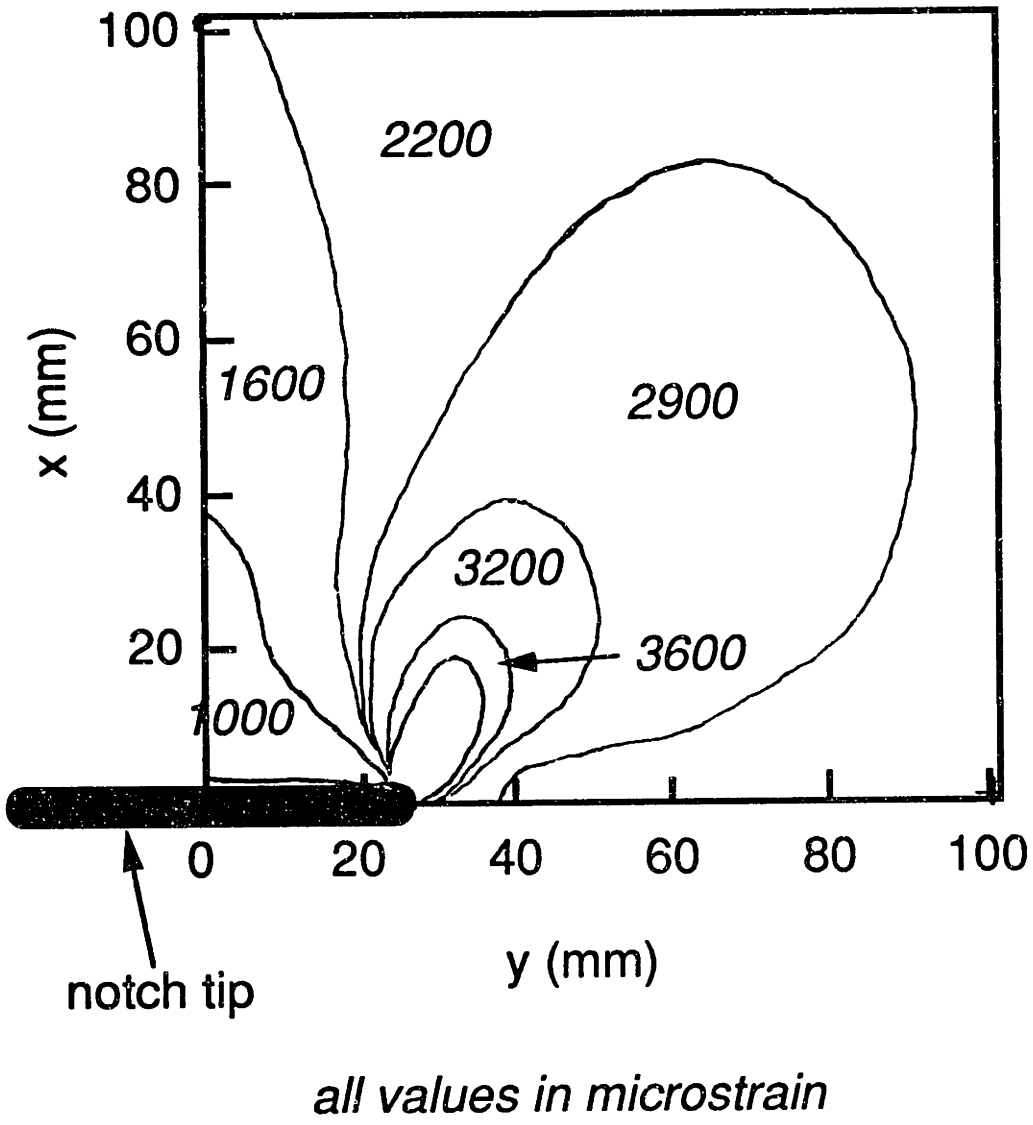

Figure 6.33 Experimental contour plot of the difference in principal strains, determined via the photoelastic technique, for a medium A specimen with a 51.2 mm notch at a far-field stress level of -90 MPa (specimen A-M-DN51).

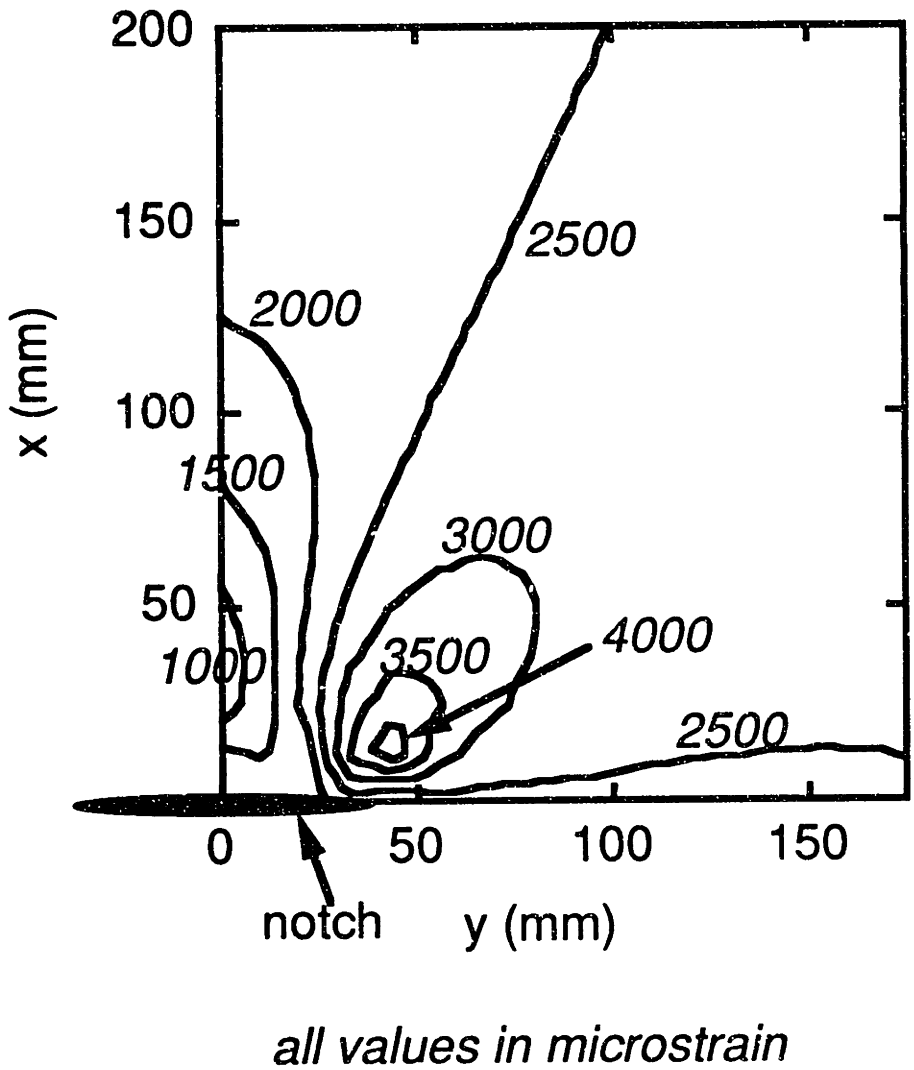

Figure 6.34 Predicted contour plot of the difference in principal strains for an A specimen with a 76.2 mm notch at a far-field stress level of -96 MPa (calculated far-field value of $\Delta\varepsilon$ is 2510 $\mu\varepsilon$).

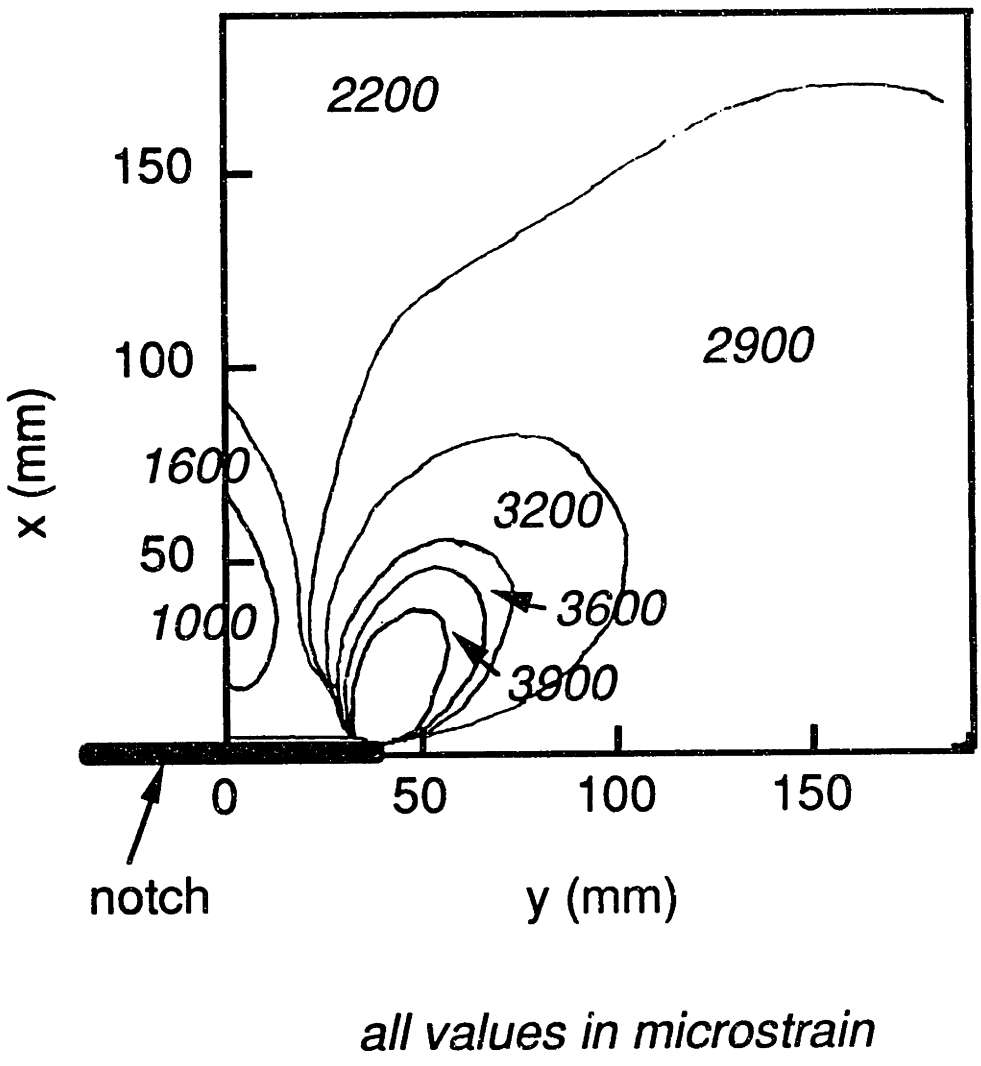

Figure 6.35 Experimental contour plot of the difference in principal strains, determined with the photoelastic technique, for a large A specimen with a 76.6 mm notch at a far-field stress level of -96 MPa (specimen A-L-DN76).

indistinct as the edge of the specimen is neared, so this boundary should be regarded as somewhat uncertain.

Among the A specimens, the strain differential level observed away from the notch is about the same for specimens at the same applied stress level. In all cases, the region of influence of the notch seems to be smaller than the specimen size. Specimens with 3.8, 6.5, 9.6, and 76.6 mm notches have boundaries which reach from the vicinity of the notch to the vertical edge of the specimen. However, this seems to be due to the overall gradual gradient previously discussed which affects the patterns observed. Also, in all cases, an approximately constant value of $\Delta\varepsilon$ is attained across the width of the specimen. This suggests that a uniform stress state has developed and that the effect of the length of the specimen is not significant. Because of these two observations, it seems that the region of notch influence is less than the specimen size.

The observed patterns of the A specimens become more similar to the predicted patterns as the notch length is increased. For small specimens with 9.5 and 12.7 mm notches, medium specimens, and large specimens, the regions of low strain differential above the notch and high strain differential off of the notch tip are similar in shape to the predicted patterns. Far-field strain differential levels are similar to those predicted, but strain differential levels in the vicinity of the notch tip are always higher than predicted.

Because the elastic properties of the panels differ, the strain patterns would be expected to be different for specimens from the different panels under the same conditions. Thus, predicted and observed strain patterns are shown for the specimens of the B layup with notches of 3.2, 6.4, 9.5, and 12.7 mm.

The predicted and experimental patterns for a B specimen with a 3.2 mm notch are given in Figures 6.36 and 6.37. The observed region of the notch influence is small. Outside of this region, the cell wall pattern dominates, making it impossible to determine a more precise reading of $\Delta\varepsilon$ in this region. In general, the cell wall pattern is more pronounced in the B specimens than in the A specimens. The strain differential level away from the notch agrees well with predictions, considering the uncertainty in the observed value. No distinct region of low strain differential is observed. The size of the lobes cannot be compared directly because the strain differential values are quite different. The observed strain differential values in that region are again much higher than predicted.

The predicted and experimental patterns for a B specimen with a 6.4 mm notch are given in Figures 6.38 and 6.39. The cell wall pattern strongly affects the outer two fringes, making them wavy and irregular. The strain differential level away from the notch is much higher than predicted, 5000 μstrain versus 3500 μstrain. However, in the region away from the notch, colors are intermingled in the cell wall pattern which correspond to 4100, 4600, and 5300 μstrain. Thus, determining what the value of $\Delta\varepsilon$ actually is in this region is difficult. A large region of lower strain differential is observed over the notch with strain values similar to predicted values. The lobe from the notch is more rounded and the strain differential level in that region is substantially higher than predicted.

The predicted and experimental patterns for a B specimen with a 9.5 mm notch are given in Figures 6.40 and 6.41. Several regions are observed from the notch that reach the boundary of the sketch. These regions are similar to those predicted. For example, the predicted contour with a value of 3500 μstrain also reaches the edge of the region considered. Although

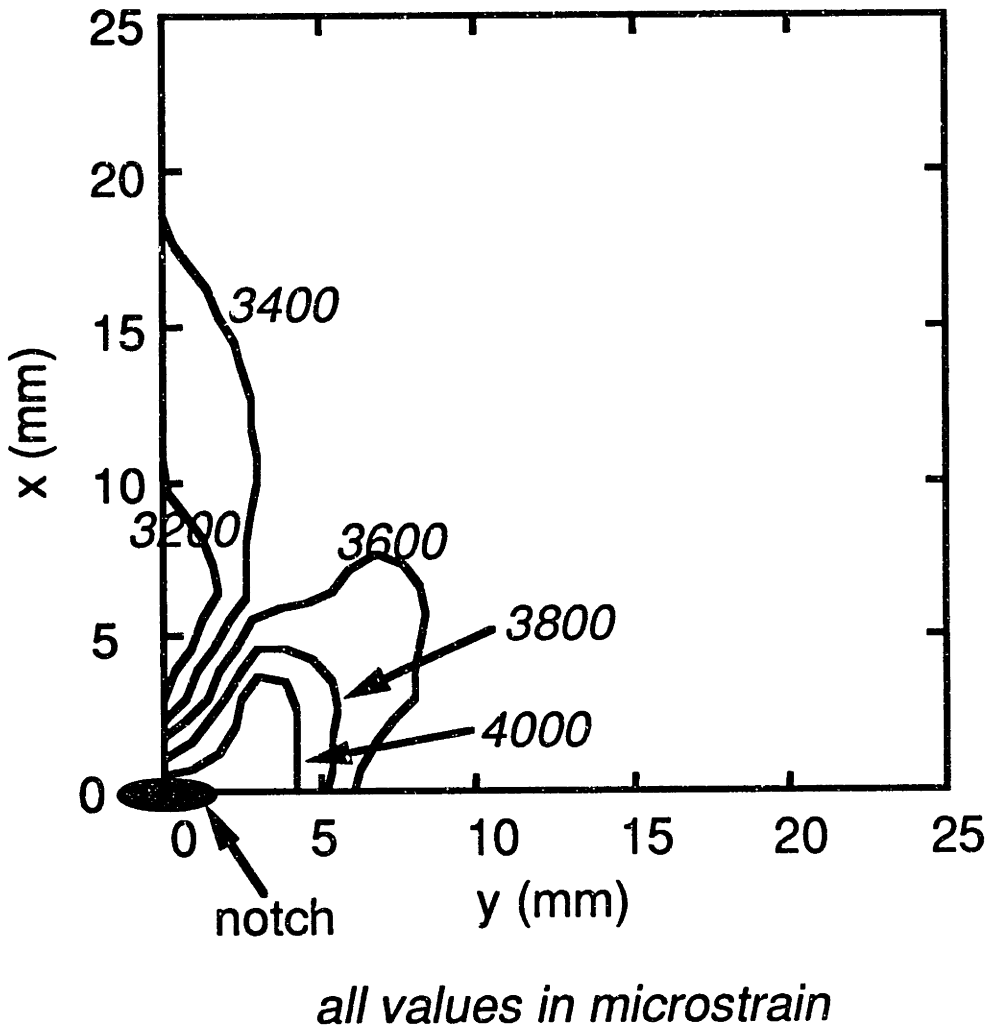

Figure 6.36 Predicted contour plot of the difference in principal strains for a B specimen with a 3.2 mm notch at a far-field stress level of -162 MPa (calculated far-field value of $\Delta\varepsilon$ is 3507 $\mu\varepsilon$).

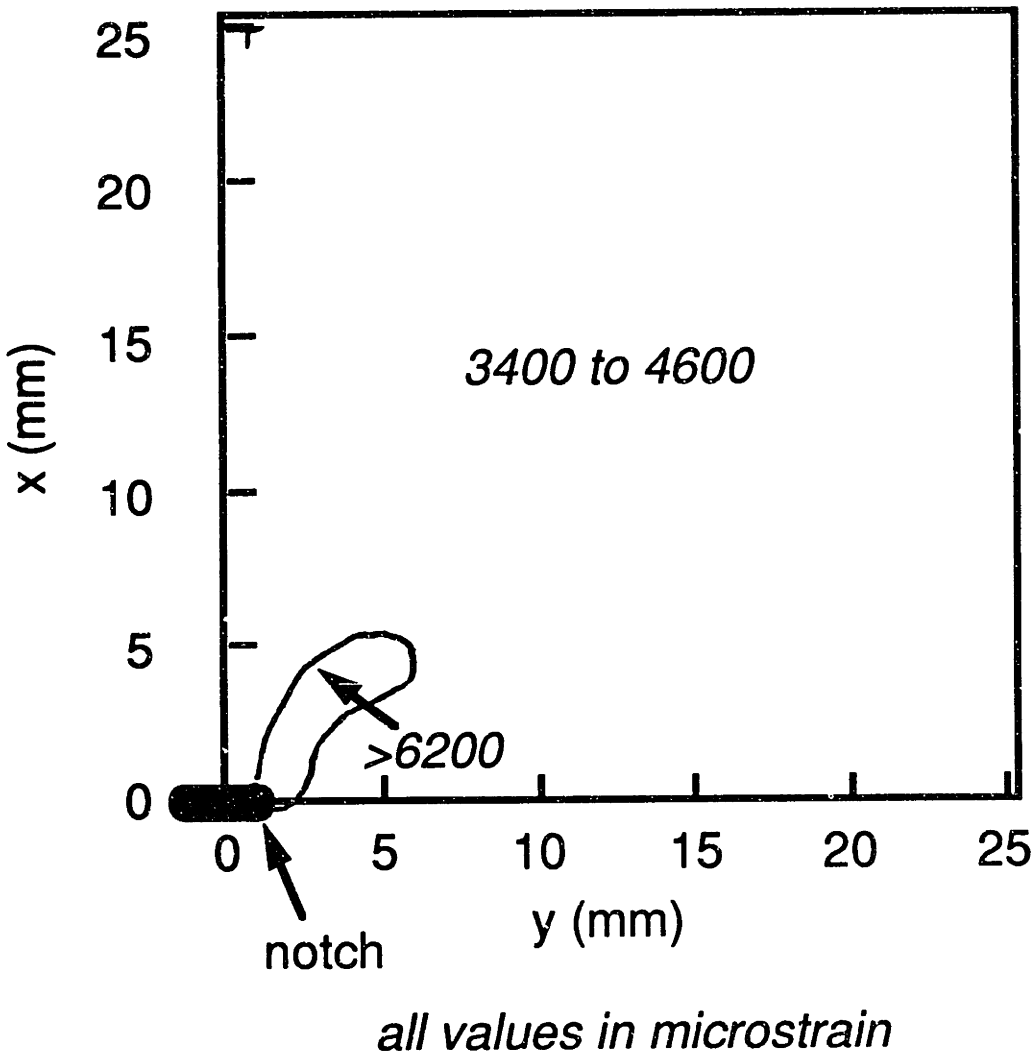

Figure 6.37 Experimental contour plot of the difference in principal strains, determined via the photoelastic technique, for a small B specimen with a 3.1 mm notch at a far-field stress level of -162 MPa (specimen B-S-SN3a).

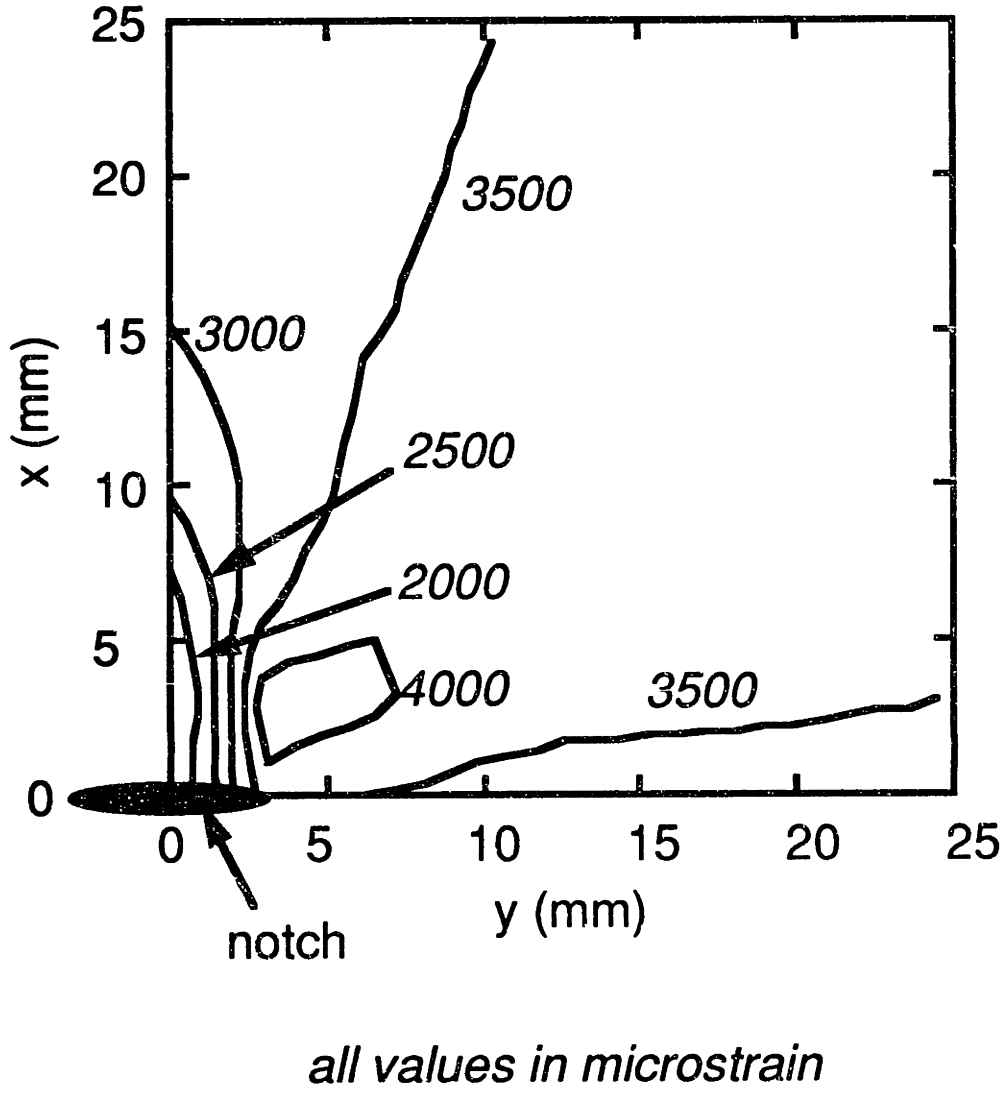

Figure 6.38 Predicted contour plot of the difference in principal strains for a B specimen with a 6.4 mm notch at a far-field stress level of -162 MPa (calculated far-field value of $\Delta\varepsilon$ is 3507 $\mu\varepsilon$).

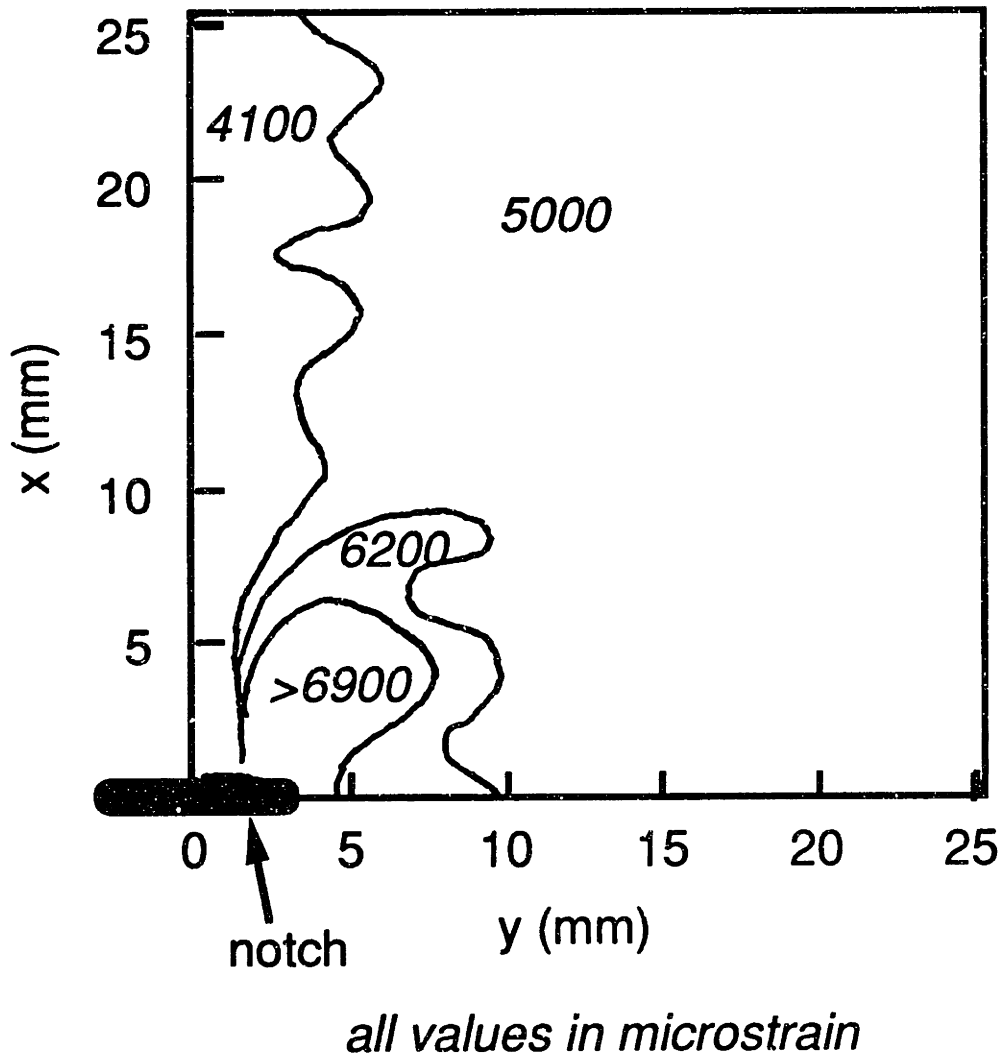

Figure 6.39 Experimental contour plot of the difference in principal strains, determined via the photoelastic technique, for a small B specimen with a 6.1 mm notch at a far-field stress level of -162 MPa (specimen B-S-SN6a).

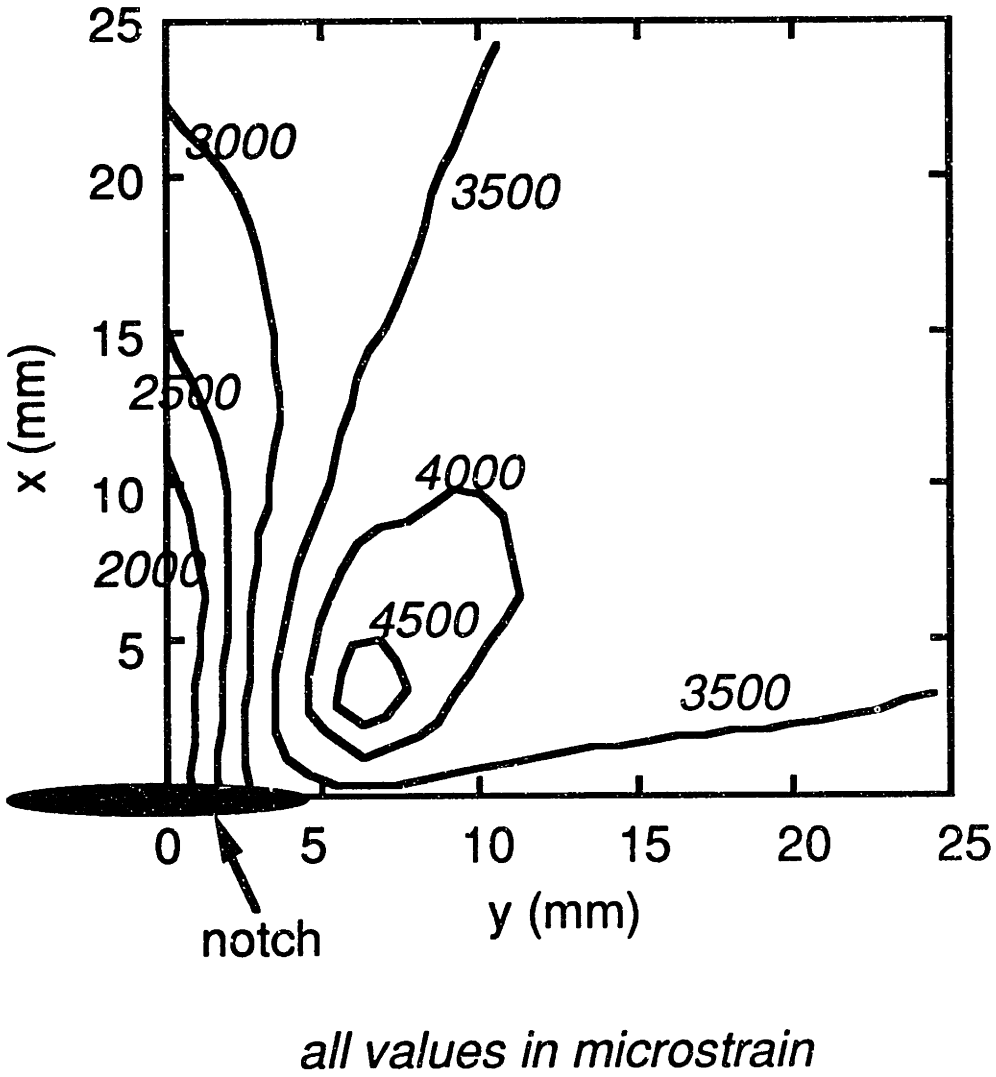

Figure 6.40 Predicted contour plot of the difference in principal strains for a B specimen with a 9.5 mm notch at a far-field stress level of -162 MPa (calculated far-field value of $\Delta\varepsilon$ is 3507 $\mu\varepsilon$).

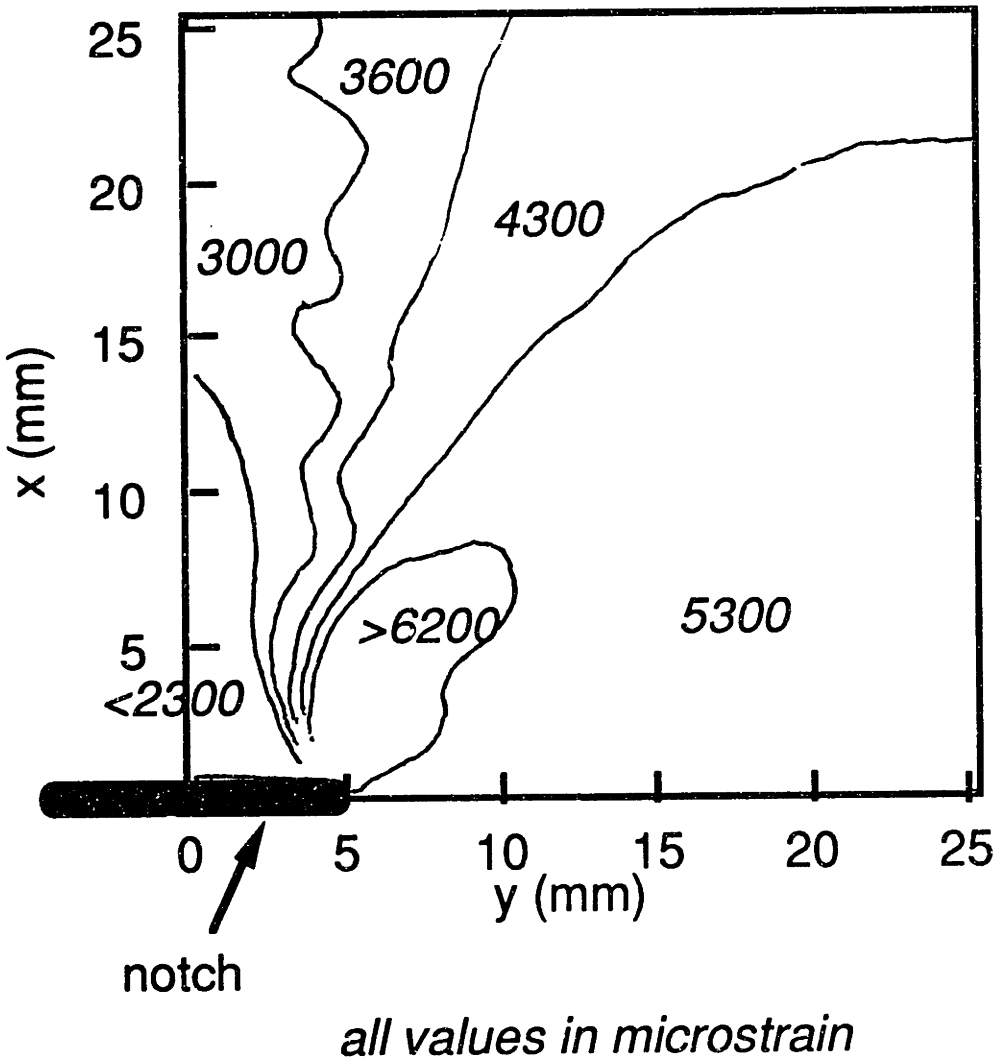

Figure 6.41 Experimental contour plot of the difference in principal strains, determined via the photoelastic technique, for a small B specimen with a 9.8 mm notch at a far-field stress level of -162 MPa (specimen B-S-SN10a).

several strain differential levels exist away from the notch, they are closer to the predicted far-field value of 3500 μstrain than previous specimens of the B layup. However, a large region with a strain differential level of 5300 με is observed above and to the right of the notch. A region of low strain differential is observed which agrees well with the prediction. The lobe shape is similar to the predicted shape, but the strain differential values in the lobe are again much higher than predicted.

The predicted and experimental patterns for a B specimen with a 12.7 mm notch are given in Figures 6.42 and 6.43. Strain differential levels away from the notch are higher than predicted, by about 25 to 30%. Ignoring the effects of the cell wall pattern, the region of low strain differential above the notch and the lobes are similar in shape to the predicted pattern. However, strain differential levels are again higher in the lobe than predicted.

The predicted and experimental patterns for a medium B specimen with a 25.4 mm notch are shown in Figures 6.44 and 6.45. Again, a region of low $\Delta\varepsilon$ is observed near the right edge of the specimen as with the A specimen with a 25.4 mm notch. Strain differential levels away from the notch are slightly lower than predicted. The region of low strain differential matches the size and numerical values of that predicted. The lobe region, however, has a more blunt and rounded shape than predicted. The numerical values within the lobe agree fairly well with those predicted, but at the very center the values observed are again somewhat higher.

The predicted and experimental patterns for a medium B specimen with a 50.8 mm notch are shown in Figures 6.46 and 6.47. Qualitatively, the observed and predicted patterns are very similar. The low-strain differential region matches the prediction quite well except in the region

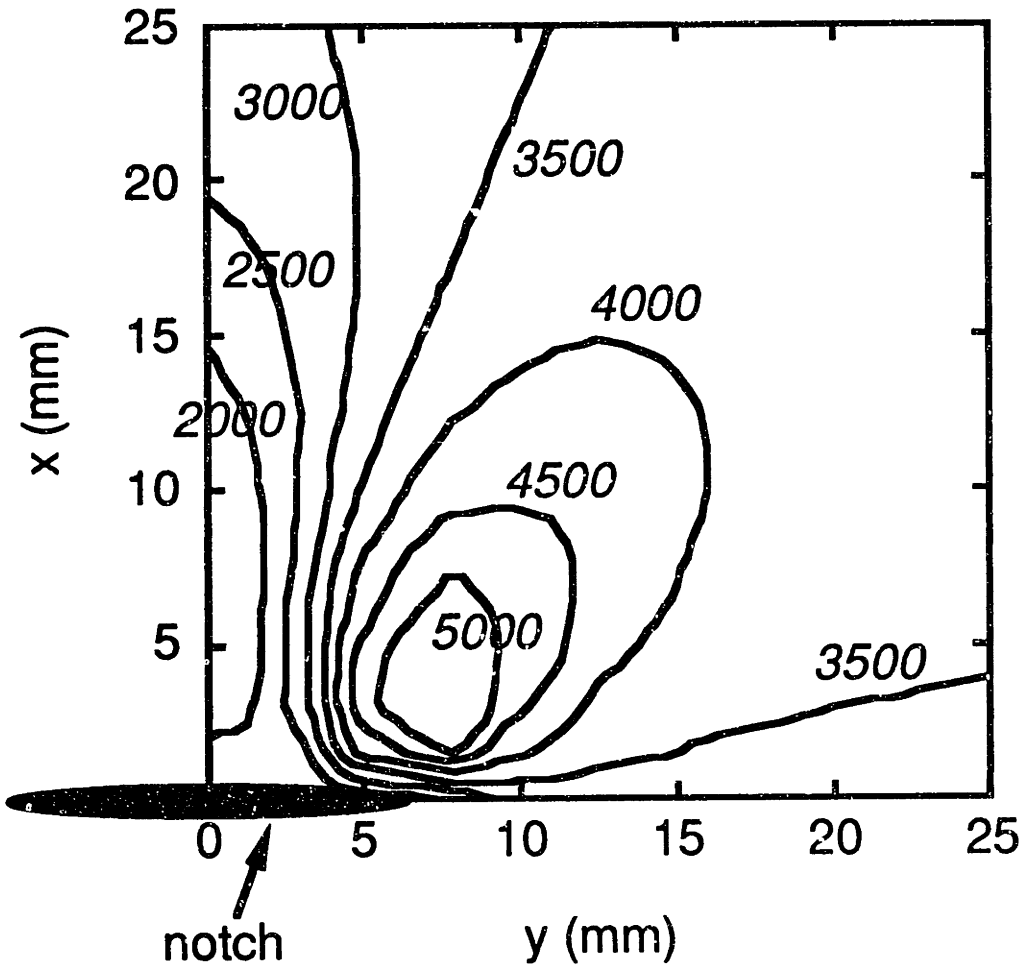

Figure 6.42 Predicted contour plot of the difference in principal strains for a B specimen with a 12.7 mm notch at a far-field stress level of -162 MPa (calculated far-field value of $\Delta\varepsilon$ is 3507 $\mu\varepsilon$).

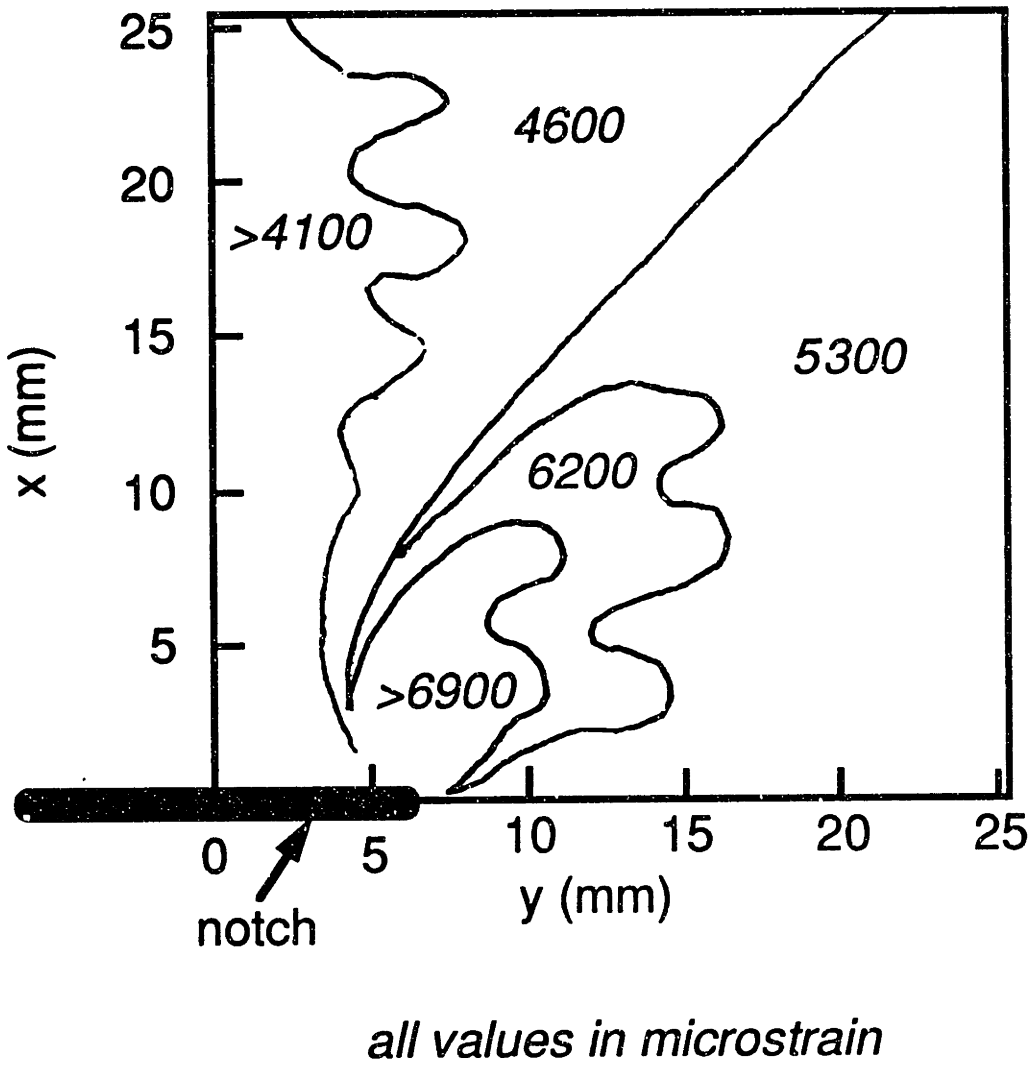

Figure 6.43 Experimental contour plot of the difference in principal strains, determined via the photoelastic technique, for a small B specimen with a 12.1 mm notch at a far-field stress level of -162 MPa (specimen B-S-SN13a).

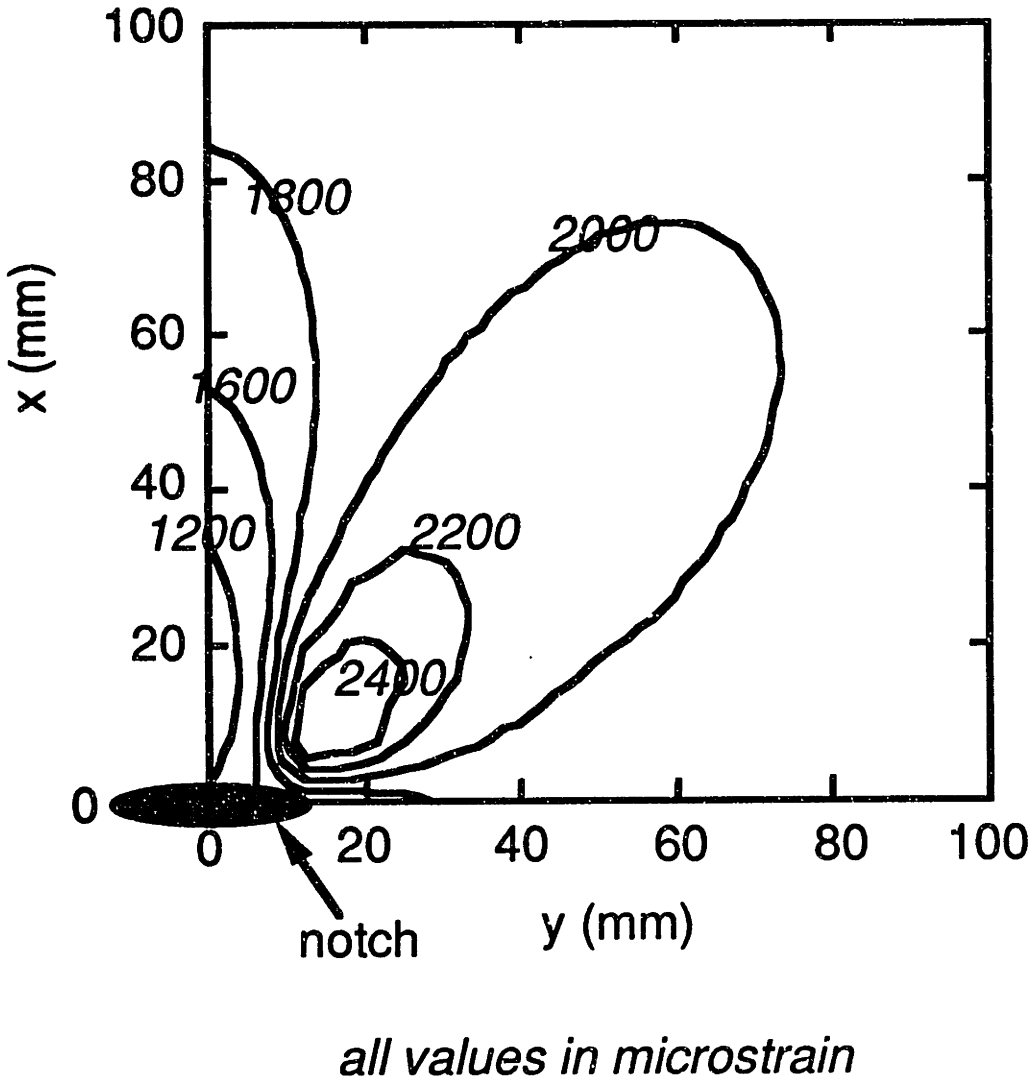

Figure 6.44 Predicted contour plot of the difference in principal strains for a B specimen with a 25.4 mm notch at a far-field stress level of -90 MPa (calculated far-field value of $\Delta\varepsilon$ is 1950 $\mu\varepsilon$).

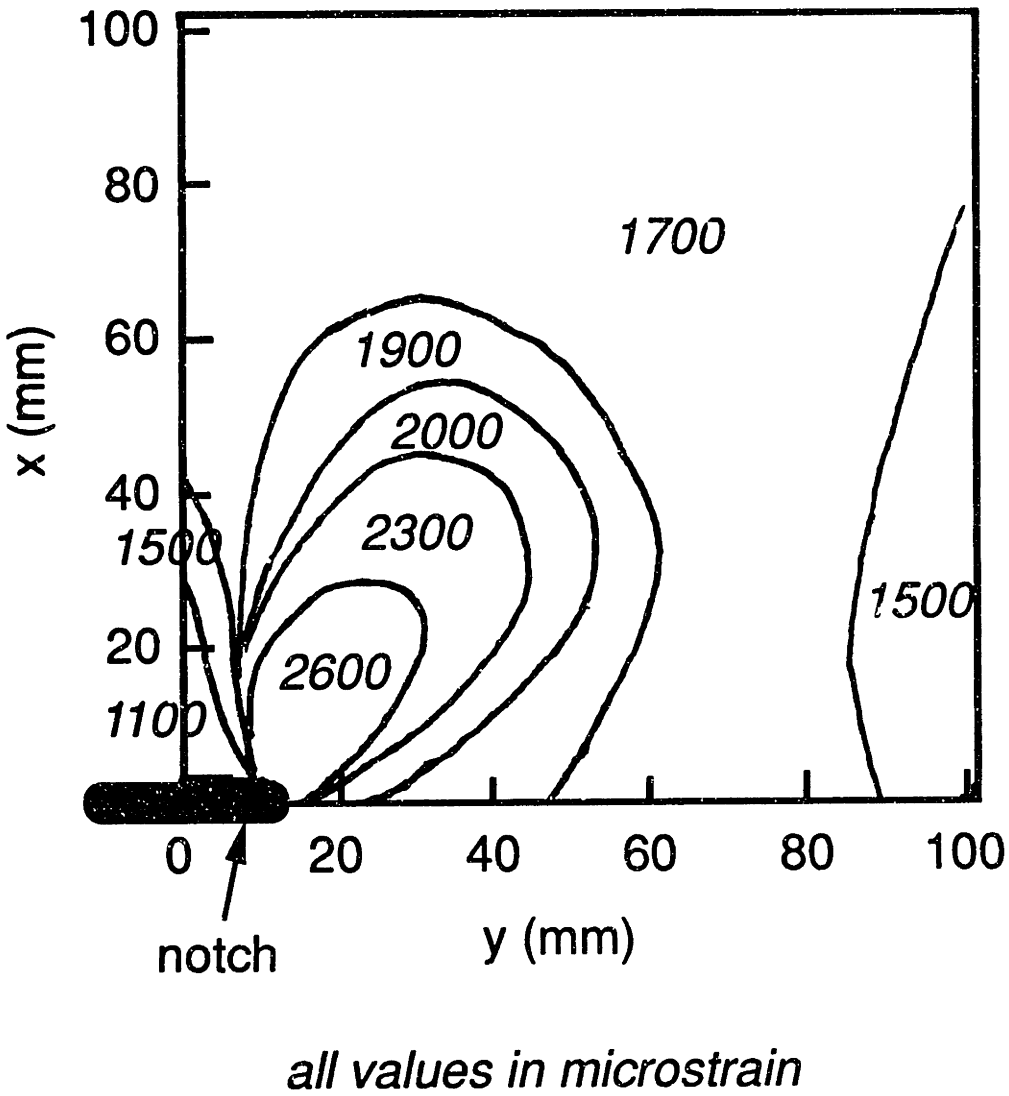

Figure 6.45 Experimental contour plot of the difference in principal strains, determined via the photoelastic technique, for a medium B specimen with a 25.6 mm notch at a far-field stress level of -90 MPa (specimen B-M-DN25).

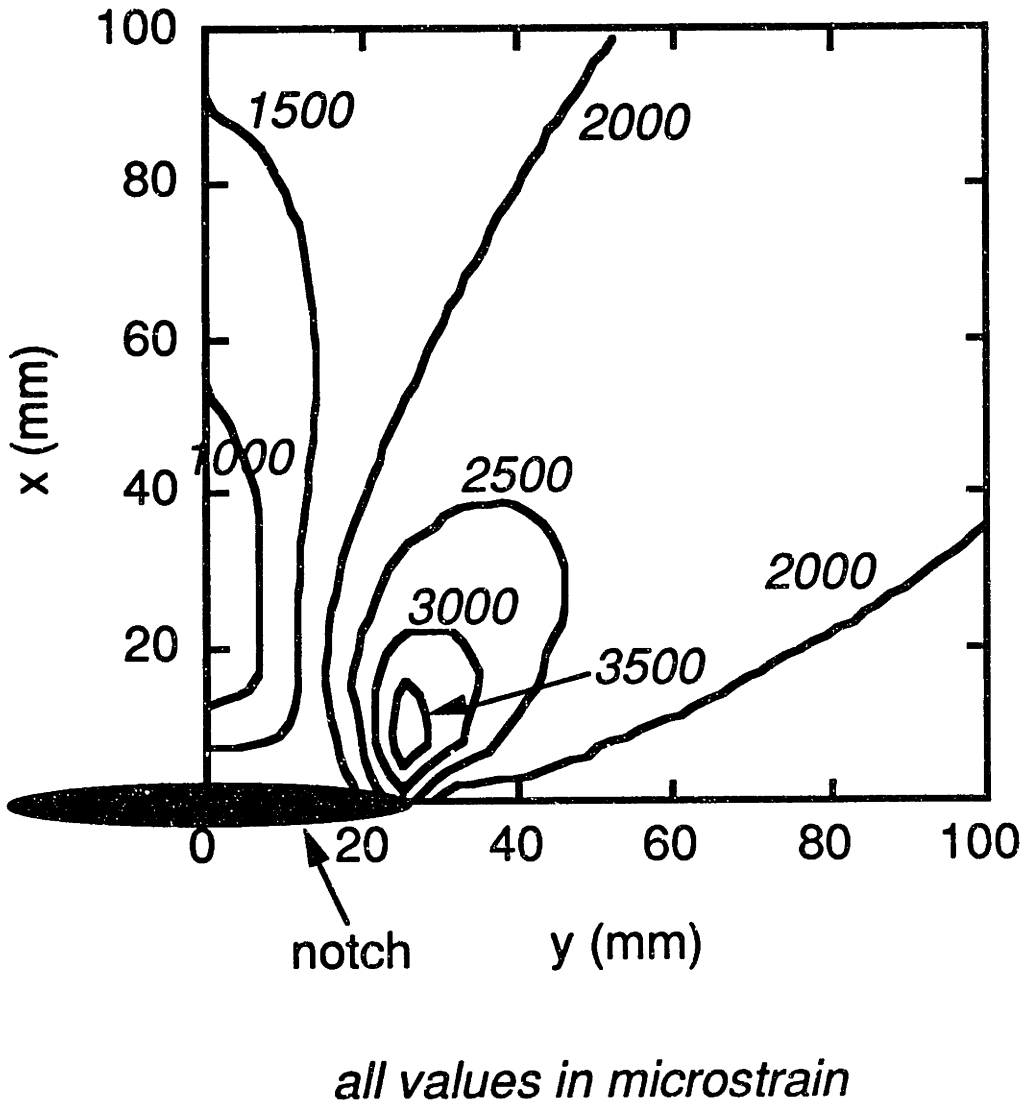

Figure 6.46 Predicted contour plot of the difference in principal strains for a B specimen with a 50.8 mm notch at a far-field stress level of -90 MPa (calculated far-field value of $\Delta\varepsilon$ is 1950 $\mu\varepsilon$).

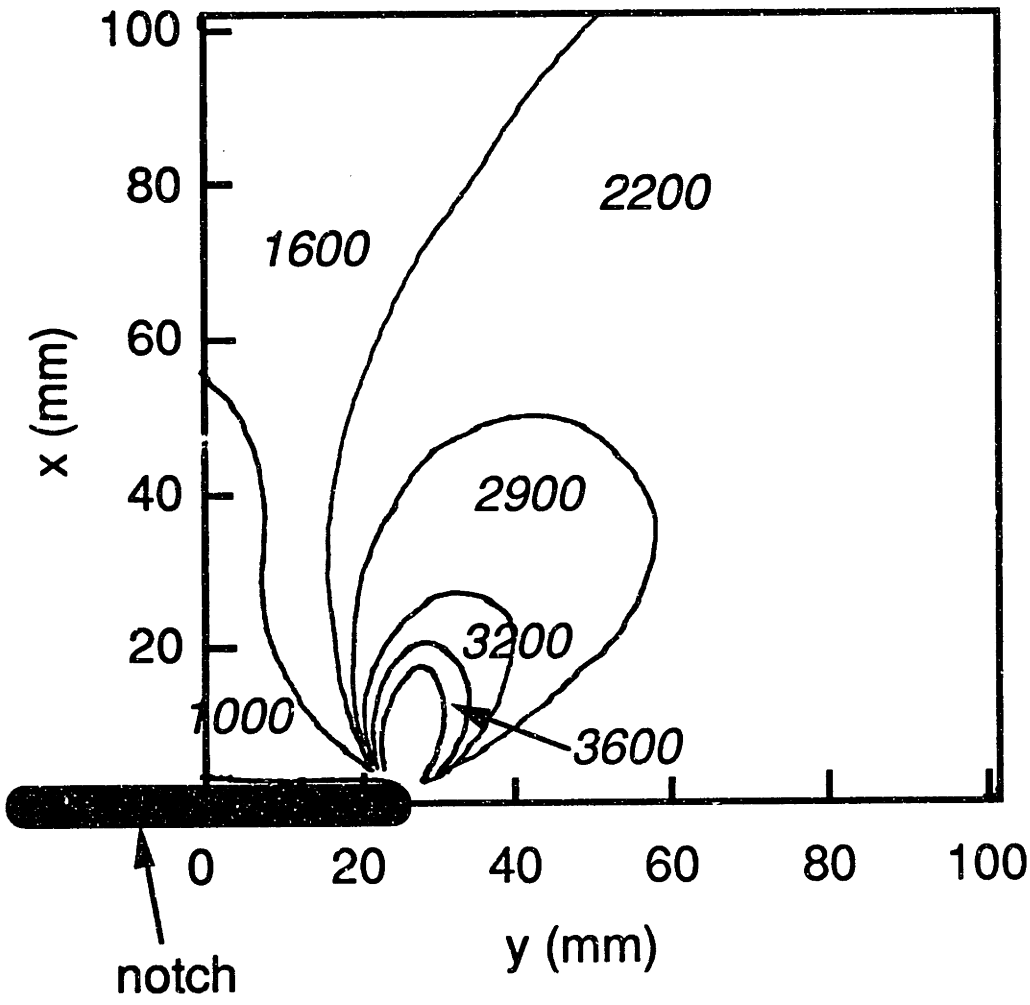

Figure 6.47 Experimental contour plot of the difference in principal strains, determined via the photoelastic technique, for a medium B specimen with a 51.0 mm notch at a far-field stress level of -90 MPa (specimen B-M-DN51).

close to the notch. It is difficult to determine the strain differential value away from the notch because of the contour observed which reaches the top of the figure. This contour is very similar to that predicted, and a value of 2000 μstrain along the observed boundary between the two upper regions is reasonable. It should be noted that this predicted contour is very close to the far-field strain level. Thus, variations around the contour are small, and its position could be changed significantly by a small change in the strain field. Observed strain differential levels at the center of the lobe are again higher than predicted.

The predicted and experimental patterns for a large B specimen with a 76.2 mm notch are shown in Figures 6.48 and 6.49. Again, the two patterns are qualitatively very similar. Values of strain differential away from the notch seem to be similar to those predicted despite the observed contour between the 1600 and 2200 μstrain regions. The region of low strain differential above the notch is similar to that predicted. The contour which crosses the top boundary is similar to that predicted. The shape of the lobe is similar to that predicted, but the strain differential levels at the center of the lobes are again higher than predicted.

Strain patterns seem to vary significantly among the B specimens with different notch lengths. Among the small specimens, the cell wall specimens affects the patterns observed and can cause a wide range of strain levels to be observed within the same region. Among the medium and large specimens, the lobe regions off of the notch tip are qualitatively similar, but the strain differential in this region increases as the notch length increases. The small specimens are more difficult to compare because of the cell wall pattern which makes the region boundaries irregular. With some specimens, especially when the ratio of notch length

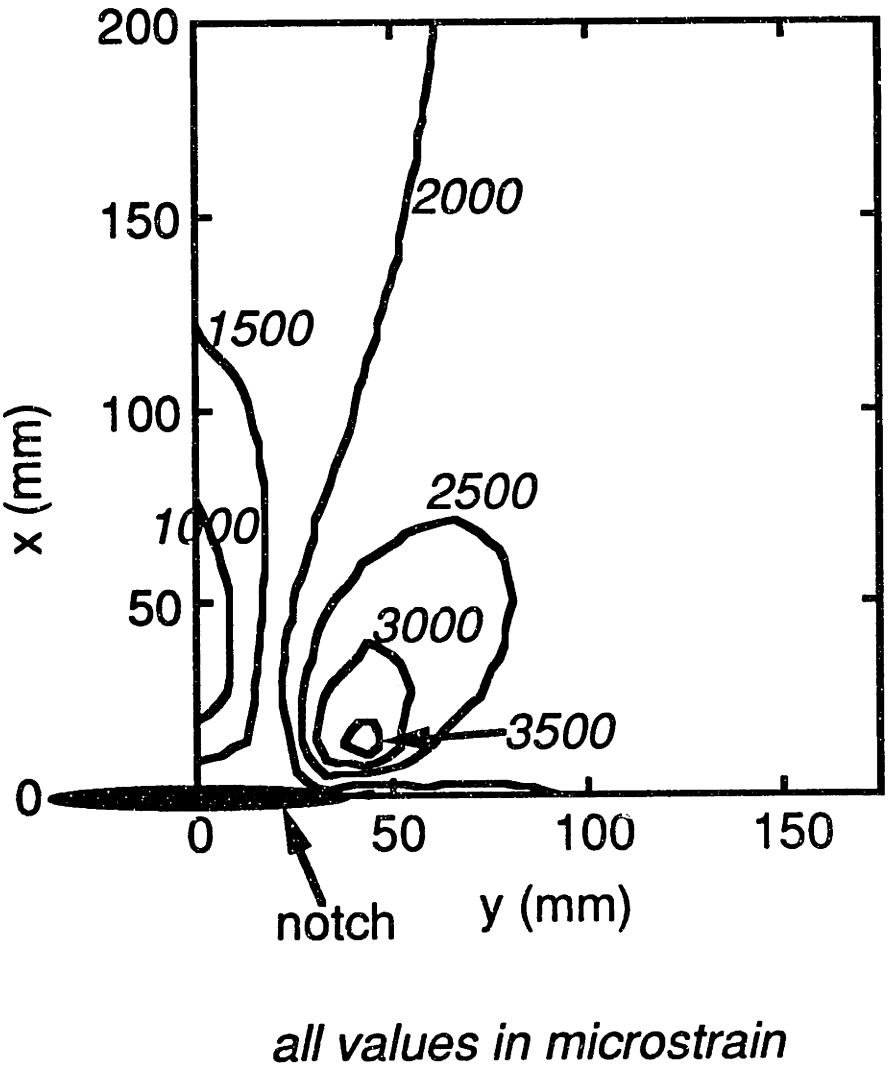

Figure 6.48 Predicted contour plot of the difference in principal strains for a B specimen with a 76.2 mm notch at a far-field stress level of -96 MPa (calculated far-field value of $\Delta\varepsilon$ is 2080 $\mu\varepsilon$).

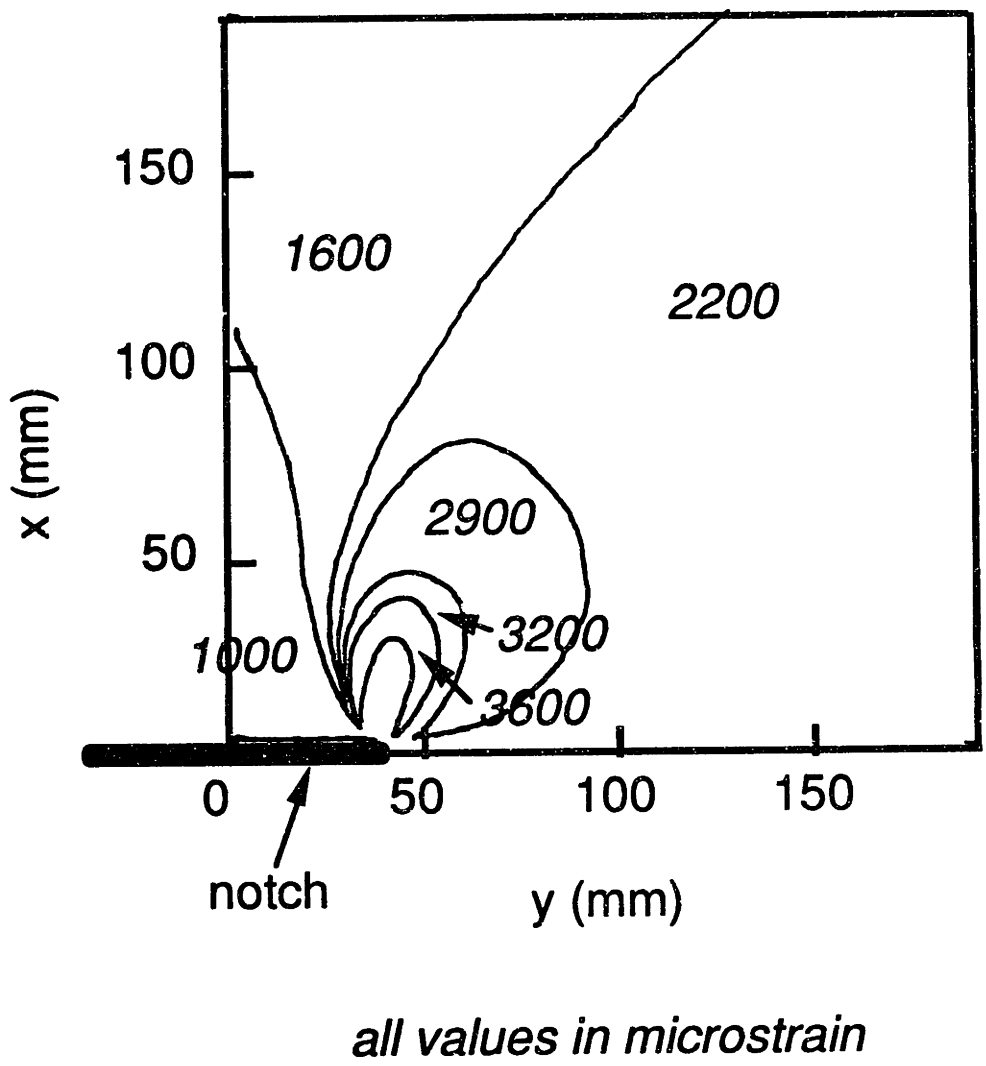

Figure 6.49 Experimental contour plot of the difference in principal strains, determined via the photoelastic technique, for a large B specimen with a 76.3 mm notch at a far-field stress level of -96 MPa (specimen B-L-DN76).

to specimen width approaches or exceeds 0.2, region boundaries are observed which go from the notch to the top edge of the sketch. It seems that these are actually regions of low strain differential which have been affected by the overall gradual gradient and possibly the end conditions of the specimen. Whether the behavior of these boundaries is significant or not will be discussed in Chapter 7.

Small specimens from the B layup display low-strain differential regions and lobes from the notches which become more similar to the predicted pattern as the notch size increases. Specimens with the shortest notches do not exhibit regions of low strain differential above the notch and have only small lobes off of the notch. As notch length is increased, the regions of low strain differential above the notch and the lobes become more defined. Numerically, the strain differential levels above the notch are similar to predicted levels, but the strain differential levels in the lobes are substantially higher than the predicted levels. Strain differential levels for the B layup away from the notch are higher than predicted. This may be due to the observed cell wall pattern which is more pronounced for the B specimens than the A specimens. This pattern makes it difficult to determine the level of strain differential as several colors may be represented at the scale of the honeycomb cell. Agreement between predicted and observed patterns is better with the medium and large specimens than with the small specimens. Qualitatively, the patterns are very similar to predicted patterns, and the far-field strain differential levels for the different specimens are similar to that predicted. However, the strain differential levels near the notch are still higher than predicted.

It is not clear that the region of influence of the notch in the B specimens is smaller than the specimen in all cases. For the specimens with

notch lengths of 9.8 and 12.1 mm. contours are observed to reach the vertical edge of the specimen. Again, however, these contours seem to be affected by the overall gradual gradient. Thus, the width of the specimen does not seem to affect the stress state of the specimens. For specimens with notch lengths of 6.1, 9.8, 51.0, and 76.3 mm, contours are observed to cross the upper boundary of the sketch, suggesting that the length of the specimen may affect the stress state in the specimen. There contours may also be affected by the overall gradual gradient. It is also possible that these contours are affected by other factors than the notch such as the loading condition of the specimen. The cause and implications of these contours which reach the upper boundary of the sketch are discussed in Chapter 7.

The patterns observed with the A specimens are quite similar to those observed for the B specimens. Strain differential levels are somewhat lower for the B specimens than for A specimens tested at the same stress level. The different strain differential levels for specimens of the two layups mean that the contours have different values and thus may be located at different positions, but the patterns observed in specimens of the A and B layups with the same notch length are very similar between specimens of the two layups. The cell wall pattern is observed to be important in both sets of small specimens, though it is stronger in the B specimens. The same types of region of low strain differential above the notch and lobe of high strain differential off of the notch tip are observed in all specimens. For several cases of both layups, the region affected by the notch may reach the vertical edge of the specimen. Whether this affects the measured strength of the specimens is discussed in Chapter 7.

The observed patterns in the medium and large specimens agree

better with predictions than patterns for the small specimens. For all patterns in medium and large specimens, the general region above the notch and the lobe region are qualitatively similar to those predicted. This was not the case for the small specimens as only the small specimens with 9.5 and 12.7 mm notches develop regions which are similar to those predicted. Measured numerical values are closer to those predicted in the medium and large specimens. However, in all cases, the strain differential levels around the notch tip are higher than predicted.

6.2.3 Failure Stress and Failure Mode

Failure of the notched specimens took place as fracture across the width of one or both facesheets. This was always easily recognized by a sharp audible noise and the damage which spread across the notch line of the specimen in the y-direction. It should be noted that the damage present in the specimen after the test is completed is observed. After failure of one or both facesheets, additional damage may be caused as the loading plates continue in motion toward each other because of the lag of the feedback response of the testing machine. This can obscure the original damage in the specimen.

Damage grows from the notch outward along the y-axis until it reaches the edge of the specimen. Except as noted below. damage leading to failure of the notched specimens always occurred along the notch line. For small specimens with notches less than 12.7 mm long, failure was followed by extensive crushing, splitting, and delamination of the region along the notch line as the two pieces of the facesheet were forced into each other. This is probably secondary damage which occurred after failure of the specimen. A typical example of this crushing and splitting is shown in a

side view of a specimen in Figure 6.50. Despite the extensive damage, it appears that all the plies of the facesheet failed within a narrow band directly out from the notch along the y-axis.

More information about the failure can be gained from certain other specimens. For small specimens with a 12.7 mm notch in one facesheet, only the notched facesheet failed. Thus, the rough side facesheet remained relatively undamaged and prevented extensive crushing from occurring in the smooth notched facesheet. For all other notched specimens, some crushing of the facesheets after failure occurred, obscuring the original damage to some extent. Although they cannot be seen in photographs, close inspection of the specimen reveals that splits in the outer ply have grown from the notch tip along the fiber direction, 45° for the A specimens and 30° for the B specimens. Additional short splits in the fiber direction of the outer ply are observed from the notch line across the width of the specimen. A side view of such a specimen is shown in Figure 6.51. Except for the outer one or two plies, the plies all fail in a narrow band directly out from the notch along the y-axis. Failure is fiber-dominated with little matrix cracking. In most cases, a side view of the failed plies reveals a through-thickness failure surface with an angle of 45° to the surface of the specimen. Some delamination is noted at the edge of the specimen, but this is probably secondary delamination because it grows from the failure surface rather than the notch region. Little damage is noted to the core except in a small zone directly under the line where the facesheet failed. Specimens with 12.7 mm notches in both facesheets experience failure of both facesheets and crushing of the failure area. In fact, all other notched specimens experienced failure in both facesheets.

Failure of the medium and large specimens was similar to that of the

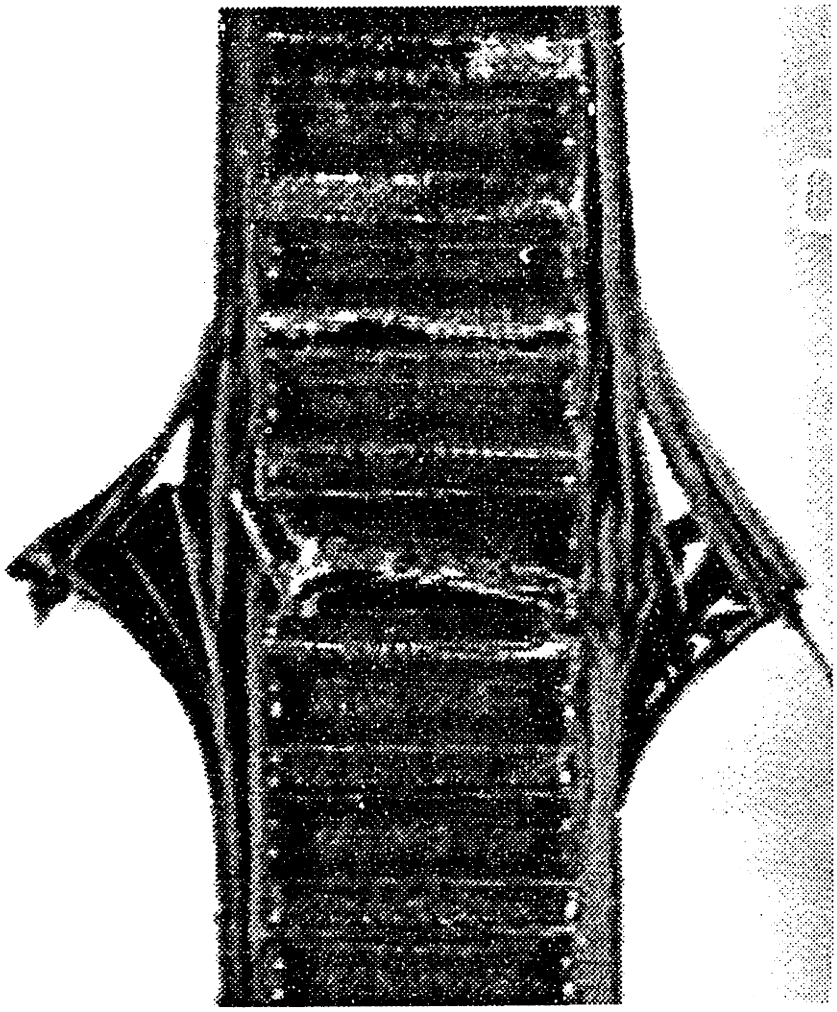

Figure 6.50 Side view photograph of a representative small notched specimen in which both facesheets failed (specimen A-S-SN3a)

Figure 6.51 Side view photograph of a representative specimen in which only the notched facesheet failed (specimen A-S-SN13b).

small specimens. Some crushing of the failure surface occurred in all cases, but it was sometimes minimized when the top and bottom of the notch came together. In all cases, failure occurred in a narrow band along the y-axis from the notch line. Again, failure is fiber-dominated with little matrix cracking. A picture of the typical damage across the width of the facesheet after failure is shown in Figure 6.52. A split along the fiber direction of the outer ply is noted, and the failure of the facesheets seems to be at approximately the same location in all plies. In two cases, the medium A and B specimens with 50.1 mm notches, a distinct pattern is observed on the surface of the specimen. This pattern is in the form of a cone growing out from the notch as the outer two or three plies delaminate and buckle outward. For the specimen shown in Figure 6.53, the pattern occurs in both the outer plies on one side of the notch and the photoelastic coating on the other side. However, this again appears to be secondary delamination, and failure in the remaining plies is fiber-dominated and straight out from the notch.

Failure at the notch appears essentially the same for all specimens regardless of size, notch length, or layup. As noted, most specimens experienced crushing of the failure surfaces after failure. However, all evidence indicates that all notched specimens failed by a fiber-dominated mechanism in a line directly out from the notch with some splitting of the outer plies and minimal matrix cracking.

In one medium and one large specimen notched in only one facesheet, a permanent deflection occurred toward the rough (unnotched) facesheet after failure, as shown in Figure 6.54. This was observed in specimens B-M-SN25 and B-L-SN25. This was probably caused by the failure of the notched facesheet before the rough unnotched side. Only in these

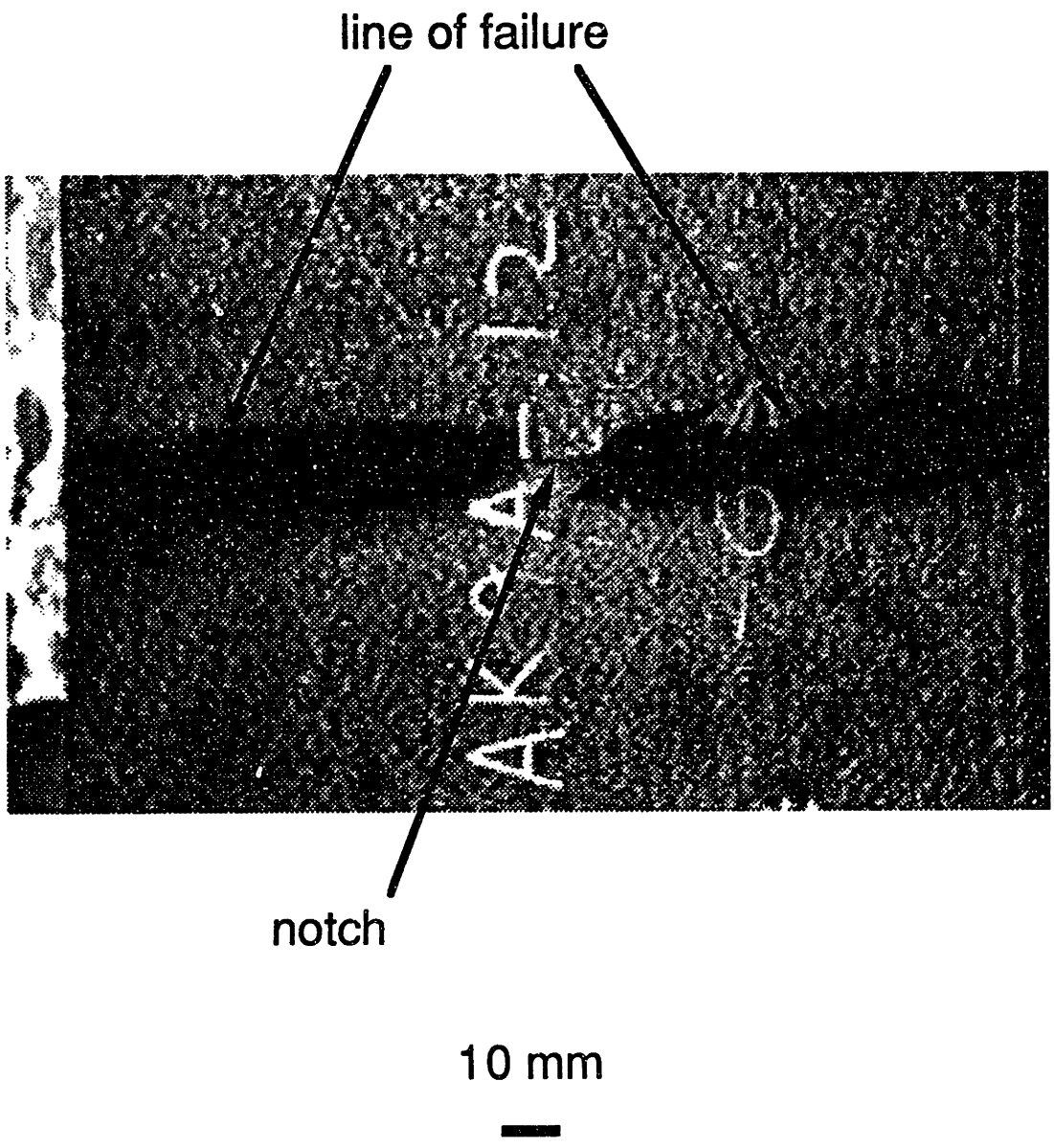

Figure 6.52 Photograph of typical failure across the width of a notched specimen (specimen A-M-DN25).

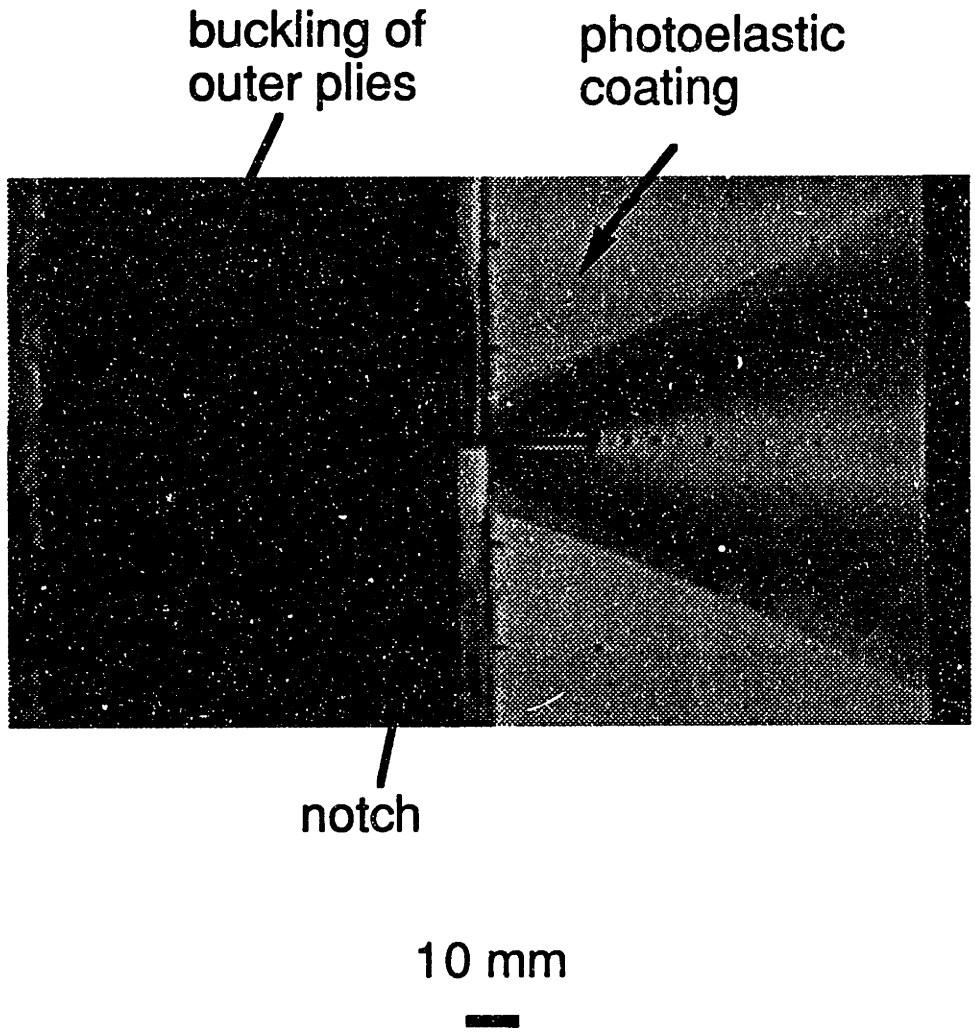

Figure 6.53 Photograph of specimen after failure in which damage has grown in a cone shape out from the notch along the y-axis (specimen B-M-DN51).

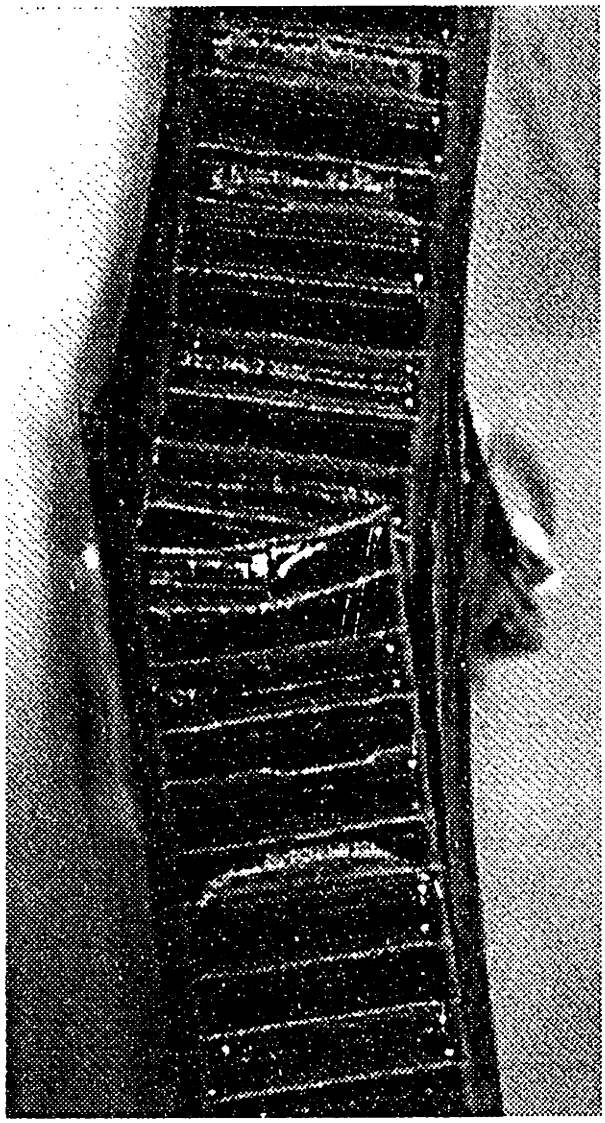

Figure 6.54 Side view photograph of a notched specimen which has a permanent out-of-plane deflection after failure (specimen B-M-SN25).

specimens was a significant permanent out-of-plane deflection of the specimen noted after failure.

For specimens with only one facesheet notched, it appears that the notched facesheet always failed first. At the least, there is no evidence to the contrary. Failure of the notched facesheet lead, in most cases, to failure of the unnotched facesheet. In the cases in which both facesheets were notched, it is possible the failure of one, in fact, triggered the failure of the other. However, the failure of the facesheets could not be detected as separate events.

In some cases, the failure in the region of the notch was accompanied by breaking of the potting material. This breakage could range from a single crack in the material to fracture in which almost all of the potting material separates from the specimen. Except as discussed in this section, the breaking of the potting material is deemed to be a result rather than a cause of specimen failure. This judgment is based upon the consistent failure of specimens in the notch region regardless of potting breakage. Failure in the notch region may trigger a stress wave which could cause fracture at the specimen/potting interface or within the potting material itself.

Certain small specimens exhibited unusual failure modes. During the testing of specimen B-S-SN6b, extensive cracking of the potting material was visually observed prior to the failure of the specimen. This cracking resulted in very irregular readings from the strain gages as shown in Figure 6.55. At a stress level of approximately 80 MPa, a large discontinuity is noted for all the gages. This may have been the initial cracking of the potting, but it was not visibly noted until later in the test. The cracking may have been due to the large thickness of shim used with this specimen.

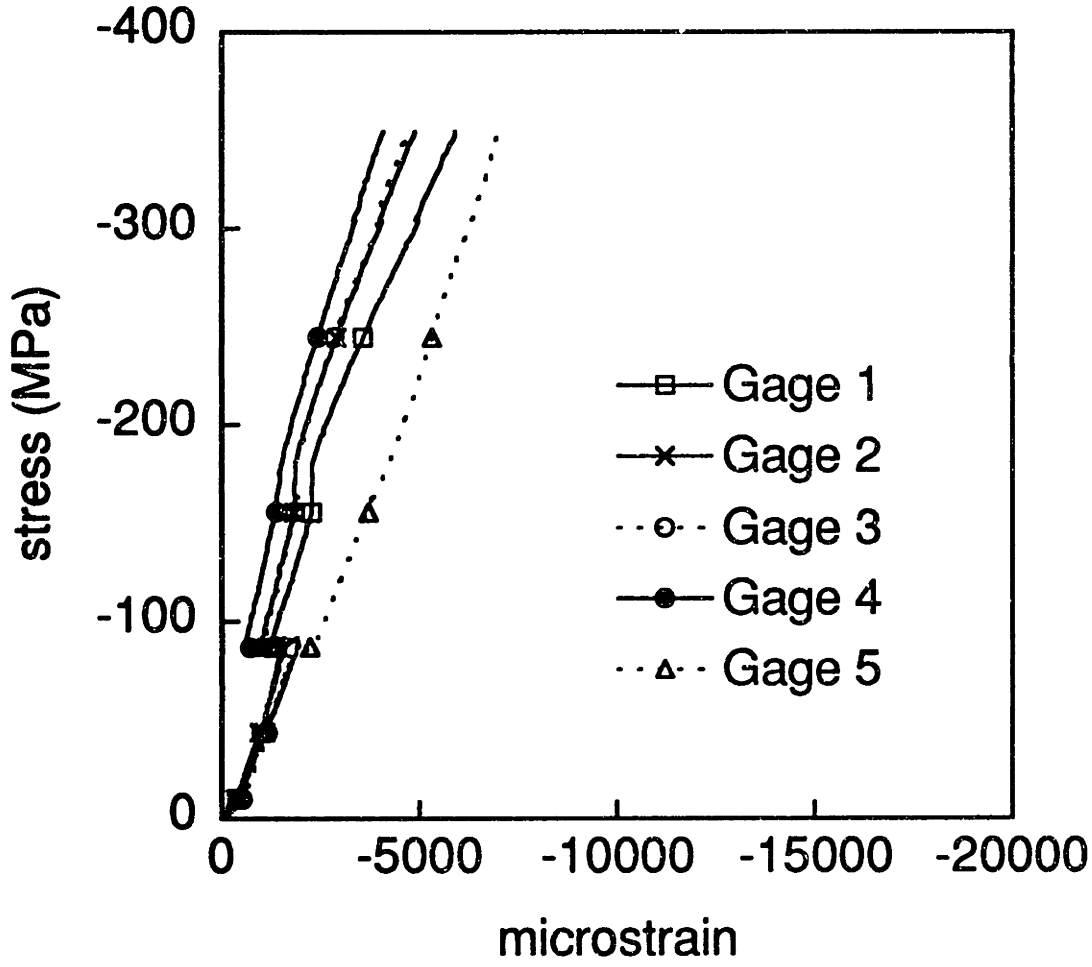

Figure 6.55 Stress-strain curves for a specimen which experienced visible cracking of the potting material during testing (specimen B-S-SN6b).

Although failure of this specimen occurred at the notch line, cracking of the potting and the unusual stress-strain behavior were observed only in this specimen. Therefore, the failure stress of 349 MPa for this specimen is not considered in further failure analyses. A second specimen, A-S-SN3b, exhibited a potting line failure identical to that observed in the undamaged specimens discussed in Section 6.1 of this chapter. Because its failure mode was different from all other notched specimens and failure does not occur at the notch, the failure stress of this specimen is excluded from further notched failure analyses.

Failure stresses for notched specimens are given in Table 6.12 for the A specimens and Table 6.13 for the B specimens. Failure stresses for the three small specimens which exhibited highly nonlinear stress-strain behavior (as discussed in Section 6.2.1), experienced potting cracking, and failed at the potting line are given but are excluded from further failure analyses. It should be noted that specimen A-L-SN25 did not fail because the load carried by the specimen exceeded the maximum capacity of the testing machine. As previously mentioned, this specimen underwent extensive deflection at its midpoint prior to when the machine shut down. Because this specimen had a notch in the smooth facesheet only, the deflection may have resulted in an additional bending moment which reduced the stress in the notched facesheet. The failure stresses of the notched specimens are discussed and analyzed using the Mar-Lin correlation in Chapter 7.

6.3 Compression After Impact Behavior

Six specimens were loaded in compression after an impact event

Table 6.12 Failure stresses for notched specimens of the A layup

Specimen	Average Notch Length (mm) [a]	Failure Stress (MPa)
A-S-SN3a	3.8	409
A-S-SN3b	3.1	384 [b]
A-S-DN3	3.4	391
A-S-SN6a	6.5	313
A-S-SN6b	6.3	316
A-S-DN6	6.7	324
A-S-SN10a	9.6	359
A-S-SN10b	9.4	311
A-S-DN10	9.5	285
A-S-SN13a	13.8	255
A-S-SN13b	12.2	268
A-S-DN13	12.9	235
A-M-DN25	25.9	193
A-L-SN25	25.4	>239 [c]
A-L-DN25	25.4	188
A-M-DN51	51.2	145
A-L-DN76	76.6	131

[a] Measured length of notch or average of measured notch lengths if both sides are notched.
[b] Specimen failure stress excluded from failure correlation.
[c] Specimen did not fail because capacity of testing machine was exceeded.

Table 6.13 Failure stresses for notched specimens of the B layup

Specimen	Average Notch Length (mm) [a]	Failure Stress (MPa)
B-S-SN3a	3.10	439
B-S-SN3b	3.25	393
B-S-DN3	3.35	368
B-S-SN6a	6.10	316
B-S-SN6b	6.66	349 [b]
B-S-DN6	6.43	275 [b]
B-S-SN10a	9.75	320
B-S-SN10b	9.78	298
B-S-DN10	9.78	245
B-S-SN13a	12.12	270
B-S-SN13b	13.06	250
B-S-DN13	12.78	225
B-M-SN25	25.91	204
B-M-DN25	25.57	202
B-L-SN25	25.35	213
B-L-DN25	25.49	212
B-L-DN51	51.03	147
B-L-DN76	76.30	130

[a] Measured length of notch or average of measured notch lengths if both sides are notched.

[b] Specimen failure stress excluded from failure correlation.

which damaged the specimen. The level 1 and level 2 impact events were conducted as detailed in Chapter 5. These events resulted in easily visible damage to the specimens including a large, visible dent in the smooth side facesheet. Those impacted at the lower level showed a small amount of surface cracking, while those impacted at the higher levels showed significant cracking and fiber breakage. Furthermore, all impacted specimens were found to have delaminations present as indicated by ultrasonic scan. The damage due to the impact events is more fully detailed in Chapter 5.

The behavior of the specimens was monitored during testing using strain gages, an LVDT, and shadow moiré interferometry. The use of strain gages and the LVDT has been discussed in this chapter with regards to undamaged and notched specimens. The data from the LVDT is either monotonic or non-monotonic, as discussed for the undamaged panels. The maximum out-of-plane deflections, along with the type of behavior, are given in Table 6.14 for the A specimens and Table 6.15 for the B specimens. Medium size impacted specimens from the A and B panels all deflect in the negative direction, toward the smooth side facesheet which has been damaged by an impact event. The deflection of these specimens is relatively small, with the level 2 specimens deflecting about twice as much as the level 1 specimens. The large size impacted specimens, however, seem to deflect in the positive direction (toward the rough side facesheet) and with a greater magnitude than the medium specimens.. However, what is actually happening during the testing of the large specimen damaged by a level 1 impact event is not completely clear. The deflection plot for this specimen is shown in Figure 6.56. Initially, there is a nearly linear region in which the deflection increases, but then the deflection remains more constant until a

Table 6.14 Maximum value and characterization of out-of-plane deflection behavior of impacted specimens of layup A

Specimen Size	Impact Level	Type of Behavior [a]	Maximum Deflection (mm)
M	level 1	nonmonotonic	-0.34
L	level 1	nonmonotonic	0.71
M	level 2	nonmonotonic / end	-0.68

[a] "non-monotonic" indicates deflection behavior is non-monotonic; "monotonic" indicates deflection behavior is monotonic and steady; "end" indicates irregular behavior near end of test.

Table 6.15 Maximum value and characterization of out-of-plane deflection behavior of impacted specimens of layup B

Specimen Size	Impact Level	Type of Behavior [a]	Maximum Deflection (mm)
M	level 1	nonmonotonic	-0.45
L	level 1	nonmonotonic	2.26
M	level 2	nonmonotonic / end	-1.12

[a] "non-monotonic" indicates deflection behavior is non-monotonic; "monotonic" indicates deflection behavior is monotonic and steady; "end" indicates irregular behavior near end of test.

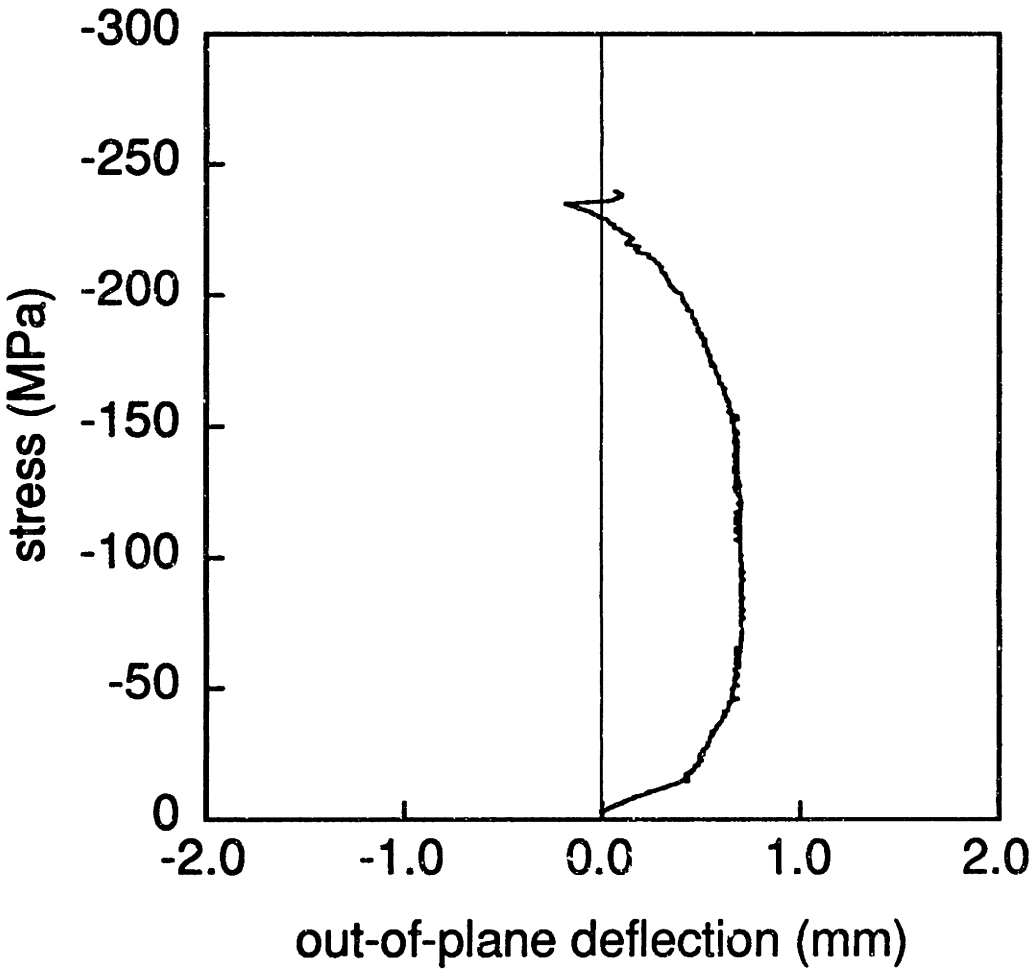

Figure 6.56 Plot of out-of-plane deflection versus far-field applied stress for a large A specimen damaged by a level 1 impact event (specimen A-L-IL1)

stress of approximately 150 MPa is reached. The deflection then decreases until it becomes negative near the end of the record. If the initial point is chosen as the zero, then the maximum deflection is positive as shown in Table 6.14. However, if the region where deflection remains stable is chosen as the zero point, then the maximum deflection is approximately the same magnitude as before but negative.

The strain gage configuration Impact, as shown in Figure 5.23, was used with all impact-damaged specimens. This configuration includes six gages: 1 and 2 are located back-to-back off of the centerlines, 3 and 4 are located back-to-back below the dimple along the vertical centerline, and 5 and 6 are back-to-back above the dimple along the vertical centerline. Odd numbered gages are located on the smooth side (impacted) facesheet, while even numbered gages are located on the rough side (undamaged) facesheet. Initial slopes for all strain gages of the six impacted specimens can be found in Appendix D.

The six strain gages tended to give slightly different values. Two types of behavior were noted. In the first type, the gages on the smooth side facesheet always give higher strain readings than their counterparts on the rough side facesheet. Also, gages located off of the vertical centerline give higher readings than those directly above or below the dimple. One exception to this is noted; for the medium B specimen damaged by a level 1 impact, gage 6 gives the highest readings though gages 1 and 2 are the next highest. The stress-strain plot for this specimen is shown in Figure 6.57. The six gages are grouped fairly well. The highest slope is for gage 3 at 61.1 MPa, and the lowest for gage 6 at 48.4 MPa. For this case, the slopes of the gage 1 & 2 pair are about the same as the slopes of the gage 5 & 6 pair. Within each of these pairs, the gage located on the smooth side has a slope 8

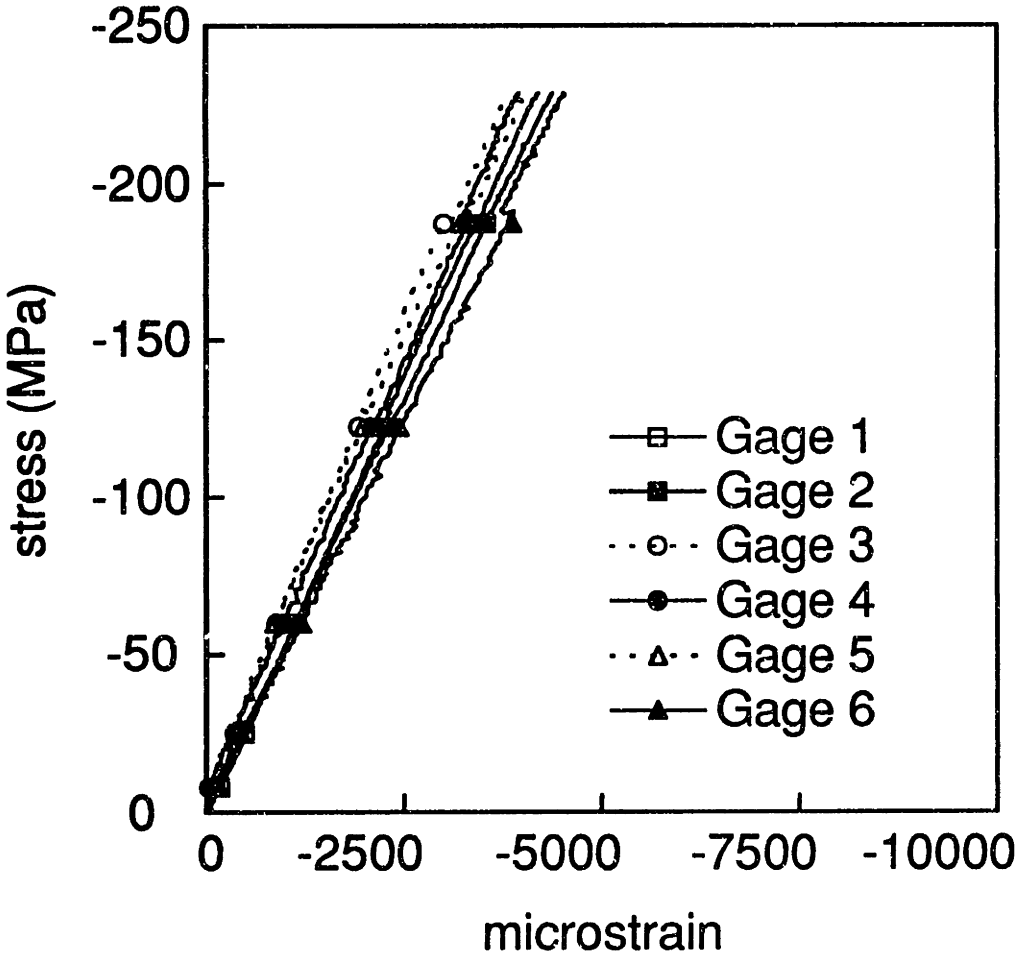

Figure 6.57 Plot of strain versus far-field applied stress for a medium B specimen damaged by a level 1 impact event (specimens B-M-IL1)

to 16% higher than its counterpart on the rough side. The average slope of the gages is 54.9 MPa, substantially lower than the calculated modulus of 64.3 MPa but closer to the measured modulus of the undamaged specimens, 58.1 MPa. The other medium B specimen displayed similar behavior as shown in Figure 6.58. The six gages are less closely grouped for this specimen, and a difference of 24% is noted between the slopes of gages 1 and 2. The gages 1 & 2 pair has the lowest average slope of the three back-to-back pairs, 53.0 MPa compared to 65.2 and 60.7 MPa. The average slope of the six gages is 59.6 MPa, which is less than the calculated modulus but more than the measured modulus of the undamaged specimens. The stress-strain plots of the two specimens from the A layup which exhibited this type of behavior are shown in Figures 6.59 and 6.60. In the first of these, the gages remain well bunched except for gage 5 which consistently reads a lower strain. The slope of gage 5 is 53.3 GPa, while the slopes of the other gages are between 42.0 and 47.8 GPa. Thus, the slope of all gages except gage 5 is lower than the calculated modulus for the A layup of 52.7 GPa and the measured modulus of 50.2 MPa for the undamaged specimens. Within each pair of back-to-back gages, the slope of the gage on the smooth side facesheet is 7 to 13% higher than its counterpart on the rough side facesheet. In the second figure, the gages show less grouping, especially as the stress level becomes higher. The slope of the gages on the smooth side stays the same or increases, while the slope of those on the rough facesheet decreases. The gage with the highest slope was gage 3 with 59.1 GPa, while gage 2 had the lowest slope with 40.4 GPa. The slope of the gage on the smooth facesheet is 9 to 36% higher than the slope of its counterpart on the rough facesheet. The average slope of the gages off of the centerline is 45.6 GPa, while the slopes of the pairs on the centerline are 50.0 GPa and 52.3

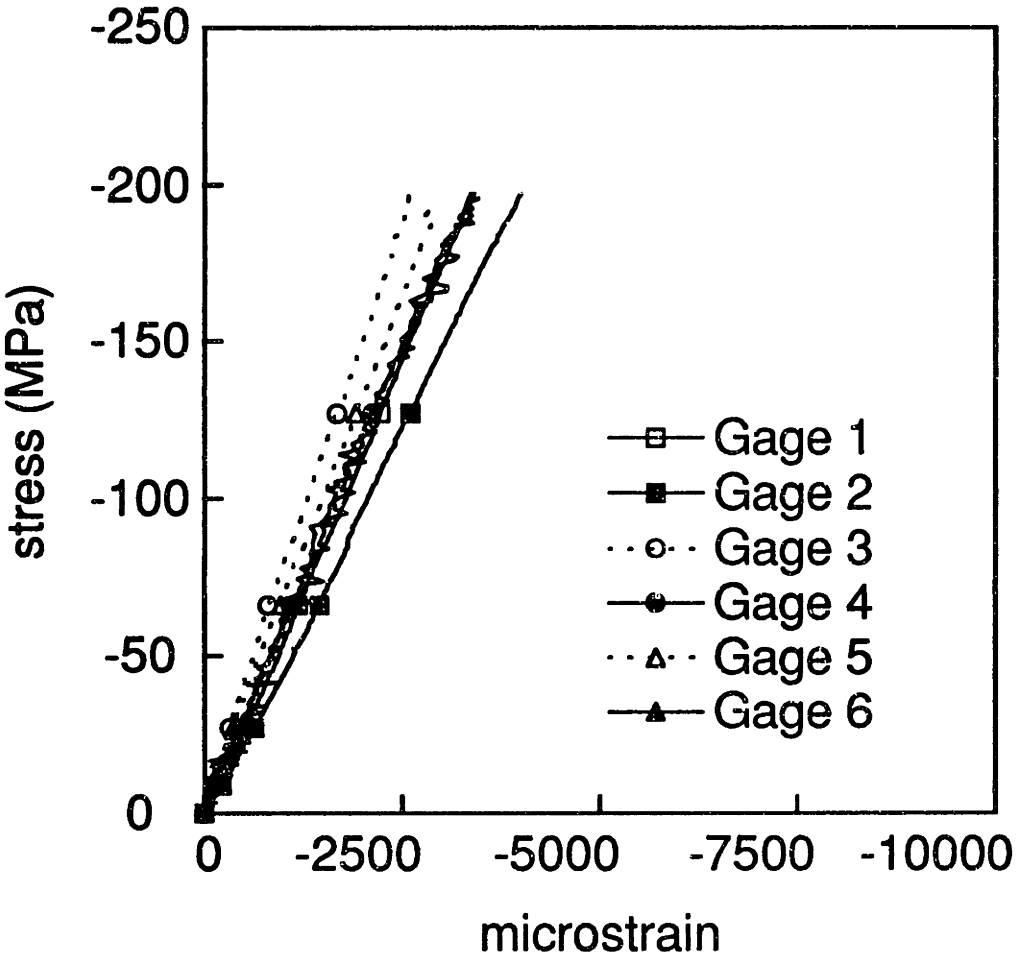

Figure 6.58 Plot of strain versus far-field applied stress for a medium B specimen damaged by a level 2 impact event (specimen B-M-IL2).

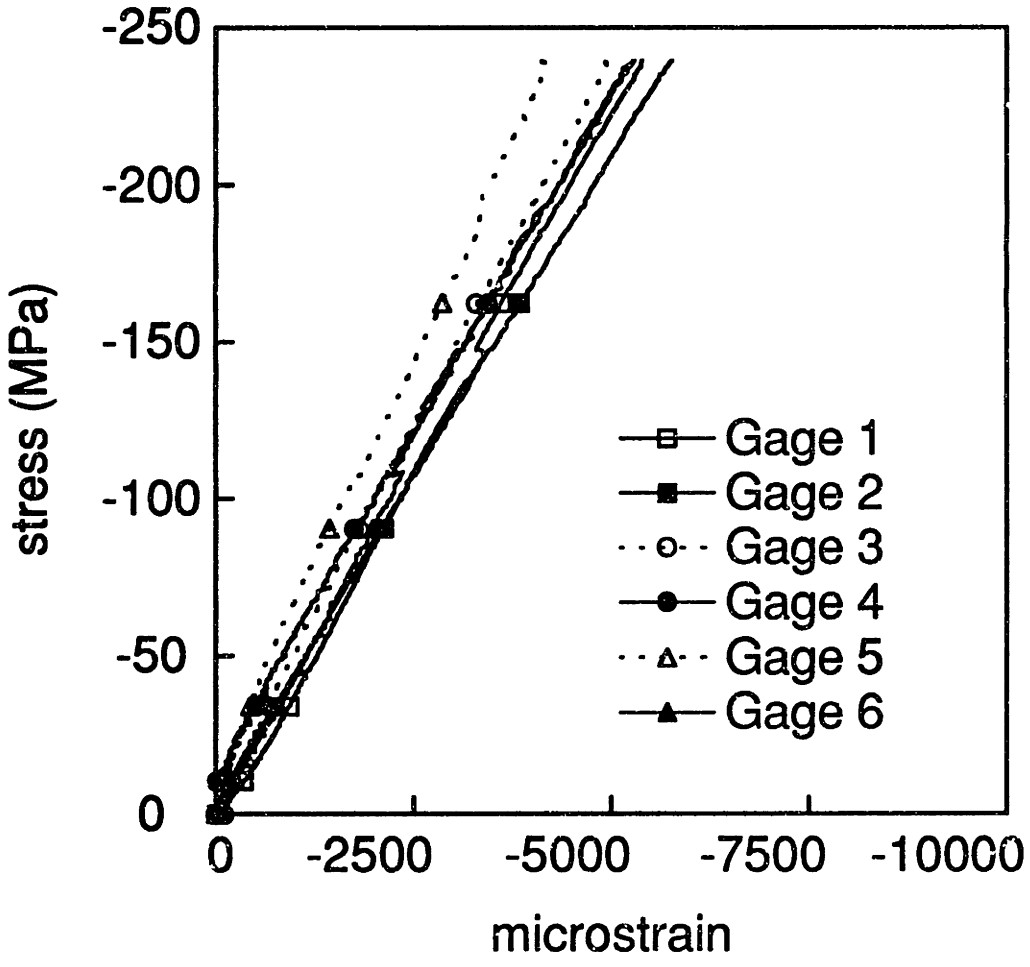

Figure 6.59 Plot of strain versus far-field applied stress for a medium A specimen damaged by a level 1 impact event (specimen A-M-IL1).

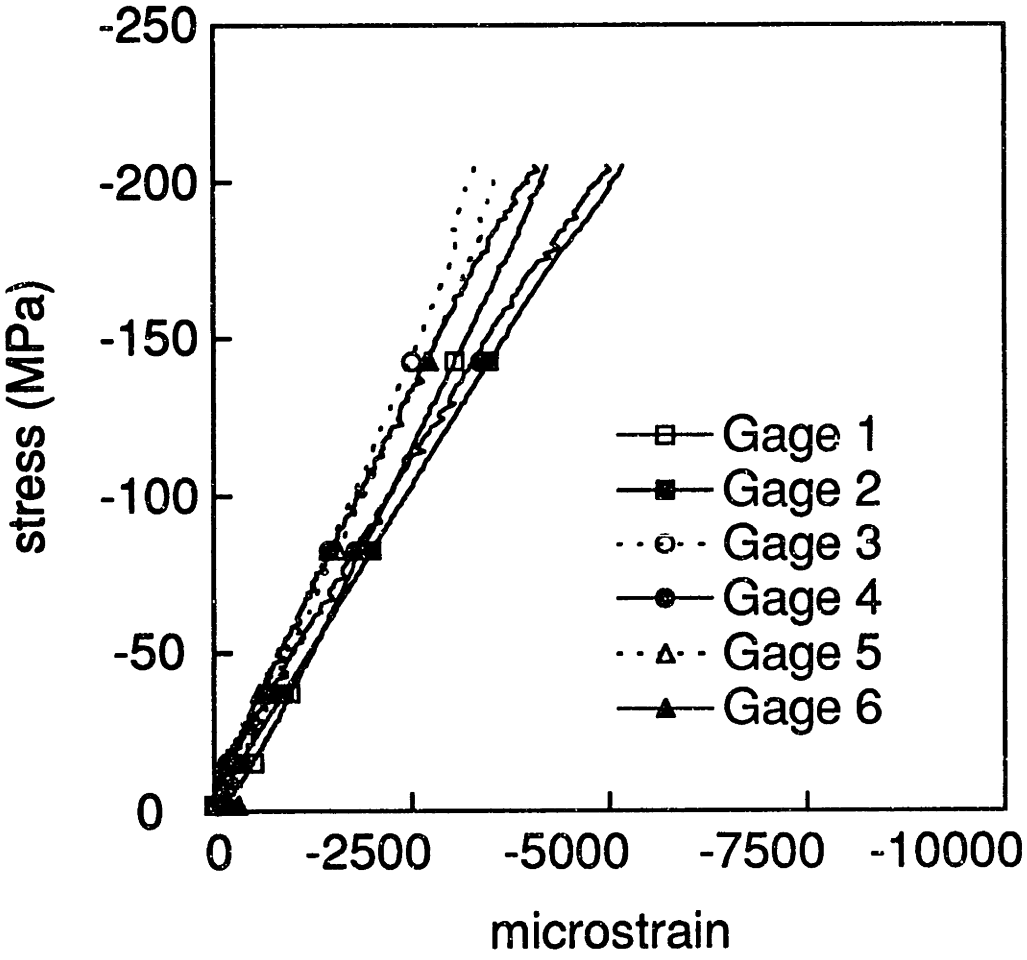

Figure 6.60 Plot of strain versus far-field applied stress for a medium A specimen damaged by a level 2 impact event (specimen A-M-IL2).

GPa, respectively. These values agree more closely with the calculated and measured moduli for the A specimens.

The second type of stress-strain behavior observed with the impacted specimens differs from the first in that the back gages no longer all read higher than the front gages. For these specimens, gage 5, which is located above the dimple, reads higher than its counterpart gage 6 on the rough side facesheet. This behavior was manifested by specimens A-L-IL1 and B-L-IL1. Plots of the strain gage data for these impacted specimens are given in Figures 6.61 and 6.62. For the specimen shown in Figure 6.61, the average slope of the gage 1 & 2 pair is higher than that of the other two pairs, 46.5 MPa versus 50.0 and 49.8 MPa. Percentage differences between the slopes of the back-to-back gages are 10 to 15%. Among the gages on the smooth side, only gage 5 has a lower slope than its counterpart on the rough side. The average slope of the six gages is 49.0 MPa, less than the calculated modulus of 52.7 MPa and the measured modulus of the undamaged specimens of 50.2 MPa. It is almost the same as the average slope of the notched A specimens. For the stress-strain behavior of the large B specimen shown in Figure 6.62, the gages off of the centerline (1 & 2) again give higher strain readings than those in line with the dimple. The average slope of this pair is 50.5 MPa compared to 55.8 and 58.3 MPa for the other two pairs. Gage 6, located on the rough facesheet, has a slope of 59.7 GPa, while the slope of its counterpart on the smooth facesheet, gage 5, is only 56.8 GPa. In fact, the pairs of gages are more closely grouped for this specimen than for most other impact specimens, showing a difference of 10%, 3%, and 5% for the three pairs 1 & 2, 3 & 4, and 4 & 5. The average slope of the six gages is 54.9 MPa, less than the calculated modulus of 64.3 and the measured modulus of the undamaged specimens of 58.1 MPa.

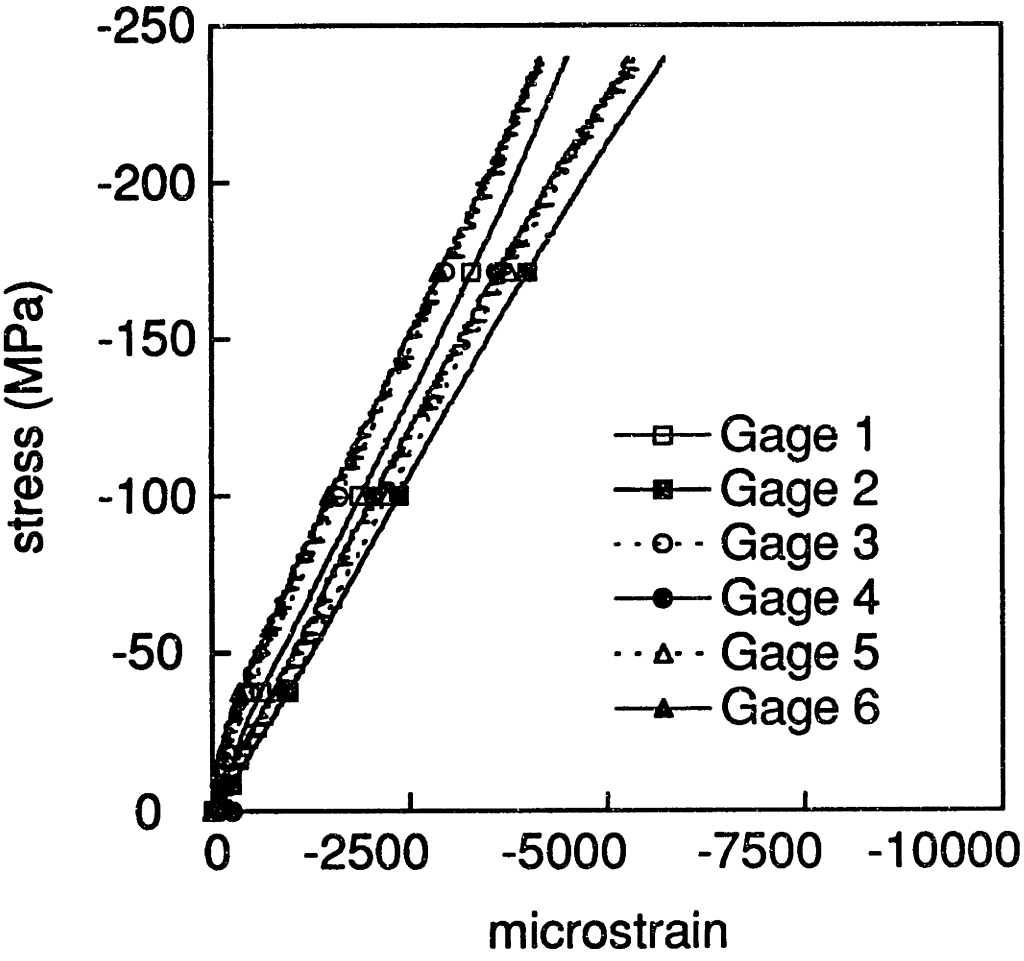

Figure 6.61 Plot of strain versus far-field applied stress for a large A specimen damaged by a level 1 impact event (specimen A-L-IL1).

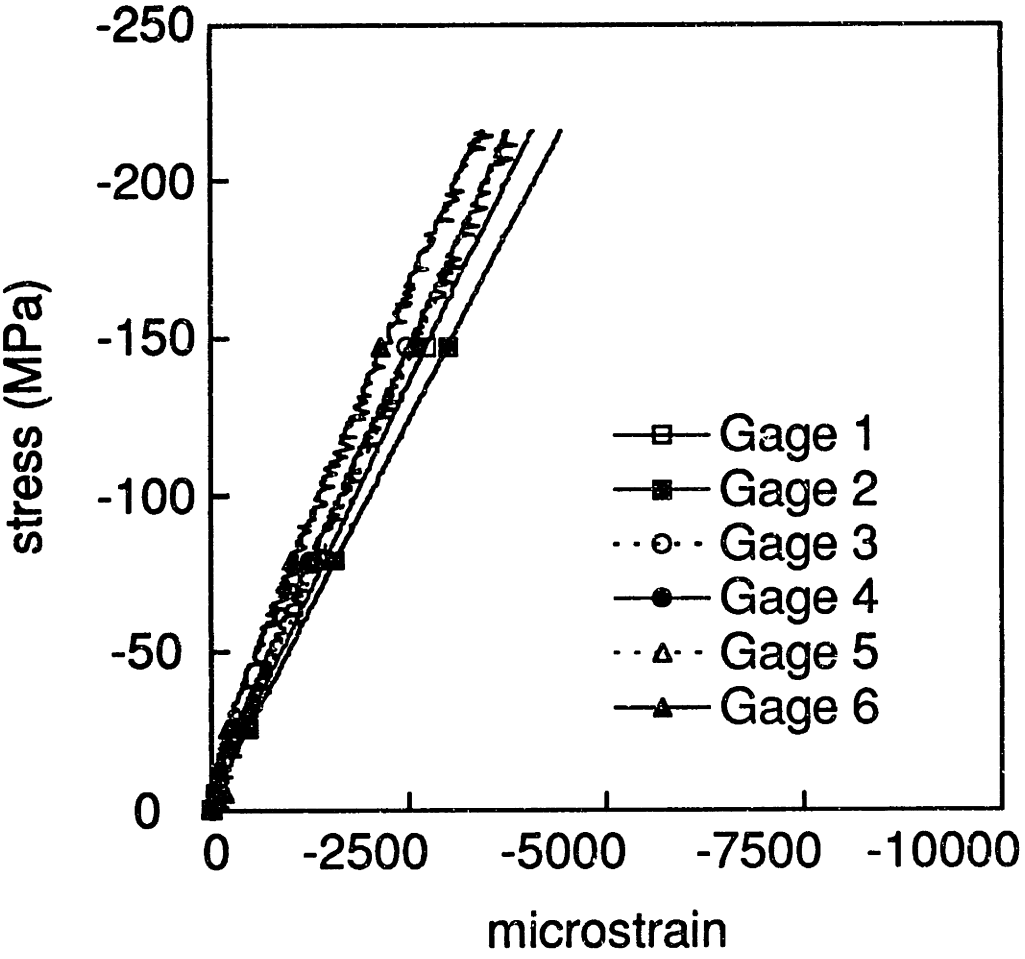

Figure 6.62 Plot of strain versus far-field stress level for a large B specimen damaged by a level 1 impact event (specimen B-L-IL1)

For all the impacted specimens, the gages are not closely grouped. There can be a substantial difference between their slopes. In general, gages 1 and 2, which are located off of the centerline, have higher strain readings and lower slopes than the other gages located above or below the notch. Also, the gages on the rough side consistently have higher strain readings and lower strains than their counterparts on the smooth side. The exception to this is the two large impacted specimens. For these, gage 5 on the smooth side has higher readings than its counterpart gage 6 on the rough side. The average slope of the gages for the three specimens of the A layup are 46.4, 49.3, and 49.0 MPa, respectively. These are all somewhat lower than the calculated modulus of 52.7 MPa, but the latter two are quite close to the measured modulus of the undamaged specimens of 50.2 MPa. The average slopes of the strain gages for the three impacted specimens of the B layup are 54.9, 59.6, and 54.9 MPa, respectively. These values are all lower than the calculated modulus of 64.3 MPa, but they are close to the measured modulus of the undamaged specimens of 58.1 MPa. No effect of specimen size or impact level on the slopes of the gages can be determined from these six specimens.

Images from the shadow moiré technique were recorded with a video camera. Images from discrete load levels were digitized, and representative images are given here. For the two A specimens impacted with a level 1 event, the dimple grows in a smooth manner. This is shown in the several digitized images of the dimple throughout the loading of such a specimen given in Figure 6.63. Initially circular, the dimple becomes ovalized by growth along the y-axis. This growth continues along the y-axis until failure occurs. It should be noted that the last image shown in this sequence, the one for 238 MPa, is the last image recorded by the camera

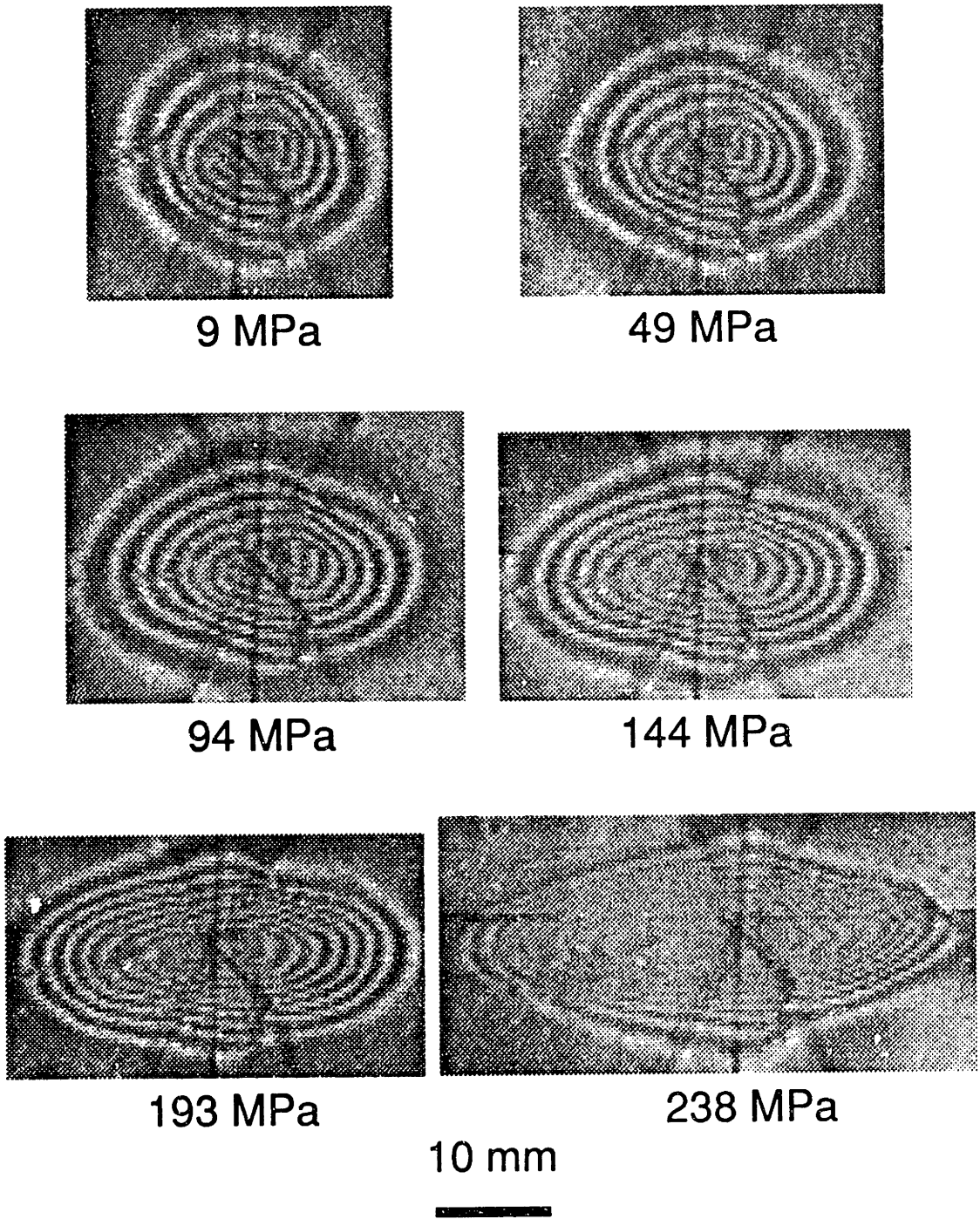

Figure 6.63 Digitized moiré fringe patterns for a medium A specimen under compressive loading after damage by a level 1 impact (specimen A-M-IL1).

before failure of the specimen.

Specimens of the B layup damaged by a level 1 impact display a slightly different dimple growth pattern. A sequence of images for such a specimen is shown in Figure 6.64. In the early stages of loading, the dimple grows as a smooth oval by elongation along the y-axis. At the 90 MPa load level, however, a perturbation has appeared in the dimple shape. Initially, the perturbation appears to be two small scooped-out regions on the edge of the dimple at an angle of approximately 45° from the vertical centerline. This perturbation grows until, at 224 MPa, it has developed a separate region outside of the main dimple. It is interesting to note the sharp boundary on the sub-dimple to the lower left of the main dimple. This pattern may represent surface cracking of the specimen or delamination. In the last image recorded before the specimen failed at 229 MPa, some type of splitting or cracking of the plies can be observed to the right of the dimple. It should be noted that this splitting or cracking occurs only in the very last stages of dimple growth, and the majority of the growth is in the form of smooth ovalization and lengthening of the dimple.

When specimens are damaged by a level 2 impact, the surface suffers extensive damage, and the facesheet damage in the impact region seems to cause irregular growth of the dimple. A sequence of such images is shown in Figure 6.65 for a medium A specimen. The initial damage can be seen in the first image. As loading progresses, growth of the dimple occurs locally, especially on the upper right portion. This region grows until it dominates the damage growth. Finally, this area becomes unstable and failure occurs. A sequence of images for a medium B specimen damaged by a level 2 impact is shown in Figure 6.66. The impact event has created extensive surface damage in the dimple region of this specimen. Growth of the dimple as the

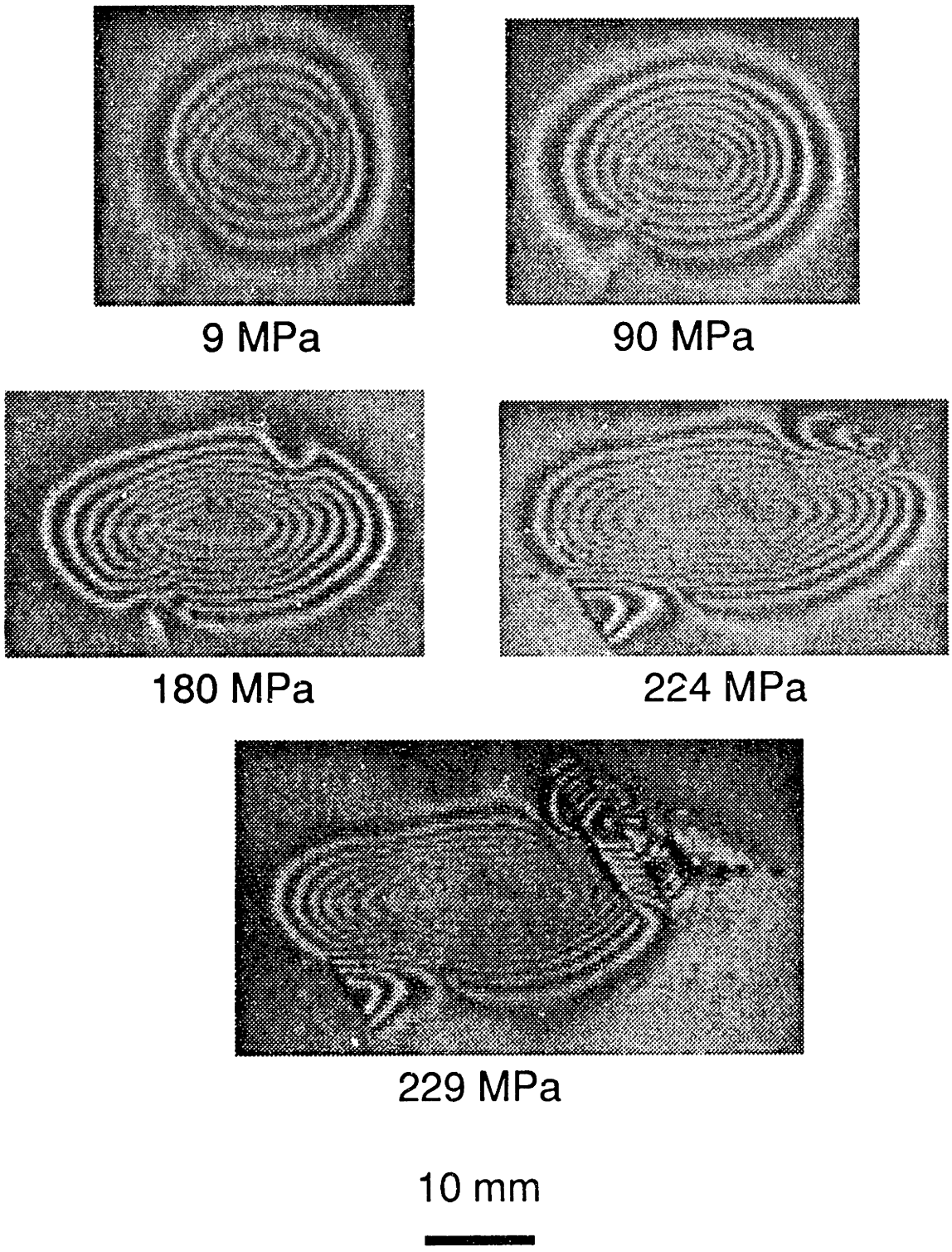

Figure 6.64 Digitized moiré fringe patterns for a medium B specimen under compressive loading after damage by a level 1 impact (specimen B-M-IL1).

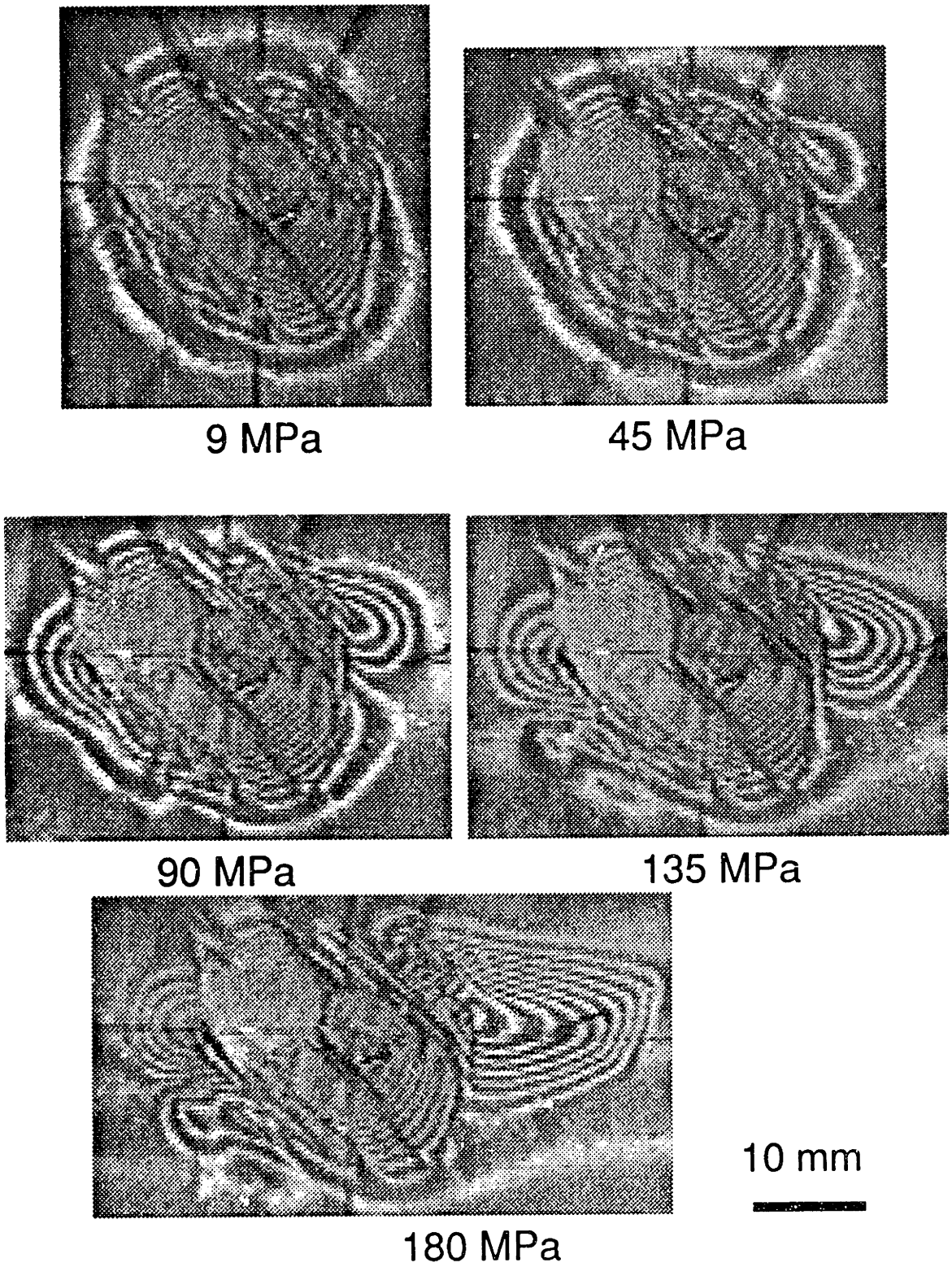

Figure 6.65 Digitized moiré fringe patterns for a medium A specimen under compressive loading after damage by a level 2 impact (specimen A-M-IL2).

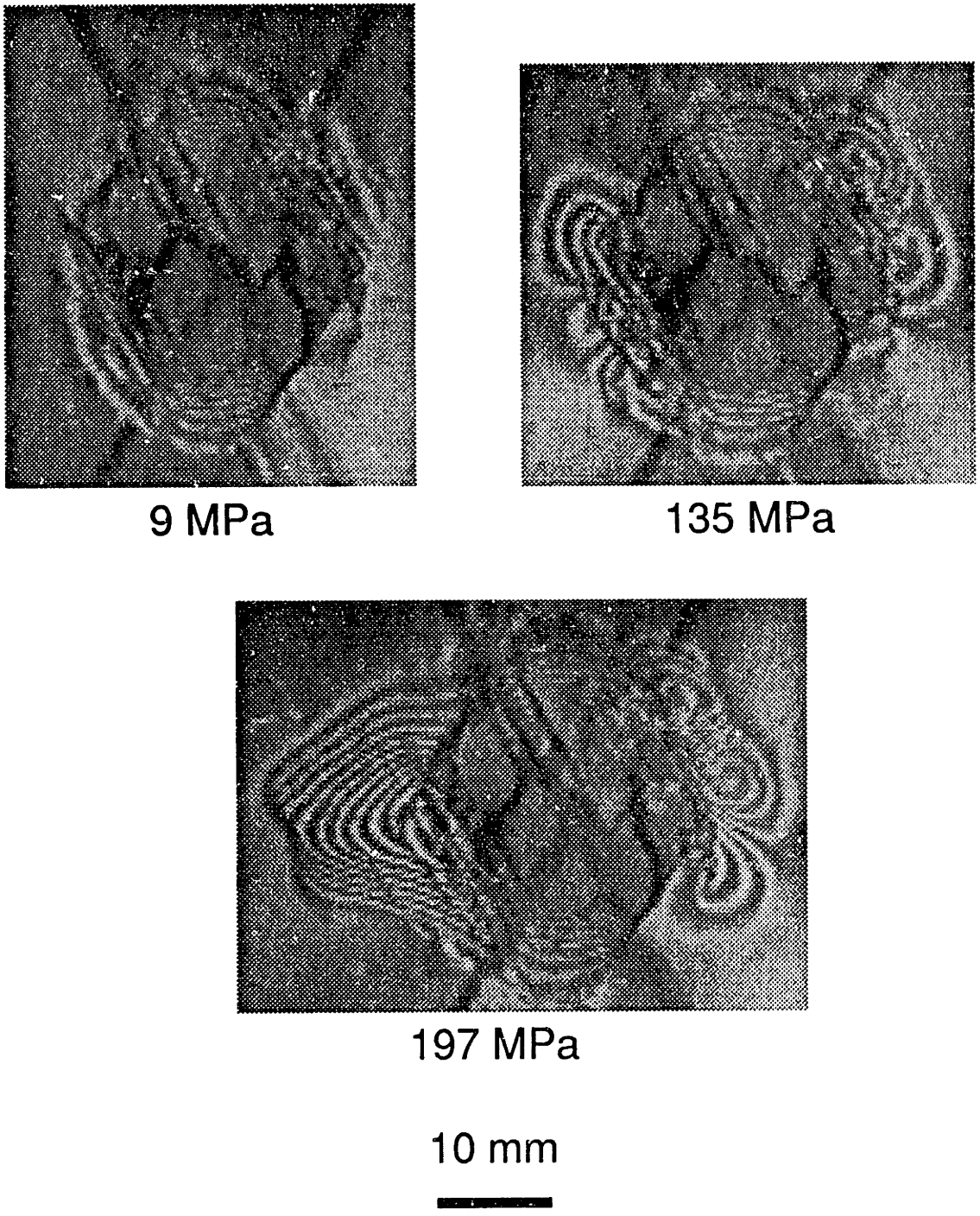

Figure 6.66 Digitized moiré fringe patterns for a medium B specimen under compressive loading after damage by a level 2 impact (specimen B-M-IL2).

stress level is raised to 135 MPa occurs in small "pockets" on the upper right and lower left portions of the dimple. At a far-field stress level of 197 MPa, the last level recorded before failure of the specimen, a small amount of additional growth has occurred on the right side, but the dimple has grown extensively on the left side. The moiré images for the two specimens impacted at level 2 appear, at first inspection, different but are actually quite similar. In both cases, growth occurs locally around much of the edge of the dimple. As loading progresses, one region grows much more than the others and dominates the damage growth before failure occurs.

For specimens impacted at level 1, the dimple profile has been determined using the moiré interferometry as described in Chapter 5. Such measurements were not possible for the specimens impacted at level 2 because of the surface damage in the dimple region. This surface damage makes it impossible to distinguish the fringe patterns in the dimple. During loading of an impacted A specimen, the dimple does not grow substantially in the x-direction, as shown in Figure 6.67. A great deal of growth does, however, occur in the y-direction as shown in Figure 6.68. The dimple becomes wider along the y-axis, but does not become substantially deeper because a relatively flat region develops along the y-axis in the center of the dimple. Growth is similar for a B specimen damaged by a level 1 impact event as shown in Figures 6.69 and 6.70.

Another way to look at the damage growth is to consider the length of the dimple in the y-direction as a function of the applied stress. This has the benefit of allowing the specimens with extensive surface damage to be considered. The growth of a dimple in A specimens for level 1 and level 2 impacts is shown in Figure 6.71. The initial damage size was greater with the level 2 impact. Growth was steady, and the last recorded dimple size

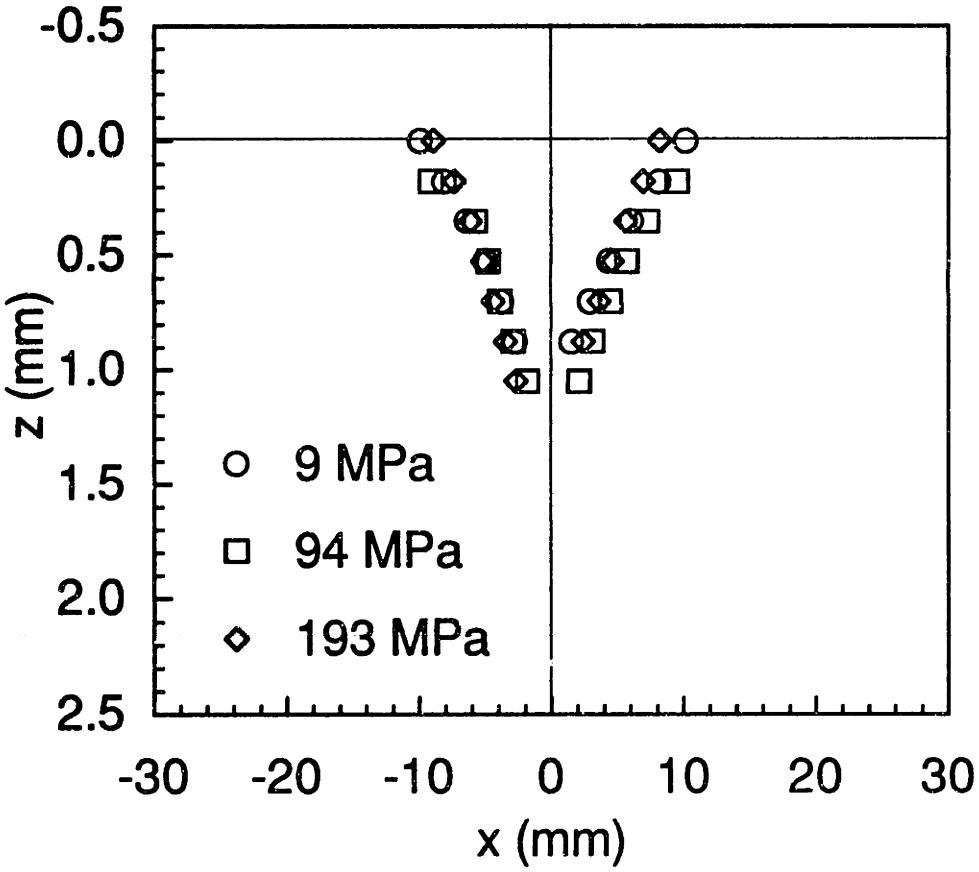

Figure 6.67 Dimple profiles along the x-axis at various applied stress levels for a medium A specimen damaged by a level 1 impact (specimen A-M-IL1).

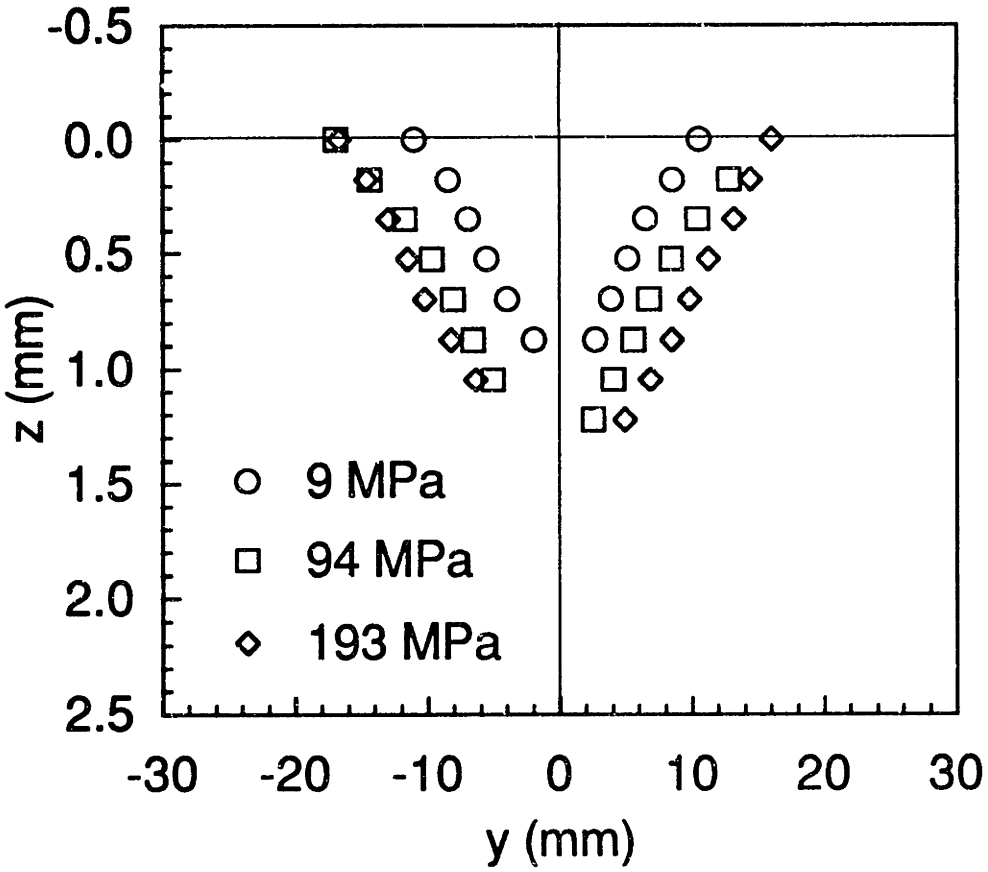

Figure 6.68 Dimple profiles along the y-axis at various applied stress levels for a medium A specimen damaged by a level 1 impact (specimen A-M-IL1).

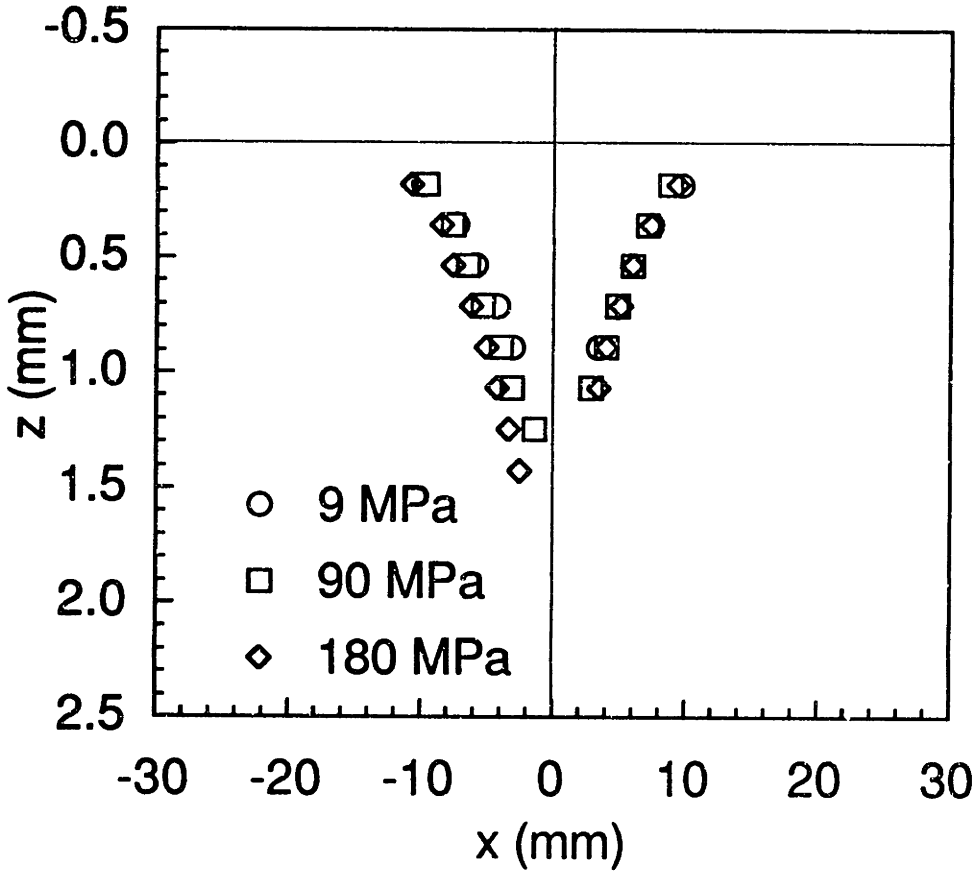

Figure 6.69 Dimple profiles along the x-axis at various applied stress levels for a medium B specimen damaged by a level 1 impact (specimen B-M-IL1).

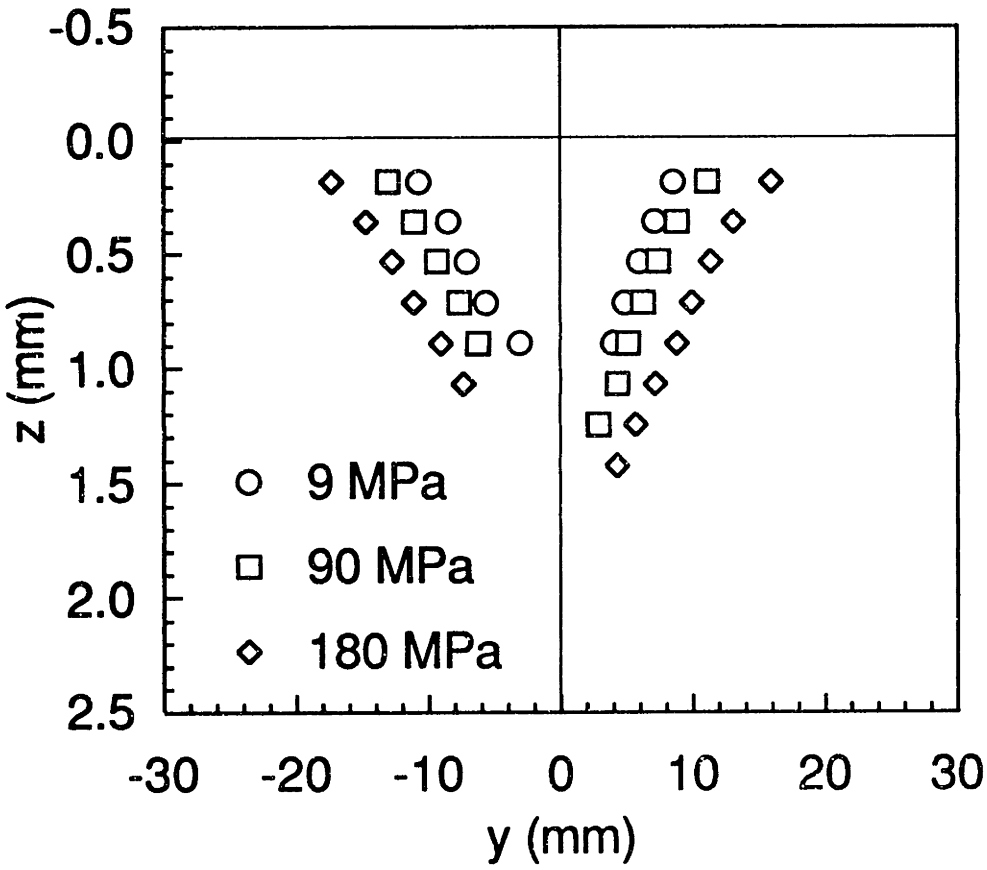

Figure 6.70 Dimple profiles along the y-axis at various applied stress levels for a medium B specimen damaged by a level 1 impact (specimen B-M-IL1).

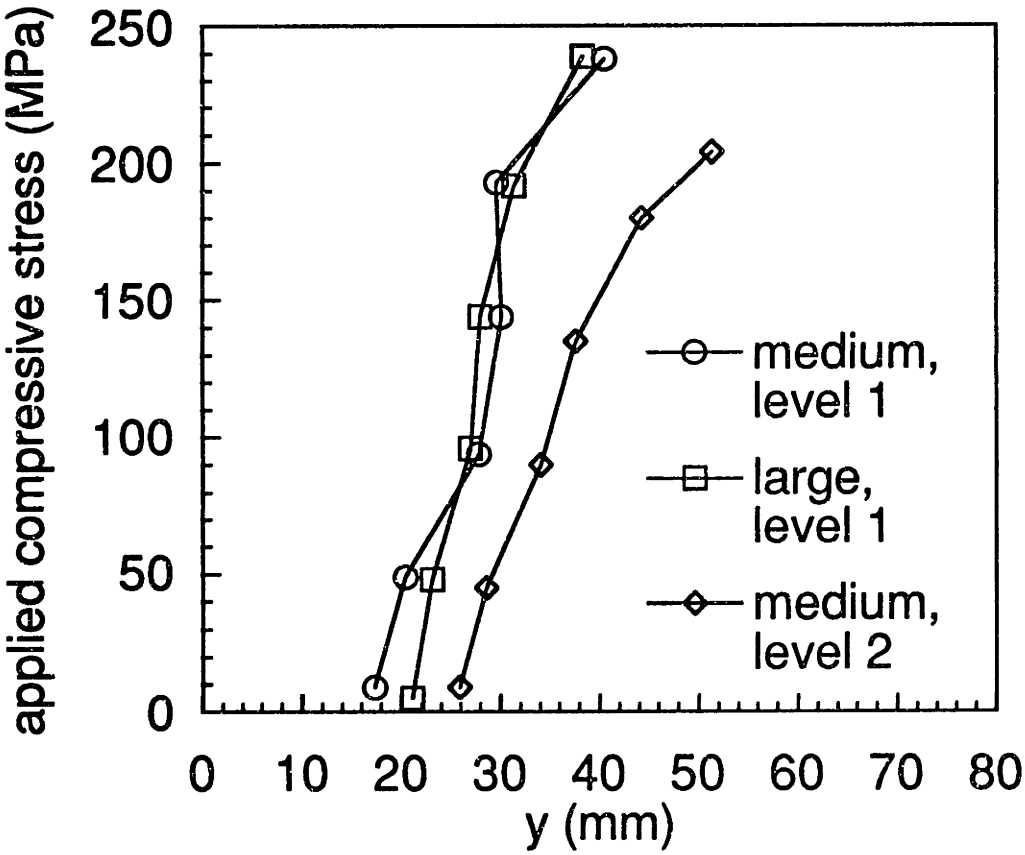

Figure 6.71 Dimension of dimple parallel to the y-axis versus far-field applied stress level for A specimens damaged by level 1 and level 2 impacts (specimens A-M-IL1, A-L-IL1, and A-M-IL2).

was approximately 51 mm. The initial dimple sizes differ slightly for the medium and large level 1 impact specimens. However, the dimple sizes for the two are very close for stress levels of 100 MPa until failure. In the range of 100 to 200 MPa, relatively little change in the dimple width occurs. Above this level, a region of rapid growth leads up to failure. The maximum dimple size recorded for these two is approximately 40 mm, which is about 20% less than the maximum size for the level 2 specimen. Growth of the dimple in the B specimens with both level 1 and level 2 impacts is shown in Figure 6.72. Again, the dimple size for the level 2 specimen is greater than for the level 1 specimens. The dimple grows steadily until the last recorded size before failure is approximately 41 mm. The medium and large level 1 specimens have similar dimple sizes for a given stress. In fact, the curves for the two cross each other twice. The last recorded dimple width is 40 mm for the medium specimen and 36 mm for the large specimen. These widths are much closer to the maximum width of the level 2 specimen than was the case for the A specimens. The maximum widths for all the level 1 specimens are within the range of 36 to 41 mm. The maximum widths for the two level 2 specimens are 51 and 41 for the two specimens.

Growth of the dimple was also predicted using the dimple propagation model described in Chapter 4. The dimple growth was predicted for an A specimen and a B specimen. Most of the parameters for the dimple growth model are given in Chapter 4, and the additional parameters specific to the damage of an individual specimen are given in Table 6.16. The initial in-plane dimple dimensions, R_X and R_Y, are chosen to correspond with the distance to the zeroeth order moiré fringe when the specimen is unloaded. R_0, the initial radius of crushed core is not measured experimentally. In his investigation, Tsang [45] found the region of core

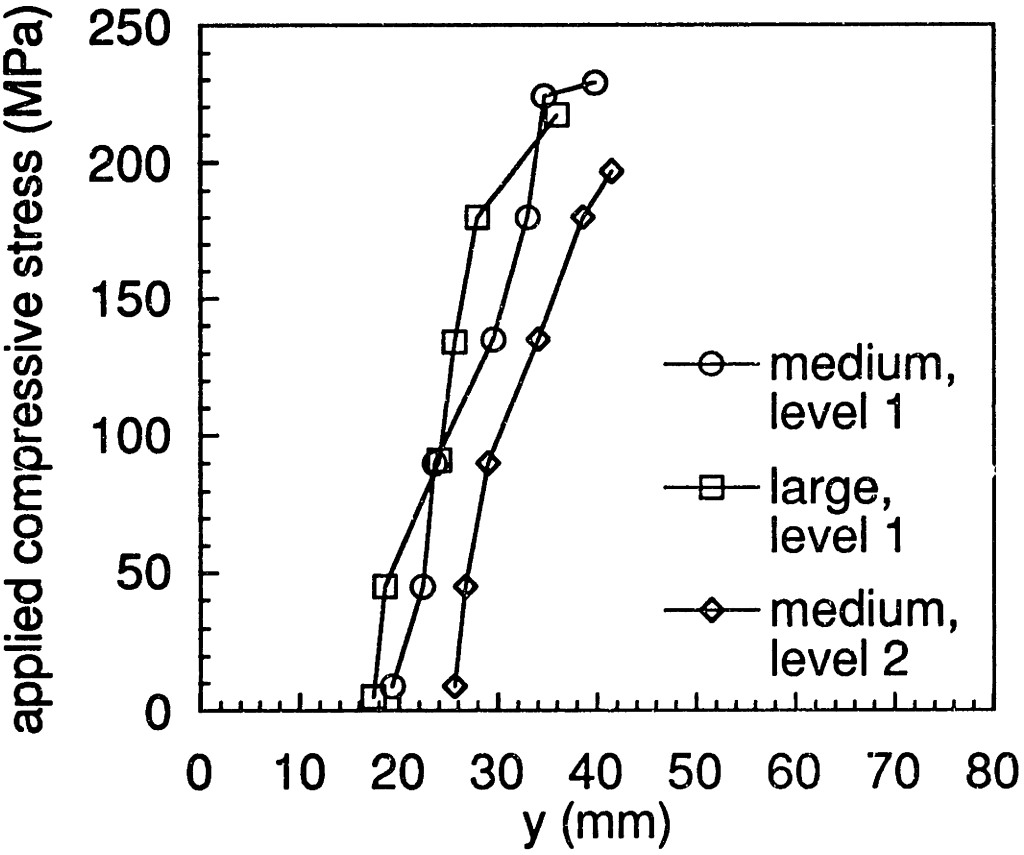

Figure 6.72 Dimension of dimple parallel to the y-axis versus far-field applied stress level for B specimens damaged by level 1 and level 2 impacts (specimens B-M-IL1, B-L-IL1, and B-M-IL2).

Table 6.16 Additional input parameters for program GROWTH for A specimen

Parameter	Layup	
	A	B
R_x	10.8 mm	11.4 mm
R_y	10.0 mm	12.5 mm
R_o	12.0 mm	14.0 mm
ξ_o	1.09 mm	1.25 mm

crushing to be nearly the same size as the dimple. Thus, as a conservative estimate, the size of the initial region of core crushing is chosen to be approximately 1 mm larger than the larger of R_x and R_y. Finally, the initial depth at the center of the dimple, ξ_o, was measured using a dial gauge. The assumed initial dimple shape and the measured initial dimple shape are shown in Figure 6.73 for the A specimen and in Figure 6.74 for the B specimen. In both cases, the assumed profile is less deep than the measured profile except at the very center. This is because of the nature of the functions used to produce the initial dimple profile. The dimple can be better approximated by using more terms in the infinite series, but this results in increased computational difficulty and will eventually make the problem intractable.

The prediction of the dimple growth in an A specimen for a stress level of -238 MPa, the experimental failure load for this specimen, is shown with the experimentally measured dimple profiles in Figure 6.75. The assumed and predicted dimple shapes are shown as lines. The dimple growth is highly underpredicted by the dimple growth model. In fact, the model predicts virtually no growth of the dimple. Similar behavior is observed when the model is applied to the B specimens, as shown in Figure 6.76.

During testing, an accidental event provided a situation which shows an interesting aspect of the growth of the dimple. One large A specimen had been impacted at level 1. When tested, this specimen sustained a load of 445 kN (100,000 lbs). At this load, the safety interlocks of the testing machine shut down the hydraulic system as they were designed to do. This immediately unloaded the specimen. The maximum stress applied to this specimen at hydraulic shutdown was 239 MPa, greater than the failure

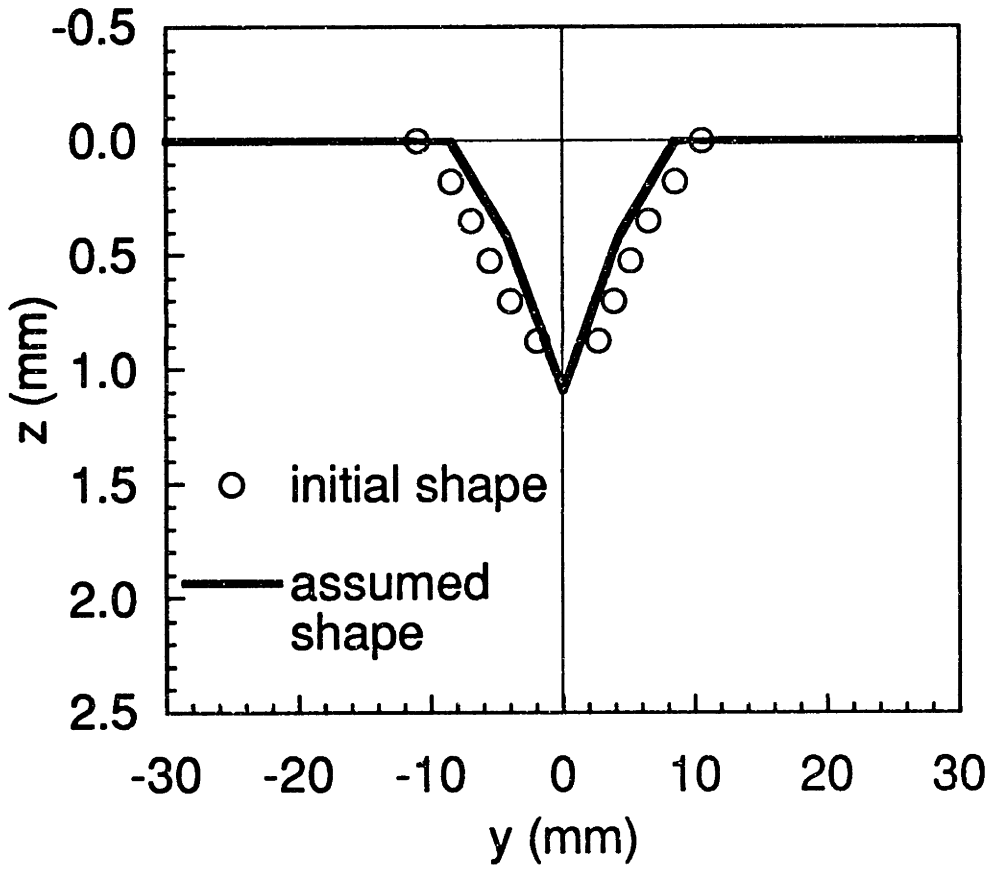

Figure 6.73 Initial measured dimple profile and the assumed dimple profile along the y-axis for an A specimen damaged by a level 1 impact (specimen A-M-IL1).

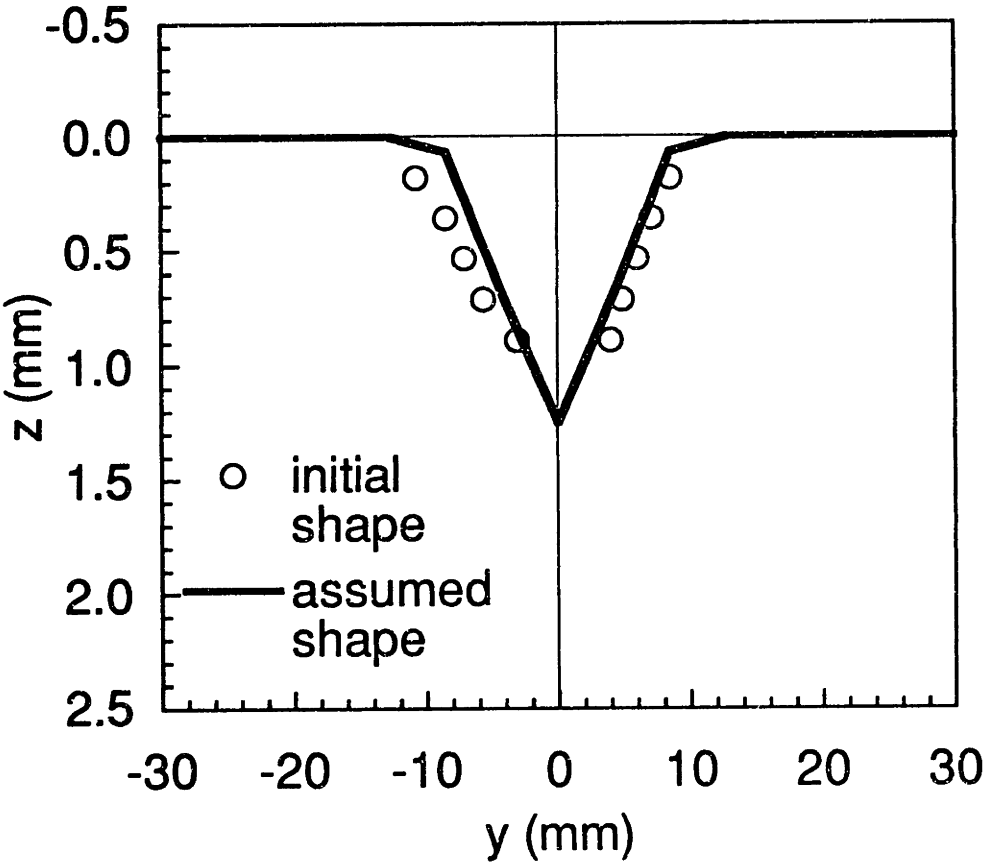

Figure 6.74 Initial measured dimple profile and the assumed dimple profile along the y-axis for a B specimen damaged by a level 1 impact (specimen B-M-IL1).

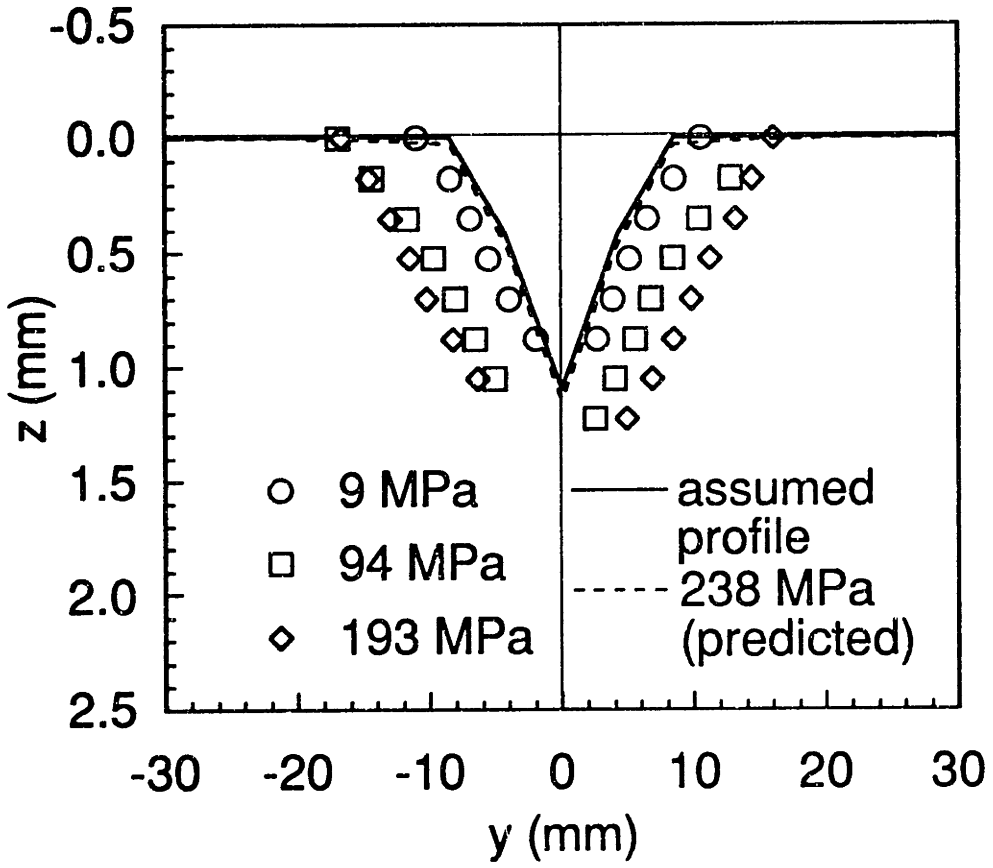

Figure 6.75 Experimental and predicted dimple profiles along the y-axis at various applied stress levels for a medium A specimen damaged by a level 1 impact (specimen A-M-IL1).

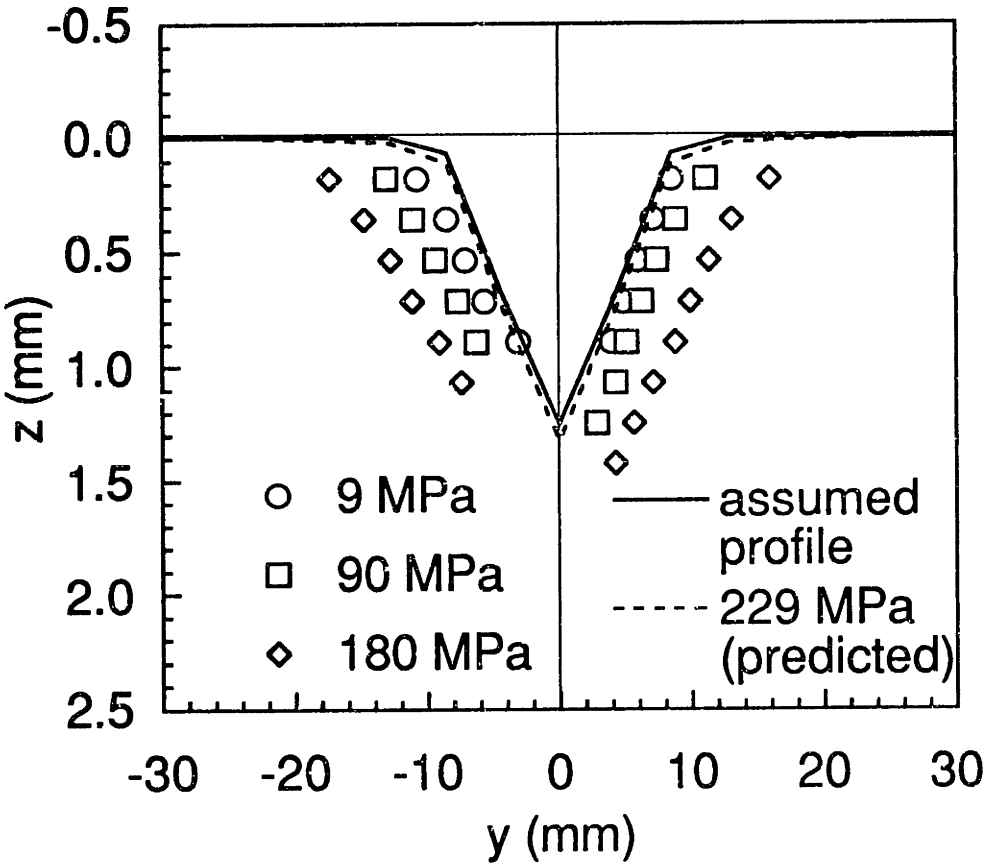

Figure 6.76 Experimental and predicted dimple profiles along the y-axis at various applied stress levels for a medium B specimen damaged by a level 1 impact (specimen B-M-IL1).

stress of the medium specimen damaged by the same impact level. Similarly, the growth of the dimple in the y-direction had reached nearly the same size as the size of the dimple in the medium specimen at failure, as shown in Figure 6.71. However, after loading was removed, the dimple returned to nearly the same size it had before testing. The recorded moiré images of the initial dimple and the dimple after unloading are shown in Figure 6.77, The moiré images show that the left edge of the dimple has been elongated somewhat on the left side of the dimple, noticeably changing the overall shape of the dimple. However, this elongation is probably not visible to the naked eye. Also, some sort or matrix cracking or ply splitting has formed on the right side of the dimple. However, the main part of the dimple has the same or a slightly less deep profile than it did initially, as can be seen from the dimple profile along the y-axis shown in Figure 6.78. The change in depth of the dimple is within the possible error for the measurements and thus may not be significant. So, despite the specimen having been loaded to a stress level very close to its failure stress, the main part of the dimple appears tc have changed little after it is unloaded.

Failure of the specimens was evident as a fracture along the y-axis in the impacted facesheet. As with the notched specimens, the plies of the facesheets failed primarily by a fiber-dominated mechanism within a narrow band along the y-axis. Some splitting was observed in the outer 45° ply of the A specimens and the outer 30° ply of the B specimens. These splits were generally short and grew from the line of failure. In the two specimens impacted at level 2, parts of the outer ply near the dimple remain intact but are delaminated and buckled off of the facesheet. A typical failure of an impacted specimen of the A layup is shown in Figure 6.79, while failure of a B specimen is shown in Figure 6.80. For three of the

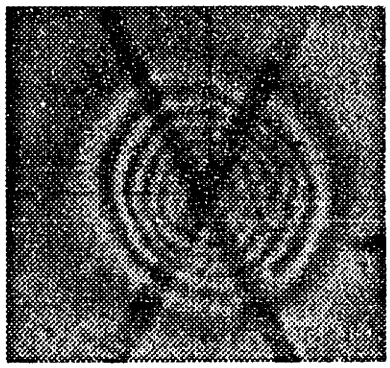

Initial Dimple

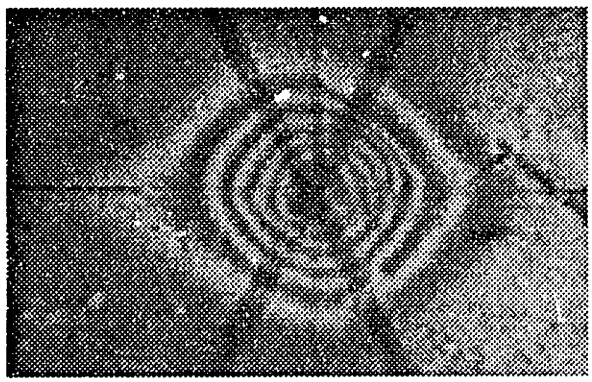

Unloaded Dimple

10 mm

Figure 6.77 Digitized moiré fringe patterns for the dimple before testing and after the shutdown of the testing machine in a large A specimen damaged by a level 1 impact event.

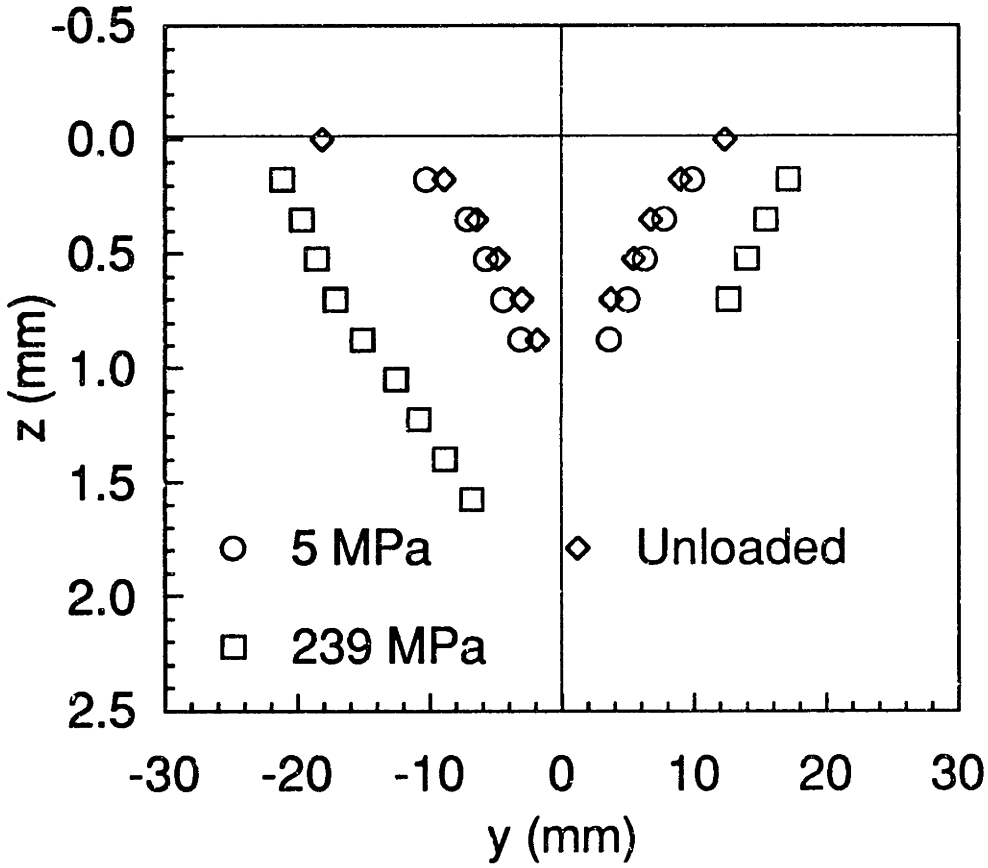

Figure 6.78 Dimple profile along the y-axis for a large A specimen damaged by a level 1 impact. Stress levels shown represent the beginning of the test, the point just prior to machine shutdown, and unloaded after hydraulic shutdown (specimen A-L-IL1).

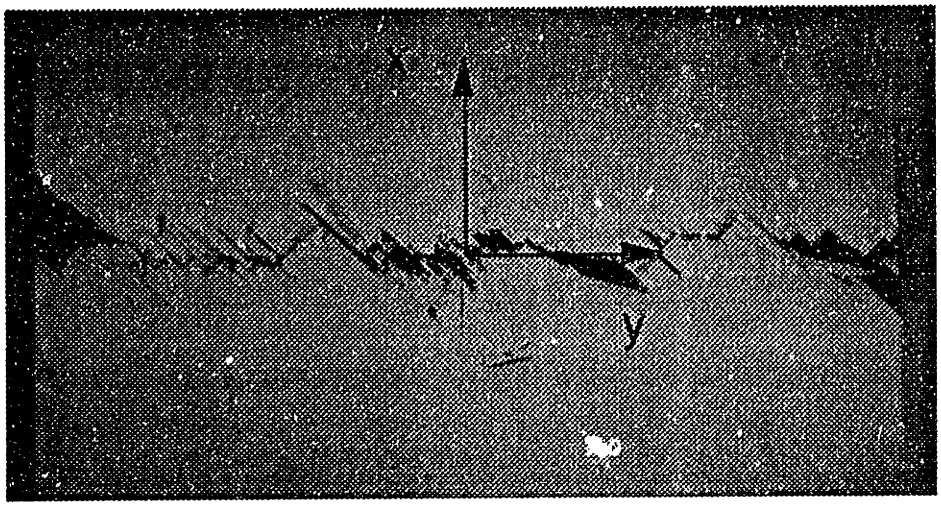

Figure 6.79 Photograph of a typical failure of an impacted specimen of the A layup along the y-axis of the impacted facesheet (specimen A-M-II.1).

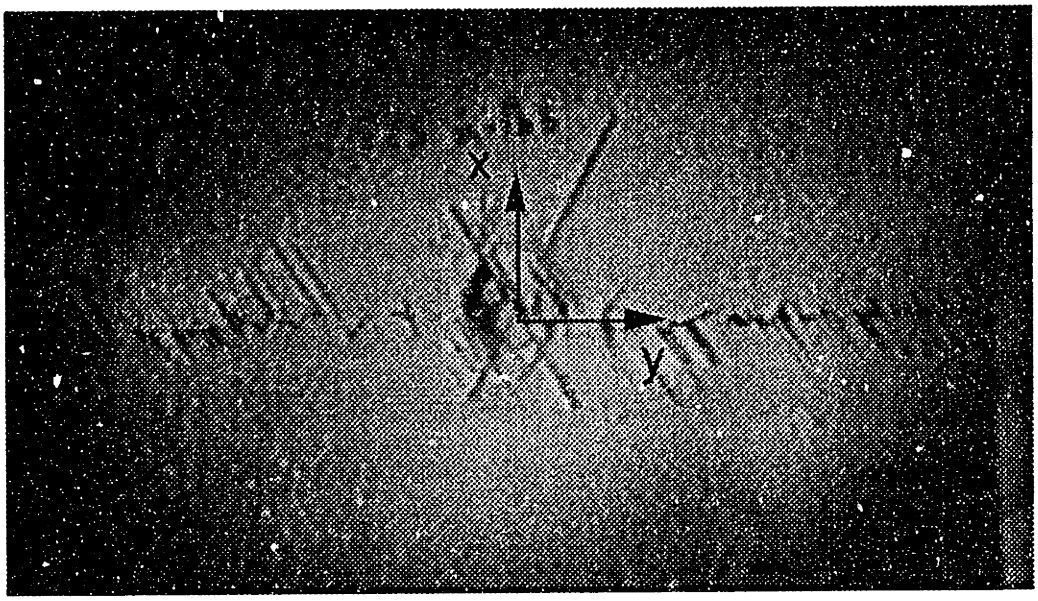

Figure 6.80 Photograph of a typical failure of an impacted specimen of the B layup along y-axis of impacted facesheet (specimen B-M-IL2).

medium impacted specimens, the back face remains visibly undamaged. However in the medium and large B specimens impacted at level 1, the back facesheet fails and a permanently bent shape results. With these two specimens, the rough side, undamaged, facesheet peels away from the core, though this probably occurs after failure of the impacted facesheet.

Failure stresses for the impacted specimens are given in Table 6.17. As already mentioned, the large A specimen damaged by a level 1 impact did not fail because the load exceeded the capacity of the testing machine. The stress at which the machine shut down is very close to the failure stress of the medium A specimen impacted at level 1. The A specimen impacted at level 2, which sustained more damage, failed at a slightly lower stress level, approximately 15% lower than the A specimen impacted at level 1. For the B layup, the medium and large specimens impacted at level 1 failed at stress levels within 5% of each other. The B specimen impacted at level 2 failed at a stress approximately 10-14% lower than the specimens impacted at level 1. Thus, the additional damage of the specimens impacted at level 2 does reduce their strengths.

Table 6.17 Failure stresses for impacted specimens

Specimen Size	Impact Event	Layup A	Layup B
M	level 1	238 MPa	229 MPa
L	level 1	> 239 MPa[a]	217 MPa
M	level 2	204 MPa	197 MPa

[a] specimen did not fail because capacity of testing machine was exceeded.

Chapter 7

Discussion

Findings of the present investigation are discussed in this chapter. Results presented in Chapter 6 are used as evidence for the discussion. Particular attention is given to assessing progress towards meeting the goals of this investigation as laid out in Chapter 3. The chapter is divided into four sections: the test method, effects of specimen size, notched compressive behavior, and compression after impact behavior. Discussion of the test method centers on the effectiveness of the test fixture and the specimens used. Discussion of the specimen size deals with the effects of the specimen length and width on the strain state and failure stress of the specimen. Within the discussion of notched behavior, the stress state in the specimen and the variables affecting failure stress are examined. Within the discussion of the compression after impact behavior, the observations on dimple growth are discussed and compared to those of previous investigations, and the use of the dimple growth model and the prediction of failure are examined.

7.1 Test Methods

Certain problems were associated with the testing methods used in this investigation. These problems must be examined and their effects, if any, on the results of the tests assessed. Most importantly, throughout the testing, difficulties in properly aligning the test fixture were encountered. These were especially noticeable when alignment was done by method 1, but

they affected the results of all tests.

Specimens tested after alignment by method 1 displayed behavior which will be termed "off-axis loading." Evidence for this behavior is obtained by considering the general region in which the strain gages were located. The four regions noted for this purpose, A, B, C, and D, are shown in Figure 7.1. Strain gages can be classified as placed in one of these regions or along the horizontal centerline. In the small undamaged specimens with strain gage configuration Undamaged 1, gage 1 (region A) gave lower readings and gage 3 (region C) gave higher readings than those on the centerline. Higher strain readings result in a smaller slope for the stress-strain curve of that gage. A similar behavior was observed in small notched specimens. Those with strain gage configuration Notch 1 had consistently higher readings from gage 1 (region B) than those on the horizontal centerline. For specimens with strain gage configuration Notch 2, gage 4 (region A) consistently read lower than gage 5 (region B). Furthermore, when a specimen was rotated in the fixture, the gage in region C gave higher strain readings than the gage located in region D. However, with all of these specimens, the out-of-plane deflection of the specimens was small and not correlated with the strain gage readings.

This phenomenon of "off-axis loading" could occur if the loading plates of the test fixture were not aligned properly with the axis of load application. A sketch of how this behavior might affect a specimen is shown in Figure 7.2. The ends of the specimen must conform to the plate in order for the load to be applied. However, equilibrium of the specimen requires that the forces applied from the ends act along the same line. Thus, the forces act preferentially on a different facesheet at each end. At the top of the specimen, the load is applied more to the rough side facesheet, and the

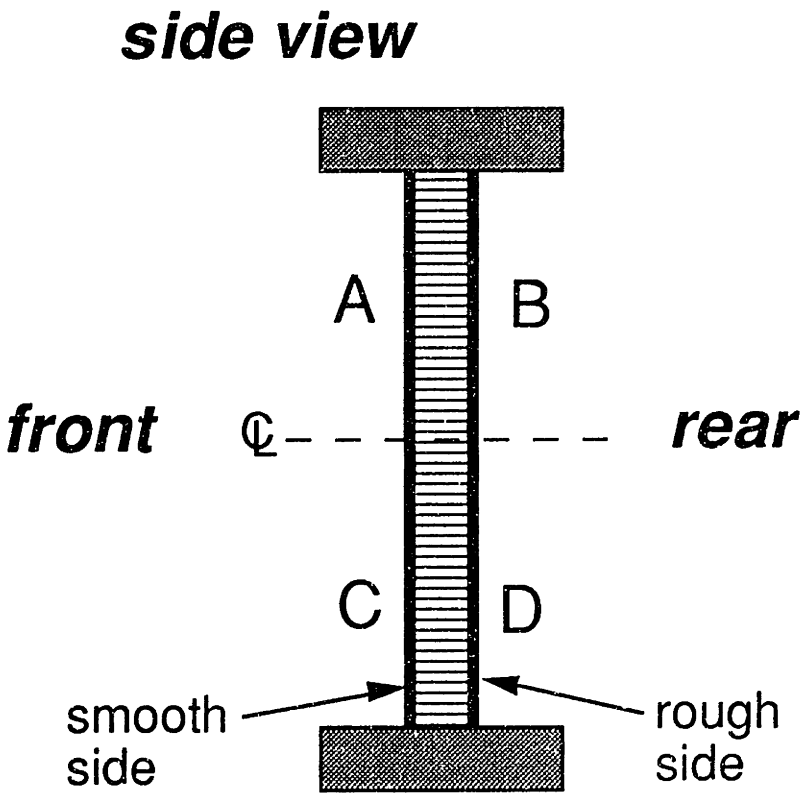

Figure 7.1 General regions A, B, C, and D of strain gage locations.

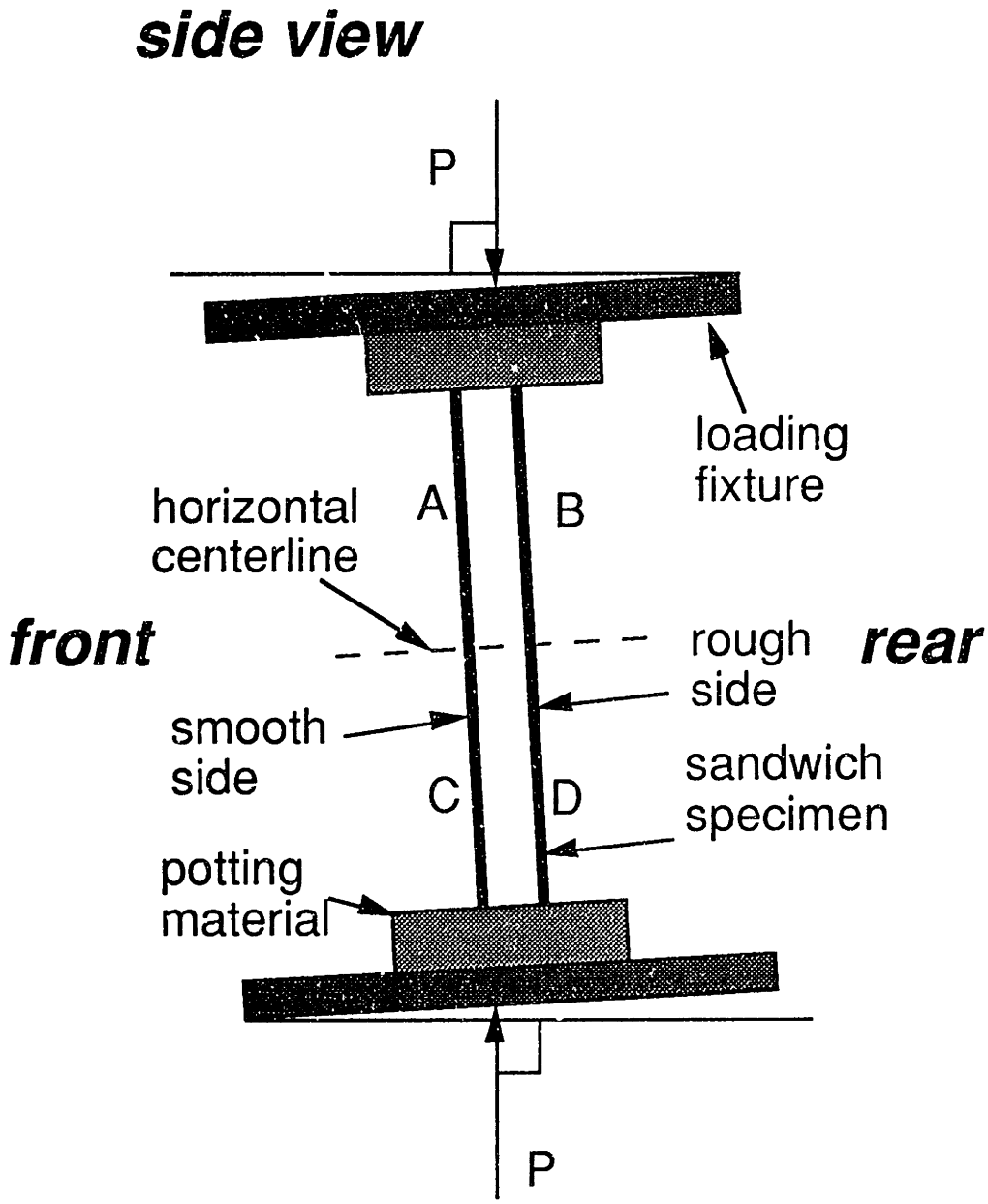

Figure 7.2 Schematic of misalignment of loading plates with axis of load application.

load is applied more to the smooth side facesheet on the bottom. Load would be transferred between the two facesheets along the length of the specimen by shear in the honeycomb core.

Such off-axis loading would result in different strain levels at different locations in the plane of the facesheets. Strain gages located at regions A (upper front) and D (lower back) would have lower strains than those on the vertical centerline, while those located at regions B (upper back) and C (lower front) would have higher strains. Again, higher strain readings result in a lower slope of the stress-strain curve and vice versa. Initial slopes of strain gages of the specimens tested after the fixture was aligned by method 1 are shown in Table 7.1. The gages are grouped according to their general location within the different general regions shown in Figure 7.2. For undamaged specimens and notched specimens with strain gage configuration Notch 1, the average slope of gages on the horizontal centerline is also included for comparative purposes. Strain gages located at the horizontal centerline would not be affected by off-axis loading. This was the case as all five gages of specimen A-S-Ub gave approximately the same reading. All other specimens tested after alignment method 1 show the same pattern of off-axis loading: strain gages located in the areas of A and D have slopes higher than those on the centerline, while those in areas B and C have lower slopes. Additional evidence of off-axis loading was also obtained from the photoelastic coating used on some small specimens. The evidence is the in-plane gradient of strain differential which increases from top to bottom. Because σ_y is zero away from the notch and the ends of the specimen, the value of strain differential $\Delta\varepsilon$ is directly proportional to the axial strain ε_x. Such a pattern

Table 7.1 Initial slopes [a] of strain gages located in regions shown in Figure 7.1, for small specimens tested after alignment of test fixture by method 1

Specimen	Maximum Out-of-Plane Deflection	Regions of Strain Gage				
		Center	A	B	C	D
A-S-Ua	0.89	47.8	53.1	-	42.7	-
A-S-SN3a	0.61	-	55.3	44.1	-	-
A-S-SN6a	1.43	-	55.2	43.5	-	-
A-S-SN6b	0.51	-	55.0	40.9	-	-
A-S-SN10a	0.20	-	54.3	42.3	-	-
A-S-SN10b	0.65	-	-	-	42.8	58.8
A-SN13a	0.78	56.3	-	46.3	-	-
A-S-SN13b	0.67	-	60.4	42.5	-	-
B-S-Ua	1.02	55.2	65.7	-	49.3	-
B-S-SN3a	-0.17	-	61.7	48.2	-	-
B-S-SN10a	-0.15	-	67.0	52.6	-	-
B-SN13a	0.33	63.6	-	51.1	-	-
B-S-SN13b	0.09	-	69.4	58.6	-	-

[a] all values in GPa

was observed in the photoelastic coatings of all specimens aligned by method 1.

Off-axis loading alone would not result in deflection at the horizontal centerline of the specimen. In fact, for almost all of the specimens, the deflection was observed to be small, indicating that global bending of the specimens was not significant.

Better alignment of the fixture seemed to reduce the off-axis loading. When the fixture was aligned with method 2, the behavior of the strain gages was changed. Method 2 involved alignment of the loading plates of the fixture to each other and to the testing machine. Specimens were also shimmed so that readings of the far-field gages were closer to each other. Initial slopes of the stress-strain curves for specimens tested after alignment with method 2 are given in Table 7.2. Small specimens with strain gage configuration Notch 3 had smaller differences between gages at locations A and B. Also, the gages at locations C had the same or higher slopes than those in location D. Furthermore, the small specimen tested with a photoelastic coating after alignment by Method 2, specimen A-S-DN10, has no noticeable in-plane strain gradient.

Because of the anti-symmetry of the off-axis loading, the region near the horizontal centerline is only minimally affected. This was seen in the undamaged specimens in which all strain gages located on the horizontal centerline gave approximately the same reading. The stress applied to the region around the notch should thus be minimally affected by off-axis loading. Therefore, it is concluded that the failure stresses of the small specimens tested after alignment with method 1 were not affected by the off-axis loading present.

Table 7.2 Initial slopes [a] of strain gages located in regions shown in Figure 7.1, for small specimens tested after alignment of test fixture by method 2

Specimen	Maximum Out-of-Plane Deflection	Region of Strain Gage				
		Center	A	B	C	D
A-S-SN3b	-0.31	-	50.2	45.6	-	-
A-S-DN3	0.42	-	45.7	38.6	47.6	47.3
A-S-DN6	-0.22	-	49.3	44.9	49.3	50.1
A-S-DN10	-0.50	-	42.9	45.3	48.2	42.9
A-S-DN13	0.26	-	51.6	40.0	52.0	47.3
B-S-SN3b	-0.19	-	65.3	59.4	63.4	58.4
B-S-DN3	-0.20	-	66.8	53.7	60.1	52.8
B-S-SN6a	1.27	-	64.9	58.1	-	-
B-S-SN10b	-0.20	-	63.9	54.0	-	-
B-S-DN10	0.14	-	59.0	49.8	61.5	57.5
B-S-DN13	-0.40	-	59.6	49.8	-	-

[a] all values in GPa

Even when specimens were aligned by method 2, variations were noted between strain readings of far-field strain gages. Among specimens with Notch 3 strain gage configuration, the slope of the gages differed for the gage pairs 2 & 3 and 4 & 5 which are located symmetrically about the horizontal centerline. The slope also differed within each pair. The largest difference noted was that of specimen B-L-SN25 which had a 25% difference between the two pairs of far-field gages. Also, this specimen had a 24% variation between the slopes of gages 4 and 5. However, the variation among the far-field strain gages was not correlated with the deflection or any other behavior of the specimens. Part of the variation may be due to the cell wall pattern observed with the photoelastic coating. However, it seems unlikely that strain gages which were placed back-to-back on a specimen would be placed differently enough with regard to the honeycomb cell to account for a 24% variation. Instead, it seems that some variation of strain in the specimen is inevitable. Careful preparation of the specimen and fixture can reduce the variation, but it is almost always present.

Variations of strain in the specimen seem to be caused by the nature of the fixture and specimens. The ends of the specimen after machining always deviated slightly from parallel. Also, the loading plates of the fixture could never be completely aligned with each other and the testing machine. Slight differences in length and alignment could result in eccentric loading of the specimen. When loading is compressive, eccentricities can be magnified. Thus, a better fixture with better alignment procedures is needed in order to produce a uniform loading state.

When testing in compression, it must be remembered that any test specimen used is, and will behave as, a structure. Depending on what property of the specimen is to be measured and the fidelity desired from the

measurement, small amounts of variation due to structural behavior of the specimen may be acceptable. These issues must be taken into account when designing a fixture and specimens and in evaluating their performance. Therefore, the fixture used in this investigation can be acceptable for certain purposes and less suited for others.

7.2 Effects of Specimen Size

A principal objective of this investigation is to determine the effects of the size of the specimen relative to the damage present on the stress/strain distribution and ultimately the failure stress of the specimen. There is some evidence to show that the length and width of the specimens was not sufficient to allow a state of uniform stress to develop. However, consideration of all available evidence indicates that the size of the specimens used in this work had little influence on the stress state in the region of the damage and the final failure of the specimen.

Certain notched medium and large specimens with photoelastic coatings have regions of higher strain differential from the notch tip which reach the vertical edge of the specimen. These are an inevitable by-product of the notch as can be seen from the predicted photoelastic patterns. If the notch is long enough as compared to the specimen width, regions of the higher strain differential will be seen to go from the notch tip to the vertical edge of the specimen. However, an observed region may have only a slightly different strain differential than the surrounding area yet appear quite distinct. Furthermore, it was experimentally observed that the far-field strain differential level is attained along the notch line well before the edge of the specimen is reached. Finally, the regions of strain differential

observed represent a combination of ε_x, ε_y, and γ_{xy}. The values of ε_x may be relatively unaffected where these regions reach the specimen boundary. Thus, for the cases examined, the failure stress of a notched specimen should not be affected by the width of the specimen.

The length of the specimen might be important if the length of the specimen is not sufficient for a state of uniform stress to develop between the ends of the specimen and the notch region. The boundary condition applied to the ends of the specimen is one of uniform vertical displacement. It is clear that the fixture is stiff enough in bending about the z-axis that the deformation of the fixture is negligible and the uniform end displacement is achieved. When the photoelastic coating is placed almost to the edge of the potting material, regions of low $\Delta\varepsilon$ are observed next to the potting. These regions probably are due not to lower axial strain but to lower transverse Poisson expansion caused by the potting material and friction between the specimen and the loading plates. A well-known example of this behavior can be found in the compression testing of metal cylinders between two metal blocks. Such specimens develop a "barrel" shape as shown in Figure 7.3. In the extreme case of no slippage, next to the loading plates, the metal specimen can have no transverse displacement because of the friction with the loading plates. The same is true of the composite sandwich panel, but with the sandwich panel, there is the additional complication of the potting material. This also acts as a constraint in the y-direction. Thus, a region near the potting line where the value of $\Delta\varepsilon$ is lower than the far-field value is to be expected.

Simple calculations can be performed to bound the effect of an end constraint on the value of the measured axial strain and $\Delta\varepsilon$. Consider an orthotropic plate with a transverse constraint such that displacement in the

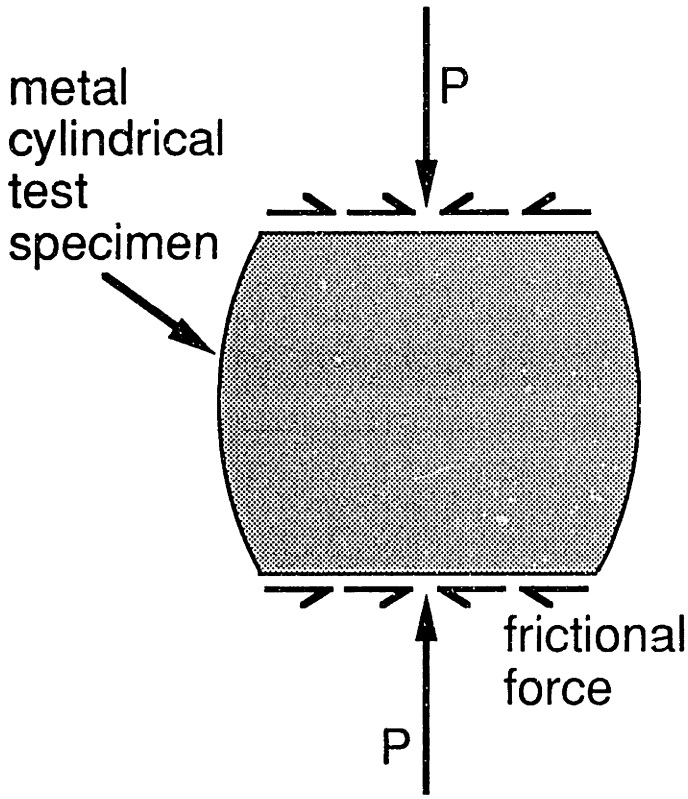

Figure 7.3 Sketch of a metal cylinder tested in compression exhibiting "barreling" behavior.

y-direction is zero. Thus, ε_y is also zero, and a transverse stress must exist in the material when an axial stress is applied. This represents an upper bound on the effect of an end constraint as the real effect of the end constraint is probably less severe because the condition of no transverse displacement is not ensured in the specimen. The stress-strain relationships for an orthotropic plate as given in Chapter 4 are:

$$\varepsilon_x = \frac{\sigma_x}{E_x} - \frac{\nu_{yx}\sigma_y}{E_y} \tag{7.1}$$

and,

$$\varepsilon_y = -\frac{\nu_{xy}\sigma_x}{E_x} + \frac{\sigma_y}{E_y} \tag{7.2}$$

However, ε_y is zero at the end constraint, so Equation 7.2 can be solved for σ_y and the results placed in Equation 7.1 to yield an expression for ε_x:

$$\varepsilon_x = \frac{1-\nu_{yx}\nu_{xy}}{E_x}\sigma_x = \frac{\sigma_x}{E_{apparent}} \tag{7.3}$$

where $E_{apparent}$ is the apparent modulus due to the stiffening of the transverse constraint. Using the calculated laminate elastic constants given in Table 4.2, $E_{apparent}$ is calculated as 58.5 GPa for the A laminates, an increase of 11% over the calculated modulus of 52.7 GPa, and 69.5 GPa for the B laminates, an increase of 8% over the calculated modulus of 64.3 GPa. These represent significant increases in the local apparent stiffness in the x-direction.

The effect of a transverse constraint on the value of $\Delta\varepsilon$ can be quite large. For the case of an A specimen with a far-field applied stress of -90 MPa, as was considered in Chapter 6 for specimens with 25.4 and 50.8 mm notches, the calculated far-field value of $\Delta\varepsilon$ is 2350 μstrain. However, if a transverse restraint of the plate exists, the value of the difference of

principal strains in the extreme case can be calculated from:

$$\Delta\varepsilon = \varepsilon_I - \varepsilon_{II} = \varepsilon_x = \frac{1 - \nu_{yx}\nu_{xy}}{E_x}\,\sigma_x \tag{7.4}$$

With this transverse constraint, the value of $\Delta\varepsilon$ is 1540 μstrain, a reduction of almost 35%. For a B specimen at the same stress level, a 34% reduction in $\Delta\varepsilon$ is calculated due to a transverse constraint. Thus, the region of constraint can show a large reduction in the value of $\Delta\varepsilon$ when the strain field is examined with a photoelastic coating.

Because the constraint of the end of the specimen is across the entire specimen width, the size of a region of lower $\Delta\varepsilon$ next to the potting line would depend upon the width of the specimen: the wider the specimen, the larger this region. This region would be expected to resemble a triangle with two corners at the edge of points where the edge of the material reaches the potting line and the third corner along the vertical centerline of the specimen. The size and severity of this region could be easily examined by testing an unnotched specimen with a photoelastic coating applied next to the potting line.

As the specimen length to width ratio is decreased, the region of low $\Delta\varepsilon$ due to the end constraint will grow toward the horizontal centerline of the specimen. It is possible that the region due to the end constraint could intersect the region of low $\Delta\varepsilon$ above and below the notch. In that case, it would be difficult to distinguish the effect of the end constraint from that of the notch. For the medium and large specimens, regions of low $\Delta\varepsilon$ due to the end constraint are observed to be as large as a quarter of the specimen length, approximately 95 mm for the medium specimens and 190 mm for the large specimens. In fact, it is possible to interpret them as reaching all the way to the notch region, which would indicate that the effects of the

notch and the end constraint have intermingled. However, the region of low $\Delta\varepsilon$ from the potting line is caused by transverse constraint; the axial strain level in this region should be relatively unchanged. Thus, it should not have a significant effect on the axial stress applied to the notch. In fact, the stress applied may be slightly higher near the x-axis because of the transfer via shear of the transverse stress from the end constraint to axial stress.

All of the observations about end constraint and the region of low $\Delta\varepsilon$ produced are specific to the geometry of the specimen and the manner in which it was tested. Changes in the size of the specimen or in the fixture could affect the end constraint observed in the specimen.

Specimen size does not seem to affect the failure stress of specimens with the same size damage based on a limited number of direct comparisons. Both medium and large specimens were tested with 25.4 mm notches. Among the A specimens, the medium specimen had a slightly (less than 3%) higher strength than the large specimen, while the large B specimens failed at a stress 4% higher than the medium specimens. Such small variations do not show a definite trend and are not regarded as significant. Furthermore, both medium and large specimens were tested with damage from a level 1 impact. While it is not known for certain that the damage states of the medium and large specimens of the same layup were the same, they were probably similar because the impact events for the two were approximately the same and the dimple size and damage size measured via ultrasound are similar. For the B specimens, the medium specimen had a failure stress of 5% higher than that of the large specimen. For the A specimens, the failure stress of the large specimen exceeded that of the medium specimen. However, because the capacity of the testing machine was exceeded causing the machine to shut down, the failure stress

of the large specimen is not known. As discussed in Chapter 6, this specimen was probably close to its failure stress when the testing machine shut down. Thus, the failure stresses of the medium and large specimens of the A layup damaged by a level 1 impact are also approximately the same. Based on these comparisons, there is no effect of specimen size on the failure stress of notched or impacted specimens for the cases considered in this investigation.

As with fixture design, the length and width of the specimen should be chosen based on the property of the specimen to be measured and the fidelity desired in the measurement. There is a trade-off involved as increasing the specimen size would decrease finite size effects but may create additional difficulties in testing and would make the specimens more expensive. The analytical solution for an ellipse can be used to examine the effect of various specimen sizes on the stress/strain state of the specimen and the notch region in particular. Using this tool and direct comparisons between specimens of different sizes shows that, for the cases considered in this investigation, the effect of the specimen size on the strain state and failure stress is negligible.

7.3 Notched Compressive Behavior

The compressive notched strength was tested for specimens of both layups with notches of seven different nominal lengths. In this section, the predicted and observed patterns of the strain differential, $\Delta\varepsilon$, and the failure of the specimens are discussed. The failure stresses are correlated using the Mar-Lin correlation in order to identify trends among the failure strengths.

7.3.1 Photoelastic Images

Recorded patterns of photoelastic coatings were used to provide an indication of the strain field over a wide region of the specimen. The observed patterns of the photoelastic coating were compared against analytical predictions of the patterns for a plate with an elliptical notch.

Strain was found to vary on a small scale within the specimen. This variation was associated with the cell patterns of the honeycomb core. The cause for this is probably the waviness of the fibers created by the cocuring process. The facesheets bulge into the cell of the honeycomb, creating a curvature in the fibers which affects the strain differential in the center of the cell. In addition, wavy plies are not as stiff as straight plies [57] which is probably the reason that the measured modulus is not as high as the calculated value. It is also possible that the honeycomb locally reinforces the facesheet in the transverse (y-axis) direction. This would reduce the value of $\Delta\varepsilon$ in the facesheet directly above the cell walls in the y-direction.

The predicted strain differential patterns were qualitatively similar to the experimental patterns. Strain levels away from the notch in the A specimens were similar to predicted values. The measured modulus and slopes of far-field gages were also similar to the predicted modulus for these specimens. However, the strain levels away from the notch in the B specimens was higher than predicted. The measured modulus and slopes of far-field gages in these specimens were always lower than the predicted modulus for these specimens. Thus, the higher strains away from the notch than those predicted are probably due to the facesheet's moduli being lower than the calculated values.

The main differences between the observed and predicted patterns seems to be the difference in shape between the ellipses used in the model

and the notches used in experiments. The observed patterns become more similar to the predicted patterns as the notch length is increased. As the length of the notch becomes large, the ellipse more closely approximates the notches used experimentally. The observed region of low $\Delta\varepsilon$ above and below the notch is similar in shape and strain value to that predicted, and it appears that this region is controlled by the length of the notch. However, the shape of the region of high $\Delta\varepsilon$ near the notch tip is somewhat differently shaped than predicted and the values in this region are always higher than predicted. While this could be partly due to material softening at higher strain levels, the strains were observed to be linear for the medium A specimen with a 25.4 mm notch. Thus the wider, more rounded shape of the notch used in the experiments seems to result in a region of $\Delta\varepsilon$ with higher values than those predicted for an ellipse.

A more accurate prediction of the pattern of $\Delta\varepsilon$ could be developed. An analytical solution exists [48] for an anisotropic plate with an oval opening. This would more closely approximate the slits used in this investigation. The existing program or one incorporating the solution for an oval opening would be very useful in a parametric or preliminary study. However, in order to properly model the specimen and notch geometry, it would be necessary to develop a finite element model and calculate the values of $\Delta\varepsilon$ from the strain output. Another important step would be to experimentally determine the in-plane elastic constants of the panels rather than relying on calculated values. This is especially important because of the waviness present in the facesheets of the sandwich panels.

7.3.2 Failure and Strength Correlation

The experimental failure strength of notched specimens is an

important piece of information for the damage tolerance design approach. Since failure data is obtained at discrete notch sizes, a strength correlation can be used to develop a continuous curve from the data points. As was discussed in Chapter 4, the Mar-Lin correlation is used in this investigation to correlate the strengths of notched specimens. As discussed in Chapter 6, certain specimens are excluded from the discussion and analyses of failure. These include specimen A-S-SN3b, which failed at the potting line, specimen B-S-SN6, which experienced cracking of the potting material during testing, and specimen B-S-DN6, which experienced very unusual and nonlinear stress-strain behavior. Also, specimen A-L-SN25 did not fail because the capacity of the testing machine was exceeded. The remaining specimens all experienced the same type of in-plane failure. Therefore, considering all notched specimens of the same layup as one data pool is valid.

The failure stresses of small specimens with both facesheets notched are generally somewhat lower than those with only one facesheet notched. Among the small A specimens, the failure stress of specimens with nominal notch lengths of 3.2 and 12.7 mm are about 10% lower when both facesheets are notched than when only one is notched, and a difference of 16% is noted for a nominal notch length of 9.5 mm. However, among the specimen with nominal notch lengths of 6.4 mm, the specimen with notches in both facesheets actually has the highest strength of the three specimens.
while the trend toward lower strengths among specimens with both sides notched is clear, there are exceptions noted. Among small B specimens, those with both facesheets notched always have lower strengths than their counterparts of the same notch length with only one side notched. For nominal notch lengths of 3.2, 9.5, and 12.7 mm, the difference is 11%, 22%,

and 14%, respectively. These are about the same reduction in strength due to notching both facesheets as was observed with the A specimens.

Among medium and large specimens, those with one or two facesheets notched have essentially the same failure strengths. One exception to this is noted as there is a significant difference between the strengths of the two large A specimens with 25.4 mm notches. The specimen with both sides notched failed at 188 MPa, while the specimen with one side notched exceeded the load capacity of the testing machine without failing, giving a specimen stress of 239 MPa. However, the latter specimen, A-L-SN25, was the only one tested which underwent significant out-of-plane deflection, suggesting that bending of the specimen also occurred. This specimen had a centerline deflection of -4.54 mm, almost twice the thickness of a facesheet. The negative value indicates that it was in the direction of the notched facesheet which would produce a tensile bending stress in the notched facesheet. A tensile bending stress would reduce the compressive stress applied to the notched facesheet so that the specimen could sustain a greater load before failing. For this specimen, the behavior of the sandwich panel as a structure was important. The measured mid-plane deflection of all other notched specimens was small and thus the structural behavior is not considered significant in all other medium and large specimens.

There are several ways that notching specimens in one or both facesheets can affect the measured failure stress of the specimen. If the notch does not significantly affect the overall stiffness of the facesheet, then there should be no effect on the stress-strain and structural behavior of the specimen prior to failure. This seems to be the case as the width of the slit is much smaller than the total specimen length. If loading of the two

facesheets is even, the stress state experienced by the notch should be the same for both cases. However, failure of seemingly identical notched specimens is not always at the same stress; there is some experimental scatter involved due to differences in specimens which go undetected. Thus, one would expect the specimen notched in only one facesheet to fail at the notched strength of the notched facesheet. On the other hand, specimens with both facesheets notched will fail at the notched strength of whichever facesheet has a lower strength. Since some variation of notched strength is inevitable, the strength of specimens notched on both sides would be expected to be lower, on average, than that of the specimens notched only on one side by an amount related to the scatter in strengths. It would also be logical for the scatter of strengths among specimens notched on both sides to be somewhat reduced.

If the loading of the facesheets is not even, strength of the specimens with both facesheets notched should still be lower, but the reasoning is somewhat different for this case. In this case, suppose one facesheet has a higher stress level applied to it for some reason. If that facesheet is notched, the specimen will probably fail in that facesheet. The stress in that facesheet is higher than the average for the two, so the specimen will probably fail at a lower stress than if the loading had been even. However, if that facesheet is unnotched, the specimen will probably fail first in the other (notched) facesheet. The stress level in that facesheet is lower than the average for the two, so the specimen will probably fail at a higher stress than if the loading had been even. Thus, random variations in loading would be expected to increase the experimental scatter but not affect the mean failure strength of specimens notched in one facesheet. Random variations in loading will reduce the average failure strength of specimens

notched in both facesheets because the facesheet with a higher stress now always has a notch which will be affected detrimentally by the added bending stress. Thus, random variations in loading will reduce the average strength of specimens notched in both facesheets.

The reduced strength of small specimens with both sides notched can thus be explained in terms of experimental scatter and uneven loading. For these specimens, the scatter can be significant. Also, in light of the previous discussion dealing with the difficulties with the test fixture and testing technique, the possibility of slightly uneven loading in the facesheets must be acknowledged. The combined effects caused by experimental scatter and uneven loading probably lead to the lower failure strengths for most specimens with both sides notched.

It is unclear whether sandwich specimens in an experimental program should be notched in one side or both. Notching both sides should reduce experimental scatter, but at the expense of lowering the measured strengths. Also, notching one or both facesheets may better represent the damage which would be present in an actual structure. However, if the key design parameter is strength for notches of 25 mm or longer, it does not seem to matter provided there is good confidence that the structural behavior of the sandwich panel is minimal.

The key value determined for the Mar-Lin correlation as used in this investigation is H_c, the composite fracture parameter. The failure strength and the measured notch length (or average of the notch lengths if both facesheets are notched) are used to calculate the value of this parameter from Equation 4.21:

$$\sigma_f = H_c\,(2b)^{-m}$$

The parameter m is set to 0.28 as discussed in Chapter 4. Measured values of notch length and failure stress and the calculated values of H_c are given for notched specimens of the A layup in Table 7.3 and for specimens of the B layup in Table 7.4.

The coefficient of variation is a good metric for the goodness of fit of the Mar-Lin correlation to the experimental data. The coefficient of variation is calculated for a group of values as one standard deviation divided by the mean value for the population. Average values of H_c and the associated coefficient of variation for different subsets of the A specimens are given in Table 7.5. In general, the coefficient of variation is about 10% for the subgroups considered and among all specimens tested. Small specimens with both sides notched have slightly lower values of H_c than those with only one side notched. The average value of H_c is about 20% lower for medium and large notched specimens than that for the small specimens. The plot of the failure stress versus notch length for the A specimens is given in Figure 7.4. Specimen A-L-SN25 is included in this plot and is shown with an arrow pointing upward indicating that this specimen did not fail because the capacity of the testing machine was exceeded. Also included is the predicted failure line from the Mar-Lin correlation of all the notched A specimens. The correlation curve fits the data quite well, especially for notch lengths of less than 20 mm. The correlation slightly overpredicts the strength for greater notch lengths. At greater notch lengths, the correlation is relatively insensitive to changes in notch length. The correlation predicts an infinite strength for the unnotched case. This is clearly not possible, so, for notches below a certain cutoff size, the undamaged compressive strength would be the strength of the specimens. The undamaged strength of the panels of this investigation

Table 7.3 Values of notch length, failure stress, and composite fracture parameter H_c for specimens of the A layup

Specimen	Average Notch Length (mm) [a]	Failure Stress (MPa)	Hc (MPa•mm $^{0.28}$)
A-S-SN3a	3.8	409	594
A-S-DN3	3.4	391	550
A-S-SN6a	6.5	313	529
A-S-SN6b	6.3	316	529
A-S-DN6	6.7	324	552
A-S-SN10a	9.6	359	676
A-S-SN10b	9.4	311	582
A-S-DN10	9.5	285	535
A-S-SN13a	13.8	255	532
A-S-SN13b	12.2	268	540
A-S-DN13	12.9	235	480
A-M-DN25	25.9	193	480
A-L-SN25	25.4	>239 [b]	591
A-L-DN25	25.4	188	465
A-M-DN51	51.2	145	436
A-L-DN76	76.6	131	441

a Measured length of notch or average of measured notch lengths if both sides are notched.

b Specimen did not fail because capacity of testing machine was exceeded.

Table 7.4 Values of notch length, failure stress, and composite fracture parameter H_c for specimens of the B layup

Specimen	Average Notch Length (mm) [a]	Failure Stress (MPa)	Hc (MPa•mm $^{0.28}$)
B-S-SN3a	3.1	439	603
B-S-SN3b	3.3	393	547
B-S-DN3	3.4	368	516
B-S-SN6a	6.1	316	524
B-S-SN10a	9.8	320	605
B-S-SN10b	9.8	298	564
B-S-DN10	9.8	245	464
B-S-SN13a	12.1	270	543
B-S-SN13b	13.1	250	513
B-S-DN13	12.8	225	459
B-M-SN25	25.9	204	507
B-M-DN25	25.6	202	500
B-L-SN25	25.4	213	527
B-L-DN25	25.5	212	525
B-L-DN51	51.0	147	442
B-L-DN76	76.3	130	438

[a] Measured length of notch or average of measured notch lengths if both sides are notched.

Table 7.5 Average values of H_c and associated coefficients of variation for various subsets of the notched A specimens

Subset of Specimens	Average Value of H_c ($MPa \cdot mm^{0.28}$)	Coefficient of Variation
small specimens with one side notched	569	9.5%
all small specimens	554	9.0%
medium and large specimens, including A-L-SN25	483	13.1%
medium and large specimens, excluding A-L-SN25	456	4.5%
all specimens tested, including A-L-SN25	532	11.8%
all specimens tested, excluding A-L-SN25	528	11.9%

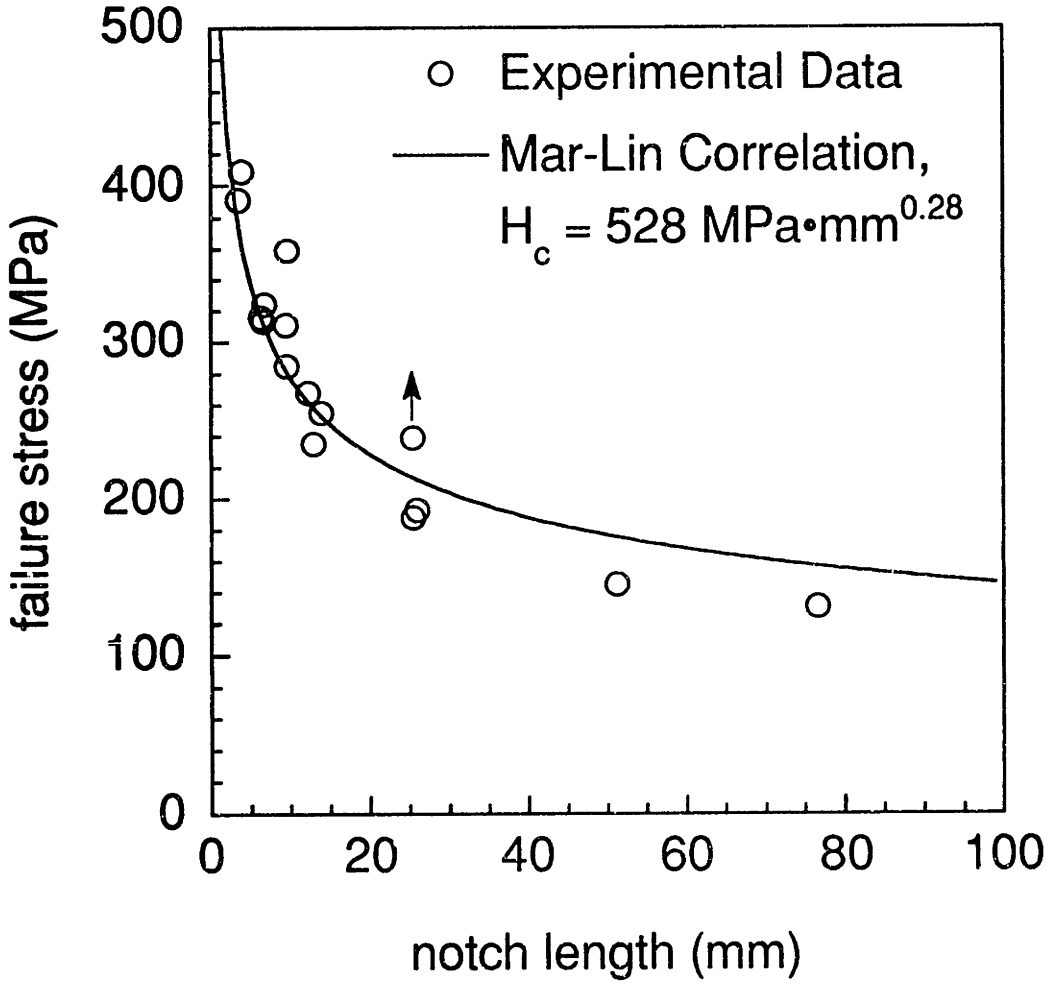

Figure 7.4 Experimental failure stress and predicted failure stress by the Mar-Lin correlation versus notch length for the notched specimens of the A layup.

was not well determined as all unnotched specimens failed at the potting line. This failure was probably due to the out-of-plane restraint of the potting material. The measured undamaged compressive strength was controlled by the method of testing and thus represents only a lower bound on the actual strength. Therefore, the failure stresses of the undamaged specimens are not shown.

The specimens of the B layup are somewhat better fit by the Mar-Lin correlation than those of the A layup. Average values of H_c and the associated values of the coefficient of variation for various subgroups of notched B specimens are shown in Table 7.6. Again, the values of H_c are lower for small specimens with both sides notched than for those with only one side notched and the value of H_c for the medium and large specimens is about 10% lower than that for the small specimens. The plot of the failure stress versus notch length for the B specimens is given in Figure 7.5. The plot is very similar to that produced for the A specimens. Failure stresses are again overpredicted for notch lengths greater than 20mm using the Mar-Lin correlation, but predictions match the experimental data well for small notch lengths. Overall, the values of the fracture parameter are very similar for the two layups.

There is a significant decrease in the composite fracture parameter H_c as the notch length is increased. This can be seen for the A specimens in Figure 7.6 and for the B specimens in Figure 7.7. The value of the parameter decreases gradually with increased notch length when the lengths are less than 30 mm, though there is significant scatter for those with notch lengths less than 20 mm. The scatter is probably due to minor differences and imperfections in specimens with nominally the same notch size. At large notch sizes, notch length dominates over minor variations or

Table 7.6 Average values of H_c and associated coefficients of variation for various subsets of the notched B specimens

Subset of Specimens	Average Value of H_c ($MPa \cdot mm^{0.28}$)	Coefficient of Variation
small specimens with one side notched	557	6.5%
all small specimens	534	9.3%
medium and large specimens	490	8.2%
all specimens tested	517	9.7%

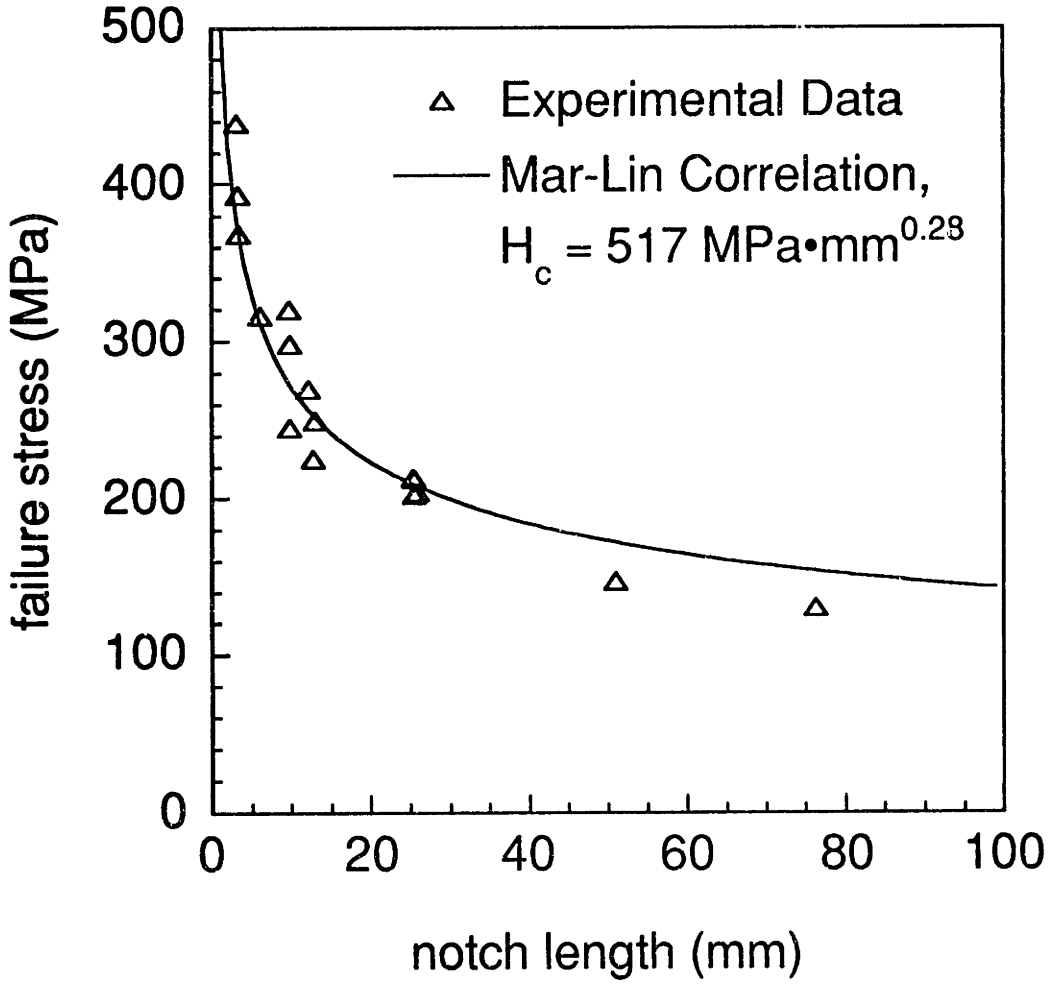

Figure 7.5 Experimental failure stress and predicted failure stress by the Mar-Lin correlation versus notch length for the notched specimens of the B layup.

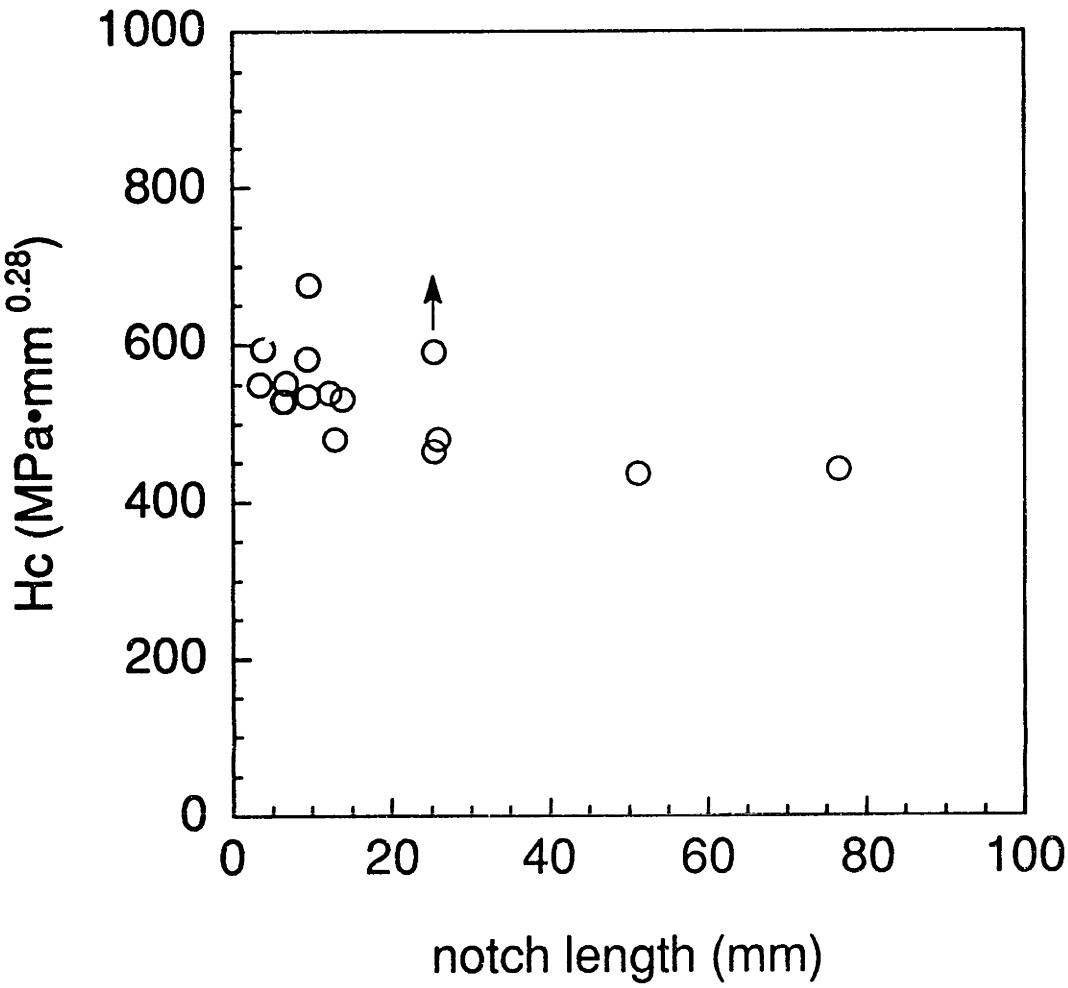

Figure 7.6 Plot of the composite fracture parameter H_c versus notch length for specimens of the A layup.

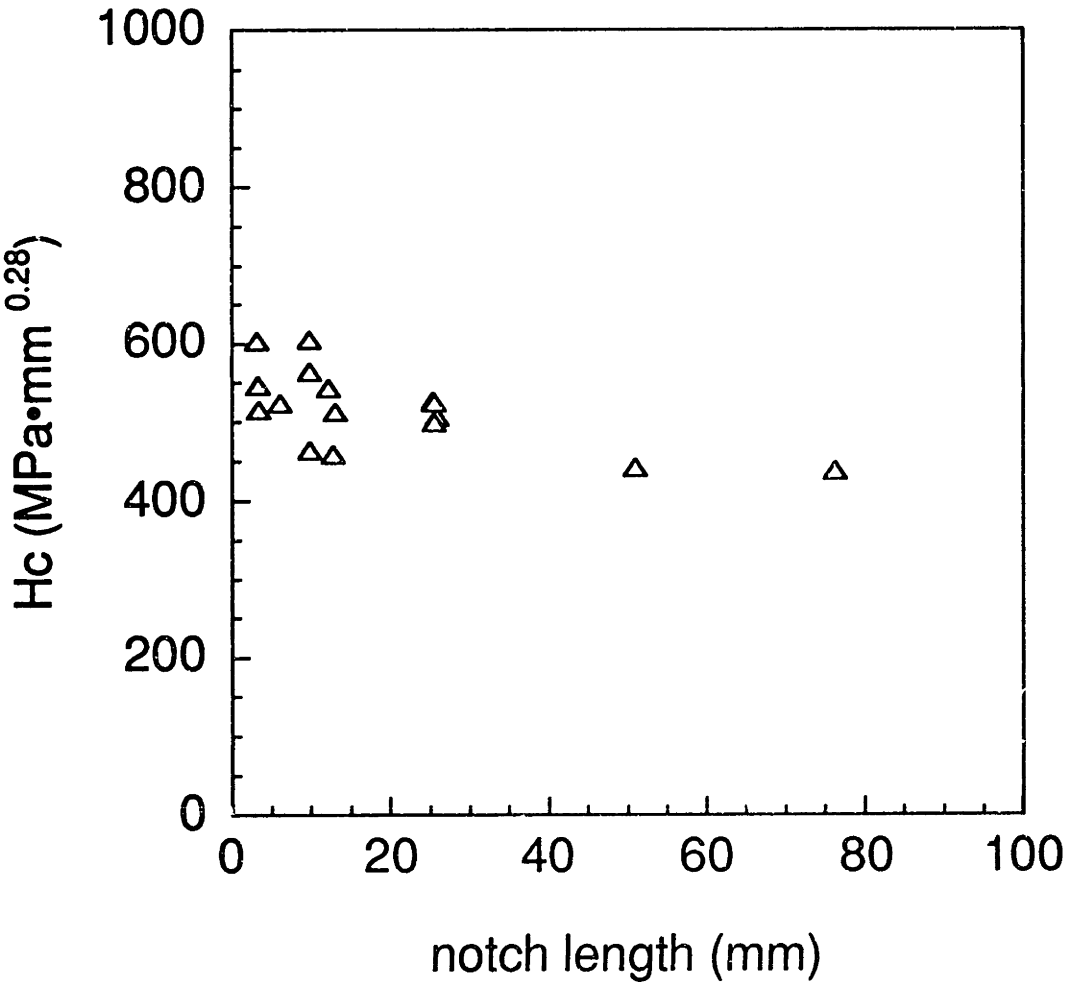

Figure 7.7 Plot of the composite fracture parameter H_c versus notch length for specimens of the B layup.

imperfections in the specimen so that the failure stress is relatively insensitive to such small differences. At shorter notch lengths, an imperfection may be of the same order of size as the notch length, making these specimens more sensitive to the variations and imperfections. This sensitivity is reflected in the scatter of the values of H_c for the small specimens. For notches longer than 40 mm, the value of the parameter is approximately constant. The cause of this decrease and leveling off is not clear. Part of the difference may be due to the difference in the shape of the notch between the small specimens and the medium and large specimens, although the shape of the notch has been shown to be relatively unimportant in previous investigations [5-7, 15].

All of the values of H_c, including those of the medium and large specimens, fall in a fairly wide scatter band between 400 and 700 $MPa \bullet mm^{0.28}$. Thus, the medium and large specimens may represent merely the bottom of the scatter band. It may also be that the decrease in H_c with increased notch size represents a limitation in the applicability of correlations such as the Mar-Lin correlation in that a single parameter may not be able to properly represent the fracture behavior over a large range of notch lengths. It is, after all, a rather simple engineering tool that does not fully account for the behavior of notched composites. However, because of the relatively small number of medium and large notched specimens, no definite conclusions can be drawn about the decrease of H_c with increased notch size.

Because on the observation of decreasing H_c with notch length, the Mar-Lin correlation must be used very carefully when predicting failure strengths for laminates with notches substantially larger than those tested. Using the Mar-Lin correlation to extrapolate for large notch sizes could

result in somewhat nonconservative values for predicted strength. Thus, notches of about the same size or larger than those in question must be tested in order to have confidence in the predictions.

7.4 Compression After Impact Behavior

Under compressive loading, growth of the dimple created by the impact event was observed, but important differences exist between the observed behavior and that reported in previous investigations. These differences make the prediction of dimple growth and failure with existing methods inaccurate. Notched compressive behavior has been used as an engineering tool to predict failure, but such an approach ignores the mode of damage propagation in impacted sandwich panels.

7.4.1 Dimple Growth

The dimple growth model of Tsang [45] was found to significantly underpredict the observed dimple growth. Because several input parameters of the model were assumed, the prediction of growth could have been affected by an inaccurate assumption. For example, the core may be less stiff or the core crushing may be more extensive than assumed. Also, it is known that damage such as delamination, matrix cracking and fiber breakage was created in the facesheets by the impact event. Such damage would decrease the bending stiffness of the facesheet in the dimple region. In order to examine whether changes in the core stiffness, core crushing size, or bending stiffness of the facesheet would affect the predicted dimple growth, these parameters of the dimple growth model are varied one at a time to determine their individual effects.

In order to determine the effect of reducing the core stiffness, the values for the two-parameter foundation of Tsang [45] are used. Because the core used in that investigation was Nomex, the core was substantially less stiff than the reinforced phenolic core of the current investigation. The parameters used to characterize the Nomex for the two-parameter model are 20.53 GN/m^3 for k_1 and -28.27 kN/m for k_2. The value for k_1 is about a quarter of that used herein for the reinforced phenolic core, and the value of k_2 is less than a tenth. All other parameters are the same as that used for the A specimen impacted at level 1 as given in Chapters 4 and 5. The dimple growth predicted with this reduced core stiffness, along with the observed dimple growth, is shown in Figure 7.8. The initial dimple depth at the center was 1.09 mm, and the predicted depth given in Chapter 6 at -238 MPa is 1.14 mm. With the reduced core stiffness, a depth of 1.15 mm is predicted. Thus, even when the core stiffness is reduced substantially, little growth is predicted in the dimple.

To examine whether the size of the region of initial core crushing is important, a larger region of initial core crushing is used in the dimple growth model. For the medium A specimen impacted at level 1, the observed area of damage in the facesheet is an approximately circular region with an area of 1300 mm^2. Because this is the largest extent of observed damage, the core is assumed to be crushed over a circular region with this area. Such a circular region would have a radius of 20.3 mm, and this value is used for the parameter R_o, the radius of initial core crushing. This is substantially larger than the value of 12.0 mm used previously. The dimple growth predicted with the larger region of crushed core is given in Figure 7.9. The predicted depth of the dimple at the center is 1.16 mm.

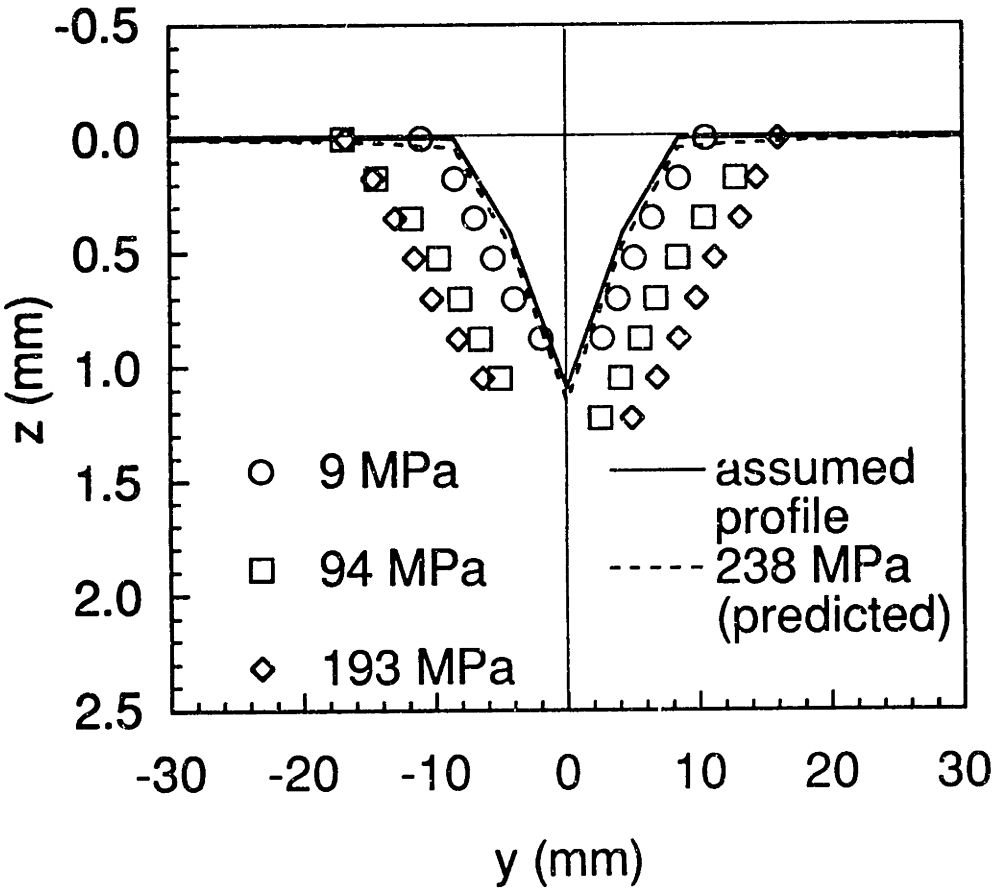

Figure 7.8 Predicted, with reduced core stiffness, and observed dimple growth of an A specimen impacted at level 1.

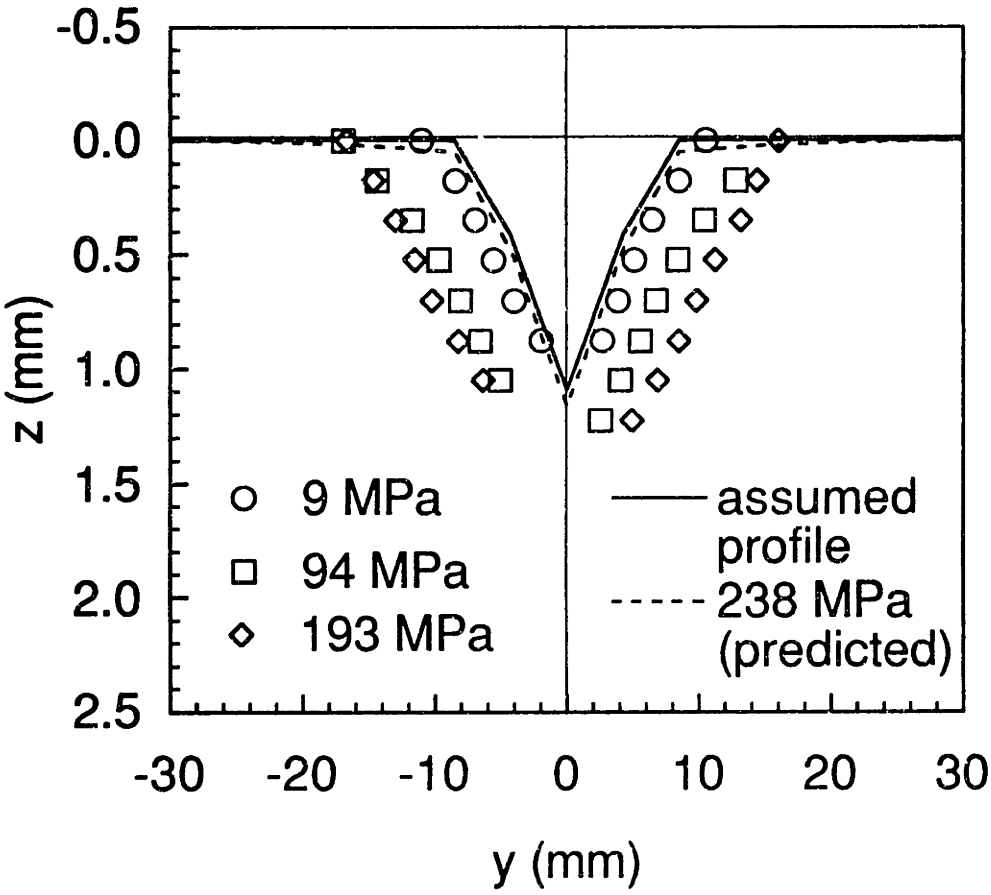

Figure 7.9 Predicted, with a larger region of initial core crushing, and observed dimple growth of a medium A specimen impacted at level 1.

Despite the increase in core crushing zone, the dimple is not predicted to grow substantially.

Finally, to examine the effect a reduction in the bending stiffness of the facesheet might have, the elements of the D_{ij} matrix are reduced by a factor of four from those given for the A layup in Chapter 4. The reduced values of D_{ij} are given in Table 7.7. This is the reduction which would occur if the facesheet were only half as thick but retained the same in-plane stiffness. Because of the formulation of the model, the stiffness must be reduced throughout the facesheet rather than restricting the reduction to the dimple region. However, since bending is confined to the dimple region, this should not affect the behavior of the facesheet outside of the dimple. The dimple growth predicted with the reduced facesheet bending stiffness is given in Figure 7.10. The model predicts little growth even with the reduced bending stiffness of the facesheet. However, the predicted depth for this case is 1.24 mm. While an increase of depth from 1.09 mm to 1.24 mm is still smaller than that observed, it is over twice the growth predicted for all other cases.

It is difficult to compare the different cases of reduced core stiffness, larger core crushing zone, and reduced facesheet bending stiffness because the variations tried are of different magnitudes. However, it is likely that further reductions in core stiffness would have little effect on growth because the core has no effect in the region of initial core crushing, which encompasses the entire initial dimple. Nor would increasing the dimple size further affect the predicted growth because the larger crushing size is already much larger than the dimple. Only reducing the bending stiffness of the facesheet substantially increased the predicted dimple growth. It is

Table 7.7 Reduced values of the facesheet bending stiffness of the A layup used as input for the dimple growth model

Parameter	Value (Nm)
D_{11}	17.9
D_{12}	5.4
D_{16}	2.0
D_{22}	10.6
D_{26}	2.0
D_{66}	5.9

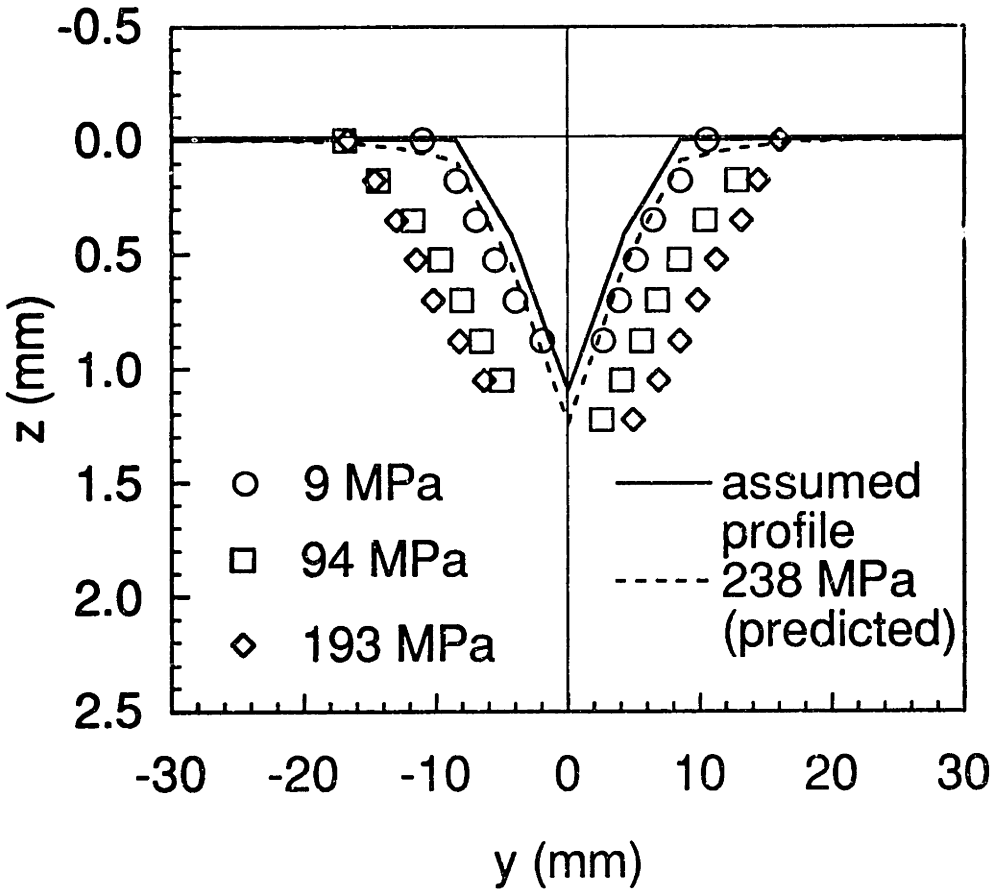

Figure 7.10 Predicted, with reduced bending stiffness of the facesheet, and observed dimple growth of a medium A specimen impacted at level 1.

also possible that various combinations of these effects could produce greater predictions for the dimple growth.

The dimple created by an impact event was observed to grow in all cases. For specimens impacted at level 1, growth occurred in a generally regular fashion from a circular dimple to an oval along the y-axis. A minor perturbation was noted in the specimens of the B layup. The exact cause of this is not known. It may be due to damage in the outer plies which are placed at angles of +30° and -30°. This is supported by the sharp line which can be seen at an angle of about 30° from the vertical axis in the lower left subregion of the moiré image at 224 MPa for specimen B-M-IL1 (see Figure 6.64). Despite this perturbation, the growth of the B specimens is still quite smooth and generally ovalized as is the case with the A specimens.

Dimple growth in specimens impacted at level 2 was very irregular. Because of the more extensive damage in the facesheets of these specimens, numerous surface cracks and fiber breakage present may serve to "guide" the damage growth. In addition, the damage present through the thickness of the facesheet may play a role in this irregular growth. The damage state of impacted specimens should be better understood for further investigations.

The observed dimple growth of the specimens impacted at level 1 is similar to that observed in a previous investigation by Tsang [45]. Growth along the x-axis was small and the dimple was observed to grow substantially along the y-axis in both the previous and current investigation. However, a direct comparison between the two investigations is not possible because of the very different specimen configurations.

The length of the dimple along the y-axis is a very simple parameter that allows comparisons between specimens. Since the dimple growth is

small along the x-axis, the important information about the behavior is in the y-axis. While a profile of the dimple is useful, it is difficult to compare profiles from different stress levels or from different specimens.

Observed dimple length growth was less than that reported by Tsang. Among the level 1 specimens, total growth of only about 50% was observed, while the growth of the level 2 specimens was 50-100%. For nearly every case he investigated, Tsang found the dimple to double or triple in size. In fact, extensive dimple growth was observed in specimens where no dimple was detectable initially. The facesheets used in this investigation are substantially thicker than those used by Tsang. Thus, they may be less able to undergo the extensive bending which would be present in a larger dimple. Also, Tsang used facesheets with fabric plies which may affect the behavior of the dimple region. Finally, the stiffer core of this investigation may have more effectively prevented the growth of the dimple.

The maximum dimple length observed before failure was found to be consistent for specimens impacted at level 1. Thus, there may be a critical dimple width for the specimens impacted at level 1. When this dimple size is achieved, the failure occurs across the width of the specimen. Failure away from the notch is primarily in-plane, but the mechanisms which trigger this failure are not known. For the specimens impacted at level 1, the critical length is between 36 and 41 mm. Further tests are needed in order to verify the existence of a critical dimple width for these specimens.

The maximum dimple length of specimens impacted at level 2 is inconsistent for the two tested. The maximum dimple size for these specimens may be less consistent because of their irregular dimple growth caused by damage in the facesheets. However, it is clear that the dimple can grow to larger sizes for these specimens, as was the case for the A

specimens where it is over 25% larger for the level 2 specimen than the level 1 specimens at failure. The reason that this specimen can sustain a larger dimple size before failure is unclear, but is probably related to the damage present in the facesheet. Based on the behavior of the specimens impacted at level 2, there may be different critical dimple lengths for different initial damage states.

The maximum dimple width may be related to the size of the initial damage in the facesheets. The width of the initial damage in the facesheets is assumed to be the diameter of a circle with the same area as the measured damage. Values for the maximum dimple width and facesheet damage width, along with the initial dimple width, are given in Table 7.8. For all six specimens, the final dimple width is remarkably close to the width of the initial facesheet damage. In fact, for the B specimens, the two widths are within 2% of each other. It is unclear why the two sets of values are close to each other. It may represent a relationship between the dimple size and facesheet damage which leads to failure. On the other hand, it may also be merely a coincidence.

The dimple can return to its original shape even after extensive loading. When the testing machine shut down during the testing of specimen A-L-IL1, the dimple returned to its initial shape except for a slight elongation on the left side of the edge of the dimple, even though the load level reached seems to have been close to the failure load for the specimen. In fact, the dimple is slightly less deep after the test, though this is probably not significant given the precision of the moiré measurements. Thus, additional damage may have been created in the specimen as a result of the loading. This possibility could complicate the job of a designer, especially if the dimple can shrink after compressive loading. It has previously been

Table 7.8 Measured damage sizes of impacted specimens

Specimen	Initial Dimple Width (mm)	Final Dimple Width (mm)	Facesheet Damage Width via Ultrasound (mm)
A-M-IL1	17.3	40.5	35.9
A-M-IL2	25.9	51.4	40.5
A-L-IL1	21.1	38.3	36.5
B-M-IL1	19.3	39.8	40.6
B-M-IL2	25.6	41.5	41.8
B-L-IL1	17.4	36.0	36.0

reported [39] that the depth of the dimple created by impact can be reduced by fatigue spectrum loading. Presumably, the spectrum loading included tensile loads which might be expected to pull the facesheet in the dimple back to the level of the rest of the facesheet. Periodic inspections would thus reveal only the size of the impact dimple, but loading could create additional damage or even reduce the size of the dimple. Thus the dimple size may not be a good indicator of the severity of the damage and the strength reduction due to the damage.

From the predictions of the dimple growth model and the observed dimple growth, it is clear that damage present in the impacted facesheet can critically affect the growth of the dimple. Only reducing the bending stiffness affects the predictions of the dimple growth model, but even then the predicted growth was small. Although a fourfold reduction of bending stiffness may seem very large, a facesheet with, for example, three of eleven ply interfaces delaminated, would be expected to have a bending stiffness which is considerably reduced from its original stiffness, depending on the through-thickness locations of the delaminations. The damage state of the panels is unknown, but it is clear that a substantial amount of damage exists. Although damage was observed in the two-ply facesheet specimens of Tsang, the damage was relatively simple and minor. A more complicated damage state could, and probably did, exist in the specimens of this investigation because of the multi-layer, multi-directional layup used. This damage reduced the local bending stiffness and perhaps the in-plane stiffness as well. Therefore, in order for the model to account for the growth, the damage state of the facesheets must be known and properly modeled.

7.4.2 Failure Prediction

Failure of impacted specimens has been predicted using the dimple growth model and using methods and data from notched specimens. However, the dimple growth model has been found to be inaccurate for the cases examined in this investigation. Because the model is not capable of modeling the dimple growth, the model is not used herein to predict failure of the specimens.

If the damage created by the impact event is considered as equivalent to a notch, the measured strength of notched specimens may be useful in predicting the failure strength of impacted specimens. Stress-strain behavior of the impacted specimens is similar to that of notched specimens in that strain gages located above or below the dimple consistently gave lower strain readings than those off of the vertical centerline. It makes sense that a gage located in-line with the impact damage would read a lower strain. The damaged region is less stiff than the surrounding undamaged material and thus carries less stress. The stress would have to "flow" around the impact zone and be concentrated in the material adjacent to the damaged area, much as a stress concentration occurs in a notched specimen. Also, failure of the notched and impacted specimens away from the dimple or notch was observed in both cases to be primarily an in-plane fiber-controlled failure directly along the y-axis. Thus, some similarity of the behavior and failure exists for the two cases. This may provide a justification for utilizing a notched failure criterion to correlate/predict the the strength of impacted specimens.

Three measured parameters of the impacted specimens could potentially be used as the damage size in a failure criterion: the initial dimple size, the final dimple width prior to failure, and the damage size in

the facesheet measured via ultrasound. All three parameters are used, and values of the three damage sizes are given in Table 7.8. The damage sizes are consistent among specimens of the same energy level. However, there is only a slightly greater damage size for the specimens impacted at level 2 than for those impacted at level 1. The predicted failure strengths using the Mar-Lin correlation with the dimple size and delamination size as damage sizes for the impacted specimens are shown in Table 7.9. The values used for the composite fracture parameter H_c are the average values for all specimens of the A and B layups, 528 and 517 $MPa \cdot mm^{0.28}$. Experimental values of failure stress are also included for comparison.

All three damage sizes provide reasonable predictions of the failure stress. Predictions made using the facesheet damage size are all ten percent or more lower than the actual values. Using the final dimple size provides predictions the same or slightly lower than those based on the facesheet damage size. However, the use of this parameter defeats the purpose of the simple engineering approach of using notched strength data because the maximum dimple width is difficult to measure and is not known prior to testing. Also, the use of this parameter is not consistent with the damage tolerant design approach because the failure is not predicted based on the initial damage present in the specimen. Finally, the dimple has been shown to return to nearly its initial shape even after extensive loading, suggesting that the initial dimple size is a good characterization of the dimple if not necessarily of the damage which leads to failure. Predictions made using the initial dimple size are within 7% of the experimental values. Predicted strengths are the same or slightly higher than the observed values for specimens impacted at level 1. For specimens impacted at level 2, predictions are slightly higher than the experimental strengths. This is not

Table 7.9 Predicted strength of impacted specimens using Mar-Lin correlation

Specimen	Predicted Failure Strength (MPa)			Experimental Failure Strength (MPa)
	Initial Dimple Width	Final Dimple Width	Facesheet Damage Width via Ultrasound	
A-M-IL1	238	187	194	238
A-M-IL2	212	175	187	204
A-L-IL1	225	190	193	>239
B-M-IL1	225	184	183	229
B-M-IL2	209	182	182	197
B-L-IL1	232	190	190	217

surprising as there was additional damage in level 2 specimens such as fiber breakage and surface cracking which was not directly related to the dimple size and is thus not accounted for by the Mar-Lin prediction.

Although all three damage sizes used in the Mar-Lin prediction provide reasonable predictions of the failure strength, this may be because the predicted failure strengths is quite insensitive to the damage size when it is larger than about 20 mm. For example, more than doubling the damage size of specimen A-M-IL1 from 17.3 mm (the initial dimple width) to 35.9 mm (the initial facesheet damage width) reduces the predicted strength by only about 20%. This insensitivity increases as damage size increases. Thus, using almost any damage size would provide reasonable predictions of failure stress in this regime.

Using notched strength data to predict the failure strength of impacted sandwich panels is a dubious proposition. The predictions made in this investigation using the dimple width as the damage parameter are very close to the experimental failure strengths. It is also true that the dimple in some sense behaves as a notch. The dimple cannot carry the same stress as the surrounding material, so the stress field is disturbed around the dimple as it would be around a notch. However, the damage mechanism for these specimens, dimple growth, was quite different from the observed behavior of the notched specimens and included out-of-plane damage and effects of the core. Although failure appears similar for the notched and impacted specimens, it is possible that the failure mechanisms at the notch tip are different from those adjacent to the dimple. It is also possible that two specimens could have the same dimple size but very different damage states. In that case, one would not expect their failure stresses to be the same. Furthermore, there is evidence that the size of the

dimple could remain the same or even shrink after loadings which could cause additional damage in the specimen. Thus, researchers and designers must be very careful in using the Mar-Lin correlation or any other form of notched strength data to predict the strength of impacted sandwich panels.

Chapter 8

Conclusions and Recommendations

The present work was conducted to investigate the effect of damage on the behavior of composite sandwich panels loaded in compression. Specifically, the research goals were to examine the stress field around the damage, to examine the effects of the finite size of the specimen on the stress field, to determine the mechanisms involved in the propagation of damage which leads to failure, and to determine the stress level at which failure occurs for specimens with different types and sizes of damage. In this chapter, conclusions are drawn from the present investigation and directions for future work are recommended.

The work conducted and particularly the discussion presented in Chapter 7 leads to the following conclusions from the present work:

1. Global bending of the specimens, with one exception, was insignificant based on the measurements of the mid-plane deflection.
2. For small specimens tested after alignment of the fixture by method 1, the misalignment of the fixture with respect to the loading axis resulted in an off-axis loading of the specimen as manifested in the behavior of the far-field strain gages and the photoelastic coating. Better alignment of the test fixture resulted in less variation in strain readings among the far-field gages, but some variation was inevitable because of the nature of the testing method. Because of its anti-symmetric nature, off-axis loading probably did not have a significant

effect on the failure stress of notched specimens.

3. Predictions of the photoelastic pattern made using an analytical solution for an elliptical hole are qualitatively similar to those observed, and the similarity increases as the notch length increases because an ellipse more closely approximates the notch as the length increases. Thus, the predictions made for the strain field around an ellipse can be used to determine the general strain field and thus aid in the evaluation of the size of proposed notched test specimens.
4. A region of low strain differential can develop near the potting line of the specimens due to the end constraint. This region can interact and merge with the region of low strain differential due to the notch. For the cases examined, this does not significantly affect the strain state near the notch, and thus effects of the finite length of the specimen are not significant in these cases.
5. Examination of the strain field shows that strain differentials along the notch line attain far-field values for much of the width of the specimen. Thus, effects of finite specimen width on the strain field near the notch are small. Based on direct comparison of specimens of different sizes with the same damage size, there is no effect of the specimen size on the failure stress for the cases considered.
6. Any compression specimen will behave as a structure to some degree. Also, the size of the specimen may affect the test results. Therefore, the property to be measured and the accuracy and precision desired in measuring it must be taken into account when designing a fixture and specimens.
7. A pattern of variation in the strain differential which matches the honeycomb core is observed with the photoelastic coating. This pattern

is likely due to the through-thickness waviness observed in the facesheets and individual plies due to the cocuring process. The ply waviness in the facesheets is also likely to be at least partially responsible for the measured modulus of the specimens being lower than the calculated modulus.

8. Specimens notched in both facesheets generally had failure stresses slightly lower than those with only one facesheet notched. This is likely due to small variations in the facesheets and slightly uneven loading of the facesheets. Thus, the condition of one or two facesheets notched should be viewed as a particular structural configuration.
9. Failure stresses are well correlated by the Mar-Lin correlation, especially for short notch lengths. At longer notch lengths, the predicted strengths are somewhat higher than those observed.
10. The composite fracture parameter H_c was found to decrease with increasing notch size. Thus, the Mar-Lin correlation should not be used to predict by extrapolation the strength of specimens with larger notches than those tested.
11. The dimple growth model of Tsang [45] significantly underpredicts the growth of the dimple caused by an impact event. This appears to be caused by the damage in the facesheets which reduces the local stiffness of the facesheet. Therefore, it is necessary to characterize fully the damage present in the impacted panel in order to predict accurately the dimple growth.
12. Dimple growth in specimens impacted at level 1 is generally smooth and regular. However, in those impacted at level 2, the dimple growth is highly irregular because of the extensive damage in the facesheets which seems to interact with and "guide" the growth of the dimple.

13. Even after extensive loading of the specimen, the dimple can return to nearly its original configuration when loading is removed. Because additional damage to the specimen can occur during such loading, the dimple size in the unloaded condition may not be a good predictor of the residual strength of the specimen.
14. Failure stresses for the impacted specimens are relatively well predicted using the Mar-Lin correlation with three different damage sizes present in the facesheet (initial dimple width, maximum dimple width, and width of facesheet damage as detected via ultrasound). However, in the regime of notches larger than about 20 mm, the predicted failure strength is quite insensitive to the notch length so that almost any damage size would provide a reasonable prediction.
15. The mechanisms for damage growth in the notched and impacted specimens are observed to be different. Thus, care must be taken when using any notched strength prediction method, such as the Mar-Lin correlation, to predict the strength of impacted sandwich panels.

The present work raises a number of issues which require further investigation. The following recommendations are therefore made:

1. Experimental and analytical tools to determine the end constraint imposed on a test specimen should be developed so that effects of finite specimen length can be examined.
2. In order to better determine effects of finite specimen width on the stress state, a more accurate prediction of the strain state should be developed by using a solution for an oval opening or a finite element model with measured elastic constants for the facesheets.

3. The effects of notching one or both facesheets in a sandwich panel should be further examined by an experimental program in which a statistically significant number of specimens of the same configuration with one or two facesheets notched are tested.
4. Additional failure stress data for specimens with large notch lengths are needed in order to determine the behavior when notches are long and to evaluate the suitability of notched strength prediction methods such as the Mar-Lin correlation over a large range of notch sizes.
5. As part of the damage tolerant design approach, the damage created in the facesheets and core of the sandwich panels by impact events should be well-determined prior to an evaluation of the residual strength.
6. The dimple growth model should be further developed to account for damage in the facesheets in order to predict accurately the dimple growth of specimens with facesheet damage.
7. Further examination of the dimple growth is needed. Specifically, the effects of loading to levels below the failure stress on the size of the dimple and the damage in the facesheet and core should be examined. Also, the effects of damage in the facesheet on the dimple growth should be examined.
8. Additional understanding of the failure of impacted sandwich specimens is needed. Specifically, further testing is needed to determine if a critical dimple width exists for specimens with a given initial damage state. Also, the observed similarity between the dimple size before failure and the initial damage size of damage in the facesheet should be investigated to determine if there is, indeed, a causal relationship between the two or if the similarity is merely coincidental. Most importantly, there is a need to understand the

mechanisms which cause failure in the impacted facesheet. A good understanding of the failure will allow the development of a failure prediction model which accounts for the mechanisms involved.

9. Until a model which accounts for the mechanisms involved in failure of impacted sandwich panels is developed, there is a need to determine under what conditions notched strength correlations are useful engineering tools for the prediction of post-impact strength.

References

1. Guynn, E. G. and Bradley, W. L., "Measurements of the Stress Supported by the Crush Zone in Open Hole Composite Laminates Loaded in Compression", *Journal of Composite Materials*, Vol. 8, March, 1989, pp. 133-149.

2. Guynn, E. G., Bradley, W. L., and Elber, W., "Micromechanics of Compression Failures in Open Hole Composite Laminates", *Composite Materials: Fatigue and Fracture, Second Volume, ASTM STP 1012*, ASTM, 1989, pp. 118-136.

3. Rhodes, M. D., Mikulas, M. M. J., and McGowan, P. E., "Effects of Orthotropy and Width on the Compression Strength of Graphite-Epoxy Panels with Holes", *AIAA Journal*, Vol. 22, No. 9, September, 1984, pp. 1283-1292.

4. Sohi, M. M., Hahn, H. T., and Williams, J. G., "The Effect of Resin Toughness and Modulus on Compressive Failure Modes of Quasi-isotropic Graphite/Epoxy Laminates", *Toughened Composites, ASTM STP 937*, ASTM, 1987, pp. 37-60.

5. Soutis, C. and Fleck, N. A., "Static Compression Failure of Carbon Fibre T800/924C Composite Plate with a Single Hole", *Journal of Composite Materials*, Vol. 24, May, 1990, pp. 536-558.

6. Soutis, C., Fleck, N. A., and Smith, P. A., "Failure Prediction Technique for Compression Loaded Carbon Fibre-Epoxy Laminates with Open Holes", *Journal of Composite Materials*, Vol. 25, November, 1991, pp. 1476-1498.

7. Soutis, C., Curtis, P. T., and Fleck, N. A., "Compressive Failure of Notched Carbon Fibre Composites", *Proceedings of the Royal Society, Series A - Mathematical and Physical Sciences*, Vol. 440, No. 1909, February, 1993, pp. 241-256.

8. Starnes, J. H. J., Rhodes, M. D., and Williams, J. G., "Effect of Impact Damage and Holes on the Compressive Strength of a Graphite/Epoxy Laminate", *Nondestructive Evaluation and Flaw Criticality for Composite Materials, ASTM STP 696*, ASTM, 1979, pp. 145-171.

9. Waas, A. M., Babcock, C. D. J., and Knauss, W. G., "Damage Progression in Compressively Loaded Laminates Containing a Circular Cutout", *AIAA Journal*, Vol. 29, No. 3, March, 1991, pp. 436-443.

10. Guynn, E. G. and Bradley, W. L., "A Detailed Investigation of the Micromechanisms of Compressive Failure in Open Hole Composite Laminates", *Journal of Composite Materials*, Vol. 23, May, 1989, pp. 479-504.

11. Whitney, J. M. and Nuismer, R. J., "Stress Fracture Criteria for Laminated Composites Containing Stress Concentrations", *Journal of*

Composite Materials, Vol. 8, July, 1974, pp. 251-265.

12. Nuismer, R. J. and Whitney, J. M., "Uniaxial Failure of Composite Laminates Containing Stress Concentrations", *Fracture Mechanics of Composites, ASTM STP 593*, ASTM, 1975, pp. 117-142.

13. Burns, S. W., Herakovich, C. T., and Williams, J. G., "Failure Modes for Compression Loaded Angle-ply Plates with Holes", *Fourth International Conference on Composite Structures*, Paisley College of Technology, Scotland, 1987, pp. 175-191.

14. Chang, F., Lessard, L., and Tang, J., "Compression Response of Laminated Composites Containing an Open Hole", *SAMPE Quarterly*, Vol. 19, No. 4, July, 1988, pp. 46-51.

15. Eriksson, I., "Strength of Notched and Unnotched Graphite/Epoxy Laminates Loaded in Compression", *Journal of Reinforced Plastics and Composites*, Vol. 10, May, 1989, pp. 222-255.

16. Joshi, S. P. and Huang, Y. W., "Damage Progression in the Vicinity of a Hole", *Proceedings of the American Society for Composites, Eighth Technical Conference*, Cleveland, OH, 1993, pp. 476-485.

17. Nuismer, R. J. and Labor, J. D., "Applications of the Average Stress Failure Criterion: Part II - Compression", *Journal of Composite Materials*, Vol. 13, January, 1979, pp. 49-60.

18. Tan, S. C., "Tensile and Compressive Notched Strength of PEEK Matrix Composite Laminates", *Journal of Reinforced Plastics and Composites*, Vol. 6, July, 1987, pp. 253-267.

19. Tan, S. C., "Notched Strength Prediction and Design of Laminated Composites Under In-Plane Loadings", *Journal of Composite Materials*, Vol. 21, August, 1987, pp. 750-780.

20. Tan, S. C., "Mixed-Mode Fracture of Notched Composite Laminates Under Uniaxial and Multiaxial Loading", *Engineering Fracture Mechanics*, Vol. 31, No. 5, 1988, pp. 733-746.

21. Tan, S. C. and Kim, R. Y., "Damage Accumulation and Fracture of Notched Composite Laminates Under Tensile and Compressive Loading", *Composite Materials: Testing and Design (Tenth Volume), ASTM STP 1120*, ASTM, 1992, pp. 414-427.

22. Awerbuch, J. and Madhukar, M. S., "Notched Strength of Composite Laminates: Predictions and Experiments - A Review", *Journal of Reinforced Plastics and Composites*, Vol. 4, January, 1985, pp. 3-159.

23. Mar, J. W. and Lin, K. Y., "Fracture of Boron/Aluminum Composites with Discontinuities", *Journal of Composite Materials*, Vol. 11, October, 1977, pp. 405-421.

24. Lagace, P. A., "Notch Sensitivity and Stacking Sequence of Laminated Composites", *Composite Materials: Testing and Design*

(Seventh Conference), ASTM STP 893, ASTM, 1986, pp. 161-176.

25. Tsai, S. W. and Wu, E. M., "A Generalized Theory of Strength for Anisotropic Materials", *Journal of Composite Materials*, Vol. 5, 1971, pp. 58-80.

26. Barenblatt, G. I., "The Mathematical Theory of Equilibrium Cracks in Brittle Fracture", *Advances in Applied Mechanics*, Vol. 7, 1960, pp. 55-129.

27. Dugdale, D. S., "Yielding of Steel Sheets Containing Slits", *Journal of Mechanics and Physics of Solids*, 1960, pp. 100-104.

28. Lo, K. H., Wu, E. M., and Konishi, D. Y., "Failure Strength of Notched Composite Laminates", *Journal of Composite Materials*, Vol. 17, 1983, pp. 384-398.

29. Levin, S. C., "Damage Tolerance Characteristics of Graphite/Epoxy Sandwich Laminates in Uni-Axial Tension", S.M. Thesis, TELAC Report 84-16, Massachusetts Institute of Technology, 1984.

30. Iki, K. N., "Notch Sensitivity of Graphite/Epoxy Under Compression", TELAC Report 87-13, Massachusetts Institute of Technology, 1987.

31. Lagace, P. A. and Vizzini, A. J., "The Sandwich Column as a Compressive Characterization Specimen for Thin Laminates", *Composite Materials: Testing and Design (Eighth Conference), ASTM*

STP 972, ASTM, 1988, pp. 143-160.

32. Abrate, S., "Impact on Laminated Composite Materials", *Applied Mechanics Review*, Vol. 44, No. 4, April, 1991, pp. 155-189.

33. Cantwell, W. J. and Morton, J., "The Impact Resistance of Composite Materials - A Review", *Composites*, Vol. 22, No. 5, September, 1991, pp. 347-362.

34. Llorente, S. and Gunther, C., "Damage Tolerance Evaluation of Sandwich Shear Panels", *National Specialists' Meeting on Advanced Rotorcraft Structures*, Williamsburg, VA, 1988, pp. 1-12.

35. Akay, M. and Hanna, R., "A Comparison of Honeycomb-core and Foam-core Carbon-fibre/Epoxy Sandwich Panels", *Composites*, Vol. 21, No. 4, July, 1990, pp. 325-331.

36. Rhodes, M. D., "Impact Fracture of Composite Sandwich Structures", *AIAA Paper 75-748*, 1975.

37. Llorente, S., Weems, D., and Fay, R., "Evaluation of Advanced Sandwich Structure Designed for Improved Durability and Damage Tolerance", *46th Annual Forum of the American Helicopter Society*, Washington, D.C., 1990, pp. 825-831.

38. Cairns, D. S. and Lagace, P. A., "A Consistent Engineering Methodology for the Treatment of Impact in Composite Materials",

Journal of Reinforced Plastics and Composites, Vol. 11, No. 4, 1992, pp. 395-412.

39. Levin, K., "Damage Tolerance of CFRP Sandwich Panels", The Aeronautical Research Institute of Sweden, 1988.

40. Adsit, N. R. and Waszczak, J. P., "Effect of Near-Visual Damage on the Properties of Graphite/Epoxy", *Composite Materials: Testing and Design (Fifth Conference), ASTM STP 674*, ASTM, 1979, pp. 101-117.

41. Caldwell, M. S., Borris, P. W., and Falabella, R., "Impact Damage Tolerance Testing of Bonded Sandwich Panels", *22nd International SAMPE Technical Conference*, Boston, MA, 1990, pp. 509-520.

42. Charles, J.-P. and Guedra-Degeorges, D., "Impact Damage Tolerance of Helicopter Sandwich Structures", *23rd International SAMPE Technical Conference*, Kiamesha Lake, NY, 1991, pp. 51-61.

43. Chen, C.-H., Chen, M.-Y., and Chen, J.-P., "The Residual Shear Strength and Compressive Strength of C/E Composite Sandwich Structure After Low Velocity Impact", *36th International SAMPE Symposium*, San Diego, CA, 1991, pp. 932-943.

44. Palm, T. E., "Impact Resistance and Residual Compression Strength of Composite Sandwich Panels", *8th International Conference on Composite Materials*, Honolulu, HI, 1991, pp. 3-G-1 to 3-G-14.

45. Tsang, P. H. W., "Impact Resistance and Damage Tolerance of Composite Sandwich Panels", Ph.D. Thesis, TELAC Report 94-5, Massachusetts Institute of Technology, 1994.

46. Tsang, P. H. W. and Lagace, P. A., "Failure Mechanisms of Impact-Damaged Sandwich Panels Under Uniaxial Compression", *Proceedings of the AIAA/ASME/ASCE/AHS/ASC 35th Structures, Structural Dynamics and Materials Conference*, Hilton Head, SC, 1994, pp. 745-754.

47. Minguet, P. J., "A Model for Predicting the Behavior of Impact-Damaged Minimum Gage Sandwich Panels Under Compression", *Proceedings of the AIAA/ASME/ASCE/AHS/ASC 32nd Structures, Structural Dynamics and Materials Conference*, Baltimore, MD, 1991, pp. 1112-1122.

48. Lekhnitskii, *Anisotropic Plates*, translated from the second Russian edition, Gordon and Breach, Science Publishers Inc., New York, 1968.

49. Fenner, D. N., "Stress Singularities in Composite Materials with an Arbitrarily Oriented Crack Meeting an Interface", *International Journal of Fracture*, Vol. 12, No. 5, October, 1976, pp. 705-721.

50. Tsang, P. H. W., "Impact Resistance of Graphite/Epoxy Sandwich Panels", S.M. Thesis, TELAC Report 89-12, Massachusetts Institute of Technology, 1989.

51. Zandman, F., Redner, S., and Dally, J. W., *Photoelastic Coatings*, Iowa State University Press, Ames, Iowa, 1977.

52. "Introduction to Stress Analysis by the PhotoStress Method", Tech Note TN-702-1, Photoelastic Division, Measurements Group, Inc., Raleigh, NC, 1989.

53. "Instructions for Bonding Flat and Contoured Photoelastic Sheets to Test Part Surfaces", Instruction Bulletin IB-223-C, Photoelastic Division, Measurements Group, Inc., Raleigh, NC, 1982.

54. Sciammarella, C. A., "The Moiré Method -- A Review", *Experimental Mechanics*, November, 1982, pp. 418-433.

55. Lagace, P. A., Brewer, J. C., and Varnerin, C., "TELAC Manufacturing Course Notes", TELAC Report 88-4B, Massachusetts Institute of Technology, 1990.

56. Vizzini, A. J., "An Efficient Algorithm to Characterize Stress-Strain Data Using Piecewise Linear Curves", *Journal of Testing and Evaluation*, Vol. 20, No. 2, 1992, pp. 126-131.

57. Lee, J.-W. and Harris, C. E., "A Deformation-Formulated Micromechanics Model of the Effective Young's Modulus and Strength of Laminated Composites Containing Local Ply Curvature", *Composite Materials: Testing and Design (Ninth Volume), ASTM STP 1059*, ASTM, 1990, pp. 521-563.

Appendix A

Specimen Designations

All specimens were assigned a simple designation describing their test conditions as detailed in Chapter 3. These designations are used throughout this document. However, medium and large specimens were also assigned a designation by the sponsor which has significance within the larger ATCAS program. Also, small specimens, which were cut from larger pieces, had a designation similar to the ATCAS designation. In this appendix, the two designations for each specimen are given together. For clarity, the designation "AK9" which proceeds each of the ATCAS designations is omitted. Those for the specimens of the A layup are given in Table A.1, while those for the specimens of the B layup are given in Table A.2.

Table A.1 Designations for specimens of the A layup

Specimen Designation	Boeing ATCAS Designation
A-S-Ua	A-13iv
A-S-Ub	A-13vi
A-S-SN3a	A-13ii
A-S-SN3b	A-13iii
A-S-DN3	A-14vi
A-S-SN6a	A-14vii
A-S-SN6b	A-13vii
A-S-DN6	A-14ii
A-S-SN10a	A-13i
A-S-SN10b	A-14iii
A-S-DN10	A-14iv
A-S-SN13a	A-14v
A-S-SN13b	A-14i
A-S-DN13	A-13v
A-M-U	A-7
A-M-DN25	A-12
A-M-DN51	A-11
A-M-IL1	A-8
A-M-IL2	A-10
A-L-SN25	A-6
A-L-DN25	A-1
A-L-DN76	A-3
A-L-IL1	A-2

Table A.2 Designations for specimens of the B layup

Specimen Designation	Boeing ATCAS Designation
B-S-Ua	B-13ii
B-S-Ub	B-13vi
B-S-SN3a	B-13v
B-S-SN3b	B-13i
B-S-DN3	B-14v
B-S-SN6a	B-14iii
B-S-SN6b	B-14ii
B-S-DN6	B-13iii
B-S-SN10a	B-13vii
B-S-SN10b	B-14vi
B-S-DN10	B-14iv
B-S-SN13a	B-14vii
B-S-SN13b	B-14i
B-S-DN13	B-13iv
B-M-SN25	B-7
B-M-DN25	B-12
B-M-DN51	B-11
B-M-IL1	B-8
B-M-IL2	B-10
B-L-SN25	B-6
B-L-DN25	B-1
B-L-DN76	B-3
B-L-IL1	B-2

Appendix B

Program Listing

The listing of the program ELLIPSE is given in this appendix. This program calculates the stresses and strains in an anisotropic plate with an elliptical hole subjected to a uniform far-field stress in the x-direction. The calculation follows the solution of Lekhnitskii [48]. The program is written in FORTRAN 77 and was compiled on a Macintosh IIci with the MPW shell.

```
      PROGRAM ELLIPSE

*     This program calculates the stresses and strains in an
*     anisotropic plate with an elliptical hole subjected to
*     a uniform far field stress in the x direction.  The
*     calculation follows the solution of Lekhnitskii.

*     Author:  Tracy Vogler
*     Date: 5/23/94

*     Copyright © 1994 Massachusetts Institute of Technology
*     Permission to use, copy and modify this software and
*     its documentation for internal purposes only and
*     without fee is hereby granted provided that the above
*     copyright notice and this permission appear on all
*     copies of the code and supporting documentation.  For
*     any other use of this software, in original or
*     modified form, including but not limited to,
*     adaptation as the basis of a commercial software or
*     hardware product or distribution in whole or in part,
*     specific prior permission and/or the appropriate
*     license must be obtained from MIT.  This software is
*     provided "as is" without any warranties whatsoever,
*     either expressed or implied, including but not limited
*     to the implied warranties of merchantability and
*     fitness for a particular purpose.  This software is a
*     research program, and MIT does not represent that it
*     is free of errors or bugs or suitable for any
*     particular task.


*     Input Files

*     ellipse.in  - input plate parameters, hole size, and
*                   stress
*     coords.in   - input x and y coordinates at which to
                    perform stress and strain calculations

*     Output Files

*     stress.out -  components of stress calculated for
*                   input x and y coordinates
*     strain.out -  components of strain calculated for
*                   input x and y coordinates
*     deltaep.out - difference of principal strains
*                   calculated for input x and y coordinates

*     Program Variables

*     i      - (complex) the imaginary number
*     u1, u2 - (complex) the roots of the characteristic
*              equation for the anisotropic plate
*     z1, z2 - (complex) complex coordinates of the form
*              z1 = x + u1*y
```

```
*     w1, w2 - (complex) intermediate step in calculation of
*              stress function values
*     root1, root2 - (complex) intermediate step for stress
*              functions
*     phi1p, phi2p - (complex) derivatives of the complex
*              stress functions at the point (x,y)
*     c1, c2 - intermediate step for stress functions
*     beta   - (complex) loading factor input for stress
*              functions
*     a      - (real) length of axis of ellipse along x axis
*     b      - (real) length of axis of ellipse along y
*              axis
*     x, y   - (real) coordinates of point in question
*     sigmax - (real) applied stress in the x direction
*     sx, sy, txy - (real) output values of stress at the
*              point (x,y)
*     epx, epy, gamxy - (real) output values of strain at
*              the point (x,y)
*     deltaep - (real) output value of the difference in
*              principal strains at (x,y)
*     j      - (integer) counting variable for DO loop to 10
*     n      - (integer) number of points at which to
*              calculate  stresses and strains to be read


c234567

      COMPLEX i, u1, u2, z1, z2, w1, w2, root1, root2,
      COMPLEX phi1p, phi2p, c1, c2, beta

      REAL a, b, x, y, sigmax, sx, sy, txy, epx, epy, gamxy,
      REAL deltaep

      INTEGER j, n

      OPEN (1, file = 'ellipse.in' )
      OPEN (2, file = 'coords.in'  )
      OPEN (3, file = 'stress.out' )
      OPEN (4, file = 'strain.out' )
      OPEN (5, file = 'deltaep.out')

**************************************************************
*                                                            *
*                    Begin Executables                       *
*                                                            *
**************************************************************

c234567
      i = (0., 1.)

*     Put headings in the output files
    1    FORMAT ( 7X, A, 14X, A, 13X, A, 12X, A, 11X, A )
    2    FORMAT ( 7X, A, 14X, A, 13X, A )
         WRITE (3, 1) 'X', 'Y', 'Sx', 'Sy', 'Txy'
```

```
      WRITE (4, 1) 'X', 'Y', 'Epx', 'Epy', 'Gamxy'
      WRITE (5, 2) 'X', 'Y', 'Deltaepsilon'

*     Read in the data and write it out
      READ (1,*)
      READ (1,*) a
      READ (1,*) b
      READ (1,*) u1
      READ (1,*) u2
      READ (1,*) ex
      READ (1,*) vxy
      READ (1,*) ey
      READ (1,*) vyx
      READ (1,*) gxy
      READ (1,*) sigmax

*     Print out entered values to the display
      WRITE (*,*) 'a   = ', a
      WRITE (*,*) 'b   = ', b
      WRITE (*,*) 'u1  = ', u1
      WRITE (*,*) 'u2  = ', u2
      WRITE (*,*) 'Ex  = ', ex
      WRITE (*,*) 'Ey  = ', ey
      WRITE (*,*) 'vxy = ', vxy
      WRITE (*,*) 'vyx = ', vyx
      WRITE (*,*) 'Gxy = ', gxy
      WRITE (*,*) 'Sigmax = ', sigmax

*     Loop through the program for each point (n total) to
*     be examined

      READ (2,*)
      READ (2,*) n
      WRITE (*,*) 'n = ', n

      DO 10 j = 1, n, 1

         READ (2, *) x, y


*        Calculate the complex variables
         z1 = x + u1 * y
         z2 = x + u2 * y

*        Calculate the stress function derivatives
*        Begin by the square root in the denominator, making
*        sure it lies in the positive imaginary half-plane

         w1 = z1*z1 - a*a - u1*u1 * b*b
         w2 = z2*z2 - a*a - u2*u2 * b*b

         root1 = CSQRT (w1)
         IF ( (AIMAG (root1) * AIMAG (z1)) .LT. 0) THEN
            root1 = -root1
```

```
            END IF

            root2 = CSQRT (w2)
            IF ( (AIMAG (root2) * AIMAG (z2) ) .LT. 0) THEN
               root2 = -root2
            END IF


*           Calculate the derivatives of the stress functions

            beta = -sigmax * b * i / 2.

            c1 = -beta*(a-i*u1*b)/(u1-u2)
            phi1p = c1 * (1.+z1/root1)/((z1+root1)*(z1+root1))

            c2 = beta*(a-i*u2*b)/(u1-u2)
            phi2p = c2 * (1.+z2/root2)/((z2+root2)*(z2+root2))


*           Calculate the stresses and write them to
*           the file "stress.out"

               sx = sigmax + 2.*REAL(u1*u1*phi1p + u2*u2*phi2p)

               sy = 2. * REAL ( phi1p + phi2p )

               txy = -2 * REAL (u1*phi1p + u2*phi2p)

               WRITE (3,*) x, y, sx, sy, txy

*           Calculate and write the strains to "strain.out"

               epx = sx/ex - vyx*sy/ey
               epy = -vxy*sx/ex + sy/ey
               gamxy = txy/gxy

               WRITE (4,*) x, y, epx, epy, gamxy

*           Calculate and write difference of principle strains
*           to the file "deltaep.out"

               deltaep = SQRT( gamxy**2 + (epx - epy)**2 )

               WRITE (5,*) x, y, deltaep


   10 CONTINUE

c234567

      END
```

Appendix C

Specimen Data

Data for the specimens tested in this investigation are given in this appendix. Measurements of the widths of the sandwich specimens at the three locations given in Chapter 5 are given for the A specimens in Table C.1, while the measurements for the B specimens are given in Table C.2. A summary of the specimen sizes, testing configuration, instrumentation scheme, and failure stress is given for the A specimens in Table C.3 and for the B specimens in Table C.4.

Table C.1 Measured widths of A specimens

Specimen	Width 1 (mm)	Width 2 (mm)	Width 3 (mm)
A-S-Ua	50.90	51.06	51.06
A-S-Ub	50.96	51.12	51.09
A-S-SN3a	51.00	51.57	51.59
A-S-SN3b	50.68	50.79	50.84
A-S-DN3	50.97	51.01	50.99
A-S-SN6a	50.88	51.01	50.96
A-S-SN6b	51.00	51.17	51.12
A-S-DN6	50.78	50.90	51.00
A-S-SN10a	50.84	50.90	50.90
A-S-SN10b	51.06	51.38	51.28
A-S-DN10	50.90	50.86	50.96
A-S-SN13a	50.94	51.15	51.14
A-S-SN13b	51.39	51.72	51.72
A-S-DN13	50.88	50.93	50.87
A-M-U	203.35	203.43	203.73
A-M-DN25	203.25	203.33	203.76
A-M-DN51	203.54	203.50	203.54
A-M-IL1	203.86	203.53	203.33
A-M-IL2	203.25	203.38	203.25
A-L-SN25	381.0	380.6	380.6
A-L-DN25	380.6	381.0	380.6
A-L-DN76	381.4	381.4	380.6
A-L-IL1	380.6	380.6	380.6

Table C.2 Measured widths of B specimens

Specimen	Width 1 (mm)	Width 2 (mm)	Width 3 (mm)
B-S-Ua	50.93	51.10	51.11
B-S-Ub	51.01	51.18	51.12
B-S-SN3a	50.94	50.94	50.85
B-S-SN3b	50.91	51.00	50.99
B-S-DN3	51.32	51.37	51.29
B-S-SN6a	51.57	51.63	51.64
B-S-SN6b	51.01	51.06	50.90
B-S-DN6	50.84	50.91	50.88
B-S-SN10a	50.78	51.02	50.98
B-S-SN10b	51.74	51.89	51.81
B-S-DN10	51.60	51.72	51.65
B-S-SN13a	50.94	50.72	50.95
B-S-SN13b	51.13	51.20	51.11
B-S-DN13	50.82	51.12	51.16
B-M-SN25	203.66	203.56	203.51
B-M-DN25	203.50	203.56	204.22
B-M-DN51	203.71	203.56	203.48
B-M-IL1	203.81	203.91	203.40
B-M-IL2	203.53	203.56	203.33
B-L-SN25	379.8	380.2	379.8
B-L-DN25	380.6	379.4	379.8
B-L-DN76	380.6	379.8	379.8
B-L-IL1	380.2	380.2	380.2

Table C.3 Summary of information for specimens of the A layup

Specimen Designation	ATCAS Designation	Specimen Width (mm)	Notch Length [a] (mm)	Impact Level [b]	Strain Gage Scheme[c]	Failure Stress (MPa)
A-S-Ua	A-13iv	51.0	-	-	U1	465
A-S-Ub	A-13vi	51.1	-	-	U3	518
A-S-SN3a	A-13ii	51.4	3.8	-	N2	409
A-S-SN3b	A-13iii	50.8	3.1	-	N2	384
A-S-DN3	A-14vi	51.0	3.4	-	N3	391
A-S-SN6a	A-14vii	51.0	6.5	-	N2	313
A-S-SN6b	A-13vii	51.1	6.3	-	N2	316
A-S-DN6	A-14ii	50.9	6.7	-	N3	324
A-S-SN10a	A-13i	50.9	9.6	-	N2	359
A-S-SN10b	A-14iii	51.2	9.4	-	N2	311
A-S-DN10	A-14iv	50.9	9.5	-	N3	285
A-S-SN13a	A-14v	51.1	13.8	-	N1	255
A-S-SN13b	A-14i	51.6	12.2	-	N2	268
A-S-DN13	A-13v	50.9	12.9	-	N3	235
A-M-U	A-7	203.5	-	-	U4	377
A-M-DN25	A-12	203.5	25.9	-	N3	193
A-M-DN51	A-11	203.5	51.2	-	N3	145
A-M-IL1	A-8	203.6	-	1	Impact	238
A-M-IL2	A-10	203.3	-	2	Impact	204
A-L-SN25	A-6	380.4	25.4	-	N3	>239
A-L-DN25	A-1	380.7	25.4	-	N3	188
A-L-DN76	A-3	381.1	76.6	-	N3	131
A-L-IL1	A-2	380.6	-	1	Impact	>239

[a] Measured length of notch or average of measured notch lengths if both sides are notched.

[b] Level 1 or Level 2

[c] U1 = Undamaged 1, U3 = Undamaged 3, U4 = Undamaged 4, N1 = Notch 1, N2 = Notch 2, N3 = Notch 3

Table C.4 Summary of information for specimens of the B layup

Specimen Designation	ATCAS Designation	Specimen Width (mm)	Notch Length [a] (mm)	Impact Level [b]	Strain Gage Scheme [c]	Failure Stress (MPa)
B-S-Ua	B-13ii	51.0	-	-	U1	451
B-S-Ub	B-13vi	51.1	-	-	U2	329
B-S-SN3a	B-13v	50.9	3.1	-	N2	439
B-S-SN3b	B-13i	51.0	3.3	-	N3	393
B-S-DN3	B-14v	51.3	3.4	-	N3	368
B-S-SN6a	B-14iii	51.6	6.1	-	N2	316
B-S-SN6b	B-14ii	51.0	6.3	-	N2	349
B-S-DN6	B-13iii	50.9	6.7	-	N2	275
B-S-SN10a	B-13vii	50.9	9.8	-	N2	320
B-S-SN10b	B-14vi	51.8	9.8	-	N2	298
B-S-DN10	B-14iv	51.7	9.8	-	N3	245
B-S-SN13a	B-14vii	50.9	12.1	-	N1	270
B-S-SN13b	B-14i	51.1	13.1	-	N2	250
B-S-DN13	B-13iv	51.0	12.8	-	N2	225
B-M-SN25	B-7	203.6	25.9	-	N3	204
B-M-DN25	B-12	203.4	25.6	-	N3	202
B-M-DN51	B-11	203.6	51.0	-	N3	147
B-M-IL1	B-8	203.7	-	1	Impact	229
B-M-IL2	B-10	203.5	-	2	Impact	197
B-L-SN25	B-6	379.9	25.4	-	N3	213
B-L-DN25	B-1	379.9	25.5	-	N3	212
B-L-DN76	B-3	380.1	76.3	-	N3	130
B-L-IL1	B-2	380.2	-	1	Impact	217

[a] Measured length of notch or average of measured notch lengths if both sides are notched.

[b] Level 1 or Level 2

[c] U1 = Undamaged 1, U2 = Undamaged 2, N1 = Notch 1, N2 = Notch 2, N3 = Notch 3

Appendix D

Slopes of Stress-Strain Curves

Initial slopes of the stress-strain curves for the strain gages of all specimens tested are given in this appendix. Slopes for the gages of the undamaged specimens with strain gage configurations Undamaged 1 and Undamaged 2 are given in Tables D.1 and D.2, respectively. Slopes for the gages of the undamaged specimens with strain gage configurations Undamaged 3 and Undamaged 4 are given in Table D.3. Slopes for gages of specimens with strain gage configurations Notch 1, Notch 2, and Notch 3 are given in Tables D.4, D.5, and D.6, respectively. Slopes for the gages of the impacted specimens are given in Table D.7.

Table D.1 Initial slopes [a] for strain gages of undamaged specimens with strain gage configuration Undamaged 1

	Strain Gage				
Specimen	1	2	3	4	5
A-S-Ua	53.1	47.4	42.7	48.7	47.4
B-S-Ua	65.7	53.2	49.3	56.7	54.7

[a] All values in GPa.

Table D.2 Initial slopes [a] for strain gages of the undamaged specimen with strain gage configuration Undamaged 2

	Strain Gage					
Specimen	1	2	2B	3	4	4B
B-S-Ub	69.4	62.8	49.5	62.7	62.7	54.4

[a] All values in GPa.

Table D.3 Initial slopes [a] for strain gages of undamaged specimens with strain gage configuration Undamaged 3 and Undamaged 4

	Strain Gage					
Specimen	1	1B	2	2B	3	3B
A-S-Ub	52.3	52.8	53.0	-	54.3	47.6
A-M-U	56.2	56.9	50.0	51.3	44.5	45.2

[a] All values in GPa.

Table D.4 Initial slopes [a] for strain gages of undamaged specimens with strain gage configuration Notch 1

	Strain Gage		
Specimen	1	2	3
A-S-SN13a	46.3	56.3	-
B-S-SN13a	51.1	66.1	61.1

[a] All values in GPa.

Table D.5 Initial slopes [a] for strain gages of notched specimens with strain gage configuration Notch 2

	Strain Gage				
Specimen	1	2	3	4	5
A-S-SN3a	37.9	46.8	52.0	55.3	44.1
A-S-SN3b	48.5	58.4	50.6	50.2	45.6
A-S-SN6a	27.1	36.1	43.7	55.2	43.5
A-S-SN6b	29.4	41.6	46.1	55.0	40.9
A-S-SN10a	27.0	37.1	45.6	54.3	42.3
A-S-SN10b	23.3	42.6	47.4	42.8	58.8
A-S-SN13b	28.1	41.0	45.9	60.4	42.5
B-S-SN3a	48.8	53.2	60.4	61.7	48.2
B-S-SN6a	26.5	37.5	53.5	64.9	58.1
B-S-SN6b [b]	-	-	-	-	-
B-S-DN6 [b]	-	-	-	-	-
B-S-SN10a	37.3	51.5	56.7	67.0	52.6
B-S-SN10b	30.0	38.4	53.7	63.9	54.0
B-S-SN13b	33.5	46.9	52.3	69.4	58.6
B-S-DN13	30.2	41.9	54.5	59.6	49.8

[a] All values in GPa.

[b] No well-established linear region observed.

Table D.6 Initial slopes [a] for strain gages of notched specimens with strain gage configuration Notch 3

	Strain Gage					
Specimen	0	1	2	3	4	5
A-S-DN3	40.1	48.1	47.6	47.3	45.7	38.6
A-S-DN6	28.6	38.4	49.3	50.1	49.3	44.9
A-S-DN10	33.3	38.5	48.2	42.9	42.9	45.3
A-S-DN13	29.6	37.1	52.0	47.3	51.6	40.0
A-M-DN25	14.5	25.0	47.4	49.0	46.1	46.1
A-L-SN25	16.1	25.4	52.1	51.1	56.0	53.1
A-L-DN25	18.8	33.3	52.3	51.4	59.4	56.0
A-M-DN51	10.4	15.2	54.4	43.2	53.2	43.5
A-L-DN76	9.4	16.2	42.0	52.0	48.8	46.6
B-S-SN3b	49.0	59.7	63.4	58.4	65.3	59.4
B-S-DN3	47.3	58.9	60.1	52.8	66.8	53.7
B-S-DN10	30.6	40.0	61.5	57.5	59.0	49.8
B-M-SN25	17.5	29.3	68.3	64.3	58.5	55.6
B-M-DN25	18.0	30.2	56.8	62.3	56.1	53.8
B-L-SN25	21.2	34.9	56.0	57.3	81.7	64.0
B-L-DN25	17.6	36.8	63.0	55.8	58.4	66.5
B-M-DN51	12.8	26.1	64.1	49.5	57.2	58.5
B-L-DN76	14.3	22.3	60.4	51.3	50.8	57.6

[a] All values in GPa.

Table D.7 Initial slopes [a] for strain gages of impacted specimens with strain gage configuration Impact

	Strain Gage					
Specimen	1	2	3	4	5	6
A-M-IL1	45.4	42.0	47.9	42.8	53.3	46.9
A-M-IL2	50.8	40.4	59.1	40.9	54.5	50.0
A-L-IL1	49.9	43.0	53.5	46.4	47.5	52.2
B-M-IL1	56.3	52.1	61.1	54.6	56.6	48.4
B-M-IL2	59.4	46.5	71.6	58.8	63.8	57.5
B-L-IL1	53.0	48.0	56.5	55.0	56.8	59.7

[a] All values in GPa.